THE EVOLUTION OF MASSIVE YOUNG STELLAR OBJECTS IN THE LARGE MAGELLANIC CLOUD

BY

JONATHAN PRESTON SEALE

DISSERTATION

Submitted in partial fulfillment of the requirements
for the degree of Doctor of Philosophy in Astronomy
in the Graduate College of the
University of Illinois at Urbana-Champaign, 2010

Urbana, Illinois

Doctoral Committee:

Associate Professor Leslie Looney, Chair
Professor You-Hua Chu
Assistant Professor Tony Wong
Robert Gruendl, Ph.D.

Abstract

This thesis presents an analysis of the largest catalog to date of infrared spectra of massive young stellar objects in the Large Magellanic Cloud. Evidenced by their very different spectral features, the luminous objects span a range of evolutionary states from those most embedded in their natal molecular material to those that have dissipated and ionized their surroundings to form compact HII regions and photodissociation regions. We quantify the contributions of the various spectral features using the statistical method of principal component analysis. Using this analysis, we classify the YSO spectra into several distinct groups based upon their dominant spectral features: silicate absorption (S Group), silicate absorption and fine-structure line emission (SE), polycyclic aromatic hydrocarbon (PAH) emission (P Group), PAH and fine-structure line emission (PE), and only fine-structure line emission (E). Based upon the relative numbers of sources in each category, we are able to estimate the amount of time massive YSOs spend in each evolutionary stage. We find that approximately 50% of the sources have ionic fine-structure lines, indicating that a compact HII region forms about half-way through the YSO lifetime probed in our study. Of the 277 YSOs we collected spectra for, 41 have ice absorption features, indicating they are surrounded by cold ice-bearing dust particles. We have decomposed the shape of the ice features to probe the composition and thermal history of the ice. We find that most the CO_2 ice is embedded a polar ice matrix that has been thermally processed by the embedded YSO. The amount of thermal processing may be correlated with the luminosity of the YSO. Using the *Australia Telescope Compact Array,* we imaged the dense gas around a

subsample of our sources in the HII complexes N44, N105, N113, and N159 using HCO^+ and HCN as dense gas tracers. We find that the molecular material in star forming environments is highly clumpy, with clumps that range from subparsec to ~2 parsecs in size and with masses between 10^2 to 10^4 solar masses. We find that there are varying levels of star formation in the clumps, with the lower-mass clumps tending to be without massive YSOs. These YSO-less clumps could either represent an earlier stage of clump to the more massive YSO-bearing ones or clumps that will never form a massive star. Clumps with massive YSOs at their centers have masses larger than those with massive YSOs at their edges, and we suggest that the difference is evolutionary: edge YSO clumps are more advanced than those with YSOs at their centers. Clumps with YSOs at their edges may have had a significant fraction of their mass disrupted or destroyed by the forming massive star. We find that the strength of the silicate absorption seen in YSO IR spectra feature is well-correlated with the on-source HCO^+ and HCN flux densities, such that the strength of the feature is indicative of the embeddedness of the YSO. We estimate that ~40% of the entire spectral sample has strong silicate absorption features, implying that the YSOs are embedded in circumstellar material for about 40% of the time probed in our study.

To my family

Acknowledgments

Having spent 20 years in school, I am amazed – and frankly thrilled – that it is over. It has been a long and sometimes rough ride, one that I never could have completed alone. Along the way there have been many people who have helped me in a number of ways (academically, personally, financially, grammatically), and before the main text of this thesis I want to express my heartfelt gratitude to the many people that made it possible.

It is difficult to overstate my gratitude to my Ph.D. advisor Professor Leslie Looney. Leslie is among the most enthusiastic people I know, a quality that makes him a great instructor and an even better mentor. I will miss his constant encouragement and weekly demands to "work harder." He was a great source of knowledge, academic inspiration, and sound advice that I would have been lost without. Leslie opened many doors for me academically by going above and beyond the typical duties of an advisor. But most of all, I want to thank him for his friendship and for getting lost with me in Gerringong, Australia.

I would also like to thank the many instructors I have had over the course of my academic career including my high school teachers (especially Mrs. Dutter and Mrs. Pickert), my undergraduate instructors, and my graduate professors. I am particularly grateful for Mrs. King, my middle school Target teacher, who was the first teacher to challenge me to reach my full potential. For their advice and kind assistance with writing letters, I wish to thank Tony Wong, You-Hua Chu, and Leslie Looney.

This thesis would not have been possible without the support of my collaborators. First and foremost, I need to thank Robert Gruendl for all the research help he provided the last five

years. Thank you for putting up with my questions and for all you taught me. I also thank collaborator and department chair You-Hua Chu for her informative classes as both an undergraduate and a graduate student, for her insightful discussions about the LMC, and her tasty homemade snacks. I thank Tony Wong for his invaluable insights, his help with ATCA data, and for involving me in his MAGMA projects. It was an honor to have Brian Fields on my preliminary exam committee, and I thank him for his involvement. I am grateful to have worked with Remy Idebetouw and Rosie Chen and hope to continue our collaborations. I wish to thank all those who have worked on the *Spitzer Space Telescope* and the *Australia Telescope Compact Array* whose data I have used in this thesis. I also thank all those involved with the *CARMA* summer school program as it was an important component of my interferometry education.

It has been a pleasure to be a part of both the physics and astronomy departments at the University of Illinois for eight years, and I owe the departments and the University as a whole a debt of gratitude. In physics, Linda Lorenz was invaluable to navigating the undergraduate bureaucratic world. The astronomy department made special accommodations to invite me to the department as a graduate student, and for that I will be forever grateful. I also owe a big thanks to Bryan Dunne, Mary Margaret O'Connor, Sandie Osterbur, Jeri Cochran, and Kevin Pointer for making the more confusing aspects of large university academia a little easier. I wish to single out Jeri Cochran for all her individualized help over the years; there is no problem she cannot fix. I will also miss her company, friendship, and Project Runway discussions.

I want to thank all of the astronomy graduate students at the University of Illinois for their support and friendship. I will especially miss the students in my class. I will miss playing softball

with Nick Indriolo and having long conversations with Nick Hackobian over the subtleties of interferometry and Donnie Darko. I will miss Brett Hayes and his great parties. I thank Hsin-Fang Chiang for being a sounding board for ideas and a great friend. Anyone who knows Amy Lien knows how fun she is to hang out with, and I will miss her laughter and her funny freeze-dried food. I also want to thank the several office mates I have had over the years: Rosie Chen, Bryan Dunne, Karen Yang, Katherine Lee, and David Rebolledo. I want to thank my dear friend Jana Bilikova for being a great neighbor, for accompanying me to the grocery store and 'Lil Porgy's, and for co-hosting all those parties. I thank former graduate students Britt Lundgren and Ashley Ross for introducing me to Fiesta Cafe and recreational softball. I know all of our paths will cross again in the small community that it astronomy, and I'm excited to see where we all go from here. I am happy to have you as colleagues and friends.

I thank my OETRTA friends for their support and for being an escape from my worries. To Jon Meyer and Joe Niedbalski, our time spent living together at Six Theta were the best years of my life. Jenny Reber, thank you for being my Sunday night movie companion and one of the most fun people I know. Michael Kirk and Marci Beals, thank you for introducing me to Sullivan, Illinois and Amish fireworks. I value your friendship and wish you all the best. My thanks to Edward Chen for photographically documenting the past eight years of my life and for being the kindest human being I've ever known. Thank you to Lana Stenger for everything. You have been a terrific friend and confidant, and I feel so lucky to have met you. I thank Carole Heisel for being so caring and for always being willing to listen and give advice. Finally, I thank Scott Guybrush Seaholm, a guy I have never lived within two hours of, yet who has become of of my

nearest and dearest friends. I love you all.

I met Joya Banerjee in second grade, and we have been best friends ever since. She has been with me through it all, and I prize her friendship as among the greatest assets of my life. Joya, I thank you for being such a wonderful friend.

Of course, I would be nowhere without the love and support of my family, to whom this thesis is dedicated. I owe my love for science to my dad Steven Seale and my grandfather Jules Paape. Dad, thank you for fostering my interest in science by taking me to the Kennedy and Huntsville Space Centers, growing crystals in a bucket in the laundry room, putting stars on my bedroom ceiling, and encouraging me to work hard in school. But most of all, thanks for being my dad, and for your endless love and kindness. My grandfather's appreciation for learning and knowledge is unparalleled. Gramp, thank you for your words of encouragement all these years and for setting an example for the man I hope to one day be. I also want to dedicate this work to my grandparents who are no longer with us, Jean Paape, Margarite Seale, and Thomas Seale.

I thank my parents Pat and Ken Dunwoody for their endless support and encouragement. You were both always there for me when I needed it most. I thank you for your counsel along the way and most of all your love. I am truly lucky. I also thank Tammy Seale. Tammy, I am grateful to have you in my life. I also thank my grandparents Ken and Marilyn Dunwoody for always encouraging me to work hard and for being proud of me no matter what. I am lucky to have them in my life. I also send thanks to Barbara and Brooks Herrold, Tony and Wally Marquardt, Jacqueline and Brian Smith, Chelsea and Josh Morris, and Brian and Lisa Holland. I have been blessed with a large and wonderful family, to whom I express my deepest gratitude.

TABLE OF CONTENTS

Chapter 1

Introduction

1.1 Massive Stars Play Massive Roles

Massive stars play a fundamental role in astrophysics at all stages of their evolution, and the full extent of this role has become even more apparent in recent years. At the most direct level, massive stars are of interest to the study of stellar evolution (see recent review by Woosley et al. 2002) and stellar feedback to the local environment (e.g., Bate et al. 2009; Wang et al. 2010), but massive stars as a population also play a major role in the structure and evolution of the interstellar medium (ISM; e.g., McCray & Kafatos 1987); the formation, metallicity, and evolution of galaxies (e.g., Ceverino 2009); and the reionization of the universe (see recent review by Barkana et al. 2001). Moreover, massive stars are the precursors to supernovae (see recent review by Janka 2007), neutron stars, and black holes (see the text by Shapiro & Teukolsky 1983), making them of particular importance in high-energy astrophysics and cosmology, including determining the rate of expansion of the universe (e.g., Kowalski 2008; Perlmutter 1999).

Despite their obvious importance, our understanding of the formation of massive stars is incomplete. There are several reasons for this, most of them related to observational difficulties.

Massive stars form within high-extinction regions, making them difficult to observe during critical early formation processes. Given the nature of the initial mass function (IMF; see recent review by Chabrier 2003), massive stars are also exceedingly rare; for every 1000 stars of approximately solar mass (0.5 – 2 solar masses), there are only about two dozen massive stars (> 8 solar masses). This makes identifying objects to study difficult. Exacerbating the scarcity of targets problem is their relatively short formation time and lifetime. The relative rarity of sources is partially offset by their high luminosity, which allows them to be detected in extragalactic environments, a property we exploit in this thesis.

Our problems with understanding massive star formation are also theoretical. While a theoretical physical picture of low-mass star formation is now generally agreed upon (see reviews by Andre, Ward-Thompson, & Barsony 2000; McKee & Ostriker 2007), the formation of massive young stellar objects (YSOs) cannot simply be a scaled-up version of the low-mass process. Unlike low-mass stars, high-mass stars begin hydrogen burning before the end of accretion (e.g., Zinnecker & Yorke 2007), which leads to two powerful feedback effects that to not apply to low-mass star formation – radiation pressure on and photoioniztion of the local ISM. Furthermore, their formation typically (perhaps always) takes place in clusters (Tan 2005) such that the interaction with nearby forming stars in the cluster environment may be important to their evolution.

Despite these difficulties, in the last few years a general picture of massive star formation has emerged from both an observational and theoretical perspective (see recent reviews by Churchwell 2002; Beuther et al. 2006; Zinnecker & Yorke 2007; Garay 2004). Below, we briefly

review the basic stages of massive star formation as they are understood today and explain how the research presented in this thesis increases our understanding of the evolution of a massive forming star.

1.2 Stages of Massive Star Formation

1.2.1 The Initial Conditions: Molecular Clouds, Clumps, and Cores

The largest structures within the Galaxy are Giant Molecular Clouds (GMC), which have sizes of 10's to 100's of pc, masses of 10^4 to 10^6 solar masses, and temperatures of 10 – 15 K (Shu et al. 1987). The most important characteristic of GMCs to the process of star formation is that they are clumpy and contain substructures on all spatial scales. The literature contains a confused lexicon of terminology to describe the GMC substructure including various definitions for "cores," "clumps," "condensations," "fractals," and "turbulent structures." In this thesis, we will adopt the terminology described by Williams et al. 2000. We define clumps to be parsec-scale structures with masses of several hundred to thousand solar masses and mean densities of ~10^5 cm^{-3}. Following the fractal nature of molecular cloud structure, cores are the substructures of clumps; they have masses and radii ~10 smaller than clumps and densities ~100 times higher. Under these definitions, clumps are the structures associated with cluster formation while cores form single stars or tight, gravitationally-bound systems. We may also refer more generally to circumstellar envelopes, by which we mean the dense circumstellar material surrounding the forming star.

These massive clumps and cores were observationally inaccessible until fairly recently;

historically, star formation research had focused on objects in later stages of evolution because their mid-infrared (IR) emission from hot dust warmed by an embedded source was more readily observable. The earliest stages of massive star formation, before an embedded heating source forms, went undetected because astronomers lacked an instrument capable of identifying them. The basic observational characteristics of dense, star-less clumps and cores should be that they are strong cold dust emitters at sub-mm wavelengths coupled with non-detections at mid-IR wavelengths indicating they have yet to form a star that can warm its environment. Since the advent of the *Infrared Space Observatory* (*ISO,* Kessler et al. 1996), the *Midcourse Space Experiment* (*MSX*; Mill et al. 1994), and later the *Spitzer Space Telescope* (*SST*; Werner et al. 2004), a large number of objects have been identified as candidates for the precursors of star formation sites. Coined Infrared Dark Clouds (IRDCs), Perault et al. (1996) was the first to identify these objects – which they estimated to have an A_V of greater than 25 – by their strong absorption at 15 microns against the Galactic background of mid-IR emission. Consistent with cold dust, IRDCs are emitters in the sub-mm; Lis & Menten (1998) fit a grey body to sub-mm observations of the Galactic center's dust ridge M0.25+0.11, a mid-IR absorber, and obtained the low temperature of ~18 K.

The first major survey of Galactic IRDCs was conducted by Egan et al. (1998) using *MSX*, who found ~2000 compact objects that were identified via their absorption against the bright mid-IR emission from the Galactic plane. Combined with IRAS images, the observations showed that IRDCs appeared to be dark from the optical all the way to the far-IR at about 100 microns. Follow-up observations using dense gas tracers such as NH_3 and H_2CO showed IRDCs

are cold (T < 20 K), have densities in excess of 10^5 cm $^{-3}$, sizes of 0.25-0.5 pc, and typical masses of hundreds to thousands of solar masses (e.g., Carey et al. 1998). In the coldest and densest regions of the clouds, molecules are depleted from the gas phase onto dust grains (Bergin et al. 1995); once an IR-emitting source has formed within the clump, these ices can absorb thermal radiation at mid-IR wavelengths and are an excellent indicator for a highly embedded young star (e.g., Boogert 2008, Pontoppidan et al. 2008). Indeed, in this thesis we exploit the ice absorption features in the spectra of massive YSOs to explore the thermal history of the circumstellar material. Coupled with their cold temperatures, IRDCs have narrow line-widths, suggesting they are not only very cold, but also devoid of embedded sources that can inject turbulence into or warm the clump (Sridharan et al. 2005). Conversely, the dense molecular gas associated with later stage massive star formation (stages where an embedded object has begun to heat or ionize its surroundings) has been found to have wider line-widths. While high-mass protostellar objects (HMPOs) and ultracompact HII regions (UCHIIs) have line widths of 2.1 and 3.0 km s^{-1}, respectively (Churchwell et al. 1990), those of IRDCs are found to have a mean of ~1.6 km s^{-1} (Sridharan et al. 2005).

IRDCs are an observational class of object (and a poorly-defined one), and they therefore do not all necessarily represent the same type of physical object. They may harbor several different evolutionary stages including not only true high-mass starless cores (HMSC), but also later stage objects that contain low- or intermediate-mass stars, or even the youngest high-mass protostellar objects (HMPO). Indeed, Lis et al. (1994) found that an H_2O maser – a signpost of the early stages of massive star formation after the creation of a protostar (see Section 1.2.3) – is

associated with the aforementioned IRDC M0.25+0.11. So while HMSCs are important for studying the initial conditions of massive star formation, the later stages are important to understanding the evolution of the clumps and how the clump is modified by the forming star. In this thesis, we have used dense molecular gas tracers to probe clumps both with and without signposts of active massive star formation to better understand the properties of clumps that lead to star formation and the manner and time scale at which the clumps evolve.

1.2.2 The Formation of an Accreting Protostar

How exactly the dense molecular material collapses to form a protostar remains one of the greatest outstanding questions in massive star formation. Two primary theoretical models have emerged: monolithic collapse and competitive accretion. In the monolithic collapse model (Yorke & Sonnhalter 2002), a core is envisioned as a long-lived, turbulence-supported, quasi-equilibrium dense molecular condensation within the larger molecular cloud that forms a massive star. Under this model, all the material that becomes part of the final star is first contained within the natal core. In the alternate competitive accretion model (Bonnell et al. 1997), the material for the final star not only comes from the core, but is also accreted from the larger clump. Because there are presumably several stars forming within the clump to form a cluster, each forming star is essentially competing for material. Stars located towards the center of the clump and cluster are located within the deepest gravitational potential well, and therefore can accrete more material, forming more massive stars. In this way, the competitive accretion model promotes the runaway effect whereby massive stars become more massive because they have a gravitational advantage

in the competition for material.

Both models make a number of predictions about the properties of very young clusters; however because of the high density and extinction of the surrounding material, these early formation stages are exceedingly difficult to capture observationally. In this thesis we make no assumptions nor come to any conclusions as to the correct accretion model. The young massive stars we have investigated have already progressed beyond these initial core collapse stages, have formed a massive star, and have already begun to heat, ionize, or blow away their surroundings.

No matter the precise process that leads up to the collapse of a portion of a molecular cloud, to form a star, gravity must at some point overcome the gas's support from thermal motion, internal turbulence, magnetic fields, and rotation. Once the gravity dominates the various repulsive forces, the gas collapses on a free-fall timescale (Shu, Adams & Lizano 1987). Collapse eventually stops when the gas becomes optically thick and the energy released from collapse matches the cloud's ability to radiatively lose the energy thermally (Larson 1969). As material continues to rain onto this core, the central object grows in mass, first forming a low-mass, then a intermediate-mass, and finally a young massive star.

1.2.3 Massive Embedded Young Stellar Objects: Masers, Hot Cores, and HII Regions

A young, accreting protostar contracts on the thermal Kelvin-Helmholz timescale, $\tau_{KM} \sim GM^2/RL$, where M is mass, R the radius, and L the luminosity of the protostar. For massive stars, this contraction time ($\sim 10^3$ yrs) is significantly shorter than the accretion time ($\sim 10^5$ yrs) so that a massive star is accreting material even after the star has begun hydrogen burning (Zinnecker &

Yorke 2007). This is unlike low-mass stars, which contract and enter the main sequence after accretion has already ceased. Therefore massive stars, with high luminosities and strong stellar winds, impart huge amounts of energy on their surroundings such that for accretion to continue, the accretion rate onto the young star must exceed the outflow rate. The force on circumstellar particles inward is gravitational, meaning it is proportional to the mass of the central object, while the force outward, caused by radiative pressure, is proportional to the star's luminosity, $L = M^{3.5}$ (Henry 2004). The significantly higher dependence of the outward force on mass means that spherically symmetric accretion cannot proceed for high-mass stars. How accretion overcomes the radiation pressure is an unsolved problem, although a number of theories have been introduced in the literature that would allow more massive stars to form (see Zinnecker & Yorke 2007 and references therein): merging lower mass stars, destruction of dust, density inhomogeneities, rapid infall, beaming, and variable accretion.

The young, embedded massive star can have a profound effect on its circumstellar environment, and while the stellar radiation itself is still unobservable, phenomena associated with the circumstellar material provide an indirect probe of the central star's properties. It is in this stage of massive star formation, after the star has reached a high mass ($M > 8\ M_{\odot}$), that this thesis is primarily concerned.

Perhaps the most basic effect a massive star can have on its environment is to warm the nearby ISM (Pontoppidan et al. 2008). The aforementioned ices in the surrounding dense material can be modified by this thermal processing, a topic we will explore in detail in Chapter 3. In regions closer to the star, the ices sublimate off the dust grain and enter the gas phase (van

Dishoeck & Blake 1998). Such an object is signposted by the emission of molecules often detected in high-excitation transitions that reflect the high temperature and density of the emitting gas. Termed hot molecular cores (HMCs; see reviews by Kurtz et al. 2000 and Cesaroni 2005), these emission regions have high temperatures ($T > 100$ K), small sizes ($R < 0.1$ pc), large masses ($10 - 10^3$ solar masses) and luminosities consistent with high-mass stars ($L > 10^4$ $L_\odot$). Multi-line and continuum observations towards HMCs indicate their density structures are a continuation of the larger molecular clumps in which they are embedded (Fontani et al. 2002). This suggests that HMCs are not discrete structures separate from the colder molecular material, but are rather simply the warmest regions of a larger clump structure. Water and methanol masers – whose emission is hypothesized to be formed from the warm, dense molecular material or in shocks associated with outflows – are often coincident with HMCs and can therefore serve as a useful tracer of massive star formation (e.g., De Buizer et al. 2005).

In time, the central star ionizes its surroundings to form an HII region, ionizing all nearby molecular material and destroying the HMC (Churchwell 2002). In this evolutionary picture, a transition object exists and has signs of both HMC and HII region emission. Indeed, Cesaroni (2005) presents observations of the star formation region G24.78+0.08 in which a number of forming stars are identified and span this proposed evolutionary spectrum including a cold, starless core, a maser-bearing HMC, a HMC with an associated UCHII region, and finally an HII region with no molecular emission.

The youngest massive stars are associated with the smallest HII regions, ultracompact HII regions (UCHII regions) and the even smaller, recently-identified hypercompact HII regions

(HCHII regions). HCHII regions are the least understood of the HII region classes (Gaume et al. 1995), but it has been suggested that they may be formed via processes distinct from the larger, later stage ultracompact, compact, and classical HII regions. HCHII regions have sizes of only ~0.03 pc (Keto 2007); the small size suggests they are related to single massive stars and could be related to the photoevaporation of the circumstellar disk (Lizano et al. 1996), tiny versions of UCHII regions being "quenched" by high accretion rates (Churchwell 2002), or jet-like HII regions tracing an outflow (Tan & McKee 2003).

While massive stars begin hydrogen burning and emitting in the UV while they are still accreting, detectable UCHII regions likely do not form until the accretion has largely ended; even moderate accretion rates of 10^{-5} to 10^{-4} $M_\odot$/yr can confine the HII to a region too small and embedded to be detected (Churchwell 2002). Note, however, that so long as the ionization radius is smaller than the radius at which the sound speed is equal to the escape speed, the star can continue growing in mass by accreting ionized gas. Typical accretion rates are estimated to be 10^{-3} to 10^{-4} $M_\odot$/yr (Churchwell 2002). At a certain point, with the mass steadily increasing, the ionizing flux of the star will increase enough to ionize material beyond the critical radius inside which the gas is gravitationally bound, and the HII region will dynamically grow in size. UCHII regions are distinguished from the later-stage compact HII region (CHII regions) by their smaller sizes (< 0.1 pc) and higher densities (> 10^4 cm^{-3}). At this size scale, UCHII regions are on the scale of clusters, and may therefore represent the combined effects of several ionizing stars. The transition from HCHII region to UCHII region could therefore represent the onset of the

destruction of the molecular clump.

UCHII regions are surrounded by their natal molecular condensations that are being heated by the embedded stars even out to large radii. The dust re-radiates the stellar radiation in the IR (e.g., Crowther 2005), making UCHII regions and massive YSOs in general among the most luminous IR sources in galaxies. Observations at IR wavelengths are among the most useful probes of this stage of the massive star formation process as they provide information about both the radiative properties of the forming star and the chemical and thermal state of the circumstellar material. For example, from a source's luminosity in the IR, the stellar luminosity of the cluster (or its most luminous member) can be estimated, and because the IR emission originates from the dust, the nature of that emission can provide insights into the nature of the dust particles. In this thesis, we heavily exploit the usefulness of mid-IR observations of massive YSOs to better understand the evolutionary stages of massive star formation.

The UCHII region, aided by stellar winds, dynamically expands into the surrounding medium to become a CHII region of a somewhat larger size and lower density (Garcia-Segura et al. 1996). In time the star destroys the entire molecular clump, or at least the portion inside the ionization front of the cluster.

1.3 Using the Large Magellanic Cloud as a Massive Star Formation Laboratory

The importance to star formation research of obtaining a galaxy-wide sample of massive forming stars cannot be understated. Among the most poorly understood aspects of massive star formation are the timescales on which the above described evolutionary stages take place. With a

complete sample of massive YSOs within a single galaxy, it should be possible to statistically estimate the answers to questions such as “When does a massive star form a detectable UCHII region?” and “How long does it take for a massive star to destroy its natal molecular clump?”

The closest laboratory in which to conduct such a survey is of course the Milky Way, and while studies of Galactic massive star formation can be conducted at relatively high spatial resolution, studies in the Milky Way are mired by a range of observational difficulties. As discussed above, massive stars are rare objects; to add to the problem of a low number of observable sources, parts of the Galaxy are observationally inaccessible due to crowding in the Galactic bulge and extreme dust obscuration along the plane of the Galaxy. Massive star formation sites that *can* be observed in the Galaxy are hampered observationally by confusion along the line of site and distance ambiguities that can lead to large luminosity uncertainties.

Many of these problems can be mitigated by observing the Large Magellanic Cloud (LMC), a nearby Galaxy in the Local Group. The LMC is located at a known distance of ~50 kpc (Feast 1999), meaning objects located in the LMC have a well-constrained luminosity. Due to its location at a high Galactic latitude, our view of the LMC is relatively unobstructed by intervening material, and at a relatively close distance, modern telescopes are also able to spatially resolve individual massive YSOs. Moreover, because it is located largely within the plane of the sky, we can view the entirety of the Galaxy, allowing us to take a nearly complete census of the galaxy's stellar and prestellar content.

1.3.1 Identification of Massive YSOs in the LMC

The above benefits of studying the LMC have made it a prime target for the study of massive star formation on a Galaxy-wide scale, and a number of star formation studies over the years have used the LMC as a laboratory. With the advent of *SST*, astronomers were able – for the first time – to image the entirety of the LMC with parsec resolution at IR wavelengths to assess the prestellar content of the LMC. From these observations, two primary studies have independently identified over 1000 objects described as candidates for young forming stars via their mid-IR emission. The first, published by SAGE (Surveying the Agents of a Galaxy's Evolution; Whitney et al. 2008), detected 1000+ YSO candidates from the excess IR point source-like emission. Because they are bright in the IR, they must still be surrounded by significant nearby dust that reprocesses the radiation into the IR.

In a competing study, Gruendl & Chu (2009), reanalyzed the SAGE images and identified nearly 1,400 YSO candidates separated into definite, probable, and possible YSO categories. Both surveys identified YSOs by first identifying point sources in the *SST* images and then "weeded-out" non-YSOs by analyzing the point sources in color-color and color-magnitude space. However, the two surveys used both a different point-source identification algorithm and color-color or color-magnitude selection criteria. Gruendl & Chu (2009) found that the SAGE YSO catalog does not include nearly 70% of the definite and probable YSOs from their survey and that 20 – 30% of the SAGE YSOs are likely in actuality background galaxies. On the other hand, the SAGE catalog contains YSOs that were excluded by the Gruendl & Chu (2009) color-magnitude criterion, and therefore contain some more evolved or fainter YSOs missed by

Gruendl & Chu (2009). It should be noted that the *SST* observations for the surveys are flux limited and therefore only included intermediate- and high-mass YSOs.

Prior to these two studies, fewer than 20 YSOs in the LMC were known and the sample was restricted to only the most luminous objects. The *Spitzer* observations represented a big step forward in characterizing the massive star formation content of the LMC. A significant portion of this thesis is dedicated to presenting follow-up mid-IR spectroscopic observations conducted by *Spitzer* on a subsample of the LMC's YSOs. We have here targeted the most luminous, and likely the most massive, YSO candidates. In Chapter 2, we present the results of the spectral survey. We identify the spectral features indicative of massive star formation and quantify the contribution of the various features. We note that there is variation in the relative contributions of the various spectral features and tie this spectral variation to a proposed evolutionary picture for massive star formation.

In Chapter 3, we turn our attention to a single spectral feature, the 15.2 μm CO_2 ice feature which can be used to assess the thermal history of the circumstellar material. The feature also provides information about the chemical state of the ice, and we have explored how the different metallicity of the LMC compared to the Milky Way may affect the composition of ices. Finally, in Chapter 4, we present ancillary data taken with the *Australia Telescope Compact Array* (*ATCA*) in order to connect the evolutionary state as inferred from the *Spitzer* spectra to the surrounding dense molecular gas.

Chapter 2

Identification and Spectral Classification of Massive YSOs in the LMC

This chapter is previously published in The Astrophysical Journal as Seale, J.P., Looney, L.W., Chu, Y.-H., Gruendl, R.A., Brandl, B., Chen, C.-H.R., Brandner, W., & Blake, G.A. 2009, ApJ, 699, 150 and is reproduced here with permission of the American Astronomical Society.

2.1 Introduction

During all stages of their lives, stars play an important role in the evolution of their host galaxy. Massive stars, in particular, have a strong influence on galactic properties (e.g., Kennicutt 2005), as they are the principal source of heavy elements and UV radiation. A single star can influence the structure and chemistry of its local interstellar medium (e.g., van Dishoeck & Blake 1998, Kwon et al. 2006, Seale & Looney 2008), and the combined effects of many evolving stars can shape galactic superstructures spanning 1000's of parsecs (e.g., McCray & Kafatos 1987, Tenorio-Tagle & Bodenheimer 1988). More specifically, during their formation, massive stars inject energy into the ISM via powerful jets and outflows (e.g., Shepherd &

Churchwell 1996). As they evolve toward and onto the main-sequence, massive stars become sources of copious amounts of UV radiation that energizes the surrounding medium creating compact HII regions (see reviews by Garay & Lizano 1999, Beuther et al. 2007). OB associations, groups of massive stars, can generate enough UV radiation to ionize large regions of the interstellar medium (ISM). Finally, massive stars end their relatively short lives with supernovae that stir up the ISM by their strong explosions. The combined effects of supernovae and fast stellar winds can form large superbubbles or giant interstellar shells that propagate star formation to distances of hundreds or thousands of parsecs (e.g., McCray & Kafatos 1987, Chu et al. 2005, Chen et al. 2009, Book et al. 2009). In addition, it is now commonly speculated that most stars – including our own Sun (e.g., Looney et al. 2006) – form in clusters, and within these clusters, massive stars dominate the overall luminosity, greatly affecting any nearby star or planet formation. Clearly, massive stars play a considerable role in galactic ISM structure and overall stellar content.

To understand the formation of massive stars, it is necessary to identify massive young stellar objects (YSOs) throughout a galaxy. YSOs are surrounded by dense envelopes of gas and dust that serve as the young stars' mass reservoirs for accretion (see reviews by Zinnecker & Yorke 2007, McKee & Ostriker 2007). Photospheric optical and UV radiation from the embedded central star absorbed by hundreds of magnitudes of extinction from the circumstellar gas and dust envelope is re-radiated in the infrared (IR). Massive YSOs spend a large fraction of their relatively short lives in these embedded stages and are therefore best identified by their point-source IR radiation (Churchwell et al. 2002). The observed IR emission, reprocessed stellar

radiation, reveals information about the state of the circumstellar material (van Dishoeck & Blake 1998).

While the formation of low-mass stars can be studied in great detail and at high spatial resolution in nearby Galactic star forming regions (e.g., Hartmann et al. 2005, Luhman & Rieke 1999, Tobin et al. 2007, Seale & Looney 2008), massive stars are much rarer, making observational studies more difficult. High-mass star formation studies within the Milky Way are plagued by numerous problems – a low number of observable sources, dust obscuration along the Galactic plane, and distance ambiguities leading to high luminosity uncertainties.

The formation of individual massive stars in other galaxies could not be resolved until recently. The advent of the *Spitzer Space Telescope* (*SST*; Werner et al. 2004) has enabled large surveys to identify YSOs in the Galaxy. Its superb angular resolution makes it possible to identify YSOs even in nearby galaxies, such as the Large and Small Magellanic Clouds (LMC & SMC). The LMC is an excellent laboratory to study high-mass star formation as it is located at a small and known distance of 50 kpc, where 1" corresponds to 0.25 pc (Feast 1999); furthermore, its low foreground extinction and nearly face-on orientation provides a clear view throughout the entire galaxy. Thus, surveys of high-mass YSOs in the LMC have been conducted by Whitney et al. (2008) and Gruendl & Chu (2009).

We have used the *SST*'s InfraRed Spectrometer (IRS; Houck et al. 2004) to obtain mid-IR spectra of nearly 300 massive YSO candidates in the LMC to assess and confirm their nature. These observations represent the most extensive and complete collection of massive YSO spectra to date. These infrared spectra are rich with spectral features from a wide variety of species,

some of which are unobservable at other wavelengths. Among the most interesting features are ice-phase molecular absorptions, deep silicate absorptions, polycyclic aromatic hydrocarbon (PAH) emission, and ionic fine-structure emission lines.

Such a large spectral survey allows meaningful comparisons with theoretically or empirically derived formation and evolutionary paths of massive stars, as reviewed by Zinnecker & Yorke (2007), Beuther et al. (2007), Krumholz & Bonnell (2007), and Garay & Lizano (1999). Star formation typically begins with the collapse of a high-density core within a large clump of a molecular cloud. A protostar forms and acquires its mass by accreting from its natal cloud via a circumstellar disk. The forming star heats the dense massive core, turning it into a hot dense massive core. Eventually, hydrogen burning will begin. It is commonly accepted that massive stars, unlike their low-mass counterparts, begin hydrogen burning while still accreting material. At this stage, the circumstellar material including the accretion disk may become photoionized, a possible origin of the so-called hypercompact HII region (Keto 2007). Initially, the accretion flow is able to quench the ionizing flux, but once accretion slows or becomes geometrically unable to contain the UV flux, the ionizing radiation can escape into the surrounding regions creating ultracompact/compact HII regions and eventually, larger classical HII regions. Over time, stellar winds and radiation will disperse the circumstellar material, revealing a newly-formed high-mass star.

In this paper we will use the term 'YSO' to describe the young central object-disk-envelope system that will eventually become a main-sequence star. The term 'protostar' is reserved to describe an object that will eventually become a main-sequence star but has yet to

begin hydrogen burning. Such a phase is extremely short lived, so the sample of YSOs studied here are likely all hydrogen-burning YSOs that are still highly embedded and may be accreting. Additionally, a large majority of them probably have massive central objects (> 8 $M_{\odot}$; see Section 3.5). Our sample of sources have mid-IR emission from warm dust, and thus are highly embedded but already contain a central heating source. True high-mass protostars, i.e. pre-hydrogen burning, accreting sources with masses above 8 $M_{\odot}$, likely only exist very briefly. Since the YSOs in our *SST* IRS spectral catalog are likely high-mass, most (possibly all) have already begun hydrogen burning.

The spectra of our objects show great variations that may reflect an evolutionary sequence during a high-mass YSO's formation. This paper discusses the spectral features present in the IRS spectra and ties them to a possible evolutionary scheme. In Section 2.2, we introduce the catalog of sources and describe the observations used in this spectroscopic study. The results of a spectral categorization are presented in Section 2.3 along with our classification method. Finally, in Section 2.4 we discuss our proposed connection between spectral classification and evolutionary stage.

2.2 Observations and Data Reduction

2.2.1 Targets

Given the benefits of studying the LMC, it is of no surprise that this galaxy has been the focus of intense star formation research in recent years. Of particular interest is the *SST* survey of the LMC (SAGE; Meixner et al. 2006), which has enabled two catalogs of high-mass YSOs in

the LMC, produced independently by Whitney et al. (2008) and Gruendl & Chu (2009), hereafter GC09. Their different selection criteria and approaches have resulted in significant discrepancies between these two catalogs (see GC09 for details). We adopt the results of GC09, a precursor of the IRS observations reported in this paper. A brief description of GC09's methodology follows. GC09 have extracted point-source photometry from all available observations of the LMC made with *SST*'s InfraRed Array Camera (IRAC; Fazio et al. 2004) in the 3.6, 4.5, 5.8, and 8.0 μm bands and Multiband Imaging Photometer for *Spitzer* (MIPS; Reid et al. 2004) in the 24 and 70 μm bands. The [4.5] – [8.0] versus [8.0] color-magnitude diagram of all LMC sources was used to identify objects with IR excesses. The nature of each object with IR excess was then assessed by simultaneously examining its images and spectral energy distribution (SED) from optical to mid-IR wavelengths. These IR objects were classified into six broad categories: Asymptotic Giant Branch (AGB) and post-AGB stars, planetary nebulae, background galaxies, diffuse sources, normal stars, and YSOs. Objects that could not be classified unambiguously were usually assigned a primary (with higher probability) classification and a secondary (possible but with lower probability) classification. The YSOs are distributed throughout the galaxy and are seen to both cluster near some of the numerous large HII complexes in the LMC and to form in more isolated environments (see Figure 14 of GC09).

For the *SST* IRS observations, we have selected 294 targets from the GC09 catalog. Of these, 269 were identified as 'Definite' or 'Probable' YSOs including all of the catalog's 'Definite' or 'Probable' YSOs with [8.0] < 8.0. In addition, we selected 10 objects with primary classification as AGB/post-AGB stars, and 2 that were probably diffuse sources. The latter 12

targets were included in our IRS observing program because they had properties that are unusual for their primary classifications, making classification as YSOs an attractive alternative. For example, seven of the observed AGB/post-AGB sources belong to a subgroup dubbed 'ERO' (Extremely Red Object) by GC09. These EROs are redder than sources identified as typical AGB and post-AGB stars, but their SEDs are also unlike the YSOs in that they peak between 8 and 24 μm. Our IRS spectra have shown that these EROs are Extreme Carbon Stars, and are reported in detail in a discovery paper by Gruendl et al. (2008). Finally, 13 of the targets were previously uncategorized because they lacked IRAC photometry in the 4.5 μm band, but they are bright sources in the MIPS 24 and 70 μm bands and are in gas/dust-rich environments, suggesting that these sources are possibly YSOs.

2.2.2 Observations

The IRS on board *SST* is composed of four modules, two of which provide low spectral resolution (R = 60 – 127) between 5.2 and 37.9 μm, and two provide high spectral resolution (R = 600) between 9.9 and 36.8 μm. To cover the entire ~5 to 37 μm wavelength range, we used the IRS modules SL (short wavelength, low-resolution), SH (short wavelength, high-resolution), and LH (long wavelength, high-resolution). The SL module has two possible configurations: SL1 for the wavelength range 7.6–14.6 μm and SL2 for 5.2–8.4 μm. The high-resolution modules, SH and LH, each consist of 10 spectral orders and cover the wavelength ranges 9.9–19.3 and 18.9–36.9 μm, respectively. A more detailed description of the IRS is presented by Houck et al. (2004).

In order to efficiently observe as many LMC YSOs as possible, we used the GC09 YSO

catalog to identify groups of targets with similar 8 and 24 μm brightnesses within 2° of one another. Each group of targets could then be observed with the same setup during a single AOR that treated the group as a fixed 'cluster.' To ensure that a background estimate was available to remove the zodiacal light contribution from the SH and LH modules, we added one off-position to each cluster. This off-position was chosen by searching for the point with lowest surface brightness in the *IRAS* 12 and 25 μm maps within the 2° constraint imposed by the targets. The exposure times for the SL1, SL2, SH and LH modules were chosen such that the observations would produce a contiguous spectrum from 5-37 μm with a signal-to-noise of ~30.

Seven sources were observed with only the SH and LH modules by our program. Five of these (053142.4–683454.3, 053943.3–693854.6, 053943.8–693834.0, 053944.3–693847.5, and 053945.9–693839.2) did not include the SL modules because the detectors would have saturated for the shortest possible exposures. The two remaining sources, 053941.9–694612.0 and 053959.3–694526.3, had previous observations with the SL1 and SL2 modules available in the *SST* archive and could be observed as part of the same cluster. For these latter two sources, we have downloaded and combined the archival data with our SH and LH observations.

2.2.3 Data Reduction

The observations were processed by the *Spitzer* Science Center's pipeline reduction software. We began each spectral extraction process with the basic calibrated data (BCD) product. The campaign-specific rogue pixel masks were applied to the BCD data and removed using the interactive IDL IRSCLEAN package (version 1.9). We further identify and remove

transient rogue pixels by examining variations between frames, also using the IRSCLEAN package. Multiple exposures at each slit position were then median averaged together.

The subtraction of a background was carried out differently for the high- and low-resolution modules because of their different slit sizes: 3.7" × 57" for SL1, 3.6" × 57" for SL2, 4.7" × 11.3" for SH, and 11.1" × 22.3" for LH. For SL1 and SL2, the slit is long enough that a local background along the slit can be determined and subtracted from the source. This is achieved by differencing the two nod positions. For the SH and LH modules, the slit is too short for a source-independent background; thus the background subtraction is performed by subtracting the cleaned BCD data from a nearby background position.

High-resolution spectra were extracted from the full SH and LH apertures using the SMART software package (Higdon 2004). For a full aperture extraction, any flux within the bounds of each order at a given wavelength is extracted and summed. The low-resolution SL spectra were extracted using the tapered column point source extraction package within SMART. Because of the large number of spectra, an automated procedure was used to detect a source in a cleaned, background-subtracted spectral image and extract its spectrum with an extraction window whose width varies to accommodate the wavelength-dependent point spread function (i.e., wider at longer wavelengths). Fifty-eight sources could not be detected by the automated procedure either because they appeared extended or resided in a crowded environment, resulting in multiple sources within the slit. These sources were extracted manually using the interactive portion of SMART. Here the position and FWHM of the source on the spectral image were visually determined and the spectrum extracted using a tapered column.

To combine (or 'stitch' together) spectra from different modules into a single contiguous spectrum, several corrections need to be made. First, the fringes in the high-resolution 1-D spectra, originating from the detectors of the SH and LH modules, are removed using the IDL package IRSFRINGE (version 1.1). Next, flux discontinuities between modules are corrected by applying scaling factors to spectra from different modules. Flux discontinuities may arise from differences in slit size and orientation, background-subtraction, and spectral extraction. To account for the latter two effects, we assume that the local background-subtraction in the SL1 and SL2 spectra are more reliable, and further scale SL1 to SL2 (scaling factor is ~1; average of 0.98 with standard deviation of 0.14). The LH spectrum is then combined with the SH spectrum after applying a scale factor determined from the ratio of fluxes in the wavelength region where the two overlap (18.9–19.3 μm). Finally, the SH + LH combined spectrum is scaled to the SL1 + SL2 combined spectrum based on the ratio of fluxes in the region where the two spectra overlap (~9.9–14.6 μm). Typical values of the net scaling factors range between 0.5 and 2.0.

2.2.4 Cautionary Remarks on Stitching Spectra

The scaling factors can be used to produce a contiguous spectrum, but may also introduce inadvertent effects. Several considerations need to be born in mind when interpreting these spectra.

If the full aperture were uniformly illuminated in both the SH and LH modules, the scale factor between them would simply be the ratio of their aperture extraction areas. If the observed source is point-like, then no scaling factor would be required. The fact that a scaling factor is

required suggests an extended and dusty nature of the objects or a significant contribution from background emission. Furthermore, the scaling factor is determined from the dust continuum, but the lines may behave differently. For example, the fine-structure lines may originate from a small compact core, while the continuum is extended; therefore, the lines may not have required scaling.

The necessity of module stitching is partly a result of each module's different aperture size and orientation which result in different spatial regions being probed. The stitching process is further complicated by possible differences in the spatial extent of the regions emitting at different wavelengths. For example, the emission at longer wavelengths may originate from cooler, more extended gas and dust surrounding a smaller, warmer region which dominates the emission at shorter wavelengths. Alternatively, since the spectrum at shorter wavelengths contains many spectral emission features associated with dust, the spatial extent of the emitting region at short wavelengths may be equal or even larger than that of the region emitting at longer wavelengths. To get a sense of how strongly the stitching is affected by spatial differences in emitting areas, we compared F^{pho}_{24} / F^{spec}_{24} (the ratio of MIPS photometric 24 μm fluxes to IRS 24 μm spectroscopic fluxes) to the scaling factor applied to the 24 μm wavelength region. We find that any source with F^{pho}_{24} / F^{spec}_{24} > 1.5 has a scaling factor less than 1. In other words, the long wavelength portion of the spectrum was scaled down to match the short wavelength portion causing the 24 μm spectroscopic flux value to underestimate the photometric value. This is consistent with the picture described above where emission contributing to the short wavelength portion of the spectrum originates from a smaller region than the long wavelength portion.

2.3 Results & Classification

The spectra are first separated by-eye into two primary categories that reflect their level of 'embeddedness.' The first category's members all have continua that rise into the red end of the spectrum, while the second category's spectra are much flatter or even begin to fall at long wavelengths. The second category also contains sources with slightly rising spectra with a strong emission feature at 10 μm. The first category are likely highly embedded objects such as YSOs while the second are likely either less-embedded, more-evolved young stars or highly evolved stars such as AGBs, post-AGBs or red supergiants (RSGs). The embedded sources are additionally organized via principal component analysis (PCA, see Section 2.3.2) into 6 groups according to their dominant spectral features. Note that the details of the use of PCA follows in Section 2.3.2 and 2.3.3, but first, we will discuss the spectra and their features more generally. The less-embedded object spectra are further subdivided by-eye into three groups based upon their very different dominant features. It is more efficient to classify these spectra by-eye since the spectra are very different among the three groups and do not suffer from the same by-eye biases that the embedded source classifications do. In this manner, the surveyed sources are separated into 9 different spectral classifications, and a sample of the spectra for each category is presented in Figures 1 and 2. The spectral catalog is shown in its entirety in Appendices A and B. A summary of the source classification is given in Table 1.

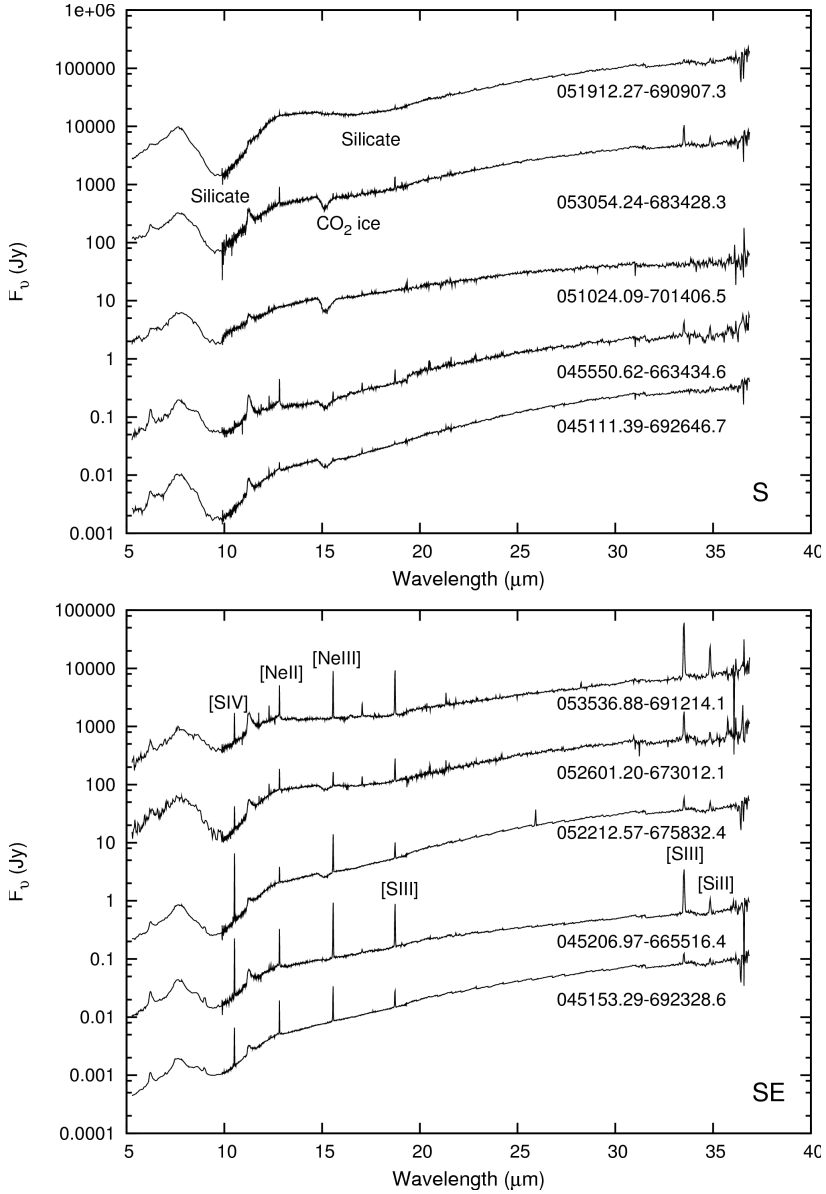

Figure 1. Representative spectra of the embedded YSO spectral groups. The source identification is given below each curve. S Group: The broad silicate absorption features at 10 and 18 μm and the 15.2 μm CO_2 ice band are indicated. The spectra from bottom to top have been scaled by the following multiplicative factors for clarity: 0.05, 1, 30, 800, and 10^4 . SE Group: Prominent fine-structure lines are indicated including [SIII], [SIV],[NeII], [NeIII], and [SiII]. The spectra from bottom to top have been scaled by the following multiplicative factors for clarity: 0.001, 0.1, 1, 10^3 , and 8×10^3. P Group: The prominent PAH emission features are identified. The spectra from bottom to top have been scaled by the following multiplicative factors for clarity: 0.05, 1, 10, 800, and $3{\times}10^4$. PE Group: Prominent fine-structure lines are indicated along with three PAH emission features. The spectra from bottom to top have been scaled by the following multiplicative factors for clarity: 1, 20, 600, 6000, and $2{\times}10^5$. E Group: Prominent fine-structure lines are indicated including [SIII], [SIV], [NeII], [NeIII], and [SiII]. The spectra from bottom to top have been scaled by the following multiplicative factors for clarity: 1 and 10. F Group: The spectra from bottom to top have been scaled by the following multiplicative factors for clarity: 1, 140, 24000, 10^5 , and 10^7 .

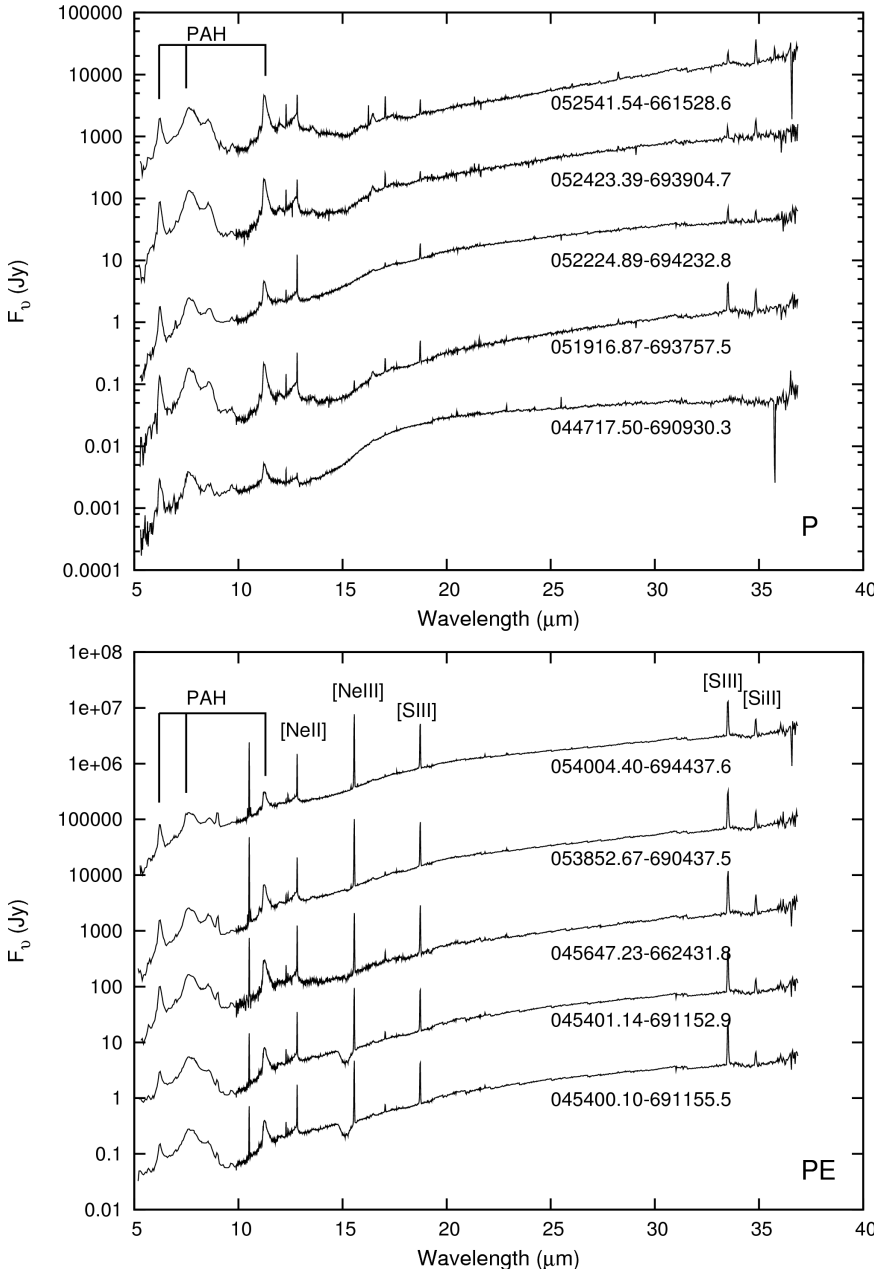

Figure 1. (Continued)

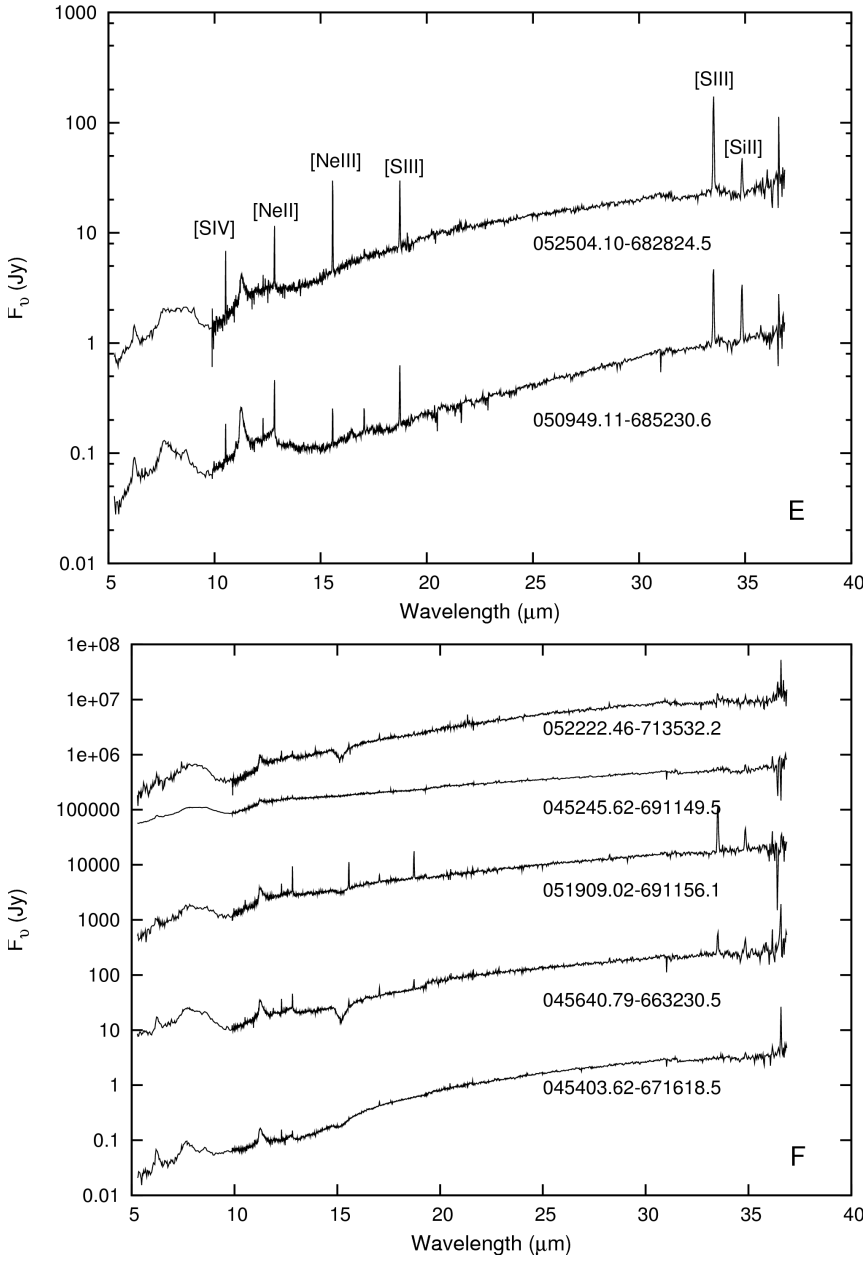

Figure 1. (Continued)

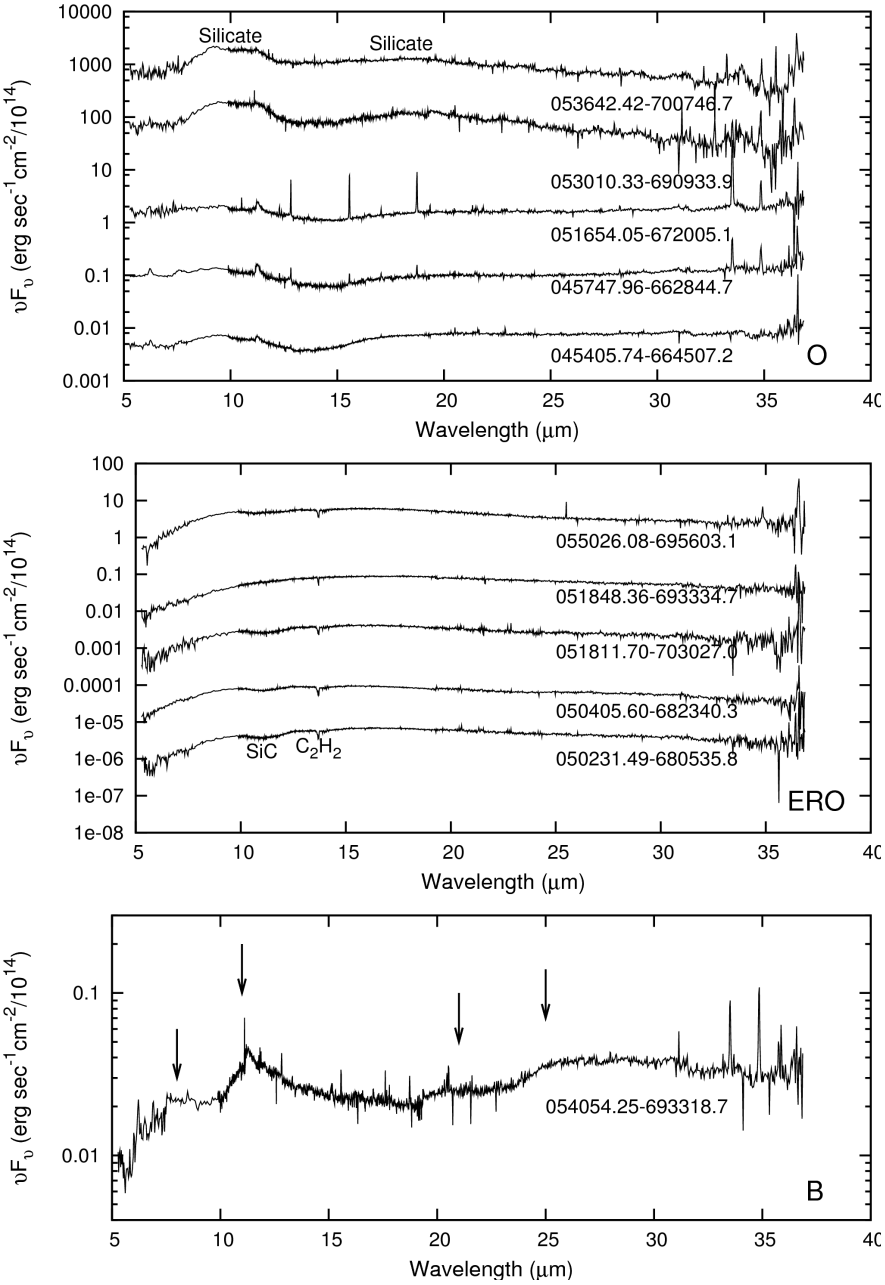

Figure 2. Representative spectra of the O, ERO, and B groups. The source identification is given below each curve. Top: Silicate emission features at 10 and 18 μm are indicated. The spectra from bottom to top have been scaled by the following multiplicative factors for clarity: 0.1, 1, 100, 4000, and 8×10^4 . Middle: Absorption features coincident with known SiC and C_2H_2 bands are indicated. The spectra from bottom to top have been scaled by the following multiplicative factors for clarity: 10^{-4}, 0.1, 1, 100, and 10^3 . Bottom: Arrows indicate the locations of unidentified broad emission features that create the step-like spectral shape.

Our categories closely resemble a portion of a classification system originally developed by Kraemer et al. (2002) to classify spectra from the *Infrared Space Observatory* (*ISO*; Kessler et al. 1996) Short Wavelength Spectrometer (SWS), hereafter referred to as the KSPW system. In the KSPW system, objects are first classified by their continuum shape into six broad groups with subclasses assigned based upon specific spectral features. Under the original KSPW system, Kraemer et al. (2002) classified over 900 objects of various astronomical origin into a total of 59 classes. All the sources we have identified as embedded would be broadly classified into the KSPW Group 5, sources with SEDs dominated by dust emission with a peak wavelength longer than 45 μm. Since *SST* IRS spectra cover a different wavelength range than ISO, and because our catalog focuses on a narrow portion of the large spectrum of categories established in the KSPW system, we have developed a modified version of the categories originally developed by Kraemer et al. (2002). In Table 1, we list both our own classification of each source along with the corresponding classification in the KSPW system. Classification by the KSPW scheme was performed by-eye, and every source was classified three times with no knowledge of prior categorization to ensure an unbiased classification. There is generally a one-to-one correlation between the two classifications, but because classifications in our system are performed automatically via PCA for the embedded sources while the KSPW system is done by-eye, there are some discrepancies.

2.3.1 Embedded YSO Spectral Features

The mid-IR is rich in spectral features including bands due to molecular ices, PAHs,

silicates, and atoms, thus spectroscopic observations provide an abundance of information about the physical and chemical properties of a forming star and its environment. The spectra of the coldest and therefore youngest YSOs peak around 100 μm (e.g., van Dishoeck 2004), corresponding to a blackbody temperature of several tens of Kelvins. In environments at high densities and low temperatures such as these, absorption from ices (particularly CO_2) and silicates are detected in the spectra. Older YSOs begin to show signs of UV radiation from a central ionizing source including UV-pumped fluorescing PAHs and fine-structure lines from ultracompact/compact HII regions.

The six groups of spectra in the first category, whose continua rise with wavelength throughout the IRS spectral range, are described below and examples are shown in Figure 1 with major spectral features marked. (1) The S group, consisting of 12 sources, are dominated by silicate absorption features including the prominent 10 μm absorption feature and sometimes including the 18 μm absorption feature. (2) The SE group, consisting of 5 sources, have both strong silicate absorption features (similar to S group) and strong fine-structure emission lines from ionized gas. (3) The P group, consisting of 100 sources, show prominent PAH emission features. The sources in this group may also show some absorption from silicates, particularly at 10 μm, but PAH emission features at 6.2, 7.7, 8.6, and 11.3 μm make it difficult to identify the silicate absorption unambiguously. For example, strong PAH emission features on either side of a weak 10 μm silicate feature may mimic a strong silicate absorption feature. (4) The PE group, consisting of 142 sources, show both strong PAH emission features and fine-structure lines. Similar to the previous group, silicate absorption features are also difficult to identify in the

presence of strong PAH emission features. (5) The E group consists of only 2 sources whose dominant features are fine-structure lines originating from ionized gas. This group appears similar to the PE group and may be an artifact of the thresholds used in the PCA. (6) The F group, consisting of 11 sources, do not meet the criteria for the above five groups, but are spectrally similar to embedded YSOs. They may show weak indications of PAHs, silicates, or fine-structure lines but are generally nearly featureless.

The largest of the six groups is the PE group, which is characterized by both strong PAH and fine-structure line emission. PAH emission features at 6.2, 7.7, 8.6, 11.3, 12.7, 14.2, and 16.2 μm, first identified in the mid 1970's in the spectra of compact HII regions and planetary nebulae (e.g. Soifer et al 1976), originate from the C-C and C-H stretching and bending modes of PAHs excited by UV radiation. Fine-structure emission lines such as [SIV] 10.5 μm, [NeII] 12.8 μm, [NeIII] 15.5 μm, [SIII] 18.7 μm and 33.5 μm, and [SiII] 34.8 μm originate from ionized gas and can be used to assess the hardness of the UV radiation field. The presence of both PAH and fine-structure line emission clearly suggests the presence of an ionizing source with UV radiation.

The deep silicate feature at 10 μm and the shallower 18 μm feature in the S and SE groups are generally smooth, indicating silicate dust in its amorphous form; however, several sources show a more structured 10 μm feature (Figure 3), possibly a result of dust processing (van Dishoeck 2004). There appears to be a range of strengths to the structure in our sample, possibly representing evolutionary changes from environmental heating. However, there are also known emission lines (e.g. H_2 S(3) at 9.64 μm) which may be contributing to the non-smooth silicate profile. Many of the sources dominated by silicate absorption also have a prominent solid CO_2

absorption at 15.2 μm. The infrared vibrational bands of CO_2 are known to be very sensitive to the environment, and are therefore excellent tracers of thermal and chemical conditions within the embedding molecular core. Similar to the 10 μm silicate band, the CO_2 absorption feature can be either double-peaked or in a smoother single-peaked form (Figure 3). The relative strength of the double/single peaked components is indicative of the environment in which the ice resides (van Dishoeck 2004) and will be explored in Chapter 3.

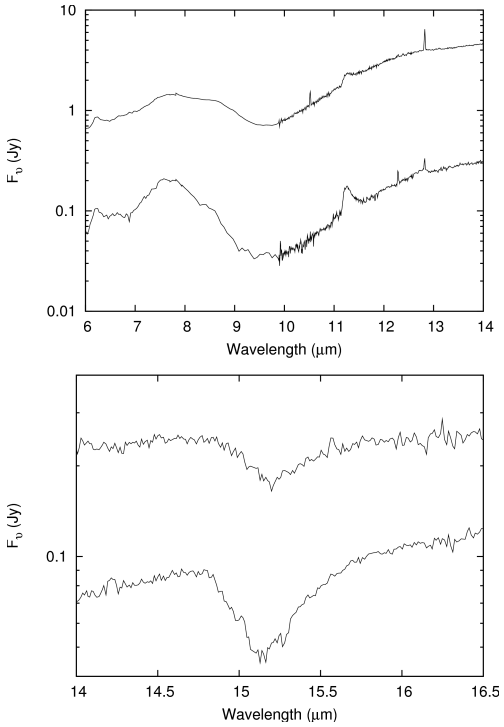

Figure 3. Top panel: Spectra of 052646.61–684847.2 (top) and 045111.39–692646.7 (bottom) showing the variation in silicate absoption band profiles. Bottom panel: Spectra of 053754.82–693435.8 (top) and 045842.47–660835.7 (bottom) showing the variation in CO_2 ice absorption band profiles. The flux values of 053754.82–693435.8 have been scaled by a factor of 2 for clarity.

2.3.2 Principal Component Analysis

For the embedded sources, we organize the spectra into groups with common spectral features by using PCA to quantify the strength of the various spectral features described above. PCA is a technique that allows for the recognition of patterns in spectra and can be used to express a set of spectra in ways that highlight both their similarities and their differences (Murtagh & Heck 1987). PCA has previously been used in the spectral classification of stars (e.g., Murtagh & Heck 1987), QSOs (e.g., Francis et al. 1992), and galaxies (e.g., Connolly et al. 1995). Given the large number of spectra in our sample and the great number of possible spectral features in every spectrum, it can be difficult to visually recognize patterns in the absence, presence, or strength of spectral features. PCA removes by-eye classification guesswork and can quantify the differences between spectra, making it an impartial and unbiased method to assign classifications to spectra. We use PCA to identify and quantify the strength of several spectral features including silicate absorption, PAH emission, and fine-structure lines. We then classify the spectra into several groups based upon the strengths of these features. What follows is the PCA recipe used in this study. For a more complete description of the process and proper implementation of PCA, see Murtagh & Heck (1987).

Suppose we have a catalog of N spectra (i = 1, 2, … N), each covering the same wavelength range sampled at M (j = 1, 2, ... M) identical wavelengths. Each spectrum can be represented by a vector S_i in an M-dimensional space containing the flux at M wavelengths where i corresponds to the specific source. We can then construct an $N \times M$ matrix, A, in which each

row contains the M flux measurements for each of the N sources. In this manner, each row represents a single point in the M-dimensional A-space. If M is a small number, i.e. if A were a low-dimensional space, it may be possible to recognize groups and classifications of spectra by their location in A-space. But when covering a large wavelength range, with even moderate resolution and many spectral features, the number of dimensions becomes too great to visualize without the aid of a statistical method. PCA allows us to reconstruct the N-dimensional space into a projection of only a handful of principal coordinates/components. PCA is an orthogonal linear transformation of data (in this case, spectra) to a new coordinate system such that the greatest variance in the data can be attributed to the first coordinate, the second most variance to the second coordinate, and so on. Each new coordinate is called a component, with those contributing the most variance being the principal components. The new coordinates can be expressed graphically by treating each coordinate as a spectrum, in the same way an object's spectrum can be represented as a vector.

To implement PCA, we must normalize all the spectra to isolate variances due to spectral features and minimize variances from bolometric luminosity differences. The first step is to scale all the spectra to the same total integrated luminosity over the wavelength range, 5.5 to 37 μm. Next, we use a spline interpolation to place all spectra in the same wavelength grid. A final normalization is performed to create a dataset whose mean is zero. To do so, the mean of each dimension is subtracted from each flux measurement in that dimension. If f_{ij} is the flux measurement for the i^{th} source in the j^{th} dimension, the full normalized spectra matrix A is constructed as follows:

$$A_{ij} = f_{ij} - \frac{1}{N}\sum_{i'=1}^{N} f_{i'j}$$

We can then compute the $M \times M$ covariance matrix, C, of the matrix containing all the spectral data:

$$C_{jk} = \frac{1}{N}\sum_{i=1}^{N} A_{ji}A_{ki}$$

where both j and k range between 1 and M, inclusive.

We can then calculate M eigenvectors and the M corresponding eigenvalues of this covariance matrix. The eigenvectors e_m and eigenvalues λ_m obey the identity equation

$$Ce_m = \lambda_m e_m$$

The eigenvector with the largest absolute value of the paired eigenvalue represents the dimension containing the largest variance, the first principal component; the eigenvector with the second largest eigenvalue is the dimension with the second largest variance, the second principal component, and so on. The fractional variance from each principal component is

$$\frac{\lambda_i}{\sum_i \lambda_i}.$$

A matrix of all M eigenvectors represents a complete set of orthogonal axes which completely describe the entire dataset. If the summed fractional variance of the first few principal

components is ~1, then the spectra can be well represented by projecting the spectra onto these first few principal components. We find that often 90% or more of the variance can be described by the first few principal components.

There are several weaknesses to using PCA including its assumption of linearity. This problem is amplified by the nature of our source catalog. Since many of our embedded sources are likely small clusters of YSOs, features from several different sources are mixed together into a single spectrum. In fact, within the HII complex N44, Chen et al. (2009) found 65% of the candidate YSOs to be resolved multiples. Therefore features that may show a strong correlation within a single source may not have as strong a correlation when originating from a clustered object. In this study, we are using PCA to extract and quantify spectral features. Since we are only using PCA to broadly categorize spectra by their major spectral features, we accept the assumption of linearity as valid to first order.

2.3.3 Automated Classification of Embedded YSOs

In order to use PCA to quantify the strength of different spectral features, four wavelength regions are chosen that contain the strongest components of a particular species type – one region highlights the strong 10 μm absorption feature, two highlight PAH emissions between 5 and 10 μm and between 10 and 13 μm, and a final region between 10 and 20 μm encompasses four ion fine-structure lines. PCA is performed on each range to quantify the contribution from various features. Each of these four wavelength regions goes through the procedure described above to find the principal components in that region. The five sources without complete spectral

coverage were excluded from this analysis.

The wavelength segment between 7 and 15 μm is used to determine the strength of each spectrum's 10 μm silicate absorption. The second principal component of this wavelength range (Silicate PC of Figure 4), primarily responsible for silicate absorption at 10 μm, accounts for 21% of the variance in this wavelength range, and is used to assess the strength of a spectrum's silicate absorption. To get a measure of the amount of silicate absorption in a single spectrum, we do a projection of the vector form of the spectrum into the principal component containing the silicate feature, in this case the second principal component of the 7 to 15 μm segment. Figure 5 displays what we call the Silicate Projection of each source, dot-products of the embedded sources' spectra with the Silicate PC. A value of zero means there is no contribution from this eigenvector in the spectrum (the spectrum's vector is perpendicular to the component's vector), while positive and negative values indicate positive and negative contributions, respectively; more positive dot-products mean larger silicate absorptions. Because PC2 is primarily the result of silicate absorption, we define all sources with a Silicate PC projection greater than 0.2 to have strong silicate absorption.

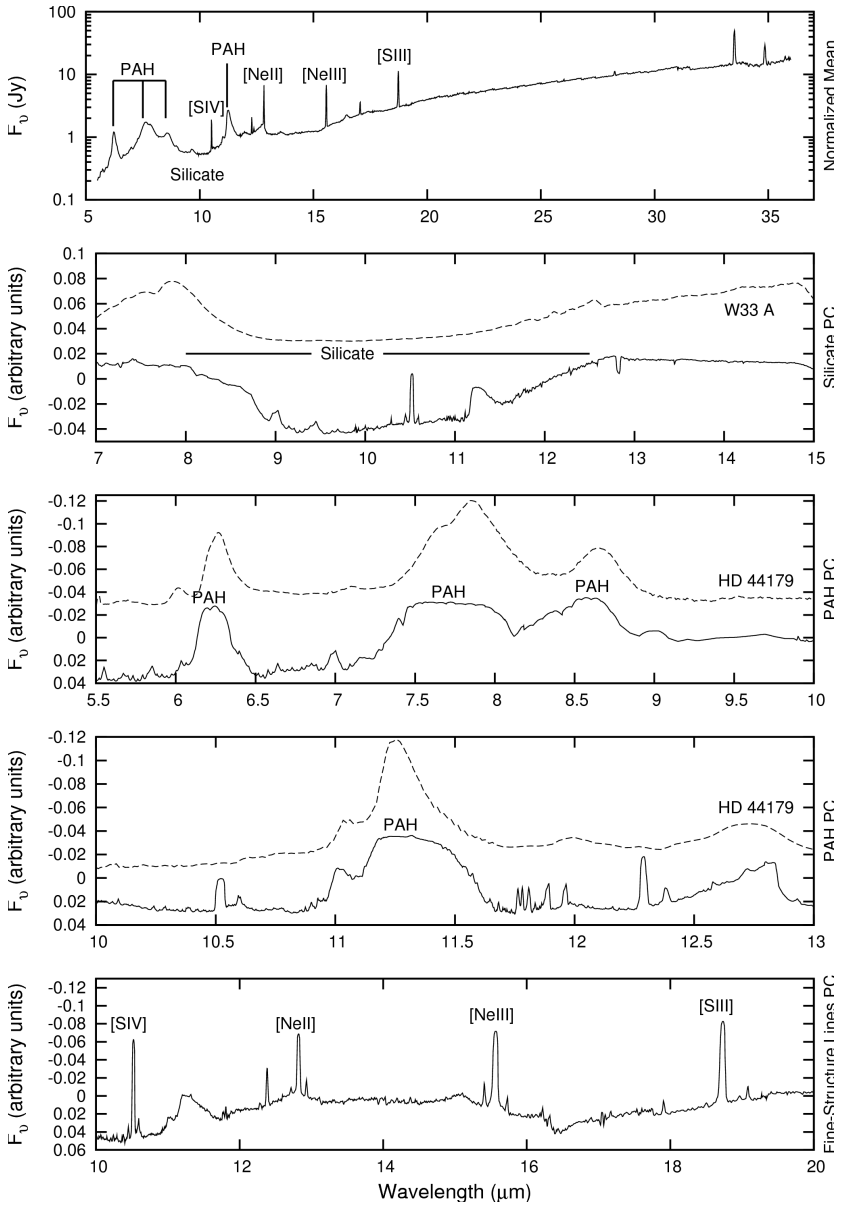

Figure 4. Top panel: the full normalized mean spectra of all the embedded YSOs. Bottom panels: the solid curves show the four principal components used in our analysis. The dashed curves are smoothed ISO data from objects with IR spectra dominated by the species represented within each particular principal component. The silicate panel shows an ISO spectrum from the highly embedded protostar W33A, while the PAH panels have the baseline-subtracted ISO spectrum of HD 44179, the post-AGB star at the center of the Red Rectangle proto-planetary neblua. Prominent features are identified in each panel.

There are two tests implemented to establish the presence of PAH emission. PCA is applied to two wavelength regions, each containing strong bands of PAH emission. The first, between 5 and 10 μm, contains PAH features at 6.2, 7.7, and 8.6 μm, and the second, between 10 and 13 μm, has a feature at 11.3 μm. Between 5 and 10 μm, the second principal component, which contains the negative of three PAH bands, is responsible for 26% of the spectral variance. Similarly, component 2 of the 10 to 13 μm range contains the negative of a PAH feature which is responsible for 33% of the variation. These components are shown in Figure 4. We again project the spectra of the sources into these components to determine the contribution from each eigenvector. Since the principal components with PAHs contain negatives of the features, objects with strong PAH features should have small or negative projections onto both these principal components. We set a cut-off of 0.33 for both ranges, and define any source with a second component projection of less than 0.33 in either wavelength range to have strong PAH emission. Figure 5 shows the dot products (PAH Projections) of all the embedded source spectra onto both the PAH principal components. Note that while most objects that demonstrate strong PAH emission from one test also pass the second PAH emission test, a minority of sources pass only one test. The relative strengths of different PAH features will depend on the specific composition of the emitting PAH (Tielens et al. 2004) and will be explored in future studies.

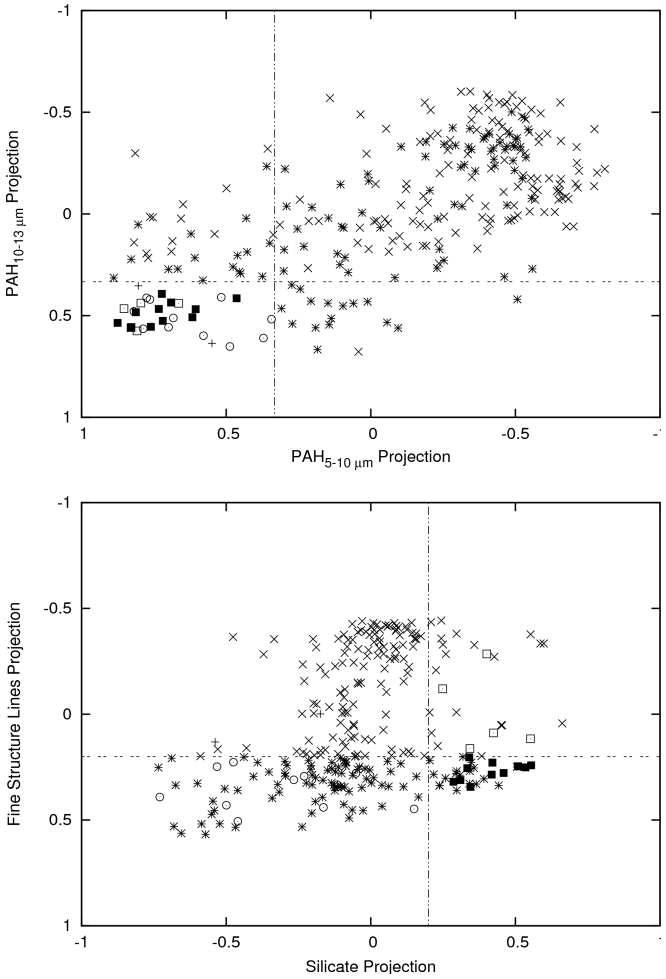

Figure 5. Top: Projections of each embedded YSO's spectrum onto both the PAH5−10μm and PAH10−13μm principal components. S group sources are indicated by solid squares, SE objects by open squares, P group by stars, PE group by X's, E group are crosses, and F objects are open circles. The vertical and horizontal dotted lines indicate the cut-offs between sources which pass and fail the PAH5−10μm and PAH10−13μm tests, respectively. Objects with projections to the right of the vertical line or above the horizontal line are considered to have PAH emission. Bottom: Projections of each embedded YSO's spectrum onto both the silicate and fine-structure line principal components. The vertical and horizontal dotted lines indicate the cut-offs between sources which pass and fail the silicate and fine-structure line tests, respectively. Objects with projections to the right of the vertical line have silicate absorption, while those above the horizontal line are considered to have fine-strucutre line emission. Symbols are identical to the top panel.

A final PCA test is implemented to test for spectral contributions from fine-structure lines. Between 10 and 20 μm, there are four lines attributed to [S IV], [Ne II], [Ne III], and [S III]. The third principal component in this wavelength range, which contains the negative of the fine-structure lines and is plotted in Figure 4, accounts for only 5% of the spectral variance. We define sources showing strong fine-structure emission lines as having a projection into the third component of less than 0.2. Figure 5 plots the Fine-Structure Line Projections, the projections onto the third eigenvector, and indicates the boundary between sources we define as with and without fine-structure lines.

To test the ability of PCA to correctly identify related spectral features and produce their proper shape, we have compared the principal components to sources with known spectral origins. The silicate principal component has a direct counterpart in the spectrum of the embedded massive YSO W33 A. The silicate principal component and W33 A's 7-15 μm spectrum are shown in Figure 4. The spectral data of W33 A (Gerakines et al. 1999) were obtained from the ISO archive via the NASA Astrophysics Data System's[1] online data function. The ISO data were reduced using SMART, multiple exposures were averaged, and the spectrum was smoothed to the resolution of the *SST* IRS. The infrared spectra of W33 A – a YSO embedded within a cold, dense envelope – is known to be dominated by deep ice and silicate absorption features. Note that the broad feature at 10 μm in the principal component matches in location and breadth the deep silicate absorption seen in the spectrum of W33 A. We further compared the PAH principal components to the ISO spectrum of HD 44179. Spectra were obtained and processed for HD 44179 in the same manner as for W33 A. HD 44179, associated

1 http://adswww.harvard.edu/

with the Red Rectangle nebula, is the prototype object showing PAH emission features. Now identified as a post-AGB star, HD 44179 illuminates the surrounding nebula and fluoresces PAH grains in the IR. The structured peaks seen in the PAH principal components match well features at 6.2, 7.7, 8.6, and 11.3 μm identified as PAH emission in the Red Rectangle (Figure 4).

Applying the four PCA cut-offs allowed us to quantitatively assess the contribution different spectral features have to a spectrum. The results of the analysis are given in Table 1. There are 54 sources which pass the 10 μm silicate absorption test, 243 which pass at least one PAH test, and 152 which pass the fine-structure line test. Using the results of the PCA, we divide the embedded objects into the 6 groups described earlier: 1) sources displaying only strong silicate absorption, 2) sources with only strong silicate absorption and fine-structure lines, 3) those with dominant PAH features, 4) objects with both strong PAH features and fine-structure lines, 5) sources with only fine-structure emission lines, and 6) largely featureless spectra. Note that although 54 sources pass the 10 μm silicate absorption test, only 12 and 5 objects are in the S and SE groups, respectively. This is due to the earlier-stated reason that the blending of PAH emission with silicate absorption makes the two features difficult to distinguish. Any source identified as having PAH emission by definition can only belong to the P or PE groups. The five embedded sources which do not have full spectral coverage cannot be properly classified into any particular group because PCA cannot be performed. Therefore, despite showing fine-structure lines, they have been left unclassified and are represented in Table 1 as embedded objects with unknown classification.

2.3.4 Classification of Non-embedded Sources

By-eye classification is implemented for the less-embedded sources whose spectra are largely flatter or fall at longer wavelengths (Figure 2). The first non-embedded group (group O) all have a broad emission feature at 9–11 μm superimposed on a cool dust continuum. The 10 μm feature corresponds to emission from silicates typical of oxygen-rich objects including O-rich AGBs and the disks of Herbig Ae/Be stars. The slope of the spectrum at the long wavelength end of the spectrum should be an indicator for how much gas and dust is around the source; since the long wavelength part of the mid-IR is dominated by thermal radiation from dust, spectra which are flat or rise into the far-IR must be surrounded by neighboring gas and dust. Objects without much circumstellar dust would be expected to have spectra which fall into the far-IR. Indeed, of the eight O group sources, two of the three with spectra that fall at long wavelengths were suggested by GC09 to be either possible AGBs or stars with an IR excess, stars which should no longer be associated with much circumstellar material. We probed the dusty environment of these sources by inspecting their IRAC images which are sensitive to both PAH emission and thermal dust emission and assessed their locations with respect to molecular clouds with CO observations from the NANTEN CO (J = 1–0) survey (Fukui 2002). Source 053642.42–700746.7, located on the outer edge of a molecular cloud, is the only source with a falling spectrum located within a dusty complex and a molecular cloud. This is in great contrast to embedded sources which are found to reside in molecular clouds ~80% of the time and virtually always sit in a larger cloud of dust. The five O group sources with flatter spectra may be highly-evolved pre-main sequence stars such as a Herbig Ae/Be stars – all are associated with either dusty filaments or larger dusty

structures, and four of the five are located within molecular clouds, suggesting they still reside with the clouds they formed from.

The seven objects in the second non-embedded group are the previously mentioned EROs. Their spectra are a mostly featureless blackbody continuum consistent with warm dust emission. Six of the spectra show a broad absorption feature at 11 μm coinciding with the SiC feature seen in Galactic extreme carbon stars. All the EROs additionally have a C_2H_2 absorption feature at 13.7 μm, confirming the C-rich nature of these objects (Gruendl et al. 2008).

The final group (group B) contains only one source, 054054.25–693318.7. It has a step-like appearance produced by broad emission features at 8, 11, 21, and 25 μm superimposed on a continuum that peaks at ~30 μm. Previously-identified sources with similar spectra have been classified as F or G supergiants or possible proto-planetary nebulae (Kraemer et al. 2002). Its identification as a non-YSO is strengthened by the fact it is not located within a molecular cloud.

2.3.5 Comparison to Previous Classifications

The catalog from which our sources were chosen (GC09) was developed via multi-wavelength photometry and image inspection. We compared our classifications with those originally proposed by GC09. Table 2 summarizes the results of this comparison. Of the 294 sources in this study, 269 had been identified as Definite or Probable YSOs by GC09. Of the 269 candidate GC09 YSOs, 262 of them have here been confirmed spectroscopically to have spectra indicative of embedded YSOs. Six remaining sources are members of the O group which may be Herbig Ae/Be stars, AGBs, or post-AGBs, and the seventh is a member of the B group. Most

LMC AGBs are excluded from the GC09 candidate YSO catalog based upon mid-IR colors bluer than YSOs. GC09 identified other candidate AGBs by their SEDs which tend to peak in the IRAC bands. We find that the spectra of members of the O Group are generally flat, explaining why they may have not been excluded from the GC09 candidate YSO catalog. Clearly, with a success rate of >95%, the CMD, SED, and image inspection criteria used by GC09 to distinguish sources with YSO-like spectra from non-YSOs constitute a robust procedure.

GC09 gave sources 052219.71–654319.0, 052335.54–675235.6, and 054033.97–692509.9 the primary classification of AGB star; additionally, 045245.62–691149.5 received a secondary classification of AGB. Source 052335.54–675235.6 has strong PAH features and is likely an embedded YSO. This object has been previously identified in the literature as IRAS 05237–6755, is listed in the online database SIMBAD[2] as a star, and has been studied previously as a candidate AGB. We agree with previous studies by Reid et al. (1990) and Loup et al. (1997) which concluded via color criterion that this source is not an AGB. Source 045245.62–691149.5, a member of the F group, has a mostly featureless spectrum with extremely weak silicate absorption and even weaker PAH emission. GC09 classified it as a 'Probable' YSO but could not rule out the possibility of it being an AGB. Previously identified as an AGB by Wood et al. (1992), we find that it has spectral properties more consistent with a massive embedded YSO. This is further supported by its location within both a molecular cloud and a complex of dusty material seen prominently in the 5.8 and 8.0 μm IRAC images. GC09 gave 054033.97–692509.9 a primary classification of AGB, and we can confirm that it has the spectroscopic properties consistent with an evolved star. Finally, the spectrum of 052219.71–654319.0 is likely a result of a

2 http://simbad.u-strasbg.fr/simbad/

miss-pointing by *SST*; its spectrum is completely feature-less and is unlike any other previously-identified spectra.

Five of our observed objects are GC09 candidate YSOs with a secondary classification of normal star. All five of these sources have now been spectroscopically confirmed to have spectra indicative of embedded YSOs. One GC09 candidate YSO, 045713.47–661900.1, has a secondary classification of background galaxy. Here, we have classified it in the PE Group. The 13 sources we observed left unclassified by GC09 due to the lack of data in at least one IRAC band are classified as follows: 3 are classified in the P Group, 9 in the PE group, and 1 in the O group. All seven EROs were photometrically identified by GC09 and have here been confirmed spectroscopically to represent a rare class of evolved star.

Two sources have GC09 primary classifications of 'diffuse' source. Diffuse sources have SEDs and images consistent with local enhancements of dust emission (see Section 5.4 of GC09). Possible characteristics of diffuse objects include extended or non-point-source IRAC images and the absence of a near-IR or MIPS counterpart. Since diffuse sources have IRAC photometry that is dominated by PAH emission, it is unsurprising that the four diffuse sources were here classified in the PE group. It is probable that both these sources truly are only local enhancements of the ISM and not YSOs. Sources 045205.39–665513.8 and 052204.85–675800.3 have no optical or near-IR counterparts, and both are located on prominent dust filaments seen in IRAC images and are extended in the direction of the filament. Two other sources have GC09 secondary classifications of diffuse sources. The two sources, 053554.94–693903.0 and 054137.57–711902.0 are spatially extended in the mid-IR, although both have tentative near-IR

counterparts – a weak K-band counterpart exists for the former, and a K-band point-source with a coincident compact Hα emission region is slightly off-set from the the latter. We concur with GC09 that 045205.39–665513.8 and 052204.85–675800.3 are likely diffuse sources, while 053554.94–693903.0 and 054137.57–711902.0 may be YSOs. It is important to note that these likely diffuse objects are spectroscopically indistinguishable from YSOs based solely upon their IRS spectra. Clearly a careful inspection of SEDs, multi-wavelength images, and spectra is required to separate sources which may be YSOs from those that are not.

The GC09 candidate YSOs are broadly separated into two luminosity categories – those with [8.0] > 8.0 and those with [8.0] < 8.0. The 8.0 μm magnitude has been suggested to be a good first-order proxy for a YSO's mass so that the brightest sources ([8.0] < 8.0) are high-mass while the dimmer sources are less massive. This is supported by several recent studies. GC09 found that the luminosity function of the [8.0] band of their Definite and Probable YSOs with [8.0] < 8.0 is consistent with recent power-law determinations of the high-mass part of the initial mass function (see Fig. 17 of GC09). Chen et al. (2008) found in a case study of massive YSOs in the LMC's N44 that SEDs of YSOs with [8.0] < 8.0 can be well-fit by radiative transfer models where the central YSO has a mass >9 $M_{\odot}$ (Table 7 of Chen et al. 2009). But their results also demonstrate that good fits to the SEDs can be achieved by using a variety of central source masses. Thus the direct application of YSO masses based upon luminosities is likely most valid when considering a large sample of sources. We observed a total of 38 objects with [8.0] > 8.0. Of those, 36 were classified as definite YSOs by GC09 and 2 as probable YSOs. The dimmest sources do not show any large biases toward a particular spectral feature. The 38 [8.0] > 8.0

sources are classified by PCA as follows: 1 source in the S group (3%), 16 in the P group(42%), and 21 in the PE group (55%). This distribution is consistent within the limits of small number statistics with the entire PCA-based classification catalog which is composed of 4% S Group, 2% SE Group, 37% P Group, 52% PE Group, 1% E Group, and 4% F Group sources.

2.4 Spectral Evolution of an Embedded Massive YSO

Since massive YSOs can take thousands of years to form, it is observationally impossible to watch a single star develop. Instead, studies are done statistically on a large sample of sources. Our catalog of sources represents the most reliable census of massive YSOs in the LMC, and given the large number of sources and the unbiased nature of their identification, we have captured YSOs at various stages of evolution. This allows us to develop a scheme for the evolution of massive YSO spectra and to tie the spectra to the astrophysics involved in star formation. Here, we primarily focus on the evolution of the most massive YSOs, and so are only concerned with those embedded sources with $[8.0] < 8.0$. We refer to these sources as massive based upon the rough mass lower-limit described in Section 2.3.5. This mass cut-off is certainly not exact, and it should be noted that when we refer to massive YSOs, we are referring not to a mass-based cut-off, but a luminosity-based one.

2.4.1 Complications of the Spectral-Evolutionary Connection

The assessment of a YSO's evolutionary state based upon its IRS spectra is primarily complicated by the possibility of spectral features originating from regions external to the YSO's

immediate star-disk-envelope system. Given the large size of the IRS slits (as wide as 11.1" – 2.6 pc at the LMC distance), any radiation from an object's environment that falls within the slit will contribute to its spectrum. As evidenced by the apparent spatially-extended nature of these objects, we suspect this type of spectral contamination from the environment may play an important role.

In particular, there may be contamination from fine-structure lines that originate external to the YSOs. To better assess the origin of the fine-structure lines, we have compared the strength of a fine-structure line in the spectrum of the IRS's full-slit to the strength of the same line when a spectrum is extracted at the position on the slit farthest from the source. The SH module has a slit size of 5×2 pixels; in the first nod position, the source is centered on the first 2×2 pixels, while in the second nod position the source is centered on the last 2×2 pixels. We have therefore extracted a spectrum for every object with fine-structure lines along a 1-pixel wide strip on the side of the slit opposite the source. At the distance of the LMC, the 'off-source' position is ~2 pc from the object. Nominally, the 1×2 pixels at these slightly 'off-source' positions would not detect emission from a point source. Consequently, if the target source is coincident with a compact fine-structure line-emitting object, then there is a concentration of fine-structure emission on the source, and the equivalent width per pixel of a fine-structure line from the full slit spectrum will be larger than the equivalent width per pixel at the 'off-source' slit position. However, if the ratio of the fine-structure line's equivalent width per pixel of the full slit and the 'off-source' position is equal to or less than one, the full slit spectrum used in our classification is likely contaminated by strong fine-structure line emission external to the source. The [SIII] line

at 18.7 μm is ideal for this investigation since its location on a relatively flat region of the spectrum allows for an easy determination of the equivalent width. We have calculated this ratio for every fine-structure line source (SE, PE, and E groups) and have provided this [SIII] concentration ratio in Table 1. It may be that objects with [SIII] concentration ratios of nearly or less than unity are being mis-identified as YSOs capable of ionizing their surroundings and producing fine-structure lines. Given the spatial resolution of the IRS, determining the exact nature of each source may require the less contaminated spectra that will be possible with the *James Webb Space Telescope* (Gardner et al. 2006).

To test the severity of environmental contamination from the presence of external dust within the slit, we compared the flux values at 24 μm from background subtracted MIPS photometry and IRS spectroscopy. Comparing the 24 μm fluxes in this manner can be a measure of the radiative contamination from thermally-emitting dust. We find that the sources with the smallest photometric to spectroscopic ratios are the dimmest sources. This implies an expected finding, that environmental contamination from dust is the most severe for the dimmest sources.

A second way the environment can affect an object's spectra is through the external pumping of UV radiation onto the outer regions of the object, a situation that is unrecognizable using the [SIII] concentration ratio. Such a scenario is certainly the case for the previously discussed diffuse sources 045205.39–665513.8 and 052204.85–675800.3. We demonstrated that these sources identified as local enhancements of dust – which are without a central heating source – can have spectra that mimic YSOs with photodissociation regions and compact HII regions. The PAHs within the local dust knot are most likely being UV-pumped from

neighboring O and B stars, while the fine-structure lines likely originate from the larger HII complexes in which they reside. Similar external radiation effects almost certainly contaminate the spectra of many objects in our sample.

Given that a majority of our sources are located within or on the edges of large HII complexes, spectral contamination from ionized gas is expected to be prevalent. This problem is difficult to identify due to the limited spatial resolution of the observations and is harder to correct since the radiation is a phenomenon local to the YSO and cannot be corrected by background subtraction. For every source, we have investigated its environment through careful examination of Hα, IRAC, MIPS, and CO maps. We obtained the Hα images from the Magellanic Cloud Emission Line Survey (MCELS; Smith et al. 1999) and downloaded available data from the NANTEN CO(J = 1–0) survey of the LMC (Fukui 2002). The results of this examination are given in Table 1. Each source is checked for four different environmental situations: whether or not it is located within a molecular cloud delineated by CO data, possible coincidence with a small (< 1pc radius) Hα source, if it is located within a larger diffuse Hα emission region, and whether or not it is located within large-scale dust complexes including filaments, rings, or more irregular shapes. We find that ~80% are located within CO clouds, approximately 1/3 of the sources are coincident with a compact HII region, nearly every embedded source is located within a dusty structure, and ~3/4 are within regions of diffuse Hα emission. A complete assessment of an object's true nature must include considerations of its spectrum along with possible environmental sources of spectral contamination.

It is important to note that many of the 277 embedded object spectra likely are the

combined spectra of several YSOs in a tight cluster that are spatially unresolvable by *SST* IRS. Should there be one source that dominates the IR-spectrum, then the following analysis is fairly strong, but if there are multiple equally-contributing YSOs, the analysis is less robust. We have inspected near-IR images of every object to look for signs of multiplicity. We obtained J and K_s band observations from the Two Micron All Sky Survey (2MASS; Skrutskie et al. 2006) and with the higher-resolution Infrared Side Port Imager (ISPI; van der Bliek et al. 2004) camera on the CTIO Blanco 4m telescope. Table 1 reports our results. Sources are considered candidates for multiplicity if they clearly show several point-sources or are extended in the J and K_s bands where IRAC images show a single source. A total of 162 embedded sources (58%) are identified as being possible multiple sources, in good agreement with the 65% finding of Chen et al. (2009) within the N44 complex. However, a majority of the possible multiple sources appear to have a single source that dominates the luminosity, a finding that is consistent with the known steep power law between mass and luminosity that allows massive stars to dominate the luminosity of a cluster. We conclude that treating the YSOs as single massive YSO systems is valid to first order with a large sample of objects.

2.4.2 Evolutionary Groups

The objects in the S group represent the earliest stages of a massive YSO's life after attaining enough mass to be included in our sample. The extremely deep absorption from silicates indicates that the sources are highly embedded in dense envelopes of material, with the deepest absorptions originating from the most-embedded sources. An alternate view is that the

strength of the silicate absorption depends on the sight line from which the YSO is being viewed. Massive star formation is poorly described by a spherically symmetric envelope model. Instead, the most recent models have included axis-symmetric (Whitney et al. 2003) or even asymmetric, 'clumpy' envelope geometries (Indebetouw et al. 2006). In the case of axis-symmetric models, the strength of the silicate feature will depend on the viewing angle with respect to a YSO's bipolar outflow. Edge-on (parallel to the plane of the disk) sight lines show prominent silicate absorption profiles, while highly inclined sight lines down the 'throat' of a bipolar outflow show little or no silicate absorption (Robitaille et al. 2006). Similarly, Indebetouw et al. (2006) showed that the 10 μm silicate feature can vary greatly in strength between different lines of sight through a clumpy envelope. In fact, the voids between the clumps allow near IR radiation to escape the envelope, resulting in little or no silicate absorption along a sight line through such a void. Given that recent modeling predicts that a significant percentage of sight lines produce silicate absorption features, the small number of objects with silicate absorption relative to the number without it suggests that silicate absorption strengths are likely not exclusively line of sight dependent. Although it is possible that S and SE group objects may be identified as P, PE, or E group objects if viewed from a different location, it should be noted that the most embedded YSOs, those enshrouded in the most material, are more likely to have sight lines through either dense clumps (in the asymmetric models) or the densest regions of the envelope not cleared by outflows, winds, or radiation pressure.

Nine of the eleven massive objects in the S stage additionally have a prominent 15.2 μm CO_2 ice feature, likely originating from the cold outer region of the YSO's envelope. These

absorption features resemble those seen in galactic sources W33 A (Gibb et al. 1998) and Elias 29 (Boogert et al. 2000), both YSOs deeply embedded in the clouds from which they formed. While silicate absorptions can arise from diffuse cloud spectra, features identified with ices are seen exclusively in dense clouds; with ice sublimation temperatures of ~100 K or less, the absorption must occur in the outer, colder regions of the stellar envelope (van Dishoeck 2004). There is a large variation in the strength of the ice band, and it is therefore an excellent diagnostic of environmental changes. In particular, the large number of S group sources with ice bands and the scarcity of sources in other groups with ice features demonstrate a gradual heating of the protostellar envelope. While 70% of the S and SE sources have a prominent CO_2 absorption, only <10% of the later-stage objects display the same feature. This finding supports the idea of gradual envelope heating due to an increase in the ratio of stellar radiation to circumstellar mass resulting from the dissipation of the envelope from accretion, outflow, and stellar wind. There also appears to be differences between sources in the line shape of the ice feature, a variation that may reflect evolutionary changes within the S group itself.

Members of the SE group likely represent a more evolved form of the highly embedded sources in the S group. Fine-structure lines likely originate from compact or ultracompact HII regions. Small HII regions can form around single massive YSOs after they begin producing a copious amount of UV radiation. SE objects are still highly embedded in circumstellar material but also show indications of a compact HII region. This suggests that the creation of a compact or ultracompact HII region can begin very early in the life of a YSO, before it has cleared much circumstellar material. The strength of SE group fine-structure lines varies by several orders of

magnitude between sources. If the emission is originating from a small HII region surrounded by a larger gas and dust shell, then the line emission may be attenuated by the intervening material by an amount determined by the optical depth of the shell. We have compared six different fine-structure line strengths for the five SE sources to the strength of the silicate feature, a measure of the column density of the surrounding material. Silicate feature optical depths are determined by fitting the spectra to model silicate spectra using the IDL PAHFIT code (Smith et al. 2007; originally written for use on low-resolution IRS observations of galaxies) modified to account for the higher resolution in our observations. For SE objects, we find a very strong inverse correlation between the fine-structure line strengths and the silicate optical depth, suggesting that the fine-structure emission is being screened and attenuated by the surrounding dust shell. However, given the small number of sources in the SE group (5), the implicit assumption of equal intrinsic line strengths (intrinsic line strengths will vary between sources with differing ionization fluxes, densities, region diameters, and abundances), and the fact that the correlation disappears after including sources of all groups, the correlation may not represent a true phenomenon. If the fine-structure-silicate correlation within the SE group is real, then the lack of a correlation among the other groups implies that either the optical depths of the dust shells are not large in these groups, or that the fine-structure emission in the other groups does not solely originate from within a dust shell at all.

Because SE objects show both the characteristics of very young (S group) and more evolved (E and PE group) objects, SE sources could represent the transition from a highly embedded to a less-embedded YSO, objects that are beginning to clear away their parent

molecular cloud. Since members of the S group show no signs of UV radiation, they are either true massive protostars (accreting, pre-hydrogen burning massive YSOs) or are accreting at a rate and with a geometry that is able to contain the UV radiation. In either scenario, the massive YSO is unable to substantially disturb its natal cloud in the S stage. Although there are only 17 total sources in either the S or SE groups, 52 sources (~20%) pass the PCA test for silicate absorption. A majority of these objects are members of the P and PE spectroscopic groups, both of which have features indicative of UV-emitting central objects. As discussed earlier, several PAH emission bands are superimposed on the 10 μm silicate absorption feature, making the strength of the silicate feature difficult to quantify in P and PE spectra. Even in the scenario that PCA is overestimating the number of silicate absorption sources by improperly separating the blended silicate and PAH features, sources with strong silicate absorption represent a minority of sources. Assuming a typical formation time of a few 10^5 years (Zinnecker & Yorke 2007), we estimate that it takes a massive YSO on the order of a few thousand to a few ten thousand years to clear its surroundings to the point where the silicate absorption feature is no longer apparent in its spectrum. In Chapter 4, we present direct observations of the surrounding dense molecular gas to better assess the relationship between silicate absorption strength and a YSO's 'embeddedness.'

Three of the five SE objects are coincident with small compact/ultracompact HII regions seen in the Hα images of MCELS. The presence of a compact Hα source strengthens our assertion that the fine-structure lines present in the spectra originate from a small region ionized by the source itself. The two objects without corresponding compact HII regions, 045206.97–665516.4 and 053536.88–691214.1, are both located within areas of high Hα emission from a

larger, more extended structure. It is therefore possible that the fine-structure lines do not originate from the source itself and were not properly background subtracted. In fact, the two sources without a visible coincident compact Hα source also have the lowest [SIII] concentration ratios of the SE group. Object 045206.97–665516.4 has a ratio less than 1, indicating that the strength of the [SIII] line is stronger at distances farther from the source and that the fine-structure line emission is likely at least in part either an environmental contamination or the result of an extended fine-structure line-emitting structure. Although the sample size is small, there seems to be a correlation between the presence of a compact Hα source and the existence of fine-structure lines in the spectra – 60% of the SE sources have accompanying compact HII region, compared with only 25% of the S group objects. Of the ten massive S objects, only three, 045111.39–692646.7, 045550.62–663434.6, and 052646.61–684847.2 show any sign of compact Hα emission on the source, and the emission is relatively faint.

The P, PE, and E groups likely represent the later stages of a YSO lifetime. Of the 239 massive embedded objects, 217 of them have either PAH emission, fine-structure lines, or both. Since both PAH and fine-structure lines are indicative of a UV-emitting central object, massive YSOs spend a substantial portion of their lives emitting in the UV. Objects with UV-produced features represent ~90% of our catalog, suggesting that massive embedded YSOs emit in the UV during a substantial proportion of their lives, possibly as high as 90%. However, note that given the possibility of environmental spectral contamination, the length of this stage may in fact be shorter.

The strengths of fine-structure lines vary by up to 6 orders of magnitude between sources,

and PAH emission power can vary by as much as 5 orders of magnitude. If fine-structure line and PAH band photons travel along a line of sight through dense circumstellar material, the intrinsic line strengths may be attenuated by a factor set by the optical depth at each line's wavelength. Given a high enough optical depth, objects with inherently strong PAH or fine-structure line emission may have the features completely attenuated by surrounding material, causing them to be improperly categorized in our spectral classification scheme. As previously discussed, we find no correlation within the P, PE, or E groups between any of the fine-structure lines and the optical depth. Similarly, there appears to be no recognizable correlation between the 7.7 μm and 11.2 μm PAH bands' strengths and the strength of the silicate absorption feature. We fit these PAH features using Lozentzian profiles on a first order polynomial baseline. This suggests that the optical depth of dust surrounding the fine-structure line and PAH-emitting regions are generally not large. We conclude and that viewing angle does not have a large effect on the strength of PAH bands or fine-structure lines, and should not affect classification.

Among the 144 PE and E group objects, the [SIII] line concentration ratios range between 0.9 and 408 with a median value of 1.4. A median value greater than 1 indicates that for a large majority of our spectra, the fine-structure line is stronger at slit positions closer to the source, suggesting that most the PE and E objects have fine-structure line peaks on the source and are less likely to be solely environmental in nature. However any object with a concentration ratio near or less than 1 is more likely to be affected by the local environment. There are a total of four sources with [SIII] concentration ratios less than 1.0; three of these are located within large complexes of strong Hα emission and lack a compact Hα object. This implies that the fine-

structure lines of these sources are more likely environmental in nature. Of all the sources located within large HII complexes, the median [SIII] concentration ratio is 1.36. Conversely, sources not located within larger HII complexes tend to have larger [SIII] concentration ratios: the median [SIII] concentration ratio of sources not located within large HII complexes is 3.37. The strong correlation between a source's location within an HII complex and its [SIII] concentration ratio suggests that this ratio is a good measure of the amount of environmental fine-structure line contamination. Note that ratios greater than 1.0 are strongly favored, even with sources within HII complexes. This implies that although environmental fine-structure line contamination likely plays a heavy role, most sources have ratios consistent with being coincident with a compact fine-structure line-emitting object. PE and E group objects with compact source-like [SIII] concentration ratios represent approximately one half the sample of massive YSO candidates in this study. A detectable compact or ultracompact HII region is likely to have formed around half of the YSOs in our catalog, suggesting that massive YSOs can create a region whose fine-structure lines are *SST* IRS-detectable approximately half-way through the massive stages of its formation probed here.

The spectra of P and PE group objects resemble those typical of photodissociation regions (PDRs); in our sample of massive YSOs, the PAH emission pumped by the YSO's own UV radiation probably originates from such a region around the forming star. High spatial resolution ISO observations of ρ Oph W within the ρ Oph molecular cloud indicate that the PAH bands and fine-structure lines are common to hot dust illuminated by O or B-type stars (Boulanger et al. 2000). The central object heats its surroundings to high temperatures,

dissociating molecules, and exciting PAH vibrational levels leading to fluorescent PAH emission. The objects in the P stage, when embedded YSOs display only strong PAH emission, may be younger than those of the PE or E stages. Although both PAHs and fine-structure emission lines are indicators of UV radiation, PAHs can absorb and reprocess longer wavelength radiation than is necessary to create an HII region. In fact, PAH spectra are produced most efficiently when the incident UV radiation is intense but relatively soft – even below the Lyman limit. P group objects may then represent YSOs who are hot enough to produce soft UV radiation, but have not yet become hot enough to produce many higher energy photons that can ionize its surroundings. The presence of PAH emission and lack of fine-structure lines can also be explained if a hot, hard UV-producing star's radiation is being quenched by a high accretion rate, preventing a detectable compact HII region from forming. In either scenario, objects in the P stage therefore are the transition objects that bridge objects that cannot form detectable compact HII regions and those that can. Externally-produced PAH emission is likely a large contaminant to both the P and PE spectra, but even given this environmental effect on the spectra, the absence of fine-structure lines in the P group indicates a source unable to produce a detectable compact HII region.

Seventeen of the 100 total P objects passed the PCA test for silicate absorption, indicating they may have a silicate feature at 10 μm. These may be the youngest of the P group, and could represent a subgroup of sources that have just begun clearing their surroundings and are still embedded in a thick molecular envelope. Alternatively, these objects could in fact be examples of objects whose line of sight passes through a dense region of the envelope, creating a strong silicate feature. The fact that there is no recognizable correlation between either PAH or fine-

structure line strength and optical depth also suggests that the PAH features and fine structure lines are not formed in a region inside a shell of circumstellar material as would be expected in a spherically-symmetric model. This is consistent with previously described models which allow radiation to scatter and escape via outflows or voids between clumps. In such a scenario, the 10 μm absorption feature originates from a dense core or clump that is both self-screening and attenuating radiation originating from behind the cloud/clump, while PAH and fine-structure line emission can originate from regions external to this line of sight (e.g. outflow cavity walls, other clumps, extended HII regions) that are being illuminated/ionized by the central source.

PE group objects represent the most evolved form of YSO in our proposed evolutionary scheme. PAH emission and fine-structure lines indicate that a high level of UV radiation is originating from the central source and has created a compact HII region surrounding the object. While the fine-structure lines originate from this HII region, the PAH emission likely originates from the PDR surrounding the HII region. PAHs are depleted within the boundary of the HII region, destroyed by the intense hard-UV radiation. P group objects may be an extreme PE source – where a full-sized compact HII region cannot form due to high accretion rates but a PDR can form outside the very small central ionized region. E group objects likely represent a type of PE object, ones with strong fine-structure lines and relatively weak PAH emission. Although the 2 objects in the E group do not pass either PCA test for PAH emission, by-eye inspections of both spectra show clear signs of PAH emission. Both the objects may be better classified into the PE group or as extreme PE sources where the PDR is relatively small.

The F group is comprised of 11 objects that did not pass any spectral feature's PCA test.

Seven may show signs of weak silicate absorption at 10 μm, 7 may have fine-structure lines, and all 11 may have weak PAH emission. It may be that these sources are better classified into other groups, but because PCA was used to quantify the strengths of spectral features, they have been dubbed 'featureless.' Since they represent a small fraction of the total sample (6%) and do not appear biased towards a particular feature, we do not consider their contribution to the above evolutionary analyses statistically important. The five sources without full spectral coverage are assigned to the U Group.

2.5 Conclusion and Future Directions

We have obtained high- and low-resolution IR spectra of 294 objects in the LMC. The sources were chosen from a catalog of IR-luminous objects developed by GC09 based on their massive YSO-like photometric and SED qualities. The *SST* IRS spectra cover the wavelength range of 5–37 μm and show a variety of spectral features including absorption from silicates and ices and emission lines from PAHs and ionized atoms. Of the 294 sources observed, 277 spectroscopically resemble embedded massive or intermediate-mass YSOs. The remaining sources are comprised of a mixture of Herbig Ae/Be stars (with O-rich emission disks) or highly evolved stars such as RSGs, AGBs, and post-AGBs.

We classified both the YSOs and non-embedded sources into distinct groups based upon their spectral features. Embedded objects were categorized automatically via the statistical process dubbed PCA. This allowed for an unbiased and quantitative classification scheme. Non-embedded sources – primarily evolved stars, and not the primary focus of this paper – were

classified into groups by-eye. The embedded sources all rise into the red end of the spectrum indicating their continuum emission is dominated by dust. Most embedded sources are identified as massive YSOs still surrounded by the dense cloud from which they formed. Our catalog largely consists of sources with luminosities consistent with YSOs of at least ~8 $M_{\odot}$, and therefore represent the later stages of massive star formation, after they have accreted a significant fraction of their mass. Individual spectra within the large sample of sources act as snapshots of massive star formation and collectively display an evolution of massive YSO spectra. The youngest sources (S and SE group) are dominated by deep silicate absorptions and ice absorptions originating from the cold outer regions of the envelope (van Dishoeck 2004). Later stages of massive YSO evolution show a gradual heating of the circumstellar envelope evidenced by the lack of ice features. Older sources also display signs of envelope depletion in the form of little or no silicate absorption. As the envelope is depleted and accretion slows or ceases, UV radiation from the young star begins to dissociate and ionize the nearby molecular material forming compact HII regions and PDRs (e.g., Hoare et al. 2007). Well-known indicators of compact HII regions and PDRs are present in the spectra of later-stage massive YSOs (P, PE, and E group) including fine-structure emission lines and PAH emission features.

The work described here is a first step in a series of investigations using this newly-formed YSO catalog into the evolution of massive YSOs and the interaction between them and their environment. Follow-up papers will address both the inter- and intra-group evolution of specific features. YSO evolution will also be tied to the state of the molecular cloud they were formed from and the nearby stellar population. Finally, work should be done to compare the

spectra of these massive YSOs and their corresponding evolutionary stage with radiation transfer models to assess both the quality of the models and the accuracy of their spectral-based evolutionary placement.

2.6 Acknowledgments

The authors wish to thank Charles Gammie for an early helpful discussion of PCA, Karna Desai and Ryan Peterson for their work on some of the figures and tables presented here, and the anonymous referee for helpful comments. This work is based in part on observations made with the *Spitzer Space Telescope*, which is operated by the Jet Propulsion Laboratory, California Institute of Technology under a contract with NASA. This study made use of observations obtained at *Cerro Tololo Inter-American Observatory*, a division of the National Optical Astronomy Observatories, which is operated by the Association of Universities for Research in Astronomy, Inc. under cooperative agreement with the National Science Foundation. This publication has made use of the data products from the Two Micron All Sky Survey, which is a joint project of the University of Massachusetts and the Infrared Processing and Analysis Center/California Institute of Technology, funded by NASA and the NSF. The CO maps are the result of the NANTEN project which is based on the mutual agreement between Nagoya University and the Carnegie Institution of Washington. This research made use of the SIMBAD database, operated at CDS, Strasbourg, France and SAOImage DS9, developed by Smithsonian Astrophysical Observatory. Support for this work was provided by NASA through an award issued by JPL/Caltech.

Chapter 3

Thermal Processing of Circumstellar Ices Around Massive YSOs

This chapter has been submitted and is under review for publication in The Astrophysical Journal.

3.1 Introduction

A central question regarding the formation of stars is how the structure and chemical composition of the molecular material surrounding forming stars evolve. Considering evidence that most stars form in clusters (Carpenter 2000; Lada & Lada 2003), how a star affects the surrounding material may in turn influence nearby current or future star formation. Such effects are strongest in regions near the formation of a massive star, which dominates the overall luminosity, ionizes its surroundings (see reviews by Garay & Lizano 1999; Beuther et al. 2007), and creates strong outflows that reshape the parental cloud (e.g., Shepherd & Churchwell 1996). Indeed, mounting evidence that the Sun was born in a cluster with a massive member (e.g., Cameron & Truran 1977; Srinivasan et al. 1996; Ellis et al. 1996; Meyer & Clayton 2000;

Vanhala & Boss 2000; Tachibana & Huss 2003; Looney et al. 2006) means that the evolution of material around massive young stellar objects (YSOs) could have ramifications for the formation of the Sun, the Earth, and even conditions for life.

Circumstellar envelopes, which act as mass reservoirs for accretion (see reviews by Zinnecker & Yorke 2007; McKee & Ostriker 2007), absorb photospheric optical and UV radiation and re-radiate in the infrared (IR). The reprocessed stellar radiation reveals information about the state of the circumstellar material (van Dishoeck & Blake 1998). The infrared spectra of massive YSOs are known to show a multitude of spectral features including polycyclic aromatic hydrocarbon (PAH) emission features, ionic fine-structure lines, silicate features in both absorption and emission, and both gas and solid-state molecular absorption bands (e.g., Gibb et al. 2000; Boogert et al. 2000; Kraemer et al. 2002; Peeters et al. 2002; Martin- Hernandez et al. 2002; Seale et al. 2009; Kemper et al. 2010). In the cold regions of a massive YSO's circumstellar envelope, molecular material is frozen onto dust grains, and the infrared spectra of such objects are known to display features characteristic of molecular ices (e.g., Tielens et al. 1984; van Dishoeck & Blake 1998; Gerakines et al. 1999; Gibb et al. 2000).

Since the development of space-based infrared observatories, about a dozen interstellar ice species have been observed with infrared spectroscopy in a multitude of environments including H_2O, CO, and CO_2, along with more complex molecules such as CH_3OH, CH_4, and HCOOH (for a review of ISM ice detections, see Gibb et al. 2004). In particular, ice absorption features are copious in the spectra of background stars through dense interstellar clouds (Bergin et al. 2005; Knez et al. 2005; Whittet et al. 2007, 2009). Comparisons of dark cloud infrared

observations with laboratory work show that the observed absorption profiles of ices such as CO and CO_2 cannot be explained by any single ice. For example, the CO_2 bending mode in dark clouds is readily fit by combining a H_2O-rich (polar) CO_2 ice mixture with that of a CO-rich (apolar) CO_2 ice mixture (e.g., Gerakines et al. 1999; Bergin et al. 2005; Knez et al. 2005). Such an observation is qualitatively consistent with a hierarchical ice mantle growth model in which an apolar mantle forms on top of a polar layer. While the polar component typically accounts for a majority of the total CO_2 column density, these observations indicate that interstellar CO_2 is formed in both apolar and polar ice mixtures that exist separately on the ice grains.

Undisturbed by star formation, quiescent dark clouds contain ices in a relatively pristine state. However, the observed interstellar spectra toward both low- and high-mass star formation regions – which are presumably more processed – display some significant spectral differences (e.g., Gerakines et al. 1999; Pontoppidan et al. 2008; Zasowski et al. 2009). The relative abundances of ice species differ between quiescent dark clouds and star forming regions, differences attributed to both the re-sublimation of the most volatile ice species out of the solid phase and the production of new molecules via chemical reactions in star formation regions (Gibb et al. 2004). Similarly, spectral profiles of features originating from star forming regions and those from cold quiescent clouds differ, reflecting chemical differences between the ices presumably due to thermal processing of grain ice mantles during star formation (e.g., Ehrenfreund et al. 1998; Pontoppidan et al. 2008; Oliveira et al. 2009). The effects of thermal processing are irreversible; thus, the degree of processing detected in the envelope reflects the

thermal history. Ice around YSOs resides in the cold outer regions of the circumstellar envelope where temperatures are below the ice's sublimation temperature, and using observations of field stars behind molecular clouds as an unprocessed ISM baseline, the shape of the ice features can serve as a chemical, thermal, and evolutionary probe if properly calibrated.

Among the most prominent ice absorption features in YSO spectra is the CO_2 bending mode at 15.2 μm. Given its location in a relatively featureless part of the mid-IR, the strength and profile of the feature can be well determined, and the feature shows an intriguing range of shapes in a multitude of environments. Toward clouds observed against background extincted stars, the band is relatively smooth (e.g., Gerakines et al. 1999; Bergin et al. 2005; Knez et al. 2005), while in clouds surrounding current star formation (that presumably trace more processed material), the 15.2 μm feature is characterized by a very distinct sharp, double-peaked structure that results from the splitting of the bending mode v_2 due to a resonance with the symmetric stretch mode v_1 and often a 'bump' or 'shoulder' at ∼15.4 μm (e.g., Gerakines et al. 1999; Gibb et al. 2004; Boogert et al. 2004; Pontoppidan et al. 2008; Zasowski et al. 2009). These profile differences are attributed to changes in the inter-molecular interactions between CO_2 and other neighboring molecules in ice mixtures, possibly a result of the thermal processing of the ice. Evidence of thermal processing is not exclusive to the bending mode of CO_2. In particular, astronomical observations of the absorption profiles of $^{13}CO_2$ at 4.38 μm (Boogert et al. 2000), H_2O at 3 μm (Smith et al. 1989), and a yet-to-be-identified ice at 6.8 μm (Keane et al. 2001) show similar changes that correlate with each other, with increased gas/solid ratios (van Dishoeck et al. 1996),

and with increased dust color temperatures (Boogert et al. 2000), suggesting that the process is induced by an increase in temperature.

Laboratory experiments with pure CO_2 ices well-match the narrow double peaks at ~15.1 and 15.25 μm of YSO-associated CO_2 ice (Ehrenfreund et al. 1996, 2001). This characteristic double peak in not seen toward quiescent dark clouds; mixtures of CO_2 with other polar and apolar molecules result in interactions between the molecules that modify the profile shape and remove the double peak. Laboratory experiments indicate that upon heating, ice mantles composed of a mixture of CO_2 with other ice species become very inhomogeneous; CO_2 molecules segregate themselves to create inclusions of pure CO_2 that reveal themselves spectroscopically through the characteristic pure CO_2 double peak (Ehrenfreund et al. 1999; White et al. 2009). Recent Monte Carlo simulations of ice diffusion by Oberg et al. (2009) show that segregation of ice constituents in CO_2 mixtures is indeed more energetically favorable. Another pure CO_2 formation process was proposed by Pontoppidan et al. (2008) to explain the presence of the characteristic double peak around low-mass stars, where temperatures may not be high enough to activate the segregation process. These authors suggest that pure CO_2 could also result from the desorption of volatile CO out of a CO:CO_2 ice matrix. In either formation scenario, interstellar observations of the double peak seen around regions of star formation are interpreted as evidence for thermal processing of CO_2 ice by the stellar radiation from the young

star.

In laboratory experiments, the addition of methanol (CH_3OH) to either pure CO_2 or a polar CO_2 ice mixture produces a broad peak at 15.4 μm, a feature coincident with the shoulder seen in the IR spectra of YSOs (Ehrenfreund et al. 1999). While the presence of the shoulder is only an indirect suggestion of the presence of methanol, its existence has been supported by the concurrent detection of CH_3OH's vibrational modes in the spectra of other protostars (e.g., Allamandola et al. 1992; Sandford & Allamandola 1993). The CH_3OH abundance relative to water ice ranges from only several percent or less in dark clouds (Chiar et al. 1996) to 3−10% in most YSOs (Brooke et al. 1999; Dartois et al. 1999) to an estimated 20 – 30% in the massive YSO W33A (Dartois et al. 1999; Gibb et al. 2000). This variation between sources suggests that CH_3OH is not formed in large abundance in dark molecular clouds, but rather has its formation stimulated by subsequent processing in regions of star formation. Like pure CO_2, its presence in high abundance can be interpreted as evidence for ISM processing.

Historically, studies of the evolution of ices have primarily been performed using infrared spectroscopy of Galactic molecular clouds and star-forming regions (e.g., van Dishoeck et al. 1998; Gerakines et al. 1999; Gibb et al. 2000; Bergin et al. 2005; Boogert et al. 2008; Pontoppidan et al. 2008; Zasowski et al. 2009). However, high-mass star formation studies within the Milky Way are plagued by a low number of sources, dust obscuration along the Galactic plane and distance ambiguities that lead to uncertain luminosities. These problems can be largely avoided in the LMC as it is located at a known distance of 50 kpc (Feast 1999), has low

foreground extinction, has a nearly face-on orientation providing a clear view throughout the entire galaxy, and has a high level of active star formation.

The LMC also offers a unique opportunity to study – at relatively high spatial resolution – the effects of a low-metallicity environment on ice chemistry. Indeed, there have been a number of recent studies of ice absorption from LMC objects. The first extragalactic detection of ice was by van Loon et al. (2005), who detected 3.1 μm H_2O and 15.2 μm CO_2 ice in the IR spectra of the LMC YSO IRAS 05328-6827. Several subsequent studies of the LMC have reported ice detections from a variety of molecules including CO_2, H_2, CO, CH_3OH, $^{13}CO_2$ and possibly XCN (an unknown molecule with the spectral signature of a CN stretch) towards numerous embedded YSOs (Oliveira et al. 2006; Shimonishi et al. 2008; Oliveira et al. 2009; van Loon et al. 2010; Shimonishi et al. 2010).

In a recent survey of massive YSOs by Seale et al. (2009, hereafter SL09), the *Spitzer Space Telescope*'s Infrared Spectrometer (IRS; Houck et al. 2004) was used to obtain mid-IR spectra of nearly 300 massive YSO candidates in the LMC selected from Gruendl & Chu (2009, hereafter GC09). The YSO-like nature of 277 of the objects was confirmed, and ice absorption was detected towards a number of the objects. The SL09 observations represent the largest catalog of LMC massive YSO high-resolution spectra at the time of publication.

In this paper, we decompose the CO_2 bending mode absorption profiles of 40 LMC massive YSOs into distinct shapes attributed to several different ice mixtures to assess their ice composition and thermal history. We compare the results of the decomposition to similar studies of Galactic objects to explore how the ice chemistry between the two galaxies differs, and we

look for evolutionary trends within the LMC massive YSO sample itself. Several other ice absorption features have been previously seen towards massive star forming regions including strong bands at 6.0 and 6.8 μm attributed to H_2O (Whittet et al. 1988) and a not-yet-identified ice, respectively. In our observations, the presence of these bands is not well established since they are heavily blended with other mid-IR spectral features, but we have tested a method of identifying their absorption. In Section 3.2, we describe the nature of the sources included in this study, and discuss the observations and data reduction process. In Section 3.3 we present our methods of ice absorption profile decomposition including the determination of an appropriate continuum and the removal of blended spectral features along with a description of the laboratory interstellar ice analogues used to fit the observations. In Section 3.4 we discuss the results of the decomposition and what they imply about the composition and thermal history of the ices. Finally we explore how the profile shape may depend on massive YSO luminosity, and use a simple envelope model to demonstrate how the observed profiles of ice absorption bands may be affected by evolution.

3.2. Observations and Data Reduction

3.2.1. Target Selection and Makeup

In recent years, the LMC has been the subject of extensive studies of star formation on a galaxy-wide scale. One of the primary observational advantages to studying the LMC is its relative proximity, which allows single instances of massive star-formation (or tightly bound systems) to be resolved even in the mid-IR. Taking advantage of the ability to readily observe the

entire galaxy, a number of studies have sought to identify and catalog all the massive and intermediate-mass YSOs in the LMC (Whitney et al. 2008, GC09). Combined with other studies that identified sites of on-going star formation via their infrared emission, maser activity, and compact Hα emission and centimeter emission, the literature now contains an extensive catalog of LMC YSOs. The objects included in this study are a subset of the catalog of intermediate and massive YSO candidate sources originally selected photometrically by GC09 and subsequently spectroscopically confirmed by SL09. The original GC09 object catalog was developed by extracting point-source photometry from all available observations of the LMC made with *SST*'s InfraRed Array Camera (IRAC; Fazio et al. 2004) and Multiband Imaging Photometer for *Spitzer* (MIPS; Rieke et al. 2004) and constructing color-magnitude diagrams to identify objects with IR excess. The nature of objects with IR excess was then assessed by examining the sources' spectral energy distributions (SEDs) and images from optical to the mid-IR wavelengths. A total of 1172 objects in this comprehensive catalog were classified as 'Definite' or 'Probable' YSOs. For a detailed discussion of source selection and classification, see GC09. Many of the candidate YSOs from GC09 had been previously identified in other studies as possible YSOs via their YSO-like emission characteristics (e.g., HII region, bright IR, and maser emission). Table 3 identifies the objects included in this study by their GC09 object IDs, but also lists alternative names given in other studies and includes notable characteristics of the YSOs from the literature.

In a follow-up study, SL09 obtained IR spectra of 290 candidate YSOs from the GC09 study and spectroscopically confirmed the YSO-like nature of 277 of the most luminous candidate YSOs. Characterized by their distinct spectral shapes and features, the SL09 catalog

includes YSOs contained within different local environments that may reflect varied levels of evolution. While some objects show clear signs of advanced development including PAH and ionized gas emission typical of photo-dissociation regions and compact HII regions, some have spectral signatures of YSOs highly embedded in their parental clouds and envelopes. The objects included in this study are a subset of the spectroscopically-confirmed YSOs of the SL09 catalog and generally span the range of spectral feature classification described in SL09. All sources from the SL09 catalog that show clear detections (from a by-eye inspection) of the most prominent ice absorption feature, the CO_2 bending mode, have been included in this study – a total of 41 objects. See Table 3 for the complete source list. The spectrum for one object, 053931.19-701216.9, has a poor signal-to-noise ratio (SNR). For this source, we have only determined the total CO_2 column density, as the spectral shape is highly uncertain.

The sources in this study are likely some of the youngest in the SL09 spectral catalog. The youngest sources are those still deeply embedded in their parental cloud core or clump, and the presence of an ice absorption feature demonstrates the presence of significant cold circumstellar material. In addition, SL09 identified silicate absorption at 10 μm – characteristic of embedded YSOs – in a majority (23/41 = 56%) of the sources included in this study. As a comparison, SL09 identified silicate absorption in less than 20% of their entire massive YSO spectral catalog.

To get an estimate of the evolutionary developmental stage and luminosity of the YSOs in this study, the spectral energy distributions (SEDs) of all the YSOs have been fit to the radiative transfer models of Robitaille et al. (2007); the model results presented here are a subset of a

larger, more comprehensive study of LMC YSO models by Chen et al. (in preparation). The SEDs, which contain data from the near- to far-IR, are fit using χ^2 minimization to pre-computed radiation transfer models (Robitaille et al. 2006) that span a large range of parameter space (e.g., stellar radius and temperature, disk mass, envelope radius). Because many of these parameters are tied to evolution, this SED fitting technique allows for not only an estimate of physical parameters, but of evolutionary state. The "Stage" classification was introduced by Robitaille et al. (2006) as a way to classify YSOs in a manner that depends not on observational characteristics like color or spectral index, but on the actual evolutionary state of the object determined by its physical properties such as disk mass or accretion rate. In this classification scheme YSOs evolve with time from Stage 0/I (high accretion rate) to Sage II (circumstellar disk and lower accretion rate) and finally Stage III (only a tenuous disk with no accretion).

By fitting the SEDs of our sources to the radiation transfer models, we are able to estimate the Stages of the YSOs; the results of the model fitting are presented in Table 3. Because there are several combinations of model parameters that provide acceptable fits to the data, a range of values for a single parameter must be considered equally valid. In Table 3 we provide the mean luminosity of all the acceptable model fits, and the uncertainty of this luminosity is taken to be the standard deviation of the acceptable model values. We also determined the Stage of each YSO based upon the output physical parameters. The mean stages are provided in Table 3, and the uncertainty of the stage is the standard deviation of the modeled Stages. Note that every source is – within the uncertainty – a Stage I YSO. However, note that the models are based on structures mostly associate with low-mass YSOs (e.g. disks and biconal

outflow cavities), so the applicability of the 'Stage' classification may best be reserved for low- and intermediate-mass YSOs. Luminosity estimates are likely among the most robust modeled parameters given ample SED wavelength coverage.

The model fits indicate that all the sources included in this study are high-luminosity YSOs, with luminosities that range between 10^3 and 10^5 $L_{\odot}$. As evidenced by both the spectral features (ice and silicate absorption) and the radiative transfer models, the sources in this catalog are young, embedded massive YSOs. The relative youth of our sample is further supported by YSO 053929.21-694719.0, which is associated with an H_2O maser (Lazendic et al. 2002), characteristic of very young sources surrounded by dense molecular material that have not yet dissipated much of their circumstellar cloud.

3.2.2. Data Reduction

The IR spectra were originally presented in SL09 and were obtained using the SL (short wavelength, low-resolution), SH (short wavelength, high-resolution), and LH (long wavelength, high-resolution) modules of Spitzer IRS. The spectra presented here are the result of the reduction process described in SL09. For a detailed description of the extraction pipeline including the procedure, a discussion of its quality and merits, and the software used, see SL09. In order to estimate the spectral flux uncertainties, we first assumed an uncertainty of 1/2 the flux difference between the two nod positions with a floor of 1%. We then compared this value to the value extracted from the uncertainty BCD product and retained the higher value. Typical flux uncertainties are on the order of a few percent with the highest values ($\sim$10%) originating

from the ends of IRS spectral orders and modules.

3.3. Decomposition of Ice Features

3.3.1. The 5 – 8 μm Wavelength Region

In the spectra of many low- and high-mass stars, prominent absorption features have been observed at 6.0 and 6.8 μm (e.g., Gibb et al. 2000; Keane et al. 2001; Boogert et al. 2004, 2008; Zasowski et al. 2009). The contributors to both these features are still under debate. The 6.0 μm band is primarily attributed to the bending mode of H_2O (e.g., Tielens et al. 1984). However, several studies (Gibb et al. 2000; Keane et al. 2001) found that the 6.0 μm feature overshoots the H_2O column density as determined by the 3.0 μm water absorption band. This suggests that other ices may contribute to the band, with H_2CO, HCOOH, and NH_3 having been suggested (Boogert et al. 2008). The 6.8 μm feature's origin remains unclear, however. Widely quoted possible sources are NH_4^+ (Boogert et al. 2008), and other organics with O-H, C-H, or C-N vibrations (Gibb et al. 2004; Zasowski et al. 2009). Detections of a number of other weaker absorption features between 5 and 10 μm have been suggested in spectra of both low- (Boogert et al. 2008) and high- (Schutte et al. 1999) mass YSOs.

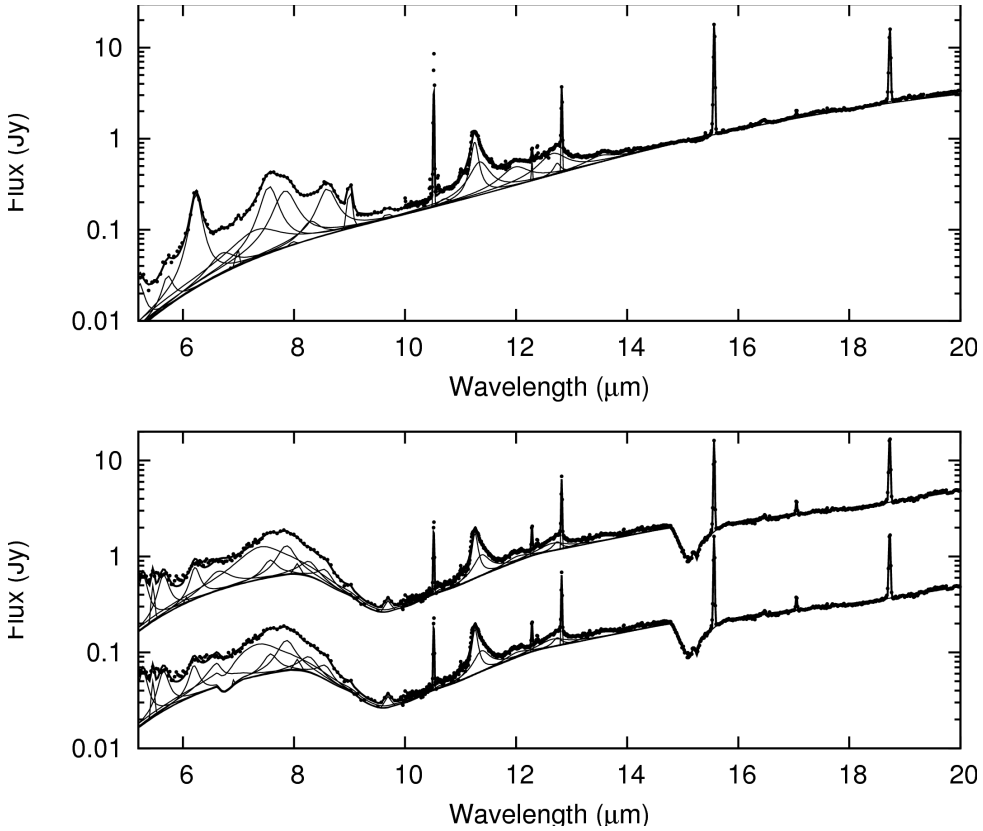

Figure 6. An example of the output from the modified PAHFIT program using sources 053852.67-690437.5 (upper panel) and 045400.10-691155.5 (lower panel). Spectral datapoints are shown in dots. Thin lines show individual spectral features that are fit by the program (PAH emission, fine-structure lines, H_2 emission lines) after attenuation from the silicate feature at 9.8 and 18 μm. The composite fit is the thick solid line. YSO 045400.10-691155.5 has been fit twice – once with (bottom) and once without (top) the 6.0 and 6.8 μm ice features.

In Figure 6, we show the spectra of two sources from the SL09 massive YSO spectral catalog. The top source, 053852.67-690437.5, is dominated by emission features from PAHs and fine-structure lines while the lower one, 045400.10-691155.5, has weaker emission features and prominent absorption bands including silicates at 9.8 and 18 μm and CO_2 at 15.2 μm. Given the presence of the deep CO_2 ice feature in the lower spectrum, the common absorption features at

6.0 and 6.8 μm would be expected to also be observed. Assuming a CO_2 / H_2O ratio of 0.32 (Oliveira et al. 2009) would give an expected H_2O column density of 5.2×10^{18} cm^{-2}, or a 3.0 μm optical depth of ∼0.3 (i.e. a 25% absorption). However significant absorptions at 6.0 and 6.8 are notably absent. This is likely due to the superposition of PAH features on top of the ice features. Indeed, strong PAH features, seen in Figure 6, overlap with the locations of the ice bands. While the presence of PAH bands is not obvious between 5 and 8 μm, the strong emission feature at ∼11 μm suggests that PAH emission is present and is likely filling in the ice absorption bands.

Because of the presence of PAH emission in our catalog of massive YSO spectra, extracting optical depths for possible ice features in the low-resolution portion of the spectra between 5 and 8 μm requires a complex procedure. The SL module slit of IRS has an aperture width between 3."6 and 3."7, corresponding to nearly 1 pc at the distance of the LMC. Such a large aperture allows a significant amount of radiation from a YSO's local environment to enter the slit (SL09). This is particularly true of the 5 – 14 μm wavelength range because of a plethora of strong PAH emission features that can originate from nearby photodissociation regions or externally-illuminated dust clumps. Consequently, any ice absorptions between 5 and 14 μm are heavily blended with PAH emission. Isolating ice absorptions between 5 and 8 μm is further complicated by their location near the blue wing of the deep silicate feature at 9.8 μm. An accurate fit of the silicate feature is required if a proper dust continuum is to be found.

In a recent study of LMC ices, Oliveira et al. (2009) found that at this spatial resolution, it is not possible to de-blend the PAH emission and ice absorption features. In fact, while

absorption at 6.0 and 6.8 μm is almost certainly present, their spectra can be well-fit using only a dust continuum with silicate absorption features and PAH emission bands superimposed. They performed a simultaneous fit of their low-resolution Spitzer IRS spectra using the popular IDL code PAHFIT (Smith et al. 2007) and found that the spectra can be well fit without ice absorption bands at 6.0 and 6.8 μm. We expand on their process and modified the PAHFIT code to attempt to de-blend the PAH emission from the ice absorption. The original PAHFIT code was written specifically for low-resolution Spitzer IRS data, and has here been adapted to accommodate the higher resolution of the data at wavelengths longer than 10 μm. Both PAHFIT and our modified version construct a continuum from eight blackbodies at varying temperatures and then add fine-structure, molecular hydrogen, and PAH emission to the continuum. Finally, the spectra are screen attenuated by model spectra of silicate features at 9.8 and 18 μm and ice absorption features at 6.0, 6.8, and 15.2 μm. Excluding ice absorption features, which can be turned on and off, there are a total of 147 variables fit by the program. Clearly, given the large number of variables and the nature of the spectral features' overlap, several different sets of parameters may exist that give equally-suitable fits to the data. For the 6.0 μm feature, we performed the fit using a pure H_2O component, while for the 6.8 μm feature, we did the fit with the H_2O:CO:NH_3 component used by Zasowski et al. (2009). Zasowski et al. (2009) simultaneously fit the 6.0 μm feature of low-mass YSOs with a number of laboratory ice profiles, but found that pure H_2O was the dominant component, and that while several different laboratory ice analogs could be used to fit the 6.8 μm feature, H_2O:CO:NH_3 is free of unresolvable

substructure and produced acceptable fits.

In Figure 6 we show the results of such a fit. We have twice fit the spectrum of YSO 045400.10-691155.5, which has a deep CO_2 absorption feature at 15.2 μm – once with and once without the use of the 6.0 and 6.8 μm ice features. The spectrum is well-fit by a model that excludes ice absorption at 6.0 and 6.8 μm, and is actually better fit by a model without the H_2O feature but with the 6.8 μm feature. Given the presence of a strong CO_2 feature, it is highly unlikely there is truly no 6.0 μm absorption. These results show that separating the PAH emission from the ice absorption is a highly impractical and complex procedure. We find that for sources with PAH emission, estimating ice column densities from the 5–8 μm region gives unreliable, and (sometimes) unreasonable results. Instead, other absorption bands (e.g., H_2O O–H stretch at 3.0 μm) have to be observed in order to explore the column density of other ices. The problem may also be mitigated with higher spatial resolution observations. Because every YSO's spectrum has some level of PAH emission, we have not used our spectra to estimate column densities of any ices in the 5–8 μm range, and choose to focus exclusively on the 15.2 μm CO_2 feature that resides in a relatively less-complex portion of a YSO's spectrum. It may be possible to de-blend the PAH emission from the CO_2 absorption if limits can be placed on the PAH emission strength. However, such an analysis is beyond the scope of this paper.

3.3.2. The 15.2 μm CO_2 Feature

Recent studies of the 15.2 μm CO_2 ice feature have focused on modeling the absorption profile in the lab to aid in its identification and determination of its physical properties. Laboratory experiments showed that the CO_2 15.2 μm bending mode profile is highly sensitive to both the composition of the ice mixture in which it resides (e.g., Ehrenfreund et al. 1996, 1997) and its temperature (e.g., Ehrenfreund et al. 1999). This makes the 15.2 μm feature a powerful probe of the chemical composition of interstellar ices, and of the thermal history of the ice since the effects of heating are irreversible.

We exploit the sensitivity of the CO_2 bending mode on composition and temperature to probe the nature of ices around LMC massive YSOs. The combined effects of mantle layer structure, ice mixture composition, mixing ratios, and temperature create a large laboratory experiment parameter space with which to compare observations. The large range of possible ice properties and shape similarities between different ices make a direct matching of astronomical observations with experimental data difficult and practically unrealistic. Instead, we decompose the ice features into a few basic profile shapes associated with likely ice constituents (e.g., Chiar et al. 1998; Gerakines et al. 1999; Bergin et al. 2005; Pontoppidan et al. 2008; Zasowski et al. 2009; Oliveira et al. 2009) and explore how these shapes are related to each other and YSO properties. What follows is an explanation of the decomposition process and the laboratory ice profiles used.

3.3.2.1. Continuum Determination and Blended Feature Removal

In order to compare our observations with laboratory work, the ice absorption bands must be converted to an optical depth, $\tau(\lambda) = \ln(I_0(\lambda) / I(\lambda))$, where I_0 is the continuum flux level and I is the flux within the absorption profile. This requires the non-trivial process of determining an appropriate continuum. Although the 15.2 μm CO_2 band is located within a wide silicate absorption feature centered at ∼18 μm and possibly the wide water libration mode at ∼13 μm, the region immediately surrounding 15.2 μm is relatively smooth. Therefore we treat the 18 μm silicate and water libration bands themselves as a 'local continuum,' relieving the far more complex task of determining the proper dust continuum along with the shape and strength of the silicate absorption band (e.g., Gerakines et al. 1999; Zasowski et al. 2009; Oliveira et al. 2009). We fit a 3rd order polynomial to the data in the wavelength ranges of 14.2−14.7 μm and 16.6−17.5 μm to act as the local continuum; data between 17.0 and 17.1 μm is excluded to avoid the H_2 line at 17.03 μm seen in many spectra.

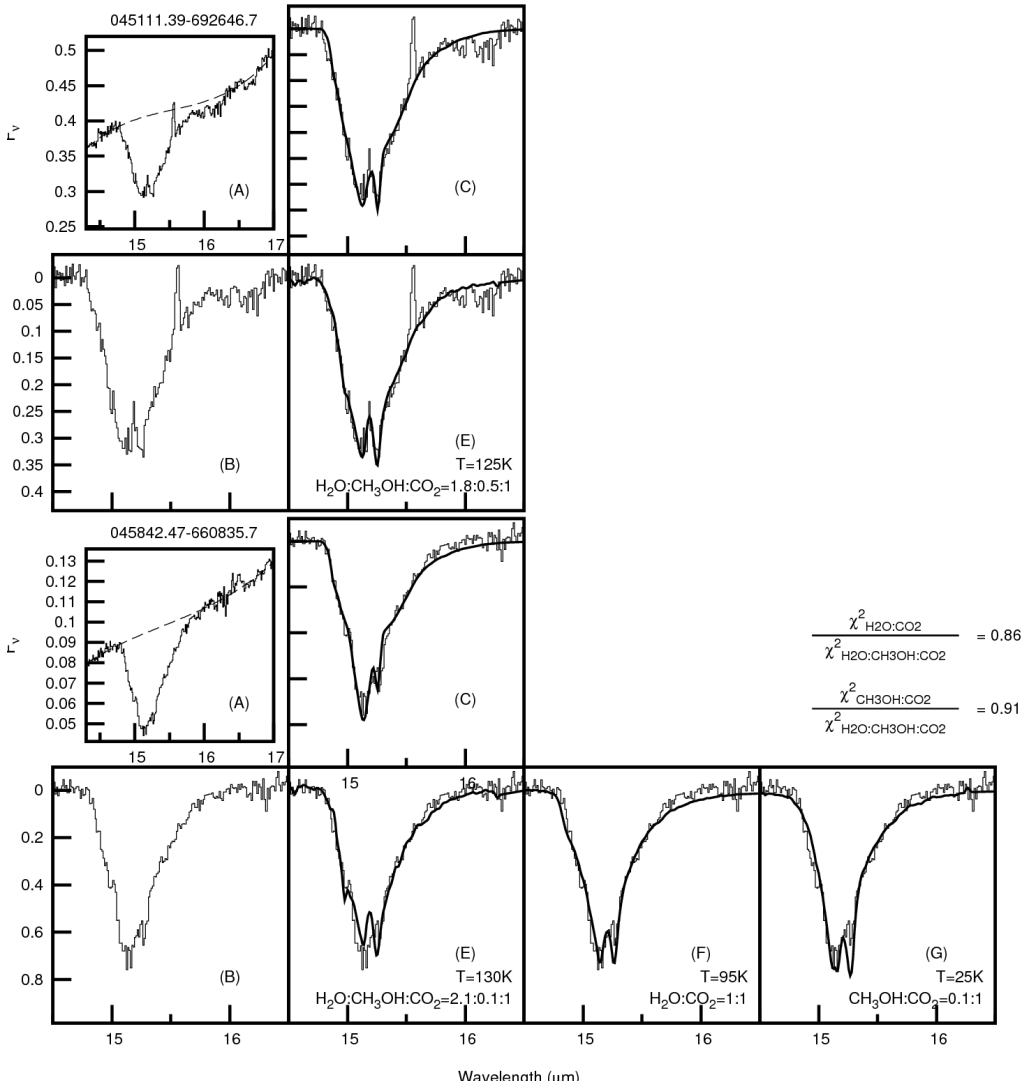

Figure 7. A representative sample of the *Spitzer* IRS spectra of the massive YSOs used in the CO_2 profile shape analysis along with their determined optical depths and best fits for each of the ice component combinations. Panel (A) shows the spectrum (solid line) and the continuum used (dashed line) to determine the optical depth for the source labeled above the panel. Directly below the spectrum panel is the resulting optical depth, panel (B). To the right of the spectrum and optical depth are the best fits (thick solid line) for each of the laboratory ice component combinations described in the text. For each object, panels (C) and (E) show the best fits for the 5-component fit and annealed fits, respectively. Panels (D), (F), and (G) are only shown for objects that resulted in good fits for their particular ice mixture (see text). Panels (D), (F) and (G) are the 2-component (polar and apolar), polar-annealed H_2O:CO_2 fit, and polar- annealed CH_3OH:CO_2 fit, respectively. Given in the bottom of each of the annealed fit panels is the best-fit ice mixing ratio and temperature. To the far right of each set of panels are the ratios of the χ^2 for the indicated annealed fits.

Two examples of results of the continuum fit are shown in Figure 7, and the results for the entire sample are presented in Apendix C. Once the optical depth has been determined from the continuum fit, laboratory ice spectra are fit to the observations using the common least-squares fitting technique. The fit is performed between 14.3 and 17.0 μm in order to contain a portion of the continuum and the large red wing of the CO_2 feature while avoiding the possible PAH emission band at 14.2 μm. Laboratory ice analogues of CO_2 typically have red wings that can extend to 16.5 μm, however due to the blending of features on the red side of the CO_2 feature, the precise extent of the red wings in our spectra is unclear. For example, many sources have a prominent PAH emission feature at 16.45 μm, so the data between 16.3 and 16.6 μm are excluded from the fit. There also appears to occasionally be a shallow peak in the optical depth at ∼16.2 μm that is coincident with a similar feature seen by Oliveira et al. (2009) in a sample of LMC massive YSO spectra. The origin of the feature is unclear and does not strongly correlate with either silicate or CO_2 ice strength. It could be an artifact of background subtraction of the adjacent PAH feature at 16.45 μm or a substructure to the 18.0 μm silicate feature. If the feature is unrelated to CO_2 ice, it may result is a small amplification in measured column density of at most ∼10%. It could also result is a slight mis-fitting of the red wing of the feature, however most of the wing is unaffected.

In addition to the above spectral features, strong absorption at 14.98 μm corresponding to the Q branch of the gas-phase CO_2 ν_2 band has been reported toward several Galactic star forming regions including the well-studied W33 A (Gerakines et al. 1999). At this resolution, all

Q-branch ro-vibrational lines are blended into a single absorption feature. In our sample and that of SL09, YSO 052333.40–693712.2 is the only one that shows this absorption. Since this study is concerned with only solid CO_2, the pixels affected by gas-phase absorption have been removed from the spectrum when performing fits to laboratory data. Most objects' spectra contain the fine-structure line at 15.55 μm of doubly ionized neon. Ionic fine-structure lines are indicative of ionized gas and likely signal the presence of a compact or ultra-compact HII region (SL09). Indeed, as reported in the Vaidya et al. (2009) study on high-resolution *Hubble Space Telescope* imaging of massive YSOs, among the YSOs overlapping with the SL09 sample, ∼80% of those with coincident compact Hα radiation have ionic fine-structure lines in their spectra compared to only ∼50% in the entire sample (SL09). Although this feature is unrelated to ice absorption, a narrow Gaussian at 15.55 μm is considered in the fitting routine to accommodate for the presence of the [NeIII] fine-structure line.

3.3.2.2. Laboratory Fit Components

The CO_2 bending mode profile in our sample displays a range of shapes, but in general, it can be decomposed into three basic components described by Pontoppidan et al. (2008): 1) a broad underlying feature with a typical FWHM of ∼0.45 μm, 2) a pair of sharp peaks at ∼15.15 and ∼15.27 μm, and 3) a broad 'shoulder' at ∼ 15.4 μm. The relative contributions of these three basic components vary between sources. For example, source 053754.82-693435.8 has a singly-peaked absorption feature compared to 052333.40-693712.2 or 045111.39-692646.7 which show quite pronounced double peaks in their optical depth spectra (Figure 8). The shoulder is weak in

most sources, but is apparent in several including 045111.39–692646.7 as a bump in the red wing of the absorption band.

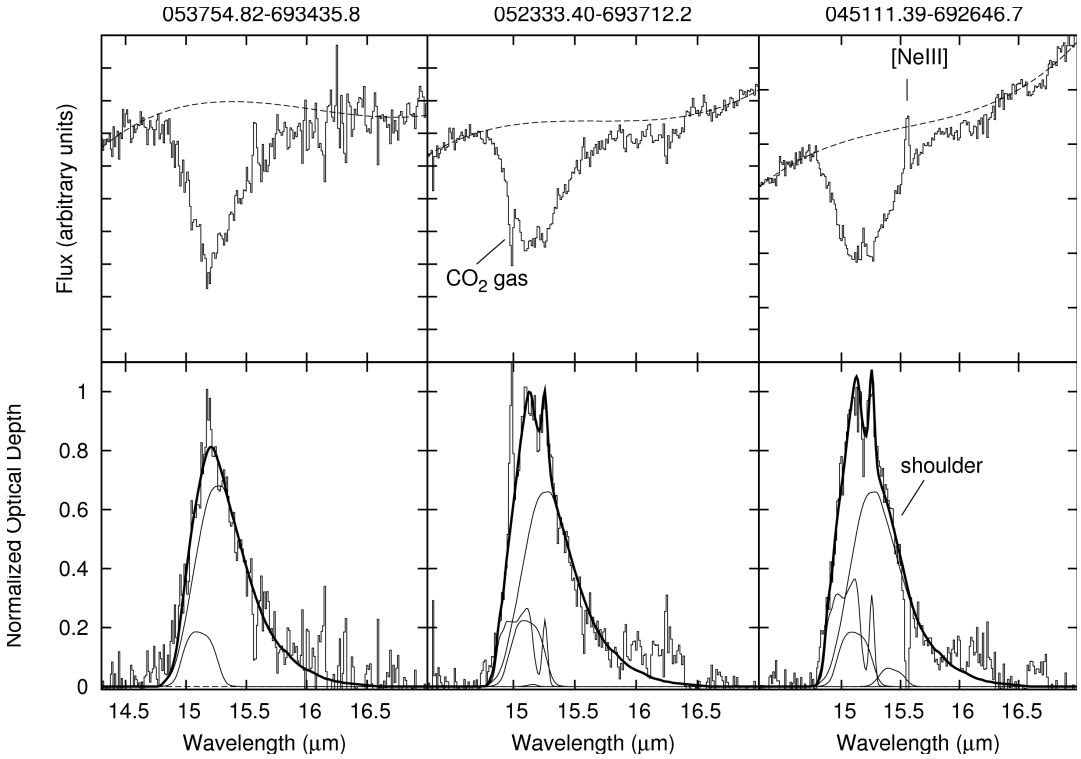

Figure 8. From left to right, the spectra (top) and optical depths (bottom) of sources 053754.82-693435.8, 052333.40-693712.2, and 045111.39-692646.7. The dotted line in the the upper panels show the adopted continuum. Also displayed in the bottom panels are the best fit components (thin solid lines) and the total best fit to the optical depth (thick solid line) for the 5-component (052333.40-693712.2 and 045111.39-692646.7) or two-component (053754.82-693435.8) fit. Note that the wavelength range containing the PAH feature is excluded from the fit and removed from the optical depth. Sources 052333.40-693712.2 and 045111.39-692646.7, with prominent double peaks, are examples of spectra best fit by the 5-component ice combination. Conversely, source 053754.82-693435.8 is equally well-fit by either 2- or 5-components. Prominent spectral features are labeled for clarity (see text).

Given the large number of parameters that can contribute to an absorption feature's profile – composition, mixing ratios, temperature among them – it is perhaps unsurprising that several different combinations of laboratory ice spectra can produce equally good fits to astronomical data. The shape of the 15.2 μm CO_2 feature is among the most-studied ice profiles,

and two primary methods of fitting the profile to laboratory data have emerged that have previously been used on some of the largest surveys of both Galactic and LMC YSOs (e.g., Gerakines et al. 1999; Pontoppidan et al. 2008; Oliveira et al. 2009): 1) a combination of polar and apolar ice mixtures and 2) a combination of annealed H_2O:CH_3OH:CO_2 and polar ice mixtures. We have fit our spectra using both of these widely-used techniques. These methods are in contrast to the more complex set of laboratory ice spectra used by Zasowski et al. (2009) for a sample of *Spitzer* IRS spectra of Class I/II low-mass YSOs: a combination of two different annealed H_2O:CH_3OH:CO_2 mixtures, pure CO_2, a polar H_2O:CO_2 ice, and a CO:H_2O mixture.

In the first method (a combination of polar and apolar ice mixtures), which we refer to as the 5-component fit, we adopt the components used by Pontoppidan et al. (2008), who empirically derived the minimum number of unique components required to fit the CO_2 absorption features of Galactic low- and high-mass YSOs as observed by Spitzer IRS's high-resolution module. They identified a total of five unique components. Two of these components contribute to the broad underlying feature, another provides the characteristic double-peak, while a fourth contributes the feature's blue wing shoulder. The fifth, a minor component, is a narrow band centered at 15.15 μm. The advantage of this fit is that the determined strength of each spectral shape (e.g. the double peak) is largely independent of the other shapes. Four of these five components are modeled with laboratory spectra, while one is modeled by a function; they are described below and shown in the same order in Figure 9. Given in bold are the names we will use to refer to each component is later sections.

1. **H_2O:CO_2 or polar component:** Referred to as the 'red component' in Pontoppidan et al. (2008) and comprising a large fraction of the underlying broad feature, this component is modeled by a 10K H_2O:CO_2=100:14 laboratory spectrum that peaks at 15.3 μm. The component is wide, with a FWHM of ∼ 0.5 μm and a red-sided tail.
2. **CO:CO_2 or apolar component:** The other main underlying feature constituent is modeled by an apolar ice at 10K with roughly equal parts CO_2 and CO and is referred to as the 'blue component' by Pontoppidan et al. (2008). This component has varying widths that reflect the precise CO:CO_2 mixing ratio. We allow all possible mixing ratios for which we could obtain laboratory data (CO:CO_2 = 100:70, 100:26, 100:23, 100:21, 100:16, 100:8), and find the mixing ratio leading to the best fit (the lowest $\chi 2$).
3. **Pure CO_2 component:** The most prominent substructure is the characteristic double peak which we model with a pure CO_2 ice. For consistency with the Pontoppidan et al. (2008) study, we adopt the pure CO_2 absorbance spectrum from van Broekhuizen et al. (2006).
4. **Shoulder component:** Although the bump on the red side of the 15.2 μm feature is associated with CH_3OH in H_2O:CH_3OH:CO_2 ice mixtures (Ehrenfreund et al. 1996), this component does not exist in isolation. Rather, it is a methanol-induced shape superimposed on a broad feature similar to that in H_2O:CO_2 ice mixtures. We adopt the model introduced by Pontoppidan et al. (2008), a superposition of two Gaussians centered

at 645 and 650 cm^{-1} (Pontoppidan et al. 2008). Using a function to approximate the shoulder's shape allows for a determination of the shoulder's strength without placing any constraints on the strength of other components. Note that since the shoulder does not exist in isolation, any component used to model only the shoulder shape is necessarily ad hoc.

5. **Dilute CO_2 component:** The final component – CO_2 diluted in an apolar ice – is the weakest feature and is modeled by a CO:CO_2 ice with a 100:4 mixing ratio centered at 15.15 μm with a narrow width. While this dilute CO_2 component plays a minuscule role in fitting our spectra, it is included in the fits for consistency with Pontoppidan et al. (2008).

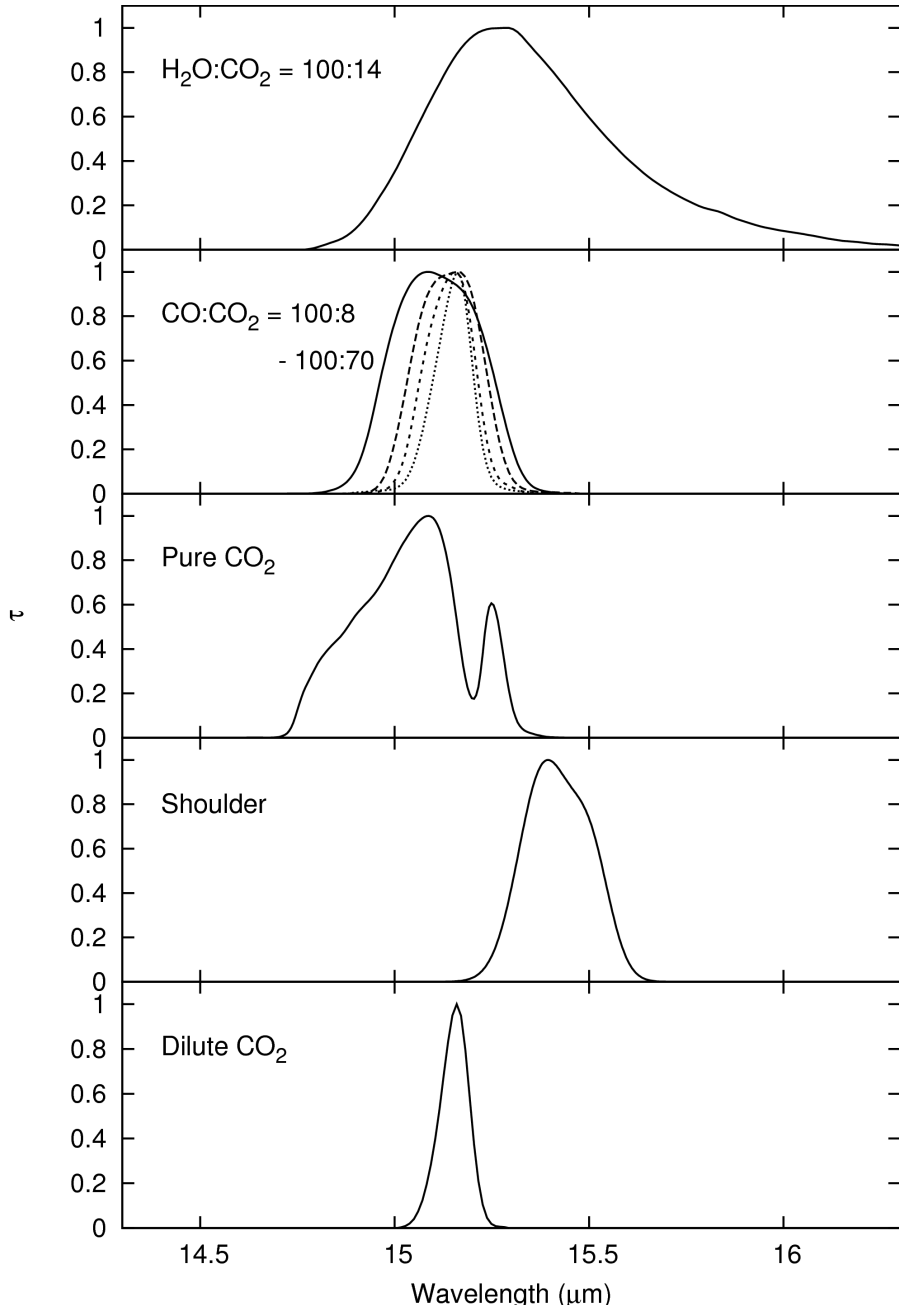

Figure 9. The 5 laboratory ice components used in the 5-component profile fitting routine. The $CO:CO_2$ ratio was allowed to vary between several laboratory mixing ratios, a sample of which ($CO:CO_2$ = 100:70, 100:26, 100:16, 100:8, plotted with a solid, long dashed, short dashed, and dotted line, respectively) are shown in the second panel from the top. Note that the width of the feature increases and the feature becomes more asymmetric with increasing CO_2 fraction. All components have been normalized to an optical depth of 1.

Note that while performing the fits, with the exception of the apolar component, the only free variable is the strength of the component. A second free variable, the mixing ratio, is allowed for the apolar component. While the above components are attractive in that they provide measurements of specific spectral feature strengths, they may give limited information about the precise composition of the ice. A more accurate assessment of the ice composition may be offered by the second fitting method (Gerakines et al. 1999), which we refer to as the annealed fit. As described above, some YSO spectral features can be well fit using combinations of annealed ices of more complex compositions with polar ices. For example, Gerakines et al. (1999) produced some good fits to observations of both low- and high-mass YSOs by using a combination of laboratory polar (H_2O-rich) CO_2 ice and an annealed ice mixture containing H_2O, CH_3OH, and CO_2 in equal amounts (H_2O:CH_3OH:CO_2 =1:1:1). This technique is quite powerful in that it ascribes a physical interpretation for the spectral shapes and doesn't rely on ad hoc features such as the shoulder component described in the 5-component fit above. However there are several disadvantages to this technique. Increasing the number of ice mixture constituents means there are a larger number of laboratory experiments required to fully cover the possible mixing ratio space. Moreover, each of these mixtures also needs to be measured at varying levels of annealing. The results of this laboratory work (e.g. White et al. 2009) reveal that the strength of the various 15.2 μm feature shapes (broad underlying feature, double peaks, and shoulder) are all dependent on both the mixing ratio and temperature of the ice and are rarely seen in isolation. The two components for this annealed fit are described below.

1. **Polar component:** This component is the same as the H_2O:CO_2 or polar component in the 5-component fit, and is modeled by a 10K H_2O:CO_2=100:14 laboratory spectrum.

2. **Annealed component:** For the annealed component, we use the large catalog of annealed H_2O:CH_3OH:CO_2 ice spectra described in White et al. (2009). There are a total of 38 different ice mixtures available in the database, and each ice mixture's spectrum is taken at several temperatures (from 5 K to evaporation at 115−170 K in steps of 5 K). The temperatures given here are those of the laboratory ice; the corresponding interstellar conditions are at a lower temperature. Mixing ratios are varied to account for different ice matrix compositions; while some mixtures are dominated by a single molecular constituent (e.g., H_2O:CH_3:CO_2 = 11:0.2:1), others have the three molecules in approximately equal amounts (H_2O:CH_3:CO_2 = 1:0.9:1).

The shape of each annealed ice spectrum is dependent on the specific mixing ratio and temperature, but there are several general trends. In most cases, ices at high temperatures (> 70 – 100K) have the characteristic double peak; possible exceptions to the rule are ices with high concentrations of a non-CO_2 molecule. The strength of the shoulder is dependent on the concentration of methanol – those with the highest concentrations (> 33% abundance) have prominent shoulders while those with the lowest have little to no shoulder. The shoulder also is dependent on temperature as it disappears at high ice temperatures. For a complete description of

ice absorption profile shapes and their dependence on ice properties, see White et al. (2009).

In this study we make use of the large number of laboratory spectra from the literature collected by the Leiden University laboratory ice spectra database[3] and the University of Alabama at Birmingham Astrophysics Laboratory[4]; with the exception of the pure CO_2 profile used in the 5-component fit, all laboratory data used in this study are from these databases. The databases provide particle shape corrections to the absorption spectra for a variety of particle shape distributions. For all the laboratory data where such a correction is required, we consider a continuous distribution of ellipsoids as they have previously been shown to best match astronomical observations (Gerakines et al. 1999). To better match laboratory profiles with our observations, we removed a first order continuum baseline from the laboratory spectra. The slopes and vertical offsets of the baselines were chosen to include the entire width of the features while removing as much continuum as possible.

3.4. Discussion

3.4.1. Ice Composition and Column Density

The column density along the line of sight for each component of the CO_2 bending mode was computed using the relation

$$N(cm^{-2}) = \frac{\int \tau(x)dx}{A}$$

3 http://www.strw.leidenuniv.nl/~lab/databases/databases.htm

4 http://www.phy.uab.edu/labastro/dataindex.html

where x = 1 / λ and A is the laboratory-determined band strength. The total CO_2 column density is calculated by integrating each source's spectrum between 14.6 and 16.5 μm and is independent of the fit results. As in other studies (e.g., Pontoppidan et al. 2008; Oliveira et al. 2009), we use the same band strength of 1.1×10^{-17} cm molecule^{-1} for every CO_2 component (Gerakines et al. 1995). The results are listed in Table 4; the uncertanties are purely statistical and do not take into account the uncertainty of the continuum, which we estimate to be ∼15% from testing several continua, identical to that estimated by Oliveira et al. (2009). We find a total CO_2 column density range of 2.0×10^{17} cm^{-2} to 1.66×10^{18} cm^{-2}, a range comparable to those previously reported in lines of sight toward Galactic low-mass YSOs, high-mass YSOs, and extincted background stars (Gerakines et al. 1999; Pontoppidan et al. 2008; Zasowski et al. 2009).

3.4.1.1. 5-Component 15.2 μm Fit

The 5-component fits as described in Section 3.3.2.2 indicate that the H_2O:CO_2 component dominates the 15.2 μm ice feature for nearly every source. In fact, for all but four sources, the water-rich component constitutes over 50% of the column density, and on average the component contributes ∼65% of the total column density. The average polar-component contribution we find is similar to that reported by Oliveira et al. (2009) – 60% – for a sample of 15 massive YSOs in the LMC observed with the low-resolution module of Spitzer IRS. The similarity of our findings suggests that the resolution afforded by the low-resolution module is ample for distinguishing the polar component of the CO_2 feature. As noted by Oliveira et al.

(2009), this average contribution of the polar component in the LMC is lower than that reported in the literature for Milky Way objects. In the Galaxy, high-luminosity YSOs and quiescent molecular clouds have a water-rich component that constitutes ∼85% of the column density (Gerakines et al. 1999; Whittet et al. 2009), and low-luminosity YSOs have contributions of ∼70% (Pontoppidan et al. 2008), both larger than those in the LMC reported here and in Oliveira et al. (2009). The larger sample size in this study strengthens the Oliveira et al. (2009) suggestion that LMC objects have lower contributions from polar ice mixtures. Note however, that there are systematic differences between some of the Galactic studies and our own. For example, Gerakines et al. (1999) considered a range of water-rich laboratory ice analogues at various H_2O:CO_2 mixing ratios and temperatures. On the other hand, we and Pontoppidan et al. (2008) use the same 5-components in our fits and find similar polar-component contributions of ∼65% and ∼70%, respectively. This suggests that changing the specific ice components used in the other analyses of Milky Way sources may bring them into better agreement with those of the LMC.

The other major component of the smooth, underlying feature, the CO:CO_2 component, makes up on average ∼10% of the total column density. The percentage contribution to the total CO_2 abundance from the CO:CO_2 mixture is smaller in our sample than that of both Galactic massive and low-mass YSOs (∼20%) reported by Pontoppidan et al. (2008). This may be a result of different continuum choices, but could also be a result of the low metallicity of the LMC which allows radiation from the central hot star to penetrate farther and heat more of its envelope. Since solid CO has a low sublimation temperature, much of the CO may have been desorbed off

the dust grains and out of the ice phase in the relatively warmer regions around a massive YSO. Additionally, there is evidence that CO is underabundant in the LMC (Fukui et al. 2001), meaning the lower contribution of the CO:CO_2 component could be due to an overall underabundance of CO-containing ices in the LMC. The distribution of CO:CO_2 mixing ratios is similar to that found in the Pontoppidan et al. (2008) study of low-mass and high-mass Galactic YSOs. While the two studies are not directly comparable because Pontoppidan et al. (2008) allows for a continuum of mixing ratios while we only allow several discrete mixing ratios, we both find a median CO_2/CO ratio of 0.6 – 0.7 with a standard deviation of ∼0.25. Oliveira et al. (2009) found a slightly larger average ratio of ∼0.9 for a sample of 10 massive YSOs in the LMC, however their study allowed CO_2 / CO >1.0, while ours did not.

On average, the second strongest contributor to the column density originates from the pure CO_2 component. The average percentage contribution of the pure CO_2 ice to the total CO_2 column density is ∼20%. This percentage has a large range of values, with a maximum value of 51% and one source with no pure CO_2 contribution. The column densities of the dilute CO_2 and shoulder components are typically very small. Both components have an average contribution of a few percent to the total column density. In fact, a majority (∼2/3) of sources are fit without any contribution from the dilute CO_2 component, and roughly 1/6 do not require a shoulder component.

The small contribution from the shoulder component is in contrast to Galactic sources

which tend to have stronger CH_3OH-induced shoulder components. Comparing these fits to Pontoppidan et al.'s (2008) sample of both low-and high-mass Galactic YSOs, massive YSOs GL 2136, W33A, and S140 IRS 1 (1/2 their massive YSO sample) all have shoulder components that contribute over 10% to the total CO_2 column density. However in the LMC, only five of our 40-source sample is estimated to have > 10% contribution from the shoulder component. In fact, Oliveira et al. (2009), the only other study of LMC CO_2 ice composition, did not even require a shoulder component in their profile fits to LMC CO_2 ice spectra. The low contribution of the shoulder implies that methanol may be less abundant in the LMC than the Milky Way, however the Galactic sample size is too small be be conclusive. The possible low abundance of methanol may be tied to its formation route, which remains under debate. For example, if methanol is formed via the hydrogenation of CO on the icy surface of grains ($CO \rightarrow HCO \rightarrow H_2CO \rightarrow CH_3O \rightarrow CH_3OH$) as can be produced in the lab (Watanabe & Kouchi 2002), then the LMC's underabundance of CO is a possible explanation. Since the formation of both CH_3OH and CO_2 are likely tied to CO, the high abundance of CO_2 in the LMC (Shimonishi et al. 2008; Oliveira et al. 2009) may appear to discount this explanation. If CO_2 ice formation is stimulated by the radiation, then the LMC's relatively high radiation field could explain the high CO_2 ice abundance (see Section 3.5). However there is also laboratory evidence for similar radiation-stimulated CH_3OH formation (Hudson & Moore 1999). Another possible explanation is the

destruction of methanol in LMC ices. CH_3OH can be destroyed via UV radiation, cosmic ray bombardment, or cosmic ray-induced UV radiation, a scenario replicated in the laboratory by Ehrenfreund et al. (1999). They demonstrated that with time, the photolysis of an annealed mixture of H_2O, CH_3OH, and CO_2 ices decreases the strength of the shoulder component, leaving only the characteristic double peak and the broad H_2O-rich component. Given the high level of star formation in the LMC, and the resulting high UV flux, methanol ice may be destroyed, reducing the CH_3OH abundance, and reducing the strength of the shoulder component.

It can be instructive to compare the results of our decomposition method with those of other studies to determine what contribution baseline continuum and the specific component choices play in the decomposition process. The study of LMC YSO ice chemistry by Oliveira et al. (2009) used low-resolution *Spitzer* IRS data for a sample of 15 objects. Only one source, 045111.39–692646.7, was included in both the Oliveira et al. (2009) and our studies. The other 14 sources did not meet the color-magnitude criteria to have been included in the SL09 IRS observations. Figure 10 is a comparison between our higher resolution spectrum and the low-resolution spectrum from Oliveira et al. (2009), reproduced from Figure 5 of Oliveira et al. (2009) of YSO 045111.39–692646.7. The spectra have very similar shapes, particularly along the blue wing. In addition, both spectra show the aforementioned shallow optical depth bump at $\sim$16.2 μm that cannot be fit by any of the ice models. Oliveira et al. (2009) suggests it may be an artifact of sky subtraction of the nearby PAH and fine-structure lines. There are two primary

differences between the two spectra: 1) The higher resolution of our data reveals the presence of the pure CO_2 double peak and 2) the lower resolution spectrum has a wider profile with a particularly large red wing. It is possible that the difference in the feature widths is real, in which case the two spectra are sampling different regions. Given that Spitzer's IRS low-resolution module has a slit width more than twice that of the high-resolution module, this cannot be ruled out. However, if the ices are within the typical radius of a massive YSO envelope of $\sim$ 0.5 pc (van der Tak et al. 2000), then both spectra probe the same material. An alternate explanation for the difference in feature widths is that differing choices of dust continua result in different optical depth profiles. In general, determining a proper continuum is a non-trivial task since the continuum is likely a combination of a base continuum with absorption and emission features superimposed. More specifically, in the regions surrounding the 15.2 μm feature there is a known silicate absorption feature at 18 μm and a complex of PAH emission bands creating plateaus of varying shape and size (Peeters et al. 2004). We have tried to avoid the PAH complex between 17 and 18 μm by only fitting the continuum at wavelengths less than 17 μm.

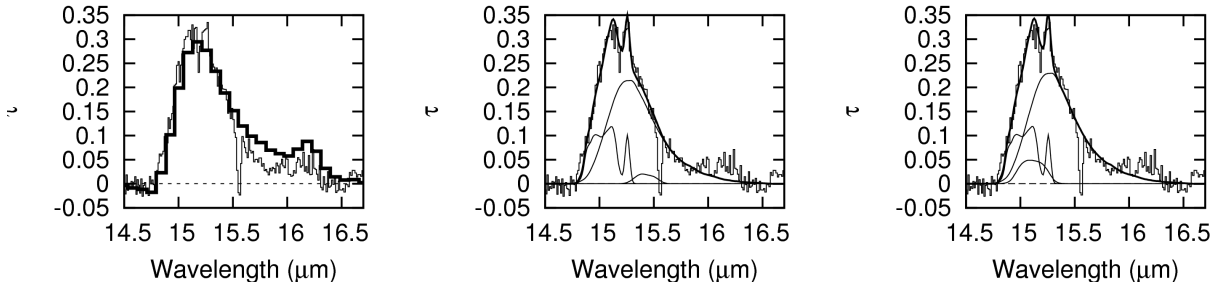

Figure 10. Optical depth spectra of source 045111.39-692646.7. Left panel: Comparison between the low-resolution data presented in Oliveira et al. (2009) (Thick solid line) and the high-resolution data used in our fits (thin solid line). Center panel: 5-component fit to the high-resolution CO_2 profile. Individual component fits are the thin lines while the thick line is the composite fit. Note that the best fit requires no dilute CO_2 component. Right panel: High-resolution data fit with only the three strongest components – H_2O:CO_2 , CO:CO_2 1, and pure CO_2. Lines are the same as the center panel.

Differences in continuum determinations can cause variations in component fits. Using 045111.39-692646.7 as a case study, we explored how different continuum choices can affect the relative contributions of the component fits. Oliveira et al. (2009) estimated a CO_2 column density from the 15.2 μm feature of 7.99 ± 0.08 × 10^{17} cm^{-2}, a factor of 1.10 times higher than our determination of 7.29 ± 0.31 × 10^{17} cm^{-2}. The smaller wing on the red side of our high-resolution optical depth spectrum is primarily responsible for the lower value. Oliveira et al. (2009) estimates that an uncertainty of ∼15% for the column density could arise from continuum choices. Adopting the uncertainty of ∼15% brings the column density measurements for our two studies into agreement within the error bars. The low-resolution spectrum was fit with a polar (H_2O-dominated) ice mixture along with two apolar (CO:CO_2 mixture and pure CO_2) components by Oliveira et al. (2009). In order to match the red wing, a significant contribution

from the polar component was required; the polar component contributed 78 ± 3% of the total column density. In our best fit to the high-resolution data, the size of the red wing is smaller, resulting in a smaller contribution from the polar constituent, 67 ± 3%. Both the high and low-resolution fits determine comparable contributions from the CO-dominated components (∼10%), however our high-resolution study finds a higher contribution (21 ± 2%) from the pure CO_2 than does the low-resolution fit (13 ± 2%). Because the characteristic double peak is only spectrally resolved in the high-resolution data, the high-resolution data may give a better estimation of the pure CO_2 contribution.

Our 5-component fits also identified a non-zero contribution from the shoulder component of 2 ± 1%, a component not considered in the low-resolution fit. Given the shoulder's location on the red side of the feature's central primary peak, the inclusion of a shoulder component contributes to the lower level of the polar ice component compared to that determined in the low-resolution fit. As a test, we removed the shoulder component from the fit and determined a new best fit component combination to the high-resolution data using the same components as Oliveira et al. (2009), which increased the percent contribution of the polar component. This demonstrates the importance of high-resolution spectroscopy as low-resolution observations can smooth out the double peak, preventing the distinct feature from being used to identify the presence of pure CO_2. Low-resolution observations instead must primarily rely on larger shape characteristics – such as profile wings – which may be more dependent on the choice of continuum.

For a number of source spectra, there are no obvious indications of pure CO_2 – i.e. no double peak. For objects such as these, one has to question the validity of a profile fit that allows a pure CO_2 component. As a test, we reduced the number of fit components to two: 1) the polar H_2O:CO_2 component, and 2) the apolar CO:CO_2 component. These two components are typical of unprocessed ices. The results of these 2-component fits are shown in Table 4 and plotted in Figure 7 (Apendix C for all sources) for sources with 2-component fits that are equally as good as the 5-component fit. We consider a 2-component fit to be statistically as good if it has a reduced χ^2 of less than unity or less than or within 10% of the 5-component fit's reduced χ^2. Visual inspection of the sources equally well fit by both five and two components shows that most of these spectra are noisy. A lower signal-to-noise ratio (SNR) necessarily means a lower value of χ^2. Moreover, all sources well-fit by two components are relatively weak detections with inferred column densities of less than 10^{18} cm^{-2}. Since no strong, high SNR ice absorption features are without clear double-peak detections, we conclude that for the sources without a visible pure CO_2 component, the feature may be hidden in the noise; longer integration times on these objects may reveal the double peak.

3.4.1.2. Polar and Annealed Ice 15.2 μm Fit

Table 5 provides the results of the fit using a polar and an annealed H_2O:CH_3OH:CO_2 component. In general, the annealed fit and the 5-component fit give equally good results. Table

5 also shows the ratio between the reduced χ^2 of the best annealed and 5-component fits for each source, $\chi^2_{anneal}/\chi^2_{5\text{-comp}}$. Approximately half the sources are better fit with an annealed fit, and half with the 5-component fit. A majority of the spectra (28/40) have annealed and 5-component fit χ^2 values within 10% of each other; 36/40 are within 20%.

In general, the best fits to the data require an annealed component that makes up a majority of the total CO_2 column density. In fact, only 4 sources have fits where the annealed component comprises less than 50% of the column density, and on average the annealed component is nearly 80% of the total column density. This is higher than the average annealed component reported in Oliveira et al. (2009) for LMC massive YSOs (∼50%), who performed a similar polar and annealed CO_2 ice fit. The higher annealed percentage found here compared to the low-resolution study by Oliveira et al. (2009) may be related to the higher pure CO_2 percentage discussed in Section 3.4.1.1; one of the primary characteristics of the annealed ices is the appearance of the double peak at high temperatures, a shape mirrored in the pure CO_2 component. Indeed, the annealed component and pure CO_2 appear to trace similar shapes as the sources with the highest percentages of pure CO_2 in the 5-component fit also are dominated by the annealed component in the annealed fits. Conversely, the four sources with the lowest annealed component contribution have pure CO_2 contributions of under ∼15%. The difference may also be a result of the different annealed ice mixtures considered here and in Oliveira et al.

(2009). While we have considered a wide variety of H_2O:CH_3OH:CO_2 mixtures, Oliveira et al. (2009) considered only mixing ratios of approximately H_2O:CH_3OH:CO_2 = 1:1:1. Considering a wider spectrum of mixing ratios may bring these values into better agreement.

The average percent of the total column density attributed to the annealed component found here is also higher than that reported in Gerakines et al. (1999) (∼55%) for Galactic massive YSOs. This suggests that while both studies find that the annealed component provides a large percentage of the total column density, the contribution may be larger for LMC massive YSOs. As the ices probed by the absorption feature reside in the molecular regions surrounding the YSOs, this suggests that LMC massive YSOs have warmed a larger fraction of their envelopes. This may reflect the differences in metallicity between the Milky Way and the LMC – a higher fraction of the envelope may be warmed in low metallicity galaxies as the lower dust content may allow deeper penetration (and therefore a larger warming radius) of a YSO's envelope. However, like the Oliveira et al. (2009) study, only H_2O:CH_3OH:CO_2 = 1:1:1 annealed ices were considered in the Galactic sources study. It is therefore possible that the difference could be related to the different annealed ices' mixing ratios considered or the relatively low number of Galactic massive YSOs in the Gerakines et al. (1999) study.

One of the benefits of the annealed fit over the 5-component fit is that it provides a more direct indicator of the composition and temperature of the CO_2 ice matrix. The best fits using annealed H_2O:CH_3OH:CO_2 ices require ices at high temperatures, typically above ∼100 K. The high level of annealing in the best-fit laboratory ices implies that the ices around massive YSOs

have been thermally processed. Even a by-eye inspection of the spectra reveals this to be true, as many of the spectra show the double peak structure that is characteristic of ices that have been warmed, segregating the ice species into inclusions of pure CO_2.

Of the 40 sources, only 4 are best fit with an H_2O:CH_3OH:CO_2 mixture dominated (> 33%) by methanol. On average, the best fit has an annealed H_2O:CH_3OH:CO_2 mixture with ~ 17% methanol, and the most common mixing ratio is H_2O:CH_3OH:CO_2 = 2.1:0.1:1 (only 3% methanol). A number of spectra contain significant amounts of noise, so it may be more reasonable to consider only those with high SNR; of the 15 least-noisy spectra, seven, five, and three are best fit with H_2O:CH_3OH:CO_2 mixing ratios of 2.1:0.1:1, 1.8:0.5:1, and 1:0.9:1, respectively. Moreover, two of the three best-fit with the 1:0.9:1 ratio can be equally well fit with ices containing no methanol. These findings seem to indicate a low level of methanol is present in the CO_2 ice mixtures. Because most authors have isolated their annealed fits to the H_2O:CH_3OH:CO_2 = 1:1:1 mixture ratio, comparing our results to other studies may not be meaningful. However, we note that Gerakines et al. (1999) finds that Galactic massive YSOs can be well fit using a polar and annealed H_2O:CH_3OH:CO_2 = 1:1:1 mixture. This suggests that ices around LMC massive YSOs may have a lower abundance of methanol than those in the Milky Way. As a test of the uniqueness of the annealed H_2O:CH_3OH:CO_2 fits, we also fit the spectra with an alternate set of annealed laboratory ices – ices without one of the non-CO_2 ices (i.e.

annealed H_2O:CO_2 or annealed CH_3OH:CO_2). We consider the H_2O:CO_2 and CH_3OH:CO_2 fits to be equally good to the H_2O:CH_3OH:CO_2 fits if the reduced χ^2 is less than or within 10% of the H_2O:CH_3OH:CO_2 value. A large majority (3/4) of the sources can be equally well fit with a 2-component model that includes a polar and an annealed H_2O:CO_2 component. In other words, methanol is not needed to fit most sources, which is consistent with the low abundance of methanol inferred from the 5-component fits and the H_2O:CH_3OH:CO_2 fits. However, we also find that about 1/2 of the sources can also be fit with an annealed CH_3OH:CO_2 component. A visual inspection shows that a significant number of those fit by the CH_3OH:CO_2 component have low SNRs, suggesting that the CH_3OH:CO_2 fits are less reliable. In fact, of the 10 sources with the highest SRNs, only one – 045842.47-660835.7 – can be fit by an annealed CH_3OH:CO_2 ice mixture, and it required the lowest methanol abundance available in the laboratory spectra database at a temperature that is probably physically unrealistic (CH_3OH:CO_2 = 0.1:1, T = 25 K). All together, there is evidence that methanol has a low abundance around LMC massive YSOs; however, given that some sources can be fit with ices dominated by methanol, the evidence is certainly not conclusive. It is also important to note that at high temperatures, the methanol-induced shoulder becomes weak, even are relatively high methanol concentrations, so distinguishing between small differences in methanol abundance is unreliable in highly processed ices.

3.4.2. Dependence on Luminosity

The 'pristine' ices in dark, quiescent molecular clouds may eventually become part of the circumstellar material around forming stars. In time, the central star grows in luminosity, sublimates the inner-most regions of its circumstellar envelope, and heats the ices in the surrounding portions of its envelope above a critical temperature to create pure CO_2 inclusions through the segregation mechanism. This picture is consistent with the double absorption peaks seen toward regions of massive star formation both in the Galaxy (e.g., Gerakines et al. 1999; Ehrenfreund et al. 1998; Gibb et al. 2000) and in the LMC (this study).

Physically, the amount of the envelope that is heated above the temperature required to segregate the ice constituents (the 'segregation temperature') is dependent on a number of factors – some of which may evolve with time – including stellar luminosity, several envelope structure parameters (mass, inner/outer radius, density gradient), and dust properties. The ratio of the pure CO_2 component to the sum of the pure CO_2 and H_2O:CO_2 components can be used as a diagnostic for the fraction of the line-of-sight material above the segregation temperature. This processing ratio, P, is an attractive diagnostic because it has a physical meaning defined in (Pontoppidan et al. 2008) as

$$\mathrm{P} = \frac{\int_{R_{sub}}^{R_{crit}} n_{CO_2}(r)dr}{\int_{\infty}^{R_{sub}} n_{CO_2}(r)dr},$$

where R_{crit} is the radius at which the temperature is the critical segregation temperature and R_{sub} is the radius where the ice sublimates. For our purposes, this definition for processing ratio

makes the assumption that pure CO_2 is formed via segregation in a H_2O:CO_2 or H_2O:CH_3OH:CO_2 ice mixture, so a second diagnostic, the fraction of the total CO_2 column density attributed to pure CO_2, is also considered as it doesn't make an assumption of the formation mechanism.

The average processing ratio of LMC massive YSOs presented here is 0.25, and a similar average value of 0.29 is found for the massive LMC YSOs presented in Oliveira et al. (2009). We also find similar fractions of the total CO_2 column density in pure CO_2 between the two studies – 0.2 here and 0.25 in Oliveira et al. (2009). Observed Galactic high-mass YSOs are limited in number, but the five Galactic high-mass YSOs whose CO_2 ice features were decomposed by Pontoppidan et al. (2008) have a processing ratio of 0.2 and a pure CO_2 fraction of 0.14. While the number of Galactic sources is too small to be conclusive, LMC massive YSOs may process a larger fraction of their envelopes than those in the Milky Way. Such a finding would be consistent with the lower metallicity in the LMC, as the lower dust content could allow deeper penetration of stellar radiation through the envelope, processing a larger fraction of the cloud.

Both the processing ratio and the pure CO_2 fraction for massive Galactic YSOs are markedly larger than those of low-mass Galactic YSOs (Pontoppidan et al. 2008), which have an average processing ratio of 0.14 and a pure CO_2 fraction of 0.07. Clearly the luminosity of a YSO is among the more significant factors in setting the fraction of a YSO's envelope that has been thermally processed. Models of circumstellar envelopes have estimated that the fraction of

processed material along the line of sight through the protostellar envelope may range from 0 to 0.1 at stellar luminosities of several $L_\odot$ to as high as 1 (a fully thermally processed envelope) at the high luminosities of 10^4 – 10^6 $L_\odot$, depending on the chosen envelope structure and the adopted segregation and sublimation temperatures (Pontoppidan et al. 2008). It may then be expected that the processing ratio may increase with increasing luminosity among our massive YSO sample itself. Indeed, with a standard deviation of 0.16, the processing ratio among the sample of LMC massive YSOs displays some range.

Figure 11 plots the processing ratio and pure CO_2 fraction as a function of the modeled source luminosity (star + disk) as given in Table 3 and described in Section 3.2.1. There is significant scatter, however statistical tests indicate there may be a general trend of an increasing processing ratio with luminosity. The processing ratio correlation in Figure 11 has a Pearson's Product Moment coefficient of 0.38, suggesting a linear positive correlation in log space. Kendall's τ, a rank coefficient, has a value of 0.18, and Spearman's ρ is 0.26, all suggesting a positive correlation. Similarly, the pure CO_2 fraction as a function of luminosity has a Pearson's Product Moment coefficient of 0.40, a Kendall's τ of 0.20, and a Spearman's ρ of 0.30. We note however that these correlation coefficients are dominated by the extremes of the distribution, namely the most and least luminous YSOs. Removing YSO 051351.51–672721.9 (which has a high luminosity of 1.5×10^5 $L_\odot$ and the highest P and pure CO_2 fraction) from the analysis reduces the Pearson's product moment to only 0.25, Kendall's τ to 0.14, and Spearman's ρ to 0.21 for the P-luminosity plot. Without YSO 051351.51–672721.9, P and luminosity are only positively

correlated to a 20% confidence level. Furthermore, if we then remove the least luminous YSO (052155.18–674730.4, L = 2.4 × 10^3 $L_\odot$, P = 0.04), the positive correlation essentially disappears (correlated to a 40% confidence level). Pontoppidan et al (2008) estimated that P may increase by only ~0.1 or ~0.2 between the luminosities of 10^3 to 10^5 $L_\odot$, so considering the relatively large uncertainties associated with the P measurements (~0.1), the weak correlation is unsurprising. We note, however, that the extremes of the luminosity range we have probed have P and pure CO_2 fractions consistent with a positive correlation between luminosity and thermal processing. The processing ratios are 0.19 and 0.49 for YSOs with luminosities L < 10^4 $L_\odot$ and L > 10^5 $L_\odot$, respectively. Similarly, the average fractions of the total column attributed to pure CO_2 are 0.16 and 0.31 for the same two luminosity bins, respectively.

Coupled with the large uncertainties, variations in envelope properties are a probable source for the significant amount of scatter seen in Figure 11. Radio observations of nearby resolved massive star forming regions reveal that massive YSO envelopes are characterized by outer radii of 10^4 – 10^5 AU, masses of 10^2 – 10^3 $M_\odot$, and visual extinctions of 10^2 – 10^3 magnitudes (van der Tak et al. 2000). Models by Indebetouw et al. (2006) propose large envelopes (‘dust cocoons’) that could extend several parsecs, and recent 3-dimensional massive star formation simulations (Krumholz et al. 2009) create highly clumpy envelopes that allow some starlight to escape the circumstellar environment unhindered. All these factors can contribute to the degree of processing along the line of sight through the protostellar envelope,

making the procedure of completely modeling the envelopes from the processing ratios alone impossible. For example, larger envelopes will have a smaller fraction of their envelope thermally processed, as will envelopes with larger optical depths or steeper density gradients. Fully modeling the thermal structure of the circumstellar envelopes requires knowledge of their sub-parsec structure.

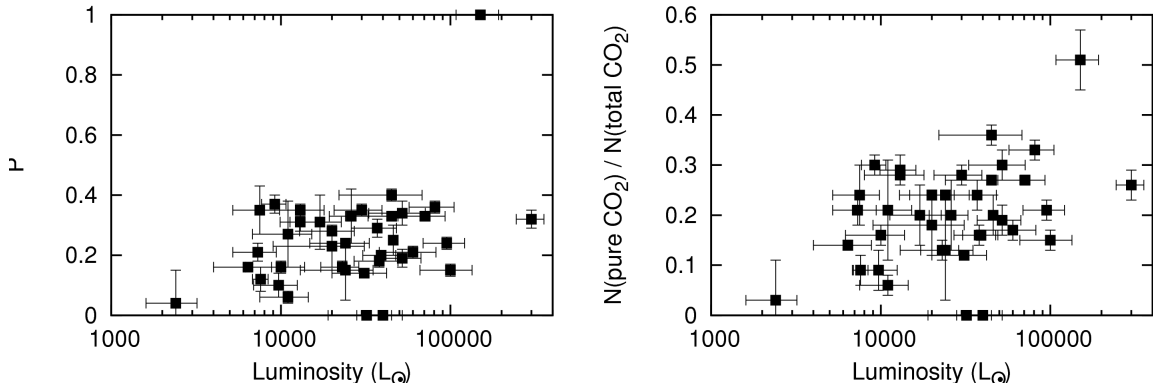

Figure 11. Left: Processing ratio as a function of central source luminosity. Right: Fraction of total column attributed to pure CO_2 as a function of source luminosity.

While there remain a significant number of unknowns, it can be instructive to build a simple model of a protostellar envelope in order to illustrate the physical processes that may be occurring as the massive YSO evolves. We construct a simple spherical model for a massive YSO using the popular radiative transfer code DUSTY consisting of a central radiative body and a spherically symmetric power-law envelope such that $\rho(R) \propto R^{-3/2}$ (e.g., van der Tak et al. 2000). We assume typical values of 100 AU and 5×10^4 AU for the inner and outer radius of the envelope, respectively. The code then calculates the radial density and temperature profiles

assuming an A_V of 50 magnitudes and the Draine and Lee silicate dust models tabulated by Zubko et al. (1996) with a standard MRN (Mathis et al. 1977) size distribution.

Figure 12 shows the resulting radial temperature profiles at several luminosities between 10^3 and 10^6 $L_\odot$ with an A_V of 50 magnitudes. The temperature decreases with increasing distance from the star, and beyond the very inner portion of the envelope, the temperature profile is a power-law (Looney et al. 2003). Note that as the stellar luminosity increases, the temperature at a given radial distance also increases. Or, in other words, as luminosity increases, the distance at which a particular temperature occurs increases. As a result, as a star accretes material and grows in luminosity, ices must lay behind an outward-propagating sublimation front. In a similar fashion, non-segregated CO_2 must lay behind an expanding 'segregation front.' While a precise value for the segregation temperature remains unknown, an estimation of the segregation front radius can be determined from the models. Figure 12 also indicates the segregation front radius as a function of stellar luminosity assuming a segregation temperature of 30 or 50 K. The front may be as close as 0.002 pc to a 10^3 $L_\odot$ star, or may disappear off the edge of the envelope once the entire envelope is heated above the segregation temperature for a high-luminosity star.

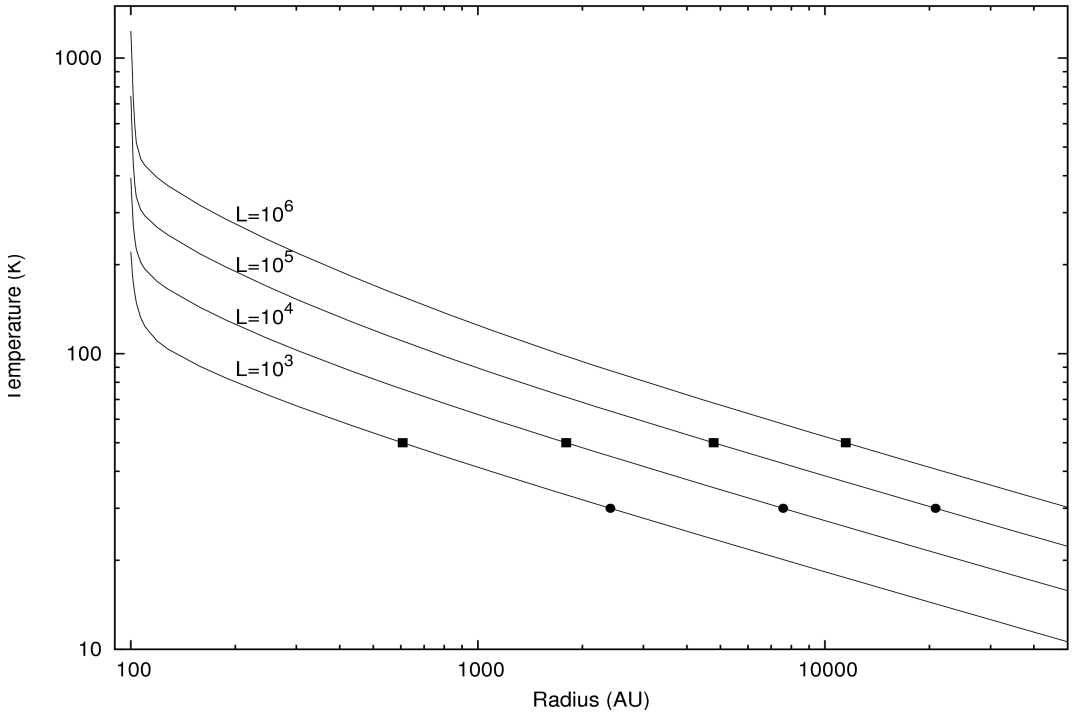

Figure 12. Dust temperature as a function of distance from the central star at stellar luminosities of 10^3, 10^4, 10^5, and 10^6 $L_\odot$. Squares mark the location of the segregation radius for a segregation temperature of 50 K, and the circles for a segregation temperature of 30 K.

Because the precise values of the sublimation and segregation temperatures remain unknown, it is currently not possible to use the processing ratios determined for the LMC's massive YSOs to deduce the properties (e.g., size and distribution) of the circumstellar material beyond some rough limits. But the model displays the potential benefit of such measurements with an increased understanding of interstellar ice properties. It is interesting to consider the implications the results of such a model have on describing the environment of the early Solar System. If, as the evidence indicates, the Sun formed in a cluster with a massive forming star, the thermal – and therefore chemical – properties of the early solar nebula may have been influenced by the presence of the nearby massive YSO. The precise temporal choreography of the Sun-

massive star system is ambiguous. It is unclear if the nearby massive star was a solar sibling (began formation process simultaneously with the Sun and died in a supernova before the Sun's T-Tauri phase) or formed first and then exploded sometime before the later stages of the Solar System's formation. There are also dynamical changes to consider – the Sun and the massive star may have moved closer or father apart with time. However, if the Sun formed from material close enough to the massive star to have been modified by it, the implications could be as far reaching as the formation of comets and planets. Since different parts of the massive envelope have different temperatures, specific regions are dominated by a variety of different gas-phase and solid-state species. Observations of comets indicate that they – and therefore the early solar nebula – have abundances typical of interstellar ices rather than those thermally processed by a nearby massive star (Allamandola et al. 1992; Chiar et al. 1996). It therefore seems probable that the ices incorporated into the early solar nebula originated from beyond the segregation radius. Assuming the Sun was formed from material that once surrounded a massive star of mass 15 to 25 $M_{\odot}$ (Looney et al. 2006), the Sun must have been located beyond the segregation radius, or at a minimum distance of $\sim$0.01 pc from the massive YSO assuming the relatively high segregation temperature of 50 K. If we assume a segregation temperature of 30 K, we can place a lower limit on the Sun-massive star distance to be $\sim$0.03 pc. The distance between the forming solar system and its proposed massive YSO sibling has been previously estimated to be between $\sim$0.02 and 1.6 pc based upon modeling of the radioisotopic enrichment of the protosolar nebula by the supernova explosion at the end of the massive star's life cycle (Looney et al. 2006), values consistent with the distance lower limits estimated here. More laboratory work that better

constrains segregation and sublimation temperatures will lead to a better understanding of the chemical properties in massive YSO envelopes and forming clusters.

3.4.3. CO_2 Abundance

As discussed above in Section 3.3.1, the detection of ice absorption features in our *Spitzer* IRS data beyond the 15.2 μm CO_2 bending mode is inhibited by the presence of strong PAH emission. Therefore our ability to determine CO_2 ice abundance (relative to H_2O ice) is limited to the availability of previously published water ice column density measurements. Oliveira et al. (2009) and Shimonishi et al. (2010) provide a detailed review of the previous H_2O and CO_2 ice column density measurements in the LMC. Four of our sources – 045640.79-663230.5, 052212.57-675832.4, 053054.24-683428.3, and 053931.19-701216.9 – were also observed with the AKARI (Murakami et al. 2007) InfaRed Camera (IRC; Onaka et al. 2007) between 2.5 and 5 μm at a low resolution (R = 20). One of those sources, 053931.19-701216.9, was not included in the above decomposition analysis because the extremely high level of noise in its spectrum prevents a meaningful decomposition of its profile shape. However, there does appear to be a CO_2 absorption feature at 15.2 μm, and from it we estimate a CO_2 column density of $5.65 \pm 3.45 \times 10^{17}$ cm^{-2}, consistent with AKARI estimations from two different studies of 6.7×10^{17} cm^{-2} (Shimonishi et al. 2008) and $5.66 \pm 0.64 \times 10^{17}$ cm^{-2} (Shimonishi et al. 2010). Our determinations of the CO_2 column density for the other three sources are consistent within the

uncertainties of the AKARI values (Shimonishi et al. 2008, 2010). Table 6 documents the CO_2 and H_2O column densities measured here and in the literature to date (van Loon et al. 2005; Shimonishi et al. 2008; Oliveira et al. 2009; Shimonishi et al. 2010) for LMC massive YSOs. For some sources several observations have been performed, in which case we provide a weighted average of all available observations. While this and the Oliveira et al. (2009) study have used the 15.2 μm features to estimate CO_2 column densities, Shimonishi et al. (2008) and Shimonishi et al. (2010) used the CO_2 feature at 4.3 μm. For the three sources which overlap between the Oliveira et al. (2009) and either AKARI study, the column density estimated from the 15.2 μm feature is lower than that estimated from the 4.3 μm feature, typically by a factor of ∼0.75. Note however that the Shimonishi et al. (2008) determinations were highly uncertain (typical uncertainties of > 50%), and therefore have an extremely limited effect on the weighted average. For the four sources in this study with AKARI observations the column density determinations of both studies are consistent within the uncertainties, and neither our *Spitzer* nor the ARAKI data consistently overestimates the other. Thus we find no evidence for a systematic discrepancy between the 4.3 and 15.2 μm column density measurements.

The CO_2 and H_2O column densities of Table 6 are plotted in Figure 13 along with the best fit CO_2 / H_2O ratio, 0.33 ± 0.01. The median value of the CO_2 abundance relative to H_2O among Galactic massive YSOs is ∼0.2 (see Oliveira et al. 2009, and references therein). A similar ratio of 0.18 ± 0.04 has been observed towards Galactic quiescent dark clouds (Whittet et al. 2007), and a higher CO_2 / H_2O ratio of ∼0.3 has been reported toward Galactic low-mass

YSOs (see Oliveira et al. 2009, and references therein). The updated CO_2 / H_2O ratio re-enforces the previous findings of van Loon et al. (2005), Shimonishi et al. (2008), Oliveira et al. (2009), and Shimonishi et al. (2010) who reported enhanced LMC massive YSO CO_2 ice abundances relative to those in the Milky Way. Oliveira et al. (2009) and Shimonishi et al. (2010) also note that the LMC massive YSO abundance is curiously similar to that of low-mass Galactic YSOs.

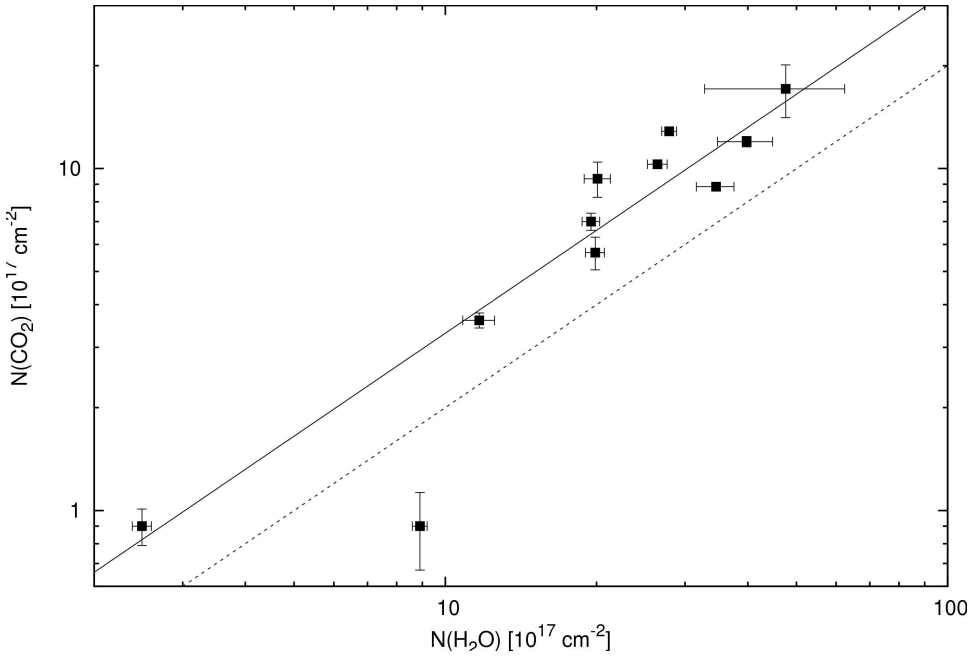

Figure 13. CO_2 column density as a function of H_2O column density. The best-fit CO_2 to H_2O ratio, CO_2 / H_2O = 0.33 ± 0.01, is plotted as a solid line. The average CO_2 / H_2O for Galactic massive YSOs of 0.2 is shown as a dashed line for comparison.

A higher CO_2 abundance in LMC massive YSOs than in Milky Way massive YSOs is a surprising result. The LMC is a low-metallicity galaxy, thus CO is expected to be underabundant (Fukui et al. 2001). Since CO is considered an important parent molecule of CO_2 (for a recent review of CO_2 production routes see Pontoppidan et al. 2008), we might expect a lower CO_2

abundance in the LMC. Oliveira et al. (2009) provide a nice discussion of possible explanations for the observed high CO_2 abundance. In short, the proposed explanations relate to the different radiation fields in the LMC and the Milky Way. Laboratory experiments show that UV radiation can stimulate CO_2 production (D'Hendecourt et al. 1986). Such an explanation is consistent with the higher ambient UV radiation field in the LMC caused by the high level of star formation; the ambient UV field is estimated to be 1 – 10 times stronger in the LMC than in the Milky Way (Bel et al. 1986; Welty et al. 2006). There is also evidence that the greater level of star formation also causes the LMC's average dust temperature to be higher (e.g., Aguirre et al. 2003; Sakon et al. 2006). Models of diffuse grain surface chemistry indicate that higher dust temperatures can enhance CO_2 production. Both explanations suggest that within the LMC, the radiation field compensates for the low CO abundance to produce an enhanced solid-state CO_2 abundance.

3.5. Summary

We have presented high-resolution mid-IR spectra of 40 massive YSOs in the LMC and analyzed the solid-state CO_2 bending mode absorption band at 15.2 μm. We decomposed the shape of the feature using two well-used methods: 1) a 5-component fit using polar and apolar CO_2 ices and 2) polar and annealed H_2O:CH_3OH:CO_2 ice components. These decompositions provide information about the chemical and thermal state of the ices, the most interesting of which are listed below:

- Both the 5-component and annealed fits provide equally good fits to the observed absorption features.
- The high spectral resolution of the observations has allowed for the first direct detection of the absorption feature's double peak characteristic of pure CO_2. From the 5-component fit, we find that pure CO_2 contributes $\sim$20% to the total column density.
- Both the annealed and 5-component fits indicate that methanol has a low abundance in CO_2 ice mixtures (< 3–20% by number), lower than the H_2O:CH_3OH:CO_2=1:1:1 ratio typically used in similar Galactic and extragalactic studies.
- The presence of the double peak in the spectra indicate that the ices have been thermally processed, and the annealed fits indicate the ices have been warmed to temperatures >100 K. Using the relative contribution of the pure CO_2 component, we determine the amount of thermal processing that has occurred in the regions surrounding LMC massive YSOs, and find evidence that the amount of thermal processing is positively correlated with the luminosity of the YSO.

The decompositions show that by the evolutionary stages being probed in this study, CO_2 ice is already significantly thermally processed in the envelopes of massive YSOs. In other words, the thermal processing mechanism – commonly suggested to be CO_2 segregation – occurs on a time scale of less that a few 10^5 years.

Finally, we refined the value of the LMC CO_2 to H_2O ratio to 0.33 ± 0.01 by combining all published CO_2 and H_2O ice abundances. This is higher than that observed around high luminosity YSOs in the Milky Way and has been explained by either the LMC's stronger ambient UV radiation field or higher ISM dust temperature.

3.6 Acknowledgments

The authors wish to thank Joanna Bridge for her work on fitting the ice spectral features and Ryan Peterson for his work on testing the quality of the fitting routine. We would also like to thank E. F. van Dishoeck and Remy Indebetouw for enlightening early discussions, and the anonymous referee for input that greatly enhanced the paper. This work is based in part on observations made with the Spitzer Space Telescope, which is operated by the Jet Propulsion Laboratory, California Institute of Technology under a contract with NASA. Use was made of Leiden University's Sackler Laboratory ice spectra database and the SIMBAD database, operated at CDS, Strasbourg, France. Support for this work was provided by the NSF grant AST 08-07323 and NASA through JPL grant 1316421. Facilities: Spitzer (IRS, IRAC, MIPS)

Chapter 4

The Life and Death of Dense Molecular Clumps

4.1 Introduction

Despite their prevalent role in shaping galactic structures and stellar content, the current understanding of massive star formation remains superficial and incomplete. There are a number of reasons for this, many of which are related to observational difficulties. Massive stars form deeply embedded in the densest regions of molecular clouds behind high extinctions, making it difficult to observe them during their early formation stages. Due to the nature of stars' initial mass function (IMF), they are rare objects. Coupled with their short formation times (~10^5 yrs), this makes finding observational targets difficult. Furthermore, high-mass stars are seldom found in isolation, meaning the interpretation of observations is complicated by the presence of other cluster members, the local environment, outflows, winds, and ionizing radiation.

In recent years a rough evolutionary scenario for massive star formation has emerged (see recent reviews by Beuther et al. 2007; McKee & Ostriker 2007; Zinnecker & Yorke 2007). A single forming star begins as a high-mass starless core, a collapsing gas condensation that is embedded inside a larger subunit (clump) of a molecular cloud (Williams et al. 2000). A

protostar eventually forms within the core and increases its mass by the accretion of nearby gas, first forming a low- to intermediate-mass protostar, and eventually a high-mass star. The Kelvin-Helmholz timescale of a high-mass star is smaller than the formation time of the star, meaning accretion can still be occurring after the star has begun hydrogen burning and entered the zero age main-sequence stage. The ionizing radiation of the star will ionize its surrounding at an increasingly larger scale until a combination of ionizing photons, stellar winds, and outflows have dissipated all of its surrounding material. However, massive stars rarely, if ever, form in isolation, meaning the above evolutionary scenario should be restated in a cluster formation context. The dense molecular clump harboring the high-mass starless core may contain several starless cores, each of which will form a high-mass star, and which together will form a cluster. We adopt the convention presented in Williams et al. (2000), where a core forms a single star or a gravitationally bound multiple system while a clump is the larger scale object associated with clump formation.

Among the keys to understanding massive star formation is the initial conditions within which massive stars form, and observations of dust and molecules provide direct insight into the nature of the material forming stars. While millimeter dust continuum emission can be a good tracer of dust mass of high mass cores and clumps, kinetic information about the gas is accessible through the rotational transitions of high-density tracer molecules such as CS, HCN, HCO^+, HNC, and N_2H^+. The use of these high-density tracers is common in Galactic studies, and thanks to the development of interferometers with long baselines, is garnering greater prominence in extragalactic studies as well. However, the interpretation of observations presents a difficult

problem as chemical effects can greatly distort the structures observed. In particular, the depletion of many molecules onto dust grains is suspected to occur in dense regions (e.g., Caselli et al. 1999; Kramer et al. 1999). The situation is probably further complicated in regions near high-mass star formation where chemical differentiation likely plays a role. For example, if HCO^+ is formed in any appreciable amount from reactions between C^+ and OH, O_2 and H_2O (Graedel et al. 1982), then the abundance of HCO^+ may be different between regions with varying levels of ionizing radiation. In coming years, with the development of instruments such as the Atacama Large Millimeter Array, an understanding of how dense tracers can be used to decipher the properties of clumps and cores will be vital to understanding the conditions leading to the formation of massive stars. We report the results of a study of several star formation regions using HCO^+ and HCN as high-density gas tracers.

Some of the problems of studying Galactic star formation can be mitigated in the Large Magellanic Cloud (LMC). Galactic star formation is concentrated along the plane of the Galaxy, where dust obscuration is high, however the LMC is located at a high Galactic latitude with substantially little intervening Galactic material. Milky Way studies are also plagued by distance uncertainties; the LMC is located at a known distance of 50 kpc (Feast 1999) making luminosity determinations relatively robust. In recent years, the LMC has been the subject of extensive studies of star formation on a galaxy-wide scale. One of the primary observational advantages to studying the LMC is its relative proximity, which allows single instances of massive star-formation (or tightly bound systems) to be resolved even in the mid-IR. Taking advantage of the ability to readily observe the entire galaxy, a number of studies have sought to identify and

catalog all the massive and intermediate-mass YSOs in the LMC (Gruendl & Chu 2009; Whitney et al. 2008). Combined with other studies that identified sites of on-going star formation via their infrared emission, maser activity, and compact Hα emission and centimeter emission, the literature now contains an extensive catalog of LMC YSOs (e.g., Indebetouw et al. 2004; Chen et al. 2009; Chen et al. 2010; Ellingsen et al. 2010).

We have conducted a study of four of the more active star formation regions in the LMC – N44, N105, N113, and N159. Each region was imaged with the *Australia Telescope Compact Array* (*ATCA*) in the 3 mm transitions of HCO^+ and HCN, which have critical densities of ~10^5 cm^{-3}. We have analyzed the observations to determine the properties of the dense gas and its association with ongoing star formation in the LMC. Section 4.2 describes our observations and data reduction procedure while Section 4.3 details how discrete regions of molecular emission are identified and how their properties are determined. Section 4.4 describes the relation between the molecular material observed and the known star formation activity in the regions imaged. In Section 4.5, we investigate how the properties of cloud clumps differ between those with and without ongoing massive star formation, and we also discuss the implications of our findings on the timescale required for a massive star/cluster to disrupt its natal clump.

4.2 Observations and Data Reduction

The regions chosen for this study were selected for their known association with massive star formation. N44, N105, N113, and N159 are all well-studied large HII complexes in the LMC with signatures of both recent (Hα emission) and on-going (e.g., maser emission and bright IR

emission) star formation. For each complex, we targeted the emission peak of the region's giant molecular cloud(s) (GMCs; 10-100 pc scale) with the aim of imaging the dense gas associated with current star formation in the cloud. Panel (a) in Figures 14 – 18 show recent single-dish ^{12}CO observations from the Magellanic Mopra Assessment (MAGMA; Hughes et al. 2010), an on-going survey of the molecular content of the Large and Small Magellanic Clouds using the Mopra Telescope. Panel (a) in Figure 14 – 16 and panel (b) in Figures 17 and 18 show the 50% sensitivity of our *ATCA* observations toward the CO emission peaks. Note that to cover large sections of the molecular clouds, mosaics were composed from several different *ATCA* pointings.

The 3 mm HCO^+ and HCN data were collected during 12 separate sets of observations between September 2006 and September 2009. At the time, the *ATCA* could be configured to observe two frequencies simultaneously, allowing us to observe both HCO^+ (J = 1–0) at 89.1885 GHz and HCN (J = 1–0) at 88.6318 GHz, redshifted to the appropriate observational frequency for v_{LSR} = 235 km/s. The average maximum antenna spacing for the array's configurations during the observations was approximately 90 m, giving a synthesized beam FWHM of ~5" × 6". Table 7 lists the dates of the observations, the number of pointings in the mosaic, the HCO^+ beam size, peak image sensitivity at both frequencies, and spectral resolution used in the analysis. Note that we have separated N44 into two distinct, non-contiguous regions: N44's northern molecular cloud, which we refer to as N44 Region 1, and the southernmost molecular cloud, N44 Region 2.

The data were calibrated and images created using the *ATCA* version of the MIRIAD package (Sault et al. 1995). Flux calibration was performed using PKS 1921–293, Uranus, and

Mars for N113, N105, and N44, respectively; N159 was flux calibrated using PKS 0637-752, PKS 1253-055, and Mars over its 5-day observation. We estimate an absolute flux uncertainty of ~20%. Quasar PKS 0637-752 was used as the phase calibrator for all observations. PKS 1921-293 was used to calibrate the bandpass for N105 and N113, while PKS 1253-055 was used for N159 and N44. After imaging the maps were CLEANed to a 2-σ level. These cleaned data cubes are then used in the clump-identification procedure described below. The HCO^+ and HCN images presented in Figures 14 – 18 are masked 0^{th} moment maps that reduce the noise by masking with a smoothed version of the cube.

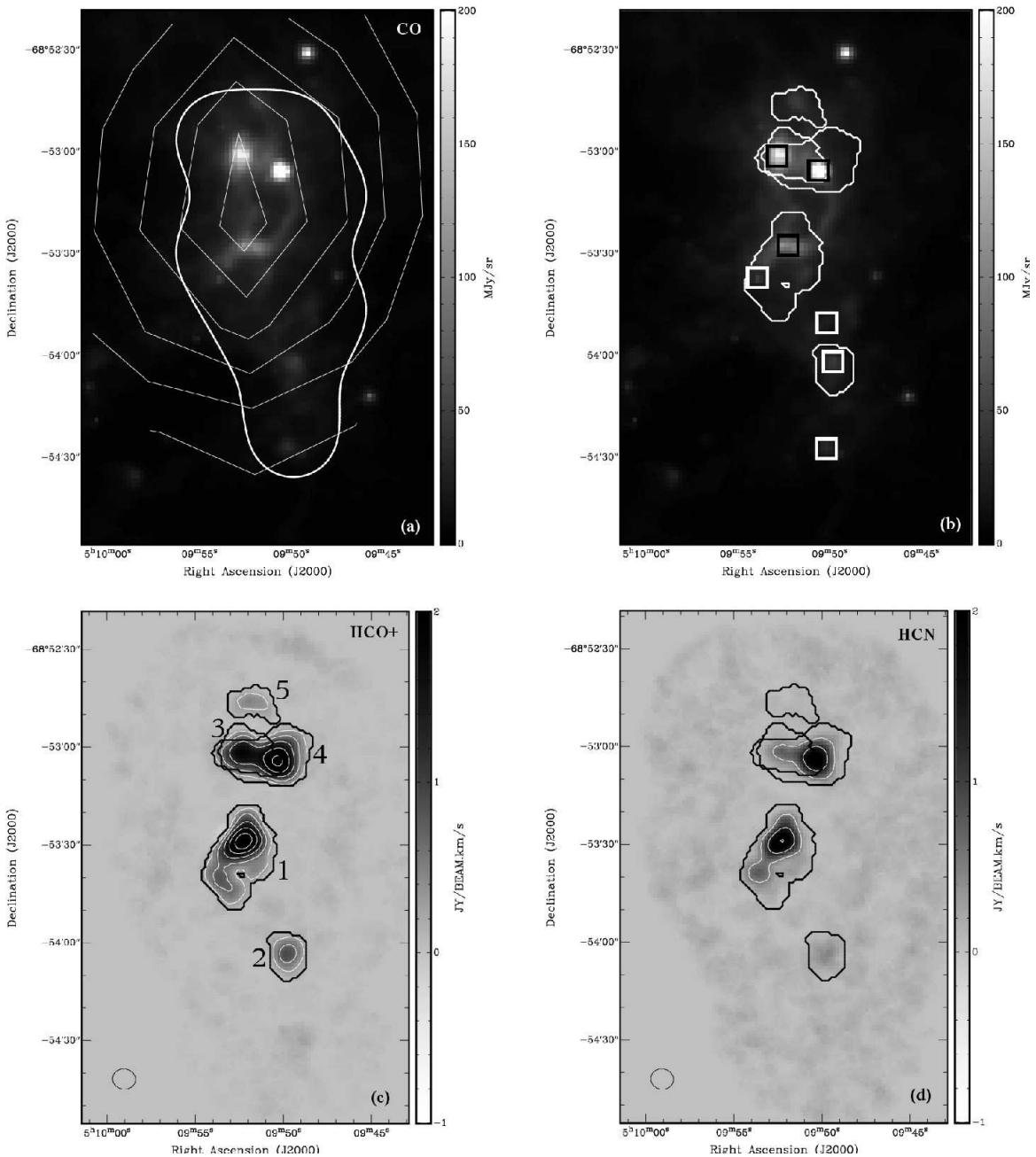

Figure 14. *Spitzer* 5.8 μm, MAGMA CO and ATCA HCO^+ and HCN images of N105. (a) 5.8 μm image showing stars and PAH emission overlaid with CO contours from MAGMA (thin lines) and the 50% sensitivity of the ATCA HCO^+ mosaic (thick line); (b) 5.8 μm image grey scale image with the positions of YSO marked with boxes. Box colors are not indicative of YSO categories, and are simply chosen for greatest contrast. White contours show the boundaries of the HCO^+ clumps; (c) ATCA HCO^+ observations in grey scale overlaid with clump boundaries and HCO^+ contours at integrated flux densities of σn^2 Jy/beam km^{-1} (n=2,3,4...), where σ is the rms noise. Clump ID numbers are indicated next to the corresponding clump; (d) ATCA HCN observations in grey scale overlaid with clump boundaries (black lines) and HCN contours (white lines) at integrated flux densities of σn^2 (n=2,3,4...), where σ is the rms noise of the observation.

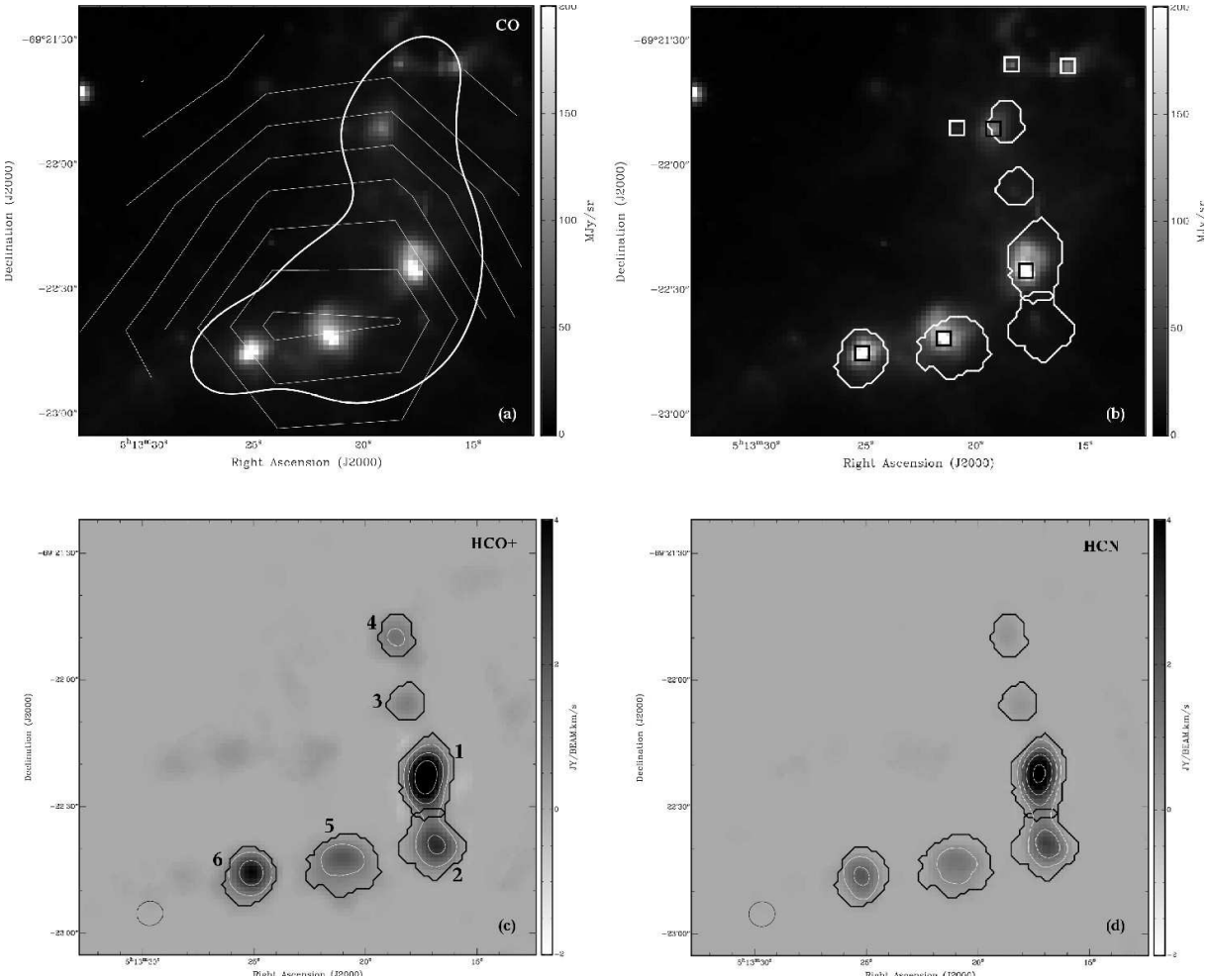

Figure 15. Same as Figure 14, but for N113.

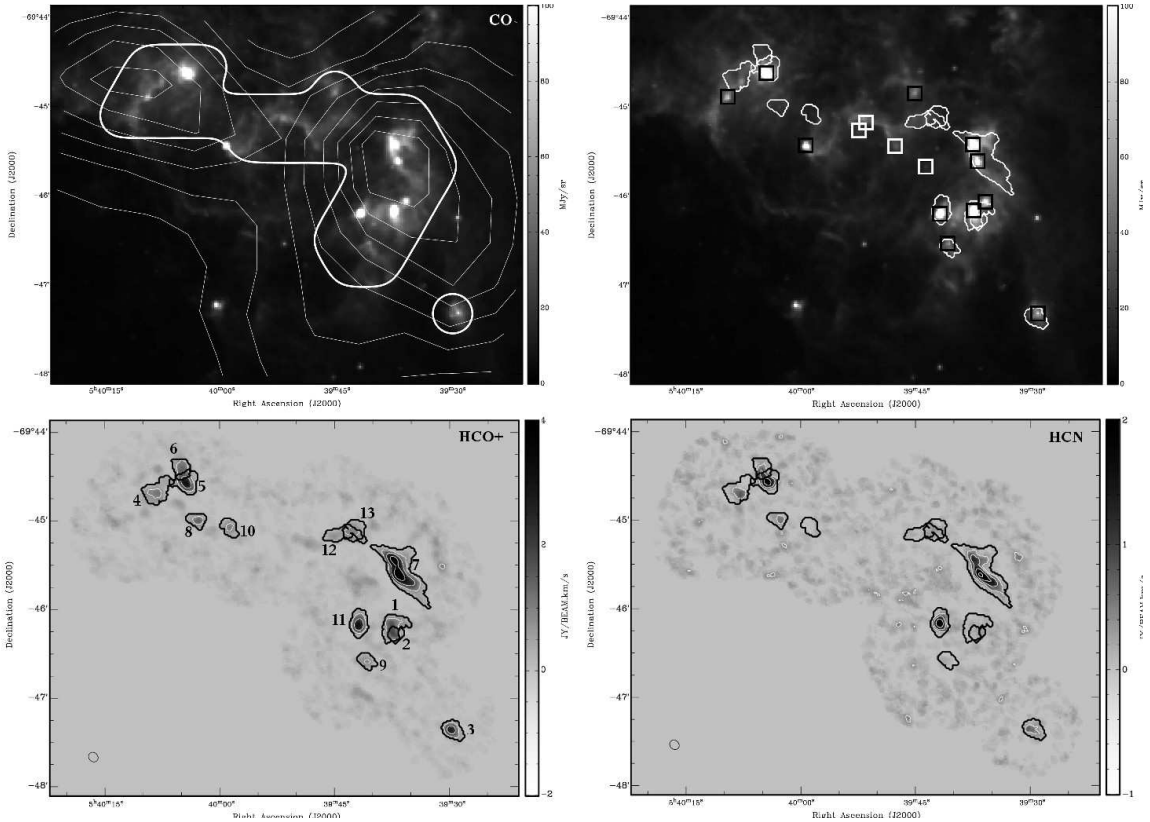

Figure 16. Same as Figure 14, but for N159.

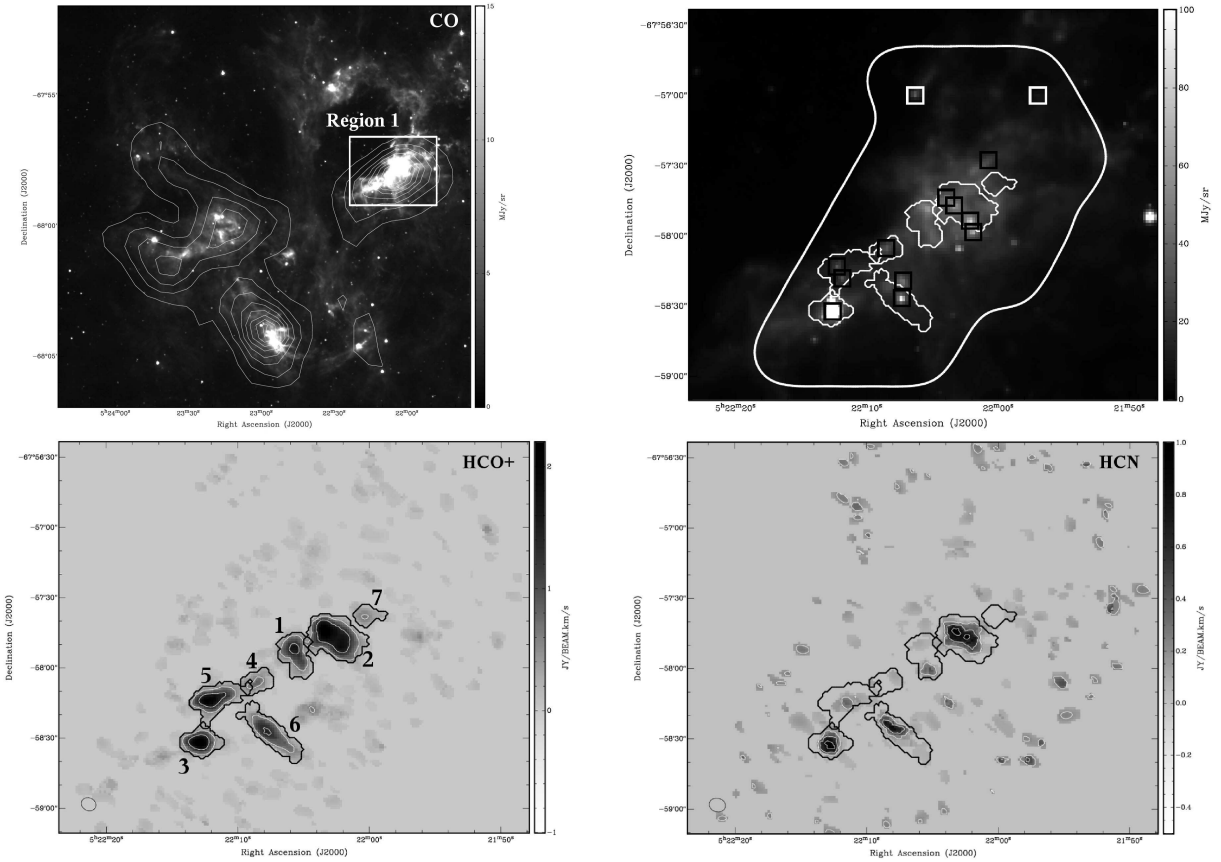

Figure 17. *Spitzer* 5.8 μm, MAGMA CO and ATCA HCO^+ and HCN images of N44 Region 1. (a) 5.8 μm image showing stars and PAH emission overlaid with CO contours from MAGMA (thin lines). Boxes indicate Regions 1 and 2; (b) 5.8 μm image grey scale image with the positions of YSO marked with boxes. Box colors are not indicative of YSO categories, and are simply chosen for greatest contrast. White contours show the boundaries of the HCO^+ clumps (thin lines) and the 50% sensitivity of the ATCA HCO^+ mosaic (thick line); (c) ATCA HCO^+ observations in grey scale overlaid with clump boundaries (black lines) and HCO+ contours (white lines) at integrated flux densities of σn^2 Jy/beam km^{-1} (n=2,3,4...), where σ is the rms noise. Clump ID numbers are indicated next to the corresponding clump; (d) ATCA HCN observations in grey scale overlaid with clump boundaries (black lines) and HCN contours (white lines) at integrated flux densities of σn^2 (n=2,3,4...), where σ is the rms noise of the observation.

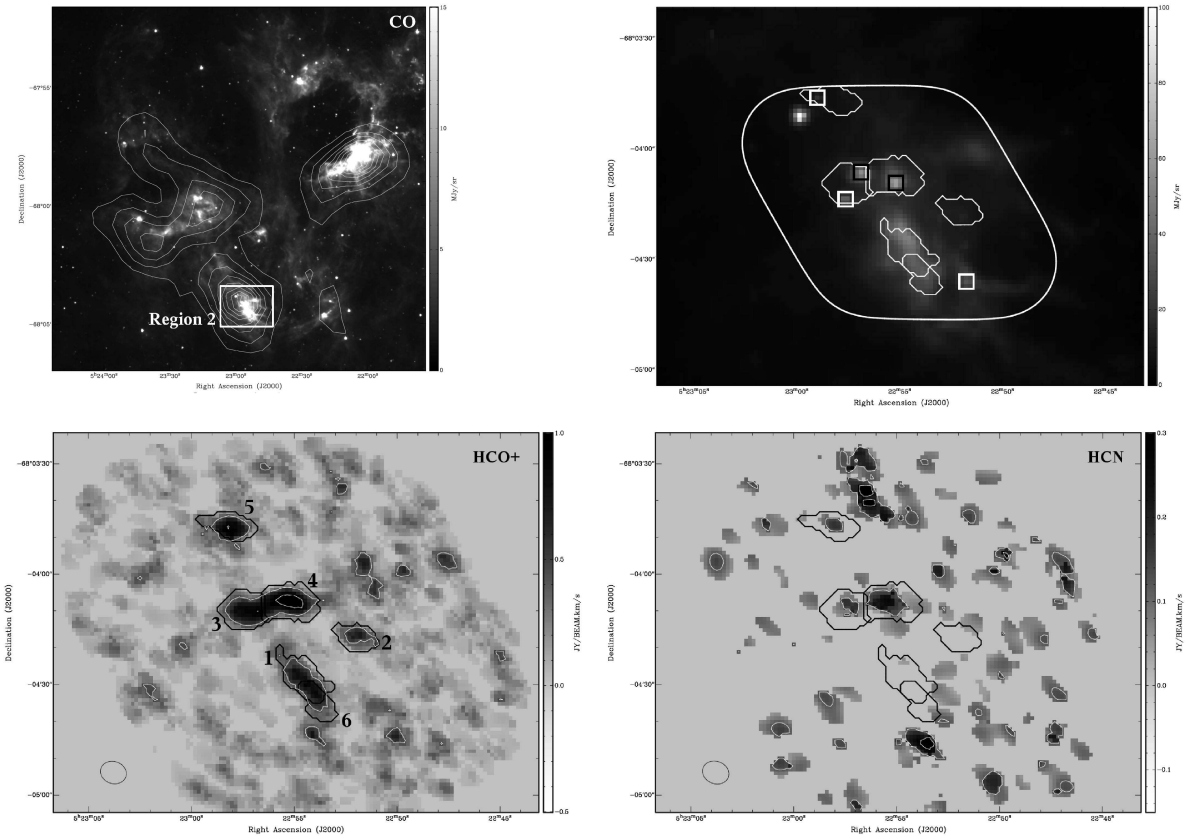

Figure 18: Same as figure 17, but for Region 2 of N44.

4.3 Identification and Characterization of Dense Molecular Clumps

The HCO^+ and HCN observations show that the molecular material within N105, N113, N159, and N44 is clumpy with emitting clouds of various sizes, shapes, and velocity structures. We investigate these variations in intensity and velocity quantitatively by first determining the sizes, linewidths, densities, and masses of the clumps.

It is important to note that all quantities measured from observations are dependent on the quality and nature of the observations. This is particularly true of interferometric observations as they are only sensitive to certain size scales. In the case of identifying discrete clumps within our *ATCA* data, the detection of a clump is firstly dependent on the sensitivity of the observations. Because the sensitivity of the observations are similar for each region, each region should be sensitive to a similar population of clumps. The clumps themselves are likely not truly discrete structures, but rather density enhancements located within a larger molecular cloud. Therefore, the edge and size of each clump depends not only on the sensitivity of the observation but on the definition of the border between high-density clump and the lower-density surrounding cloud.

4.3.1 Identifying Clumps

We use the HCO^+ (J = 1–0) data as the primary clump tracer. The HCN (J = 1–0) transition at 88.6318 GHz has three resolved hyperfine components within the observed bandwidth, preventing us from using the HCN data in the clump-identifying procedure described below. Doing so would result in the misidentification of each hyperfine component as a separate clump at a different central velocity. Moreover, the HCN data has a lower overall signal-to-noise

ratio (SNR) than that of HCO^+ because of the weaker HCN flux. To identify HCO^+ clumps in the *ATCA* data we use the algorithm described in Rosolowsky & Leroy (2006) by using the software version of the procedure available as an IDL package called CPROPS. The procedure is described in detail by Rosolowsky & Leroy (2006) and in the CPROPS users guide, but a description of the basic steps of the algorithm follows. A mask is first generated from the data to isolate significant emission by estimating the noise variance (σ_{rms}) and identifying emission cores of four adjacent channels with flux density > $2.5\sigma_{rms}$. Each core is then expanded to include all connected emission above the $2\sigma_{rms}$ level. These masking levels (called the 'threshold' and 'edge' values in CPROPS) can be user-defined, and we explored a range of values. We found that threshold = $2.5\sigma_{rms}$ and edge = $2\sigma_{rms}$ was able to distinguish significant emission from noise while also identifying faint clumps.

Once the images have been broken into these 'islands' of significant emission, CPROPS assigns the emission to individual clouds. We chose to use the ECLUMP keyword when separating the islands into individual clumps. Molecular clouds are known to be clumpy, and the clumps identified here (islands) often contain substructure themselves. Without the ECLUMP keyword, emission that is shared by two separate clumps within an island (below the merge level) is not assigned to either clump. Because many of our clumps are marginally resolved, we chose to use the ECLUMP keyword to assign as much emission to a specific cloud as possible.

Using CPROPS, we initially identified a total of 37 HCO^+ clumps in the 5 regions. A visual inspection of clump 2 in N44 Region 1 shows what appears to be 2 separate clumps

(Figure 17). The east and west sub-clumps have different central velocities of 286.5 km/sec and 281.9 km/sec, but share emission in the wings of their line emission, likely causing them to be identified as a single clump. To differentiate their emission, we have run CPROPS on separate data cubes that detach between the two clumps at v = 284.0 km/sec and have labeled the east and west clumps 2.1 and 2.2, respectively. Treating these two clumps individually, we have identified a total of 38 clumps in the 5 mosaic regions. Separating the clump into clumps 2.1 and 2.2 does not have a significant effect on the clump property analysis that follows. If we were to leave the clumps together as a single clump (clump 2), the number of clumps with only intermediate mass YSOs (see Section 4.5) would be reduced by one, and the total mass of one of the clumps with a massive YSO at its center would increase by a factor of 2. The clump masses are likely only reliable within a factor of 2, so the change would not significantly alter the interpretation of our results.

A visual inspection of the *ATCA* data shows that the HCO^+ emission for each clump emanates from a somewhat larger region than the HCN emission. This is consistent with a previous study of N113's clump 1 (Wong et al. 2006) who found a decreasing HCO^+/HCN ratio on longer interferometer baselines. As larger baselines probe smaller scales, this suggests that the HCO^+ emission originates from a larger, more diffuse region than that of HCN. Such a radial dependence could be explained if HCN probes higher densities than HCO^+. Alternatively, as described in Heikkila et al. (1999), the abundance of HCO^+ may be enhanced in photon-dominated regions via chemical reactions involving C^+, which is expected to be abundant in

regions exposed to UV radiation. Each of the HII complexes studied here contain a number of UV-producing O and B-type stars, plausible sources of ionizing radiation. If the latter explanation is accurate, the size of the clumps as determined from HCO^+ (see below) is an overestimate. Wong et al. (2006) estimates the HCN-determined radius of N113's clump 1 is 89% of that determined from the HCO^+.

4.3.2 Derivation of Clump Physical Parameters

The literature contains a number of methods to determine the sizes of molecular clouds. One approach is to approximate the radius, R, of the cloud as $R = (\sigma / \pi)^{1/2}$ where σ is the cross section of the clump (e.g., Muller et al. 2010; Larson 1981). The validity of this method is of course highly dependent on the sphericity of the cloud. Other authors have approximated the radius as the mean RMS distance to the center of the pixels within a cloud, with some advocating for weighting each pixel by its flux density (Solomon et al. 1987; Rosolowsky & Leroy 2006). As the above methods can be dependent on the sensitivity of the observations, some authors have developed ways to determine the 'true' size of a cloud (i.e. the cloud's size with zero noise). The CPROPS package attempts such a prodecure by extrapolating the size of a cloud under various levels of $T_{noise} > 0$ K noise out to what would be expected for a perfect ($T_{noise} = 0$ K) observation. Alternatively, if the clumps are fairly Gaussian in shape, their images can be approximated with Gaussians such that the clump radii are determined from the radii of the best fit (e.g., Wong et al. 2006; Lee et al. 2010). Of course in all of the above cases, the observed size of the cloud is dependent on the resolution of the observations, meaning the beam must be

deconvolved.

We tested several of the above methods on the HCO^+ observations, and found that they in general give similar results. In Table 8, we list the radius of each clump estimated by CPROPS; the radius is determined by taking the flux-weighted RMS size of the cloud, extrapolating the measured size to its zero noise size, deconvolving with the beam, and then converting this RMS size to the clump's radius assuming a particular brightness profile. If the extrapolated size of the cloud is smaller than the beam along either the beam's major or minor axis, it cannot be deconvolved. We note that CPROPS estimates the deconvolved radius for several clouds with non-extrapolated (i.e. directly determined from the image) sizes smaller than the beam. As can be seen in Figure 14, a significant number of the clumps are comparable in size to the beam (~1 pc at the distance of the LMC). This is consistent with the sizes of dense molecular clumps in Galactic massive star forming regions with measured sizes of ~0.1 – 1 pc. Given the angular resolution limitations of 3 mm observations, at the distance of the LMC, only the largest clumps are resolved.

CPROPS calculates the velocity dispersion σ_v (the velocity size) of each cloud in a similar manner as the spatial size by determining the flux-weighted rms velocity of the pixels within the clump, extrapolating to a zero-noise observation, and deconvolving with the channel width. For a Gaussian line profile, the full-width half-maximum (FWHM) line width is then given by $\Delta v = (8\ln(2))^{1/2}\,\sigma_v$.

Given the uncertainties of the HCO^+ and HCN abundances, it is difficult to directly infer the mass of the clumps from the line integrated flux density. Moreover, because of the high

optical depth, our observations likely trace only the molecular material near the surface of the clumps. However, numerous previous studies of massive star forming clumps indicate the masses of the clumps can be well-approximated via the virial theorem (e.g., Larson 1981; Solomon et al. 1987; Saito et al. 2006; Wong et al. 2006). Assuming the clumps are spherical, have radial density profiles described by a power law, and are virialized, the virial mass is given by the formula (Solomon et al. 1987)

$$M_{VT} = 125\ M_{\odot}\ [(5 - 2\beta) / (3 - \beta)]\ \Delta v^2\ R,$$

where β is the power law exponent of the density profile, R is the radius in parsecs, and Δv is the FWHM of the velocity line width in km/sec. The calculation of the virial mass clearly depends on the density profile of the clump, and a single value for β is not agreed upon – the shallower the density profile is, the more mass is required to support the clump's turbulence. Recent observations have found typical values of $\beta = 1 - 2$ (van der Tak et al. 2000); decreasing the power from 2 to 1 has the effect of increasing he calculated virial mass by a factor of 3/2. Given the uncertainty of both β and R, we estimate there is an uncertainty of a factor of ~2 in the virial mass. The virial mass provided in Table 8 assumes the CPROPS-determined radius and a density profile with β=1; the provided uncertainty assumes only observational effects (uncertainties in Δv and R) and does not account for the uncertainty of β. As they do not have radius estimates, the virial mass cannot be determined for clumps with imaged sizes smaller than the beam.

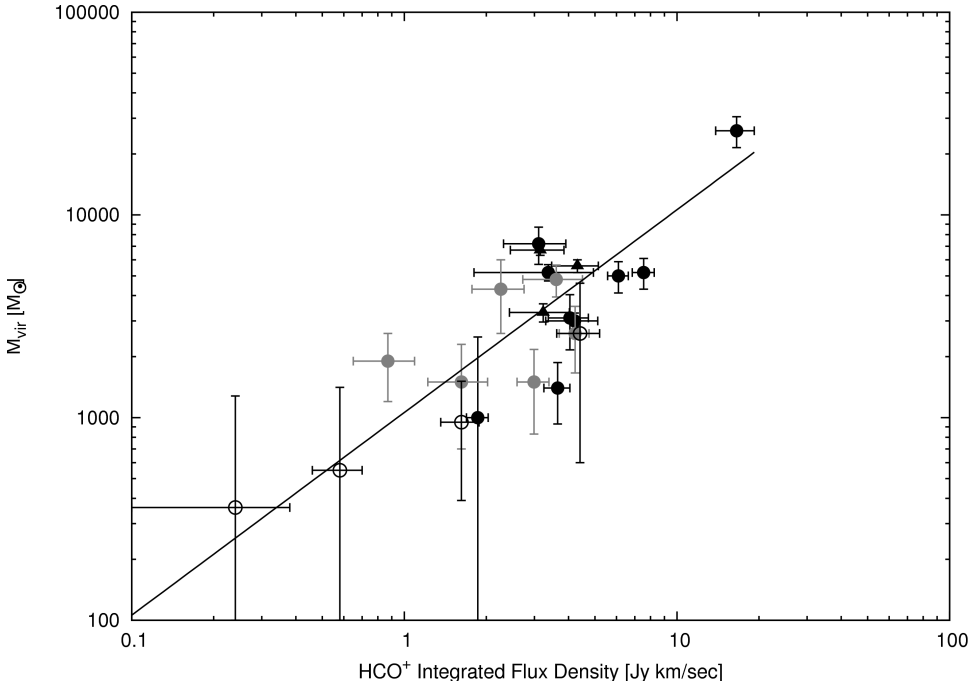

Figure 19. Clump virial mass as a function of HCO^+ flux. The four clump categories are differentiated by symbol: black circles are clumps with centralized massive YSOs, grey circles are clumps with massive YSOs at their edges, open circles are clumps containing no YSOs, and triangles are clumps containing only intermediate-mass YSOs. The line shows the best linear fit to the data, $M_{vir} = 1060\ F_{HCO+}$.

Figure 19 shows the correlation between the virial mass and the HCO^+ integrated flux density, *F*, for the clumps with determinable virial masses. We find the correlation is positive and fairly strong, with a Pearson's product moment correlation coefficient of 0.7. We fit the correlation with a simple polynomial of the form $M_{vir} = 1060\ F$ (Jy km/sec), and using this correlation as a primer, we can estimate the mass of the clumps that are unresolved in the observations, which we call the luminosity mass. It should be noted that a clump's virial mass

and HCO^+ flux will naturally exhibit a correlation because they are both dependent on clump size and linewidth, and the correlation should not be interpreted as evidence of clump virialization. We find that the masses (both virial and luminosity) of the clumps range between several 10^2 $M_\odot$ to a few 10^4 $M_\odot$.

Clump 1 in N113 has been analyzed previously by Wong et al. (2006), and serves as a way to compare our clump property determination methods with another study. Wong et al. (2006) determined the mass of the clump with two different methods, with estimates of 7.3×10^3 $M_\odot$ and $< 1.3 \times 10^4$ $M_\odot$, both values similar to our luminosity mass estimate of $1.1 \pm 0.2 \times 10^4$ $M_\odot$. Note that the luminosity mass uncertainties quoted in Table 8 are statistical and do not include uncertainties in the HCO^+ flux due to flux calibration (20%) or the uncertainty of the HCO^+ flux-mass relationship which we estimate to be 50% from the scatter in Figure 19. The agreement between our and the Wong et al. (2006) mass estimates gives us confidence in our mass determination procedure.

4.4 Star Formation Activity within the HII Complexes

The two most extensive surveys of LMC YSOs, Gruendl & Chu (2009) (hereafter GC09) and Whitney et al. (2008) (hereafter W08), identified a total of 1000+ sources described as candidate YSOs. In a follow-up study of a subsample of these candidate YSOs, Seale et al. (2009) (hereafter SL09) spectroscopically confirmed the YSO-like nature of 277 of these including all of the most luminous definite YSO from GC09. We have used these three surveys as

the primary catalogs from which we determine the locations of YSOs within the HII complexes studied, but we have also combed the literature for further YSO identifications. In particular, detailed IR studies of N44 by Chen et al. (2009) and of N159 by Jones et al. (2005) and Chen et al. (2010) have identified several YSOs not identified in GC09 or W08, and numerous compact HII region (e.g., Indebetouw et al. 2004; Martin-Hernandez et al. 2005) and maser surveys (e.g., Brooks & Whiteoak 1997; Lazendic et al. 2002; Ellingsen et al. 2010) have been used to strengthen their classification as YSOs.

Figures 14 – 18 mark the locations of sources identified as being YSOs in the literature through either their characteristic photometry, spectra, maser activity, or HII region-like emission. These means of detecting YSOs are either flux limited or restricted to phenomena only associated with the most massive YSOs. Therefore only massive and intermediate-mass YSOs can currently be identified in the LMC. A by-eye inspection shows there is a strong correlation between the location of the YSOs and the dense gas in the clumps seen in the *ATCA* data. The relationship between the YSOs and clumps can be quantified by comparing the proximity of the YSOs and clumps to a hypothetical field of YSOs randomly distributed throughout the region. A random distribution of objects in region N159 (the region we have most completely imaged) has a probability distribution that peaks at ~30", meaning if a YSO were to be randomly placed in N159, it is most probable that it will be located a projected distance of 30" from the center of the nearest clump. Furthermore, we find that a randomly placed YSO has only a 10% probability of being located within 12" of a clump. A majority of the YSOs identified in N159 are found to be within only a few (<10) arcseconds of the nearest clump, indicating their positions are

significantly different than a random distribution and are highly correlated with the positions of the clumps. What follows is a description of the star formation activity within each of the star formation regions imaged by *ATCA* and its relation to the molecular clumps.

4.4.1 N105

N105, situated along the western side of the bar of the LMC, is an HII complex (Henize 1956) characterized by a series of HII bubbles, molecular material, and several young clusters (Ambrocio-Cruz et al. 1998). Embedded within N105 is the young, sparse cluster NGC 1958, estimated to have an age of 8-17 Myr (Ambrocio-Cruz et al. 1998 and references therein). Among the members of the cluster is OB association LH31 (Lucke & Hodge 1970). These OB stars have wind-blown a complex set of loops and bubbles that are seen in Hα images (Ambrocio-Cruz et al. 1998).

The dense center of the region, N105A, was the site of the first water maser detection in N105 by Scalise & Braz (1982) that was later confirmed by Whiteoak et al. (1983). Since then, numerous OH and H_2O maser detections have been reported in the literature at the same position. The maser is coincident with what was identified from its infrared emission as a protostar by Epchtein et al. (1984). These were the first signposts of ongoing, active star formation within N105, and several other studies have since identified over a dozen candidate YSOs (Oliveira et al. 2006; W08; GC09; SL09).

Molecular clouds contain the material from which stars form, so it is no surprise that the recent star formation within N105 is concentrated within the region's ~90 pc in diameter molecular cloud. The most common tracer of molecular gas is CO, which traces gas densities of

~10^2-10^3 cm^{-3}. Figure 14 shows a map of N105 from the recent MAGMA CO survey of the LMC. About 65% of N105's YSOs are found within the contour of the molecular cloud, which is comparable to the 70% and 75% found in the molecular clouds of N159 and N44, respectively (Chen et al. 2009; Chen et al. 2010). Our *ATCA* observations targeted the peak of the CO emission located on the western side of the cloud, and we extended the *ATCA* observations to the southern end of the cloud which contains a large sample of YSOs.

Figure 14 also shows the 5.8 μm *Spitzer* image of the *ATCA* imaged area. In the infrared, YSOs appear as point-sources and candidate YSOs are indicated in the figure. The positions and names of the region's candidate YSOs are taken from GC09, but have been verified via their inclusion in other LMC YSO studies in the literature. We do not find N105 YSOs in the literature not also identified in GC09.

YSO 050952.26–685327.3 is located within N105's clump 1, which has a mass of 6.0 ± 0.7 × 10^3 $M_\odot$. The YSO is coincident with the aforementioned OH and H_2O masers (Brooks & Whiteoak 1997; Lazendic et al. 2002; Ellingsen et al. 2010). Masers are associated with the early stages of massive star formation and can even precede the compact HII region phase. Its *Spitzer* IRS spectrum from SL09 is classified in the PE group, meaning it is dominated by PAH emission and ionic fine-structure lines; such a spectrum would be expected from a source containing an HII region and a photodissociation region (PDR). However, the dusty and highly-ionized environment could be a possible source for spectral contamination. The IRS slit is large enough that a source's extracted spectrum is both that of the source and as much as ~2.75 pc of the YSO's environment (SL09). The *Spitzer* 5.8 μm image (which includes a PAH emission complex

between 5-9μm) of N105 indicates the YSO's environment is a highly dusty, PAH emission dominated region. This suggests that the environment may contribute to the PAH emission seen in LMC YSO spectra. Similarly, the prevalent ionic fine-structure lines in the spectrum – typical of HII regions – may result from the high level of ionized gas in the region seen in the Hα and [OIII] images provided in Ambrocio-Cruz et al. (1998). Another possible source of the fine-structure lines is the CHII region B0510-6857(s) located only 3" away and within the IRS slit. The contamination of a YSO's spectrum with nearby emission is a common problem with YSOs at distances as large as the LMC, and likely plays a significant role in the spectral classification in SL09. Jones et al. (2005) classified IR point sources in the LMC by their mid-IR *Spitzer* colors, and according to their criterion, 050952.26–685327.3 has the colors of an HII region, an advanced evolutionary stage of a YSO. However, the mid-IR colors cover a similar wavelength space as IRS and may suffer from a similar contamination problem as the spectral classification scheme. Having photometric colors similar to that of an HII region could simply be indicative of being in a dusty, PAH emission prevalent region. Moreover, the color classification used by Jones et al. (2005) was defined using the colors of low-mass protostars which should be devoid of PAH and fine-structure line emission. It is therefore not clear that similar color criterion can be used to differentiate stages of massive YSO evolution.

A second YSO – 050953.89–685336.7 – is located within clump 1 about 12" southeast of the maser. It is spectrally classified as a P group source (PAH dominated IRS spectrum) in SL09. GC09 identified a third possible YSO on the eastern side of clump 1, 050951.31–685335.6. It has no associated JHK point source and it's SED is more reminiscent of a dust clump being

illuminated by a star. Oliveira et al. (2006) identified a star at a projected distance of only ~1/4 pc from the IR emission which may be the illuminating star. The evidence suggests it is dust clump, and not a true YSO.

South of clump 1 is clump 2, a clump of smaller mass and size than clump 1. It contains a single candidate YSO – 050949.80–685402.1. GC09 identifies this sources as a probable YSO, although it does have some properties suggestive of a dust clump. Immediately north of clump 2 is candidate YSO 050950.11–685349.4 which is substantially dimmer in the *Spitzer* IRAC bands (2.6, 4.5, 5.8, and 8.0 μm) than the YSOs in both clump 1 and 2. It has been suggested by SED fitting with radiation transfer models that the 8.0 μm flux of a YSO may be a good proxy for its total luminosity, and therefore, its mass (GC09). We adopt a 8.0 μm magnitude ([8.0]) boundary of 8.0 mag between massive ($M > 8\ M_{\odot}$) and intermediate mass ($M < 8\ M_{\odot}$) YSOs (GC09). However, given the possible presence of PAH emission within the band, the magnitude limit should certainly not be considered exact. The [8.0] magnitude may also dependent on geometrical factors such as outflow cavities and envelope 'clumpiness.' Moreover, Chen et al. (2009, 2010), who fit model SEDs to that of observed LMC YSOs, has demonstrated that the magnitude limit may be too conservative; YSOs with [8.0] = 9 mag can be fit with massive ($M > 8\ M_{\odot}$) YSO models. At the farthest southern extent of our *ATCA* imaged area is YSO 050950.12–685426.9, which with a [8.0] = 8.16 we also identify as an intermediate mass YSO. The YSO is not located within a detected HCO^+ clump, however the data cube indicates there may be a low level (2σ) of HCO^+ emission.

The northern region of N105 has clumps 3 and 4 which contain YSOs 050952.73–

685300.7 and 050950.53–685305.5, respectively. Clumps 3 and 4 appear attached in the 0^{th} moment map and indeed share some low level emission in the more diffuse outer regions. However, their peaks are separated in velocity space and each clump is individually distinguishable by CPROPS. YSO 050950.53–685305.5 was identified as a 'protostar' by Epchtein et al. (1984) and is coincident with near-IR source N105A IRS1 from Oliveira et al. (2006). The source is detected in the L' and K_s bands but not in J or H, indicating it is highly extincted (estimated A_V of ~40 mag) and therefore located within or behind and not simply projected on top of the HCO^+ and HCN clumps (Oliveira et al. 2006). Its near-IR spectrum shows a free-free emission continuum underlying H recombination line emission (Oliveira et al. 2006), which is consistent with its *Spitzer* IRS spectrum which contains strong fine-structure lines. Moreover, according to the color criterion of Jones et al. (2005), it has the colors of a reddened HII region. The YSO in clump 3 is a PE group source with an associated CHII region that is identified from its 3 and 6 cm continuum emission (Indebetouw et al. 2004) and its membership in the PE spectral group. However, the YSO does not have clearly identifiable Hα emission, again indicating the source is highly embedded in the molecular clump. It is associated with N105 L'-band blobs A and B from which Oliveira et al. (2006) estimates a lower extinction than for the YSO in clump 4. The lower extinction is consistent with both 050952.73–685300.7's weaker 10 μm silicate feature (see Section 4.5) and the lower HCO^+ and HCN brightness of clump 3 compared to that of clump 4.

At the northernmost point of the *ATCA* observations is clump 5, the least massive clump in N105, but whose calculated mass and radius may be underestimated due to its location on the

edge of the observations; the northernmost portion of the clump may not be detected due to poor signal-to-noise. The clump's low mass is substantiated by the very low level ($< 2\sigma$) of HCN emission. While there is no YSO identified to be associated with the clump, there is a coincident low level of 3 and 6 cm continuum emission possibly arising from a diffuse HII region. Indebetouw et al. (2004) estimates that the ionizing flux required for the radio emission is that of an O9 V star. The clump, which has the lowest estimated mass and surface brightness of the clumps in N105, may be the remnant of the molecular gas from which this high mass star was born.

4.4.2 N113

Star formation region N113 contains a molecular cloud with a linear size of ~40×35 pc and a total gas mass estimated at ~8×10^4 $M_\odot$ contained within a larger filamentary HI cloud (Wong et al. 2006). Ongoing star formation activity within the region is evident from the prevalent Hα emission and several compact 1.3 cm radio continuum sources that run in a string from the southeast to the northwest of the molecular cloud (Brooks & Whiteoak 1997; Wong et al. 2006). This linear structure that traces the recent star formation is coincident with the western side of a larger dust shell evident in mid-IR images (Figure 15). Low angular resolution single dish observations with the MOPRA telescope reveal the presence of HCO^+ and HCN (Wong et al. 2006); however, the implied density of the molecular cloud is ~200 cm^{-3}, significantly lower than the critical densities of HCO^+ and HCN (~10^5 cm^3). The implication is that the molecular

cloud is clumpy, and our mosaic *ATCA* observations target the peak of the molecular cloud and directly reveal this clumpiness.

The most massive clump in N113 is clump 1, with an estimated luminosity mass of 1.1 ± 0.2 × 10^4 $M_\odot$ and a correspondingly high line width of FWHM = 6.24 km/sec. There have been a number of H_2O maser detections within the clump (e.g., Lazendic et al. 2002; Ellingsen et al. 2010), all of them within a projected distance of ~1 pc of YSO candidate 051317.69–692225.0. The YSO is coincident with an obscured near-IR source and a strong cm continuum peak from an embedded HII region. The 86 GHz emission is elongated to the north in the direction of the H_2O maser that is offset from the YSO. Since Galactic masers are often found in linear structures along the axis of an outflow, such a structure within clump 1 is highly suggestive of a maser-inducing outflow being traced by the 86 GHz emission. From the measured 24 and 86 GHz fluxes, Condon (1992) estimates an ionizing photon output of 1.5–3 × 10^{49} s^{-1}, equivalent to the output of one or two O6 stars (e.g., Turner et al. 1998).

Connected to and south of clump 1 is clump 2, with a virial mass of 2.6 ± 0.4 × 10^3 $M_\odot$ and a radius of ~1 pc. Clump 2 contains the YSO candidate 051317.30–692236.7, identified by W08 but not identified by GC09 as a YSO. The exclusion of the source by GC09 resulted from the lack of a point source at 8 μm; in the 8 μm image, the source is extended in one direction. W08 also did not detect an 8 μm point source, but did in the other three bands, sufficient enough to meet their criteria for a possible YSO. If it is a true YSO, its [8.0] flux suggests it is of intermediate mass. However if it is not a YSO, then clump 2 would be devoid of signs of ongoing

star formation. Such a clump may be the precursor to clumps currently forming stars or may already contain a massive YSO at an earlier evolutionary state than can be detected in the near/mid IR. Such a clump could be an observational target for surveys of 'Class 0' massive YSOs in the LMC.

Clump 3, located ~20" north of clump 1, is YSO-less and has an estimated luminosity mass of $7.0 \pm 1.7 \times 10^2$ $M_\odot$. However, a possible YSO – 051317.54–692208.5 – is located just outside the border of the clump. Like 051317.30–692236.7, due to its lack of an 8 μm point source this YSO was only detected by W08. If this is a true YSO, the nearby clump may be the remnant left over from its formation. North of clump 3 is clump 4, which contains the massive YSO candidate 051319.14–692151.0 of the PE spectral group. East of clump 4 is the YSO candidate 051320.75-692151.4. YSOs 051318.26–692145.5 and 051315.73-692135.9 are located at the northernmost extent of the 50% sensitivity of our *ATCA* observations and do not appear to be located within a clump. Source 051318.26–692145.5 is the only YSO within the *ATCA* observed region that has both a near-IR and an optical counterpart, consistent with its location outside of a dense, obscuring clump. Similarly, 051315.73-692135.9 has coincident JHK point sources which would not be expected of a deeply embedded YSO.

Just as the brightest cm continuum source in N113 is located within a clump (clump 1), so too are the other two brightest cm continuum sources. One is located on the edge of clump 5 which has a virial mass of $7.3 \pm 1.5 \times 10^3$ $M_\odot$, and the other is coincident with clump 6 of virial mass $3.1 \pm 0.5 \times 10^3$ $M_\odot$. Each continuum source also has an associated IR-identified YSO –

051321.43–692241.5 and 051325.09–692245.1 in clumps 5 and 6, respectively. However, YSO 051321.43–692241.5 in clump 5 is notably offset from the continuum source and a corresponding compact Hα source by ~4" (labeled B in Oliveira et al. 2006). Moreover, in near-IR JHK band images, a point source can be seen at the center of the small Hα blob. These signs suggest that the YSO may not be the ionizing source. This is in contrast with the YSO in clump 6 which is precisely coincident with both the continuum source and a compact source of Hα emission (GC09).

4.4.3 N159

The HII complex N159 has three large molecular clouds, each about 30–50 pc in diameter. As evidenced by their differing levels of ionized gas, the northern two clouds (here called the eastern and western clouds) have undergone significantly more star formation within the last few million than has the southern cloud (Chen et al. 2010). Star formation within the eastern cloud appears to have been occurring for a longer period of time than in the western cloud: while stars within the eastern cloud have ages ranging between $< 3 - 10$ Myrs (Farina et al. 2009), the absence of supernova remnants in the western cloud suggests star formation has only begun with the last 5 Myrs (Chen et al. 2010 and references therein). N159A, the region with the highest Hα surface brightness in N159, is located at the central peak of the western cloud. Two other very bright compact HII regions, N159AN and the Papillon (named for its physical similarity to a butterfly shape) are located in the western and eastern clouds, respectively. N159A, N159AN, and the Papillon are also the brightest objects in the *Spitzer* IRAC passbands (see Figure 16).

N159AN is located within clump 7, the most massive in N159 with a virial mass of 2.6 ± 0.2 × 10^4 $M_\odot$. CPROPS determines a radius of 2.5 pc, however the clump is highly elongated and has a 2:1 major to minor axis ratio. Clump 7 has two emission peaks, however because the peaks share significant emission, CPROPS identifies them as a single clump. The two peaks' central velocities are separated by ~1 km/sec and there is some evidence of a small velocity gradient across the clump. Combined, this velocity structure has the effect of overestimating the virial mass. Using the mass-HCO+ integrated flux density relation from Section 4.3.2, we find a smaller mass of 1.8 ± 0.3 × 10^4 $M_\odot$, ~70% of the virial estimate. Each peak in clump 7 is coincident with a YSO candidate. The northern peak contains YSO 053937.56-694525.3 with a IRS spectral type in the PE group. The presence of fine-structure lines in its mid-IR spectrum is consistent with the the presence of the HII region that is seen as a compact 5 GHz continuum source (Jones et al. 2005), however there is no Hα emission towards the source. The lack of Hα emission towards a definite HII region implies that the HII region is located behind or within the dense molecular clump. Martin-Hernandez et al. (2005) estimates from its cm emission that the HII region is powered by an object(s) with the ionizing flux of two O4 or O5 stars. YSO 053937.56-694525.3 is also coincident with an OH maser (Brooks & Whiteoak 1997). The southern peak of clump 7 contains massive YSO candidate 053937.04-694536.7. Like the other YSO in the clump, 053937.04-694536.7 is embedded in the clump deep enough that it is not visible at near-IR wavelengths. In a recent study of deep mid-IR *Spitzer* images of N159, Chen et al. (2010) estimated the YSO has a mass of ~29 $M_\odot$ and is in evolutionary Stage I, which is

defined physically as a YSO surrounded by a thick envelope of material. Jones et al. (2005), based on their IRAC colors, classified 053937.04-694536.7 a 'Class I' YSO and 053937.56-694525.3 as an HII region.

South of N159AN is N159A, which breaks into two separate peaks in the 5 GHz map (Hunt & Whiteoak 1994). The western peak is coincident with the YSO candidate 053935.99-694604.1, explaining the fine-structure lines in its spectrum. Jones et al. (2005) classifies the source, which is located immediately outside of clump 1, as an HII region. To the southeast of 053935.99-694604.1 within clump 1 is YSO candidate 053937.53-694609.8. The YSO is likely powering the coincident HII region seen in the radio continuum images. Indebetouw et al. (2004) estimates it has the ionizing flux output of an O7–7.5 V star. Connected to clump 1 is the low-mass clump 2, which is separated from clump 1 in velocity space by ~5 km/sec. A velocity slice through clump 2 indicates its low level (~2σ) of HCO^+ emission has a large spread in velocity, much of which overlaps with the velocity of clump 1. Clump 2 may be part of clump 1 or may be part of a flow of gas into the higher-mass clump 2. If clump 2 is truly part of clump 1, then clump 1's mass may be underestimated; however, the difference is negligible because the level of emission associated with clump 2 is so low. YSO 053941.89-694612.0 is located near the eastern 5 GHz peak in N159A, but is not coincident with it. The second YSO candidate identified in N159, is often referred to as P2 in the literature (Jones et al. 1986). The exact nature of this source is under debate. Jones et al. (2005) concludes from its IRAC colors that it is a 'Class I' YSO but not an O-type star. However, some authors claim the YSO is associated with the nearby HII region (e.g., Nakajima et al. 2005). Chen et al. (2010) finds that its SED can be fit with a

massive YSO with a central star of mass M = ~34 $M_{\odot}$. It is the second brightest IR source in N159 ([8.0] = 5.93) and is almost certainly a high-mass YSO.

Just south of N159A and located within the small clump 9 is YSO 053940.78-694632.1. North of N159A is YSO 053943.74-694540.3, which was identified as a Type III YSO by Chen et al. (2010). Type III YSOs have significant optical emission from a point source, meaning there cannot be significant intervening material. Indeed, we do not identify a dense clump at the position of the YSO. However, the *ATCA* data indicates there may be a very low level (~1.5σ) of diffuse HCO^+ emission in the area immediately surrounding the YSO.

Located within clump 3 is YSO 053929.21-694719.0, labeled source 2.1 in Jones et al. (2005) who identifies it as a YSO with a possible circumstellar disk and a small HII region. The YSO is located very close to a second source named 3.1 in Jones et al. (2005) which they state is coincident with an H_2O maser. However, the position of the maser was from unpublished data (Hunt & Whiteoak 1994), and in a later study by Lazendic et al. (2002), the maser's position was updated to be coincident with the YSO, indicating the maser is most likely associated with the YSO and not the neighboring source. Source 3.1 from Jones et al. (2005) is more likely the B0 V star that is located within a small emission nebula located 3" southeast of the maser (Deharveng & Caplan 1992).

Also called P1, YSO 053959.34-694526.3 is very isolated compared to those in N159A and N159AN. It is not located within a clump, explaining its relatively blue mid-IR color Jones et al. (2005) and its coincidence with a JHK point source (Chen et al. 2010). At the northwestern

side of our *ATCA* observations are clumps 12 and 13, both of relatively low masses of ~10^3 $M_\odot$. The two clumps share significant emission and their centers are only separated in velocity space by <1 km/sec. Their combined shape is reminiscent of a filament such that they may be better described as a single clump with an estimated mass of ~2.6 × 10^3 $M_\odot$. While they are both YSO-less, just north of the clumps is YSO 053945.18-694450.4, perhaps a former resident of the clump. Two more clumps without YSOs are located in the east – clumps 8 and 10. Like clumps 12 and 13, they have relatively low masses.

One of the most studied objects in N159 is the Papillon, a butterfly-shaped HII region located on the northeastern side of N159. Several studies have identified an infrared source at the Papillon, YSO 054004.40-694437.6 (GC09; Chen et al. 2010). The Papillon also is a strong Hα and 5 GHz source, indicating that it is not as embedded as N159AN and may in actuality be located in front of clump 5. A YSO that is not as embedded in its natal clump is presumably more evolved, and the fact that the YSO is not located at the emission peak of the clump further supports its evolved nature (see Section 4.5.1). The source's non-embedded nature is further supported by the weak strength of the 10 μm silicate feature in its IRS spectrum. We will return to the topic of the relationship between a source's 'embededness' and the strength of the silicate absorption feature in Section 4.5.2. While clump 5 is connected to clumps 4 and 6 in the 0^{th} moment map, each clump is clearly separated from the other in velocity space. To the east of the Papillon is YSO 054009.49-694453.5. While not located in a clump, clump 4 is directly to its west and may be the remnant of the material from which it formed.

In the center of N159 are YSO candidates 053947.68–694526.1, 053951.60–694510.5, and

053952.60–694517.0 – none of which were identified by GC09 or W08. Chen et al. (2010) identifies 053947.68–694526.1 as a Type II YSO, indicating it has a near-IR counterpart, which may be expected from a YSO not obscured by a clump. Sources 053951.60–694510.5 and 053952.60–694517.0 were not identified by GC09 or W08 because they lack a strong IRAC point source. However, they both have strong 24 μm point-like emission, indicating they may be YSOs. Source 053951.60–694510.5 was observed by SL09 and has a spectral classification of PE. Source 053952.60–694517.0 (identified by Chen et al. (2010) as having an optical and near-IR counterpart) is likely associated with source 053952.29–694516.5 (~1" away) that was observed by SL09 because of its strong 24 μm emission and classified spectrally in the P group. The lack of strong IRAC point sources for both these YSO candidates suggests that their spectral classification as having strong fine-structure line and/or PAH emission is a result of their environments and may not reflect the presence of a PDR or HII region.

4.4.4 N44

We imaged two separate sections of the HII complex N44: one mosaic is centered on the core of the central molecular cloud peak while the second is of the southern molecular cloud peak. The central molecular peak is associated with a large, bright Hα shell rimmed with numerous HII regions. Star formation has been occurring within the central peak for an extended amount time; the center of the supershell contains stars of ages ~10 Myrs and the surrounding HII regions contain massive stars ~5 years old (Oey & Massey 1995; Chen et al. 2009 and references therein). The smaller spatial extent of the Hα emission in the southern peak and the

lack of any supershells suggests that star formation has only started in the last few million years in the southern part of N44 (Chen et al. 2009).

The *ATCA*-imaged region of the central molecular peak contains a total of 8 clumps, many of them containing massive and intermediate-mass YSOs. The southern-most is clump 3 which contains the highly embedded YSO 052212.57–675832.4. Its IRS spectrum contains the prominent 15.2 μm CO_2 ice feature indicating it is embedded in significant cold, dense material. Indebetouw et al. (2004) identified an ultracompact HII region (B0522–5800) that is coincident with the YSO, consistent with the fine-structure lines seen in its mid-IR spectrum.

Clump 6 contains intermediate-mass ([8.0] > 8) YSO 052207.32-675826.8 and has high-mass YSO 052207.27-675819.7 at its edge. Chen et al. (2009) made note of the HII region around source 052207.27-675819.7 and determined it has an electron density lower than would be expected for a compact HII region. Combined with the fact that the YSO is visible at optical wavelengths, this suggests that it is a more advanced stage YSO. Clump 5 contains two YSOs with [8.0] > 8.0 (052211.86–675818.1 and 052212.24–675813.2), but whose SEDs can be fit with stars between ~5 and 25 $M_\odot$. The nearby lower-mass clump 4 contains a single intermediate mass YSO – 052208.6–675805.5.

The IRAC images of clumps 1, 2.1, and 2.2 appear to have many point-like sources, however many of these have SEDs more consistent with those of dust clumps. While GC09 only identifies two YSO candidates within the clump complex, Chen et al. (2009), who used slightly relaxed selection criteria, identified several more. As many as a half dozen YSOs may be located within and immediately outside of clumps 1, 2.1, and 2.2. The northern most clump is clump 7,

which does not contain any YSOs.

Farther north of all the clumps is YSO 052159.6–675721.7. Consistent with its location outside of a clump, the YSO is visible at optical wavelengths and is a Type III YSO according to (Chen et al. 2009), meaning its optical photosphere is visible. Using fits of its SED to radiation transfer models (Robitaille et al. 2006), Chen et al. (2009) determined that the YSO must have evacuated its surrounding to a distance of at least 1000 AU. At the northernmost extent of our *ATCA* observations, are two YSOs not located within clumps – 052206.28–675659.1 and 052156.97–675700.1. Both are visible at near-IR wavelengths, and 052156.97–675700.1 is even visible in the optical. We find the expected trend that YSOs not in clumps tend to be visible at wavelengths short of the mid-IR; we will explore this further in the following section.

In Region 2 of N44, there are 6 total clumps, all of them of relatively low mass, size, and surface brightness. Clumps 1, 2, and 6 do not contain YSOs. Like several clump pairs identified above, clumps 1 and 6 appear attached in the 0^{th} moment map, but their centers are separated by ~2 km/sec in velocity space. To the west of clump 6 is YSO candidate 052251.62–680436.6. Farther north are clumps 3 and 4 which contain a number of YSOs: 052255.12–680409.4, 052256.79–680406.8, and 052257.55–680414.1. Being located within the clumps, none of these three are visible at optical wavelengths. Clump 5 contains YSO 052259.0–680346.3, which with a [8.0] of 10.46, is the least luminous YSO in any of the HII complexes studied here. Indeed, its SED is best fit by a YSO with a central stellar mass of only 6 $M_{\odot}$.

4.5 Discussion

In this study we have targeted the densest peaks of the molecular clouds of known star forming regions and have identified a total of 38 dense molecular clumps form their HCO^+ emission. The images of these regions along with the derived properties of the clumps have been presented above. Of these 38 clumps, 25 contain what have been identified as YSOs within their borders, 5 of those with associated maser emission. As described above, we have classified the YSOs into two broad mass categories based upon their 8.0 μm magnitudes, as it has been suggested that it may be a good proxy for the stellar mass. Of the 25 clumps containing YSOs, 18 have at least 1 high-mass YSO ([8.0] < 8), while the others have only intermediate mass ([8.0] > 8.0) YSOs.

In a number of cases, the YSO positions as determined from their mid-IR emission is well offset from the emission peak of the clump determined from the 0^{th} moment map of the HCO^+ emission but is still located within the contours of the clump. Recent modeling has shown that massive YSOs will form at the densest centers of their natal parsec scale clouds, so the YSOs significantly offset from the core of the clump are presumably more evolved than those more coincident with the core. Hill et al. (2005) noted several Galactic massive star-bearing cores/clumps with star formation tracers that are offset from the peak of the cloud, but find no evolutionary correlation with the distance between the star formation tracer and the clump's emission peak. However, because the clumps they studied have sizes that range between ~0.1–2 pc, the distance between the clump centers and the YSO may simply reflect the size of the clump as a whole. In other words, small YSO-bearing clumps will necessarily have YSOs close to their

centers. To remove the dependence on clump size, we have determined a 'closeness factor' that takes into account both the projected YSO-clump center distance and the size of the clump. The closeness factor, d, is defined as

$$d = C / (C + E) ,$$

where C is the distance between the YSO and the clump center and E is the distance between the YSO and the nearest edge of the clump. Under this definition, YSOs at the emission peak of a clump have closeness factors of 0, while YSOs located directly on the edge have closeness factors of 1. We define the edge of the clump as the outermost extent of a clump's emission $>2\sigma_{noise}$. Remember that the edge of a clump may not be a discrete entity, and is likely dependent on the sensitivity of the observation. Several clumps have YSOs located directly outside their 2σ detection threshold; such sources may be examples of YSOs located within a more diffuse clump "envelope" below the 2σ threshold. For YSOs located outside of clumps, we have determined the closeness factor to the nearest clump. For such a case, E is negative, making $d > 1$. For clumps containing more than one central peak, Table 9 reports the smallest value of d.

The HCO^+ clumps detected in this survey comprise four distinct classes:

1. **YSO-less clumps:** clumps with no indications of recent star formation.
2. **Intermediate-mass YSO clumps:** clumps containing ($d \leq 1.0$) at least one intermediate mass YSO and no high-mass YSOs.

3. **Centralized high-mass YSO clumps:** clumps containing at least one massive YSO that is closer to the clump's center than its edge, i.e. $d \leq 0.5$.
4. **Off-center high-mass YSO clumps:** clumps with at least one massive YSO that is close to the clump's edge, i.e. $0.5 < d \leq 2.0$ and no YSOs with $d \leq 0.5$.

In Section 4.5.1, we compare the properties of the clumps within each of these classes.

Our hypothesis that a YSO located near the center of a clump is evolutionarily younger than those located near the clump edge is supported by the finding that most YSOs with maser emission, associated with the very early stages of massive YSO evolution (see reviews by Ellingsen 2004; Fish 2007), are located at the center of their clumps .

4.5.1 Distribution of Clump Properties

The histograms showing the virial mass distributions between the different types of clumps (Figure 20) show that the starless clumps are in general less massive than those associated with current star formation. The clumps without YSOs have a mass range of 3.6×10^2 – 2.6×10^3 $M_\odot$ and a mean and median mass of 1.1×10^3 and 7.5×10^2 $M_\odot$, respectively. Compare this to the mean and median mass of YSO-bearing clumps of 4.9×10^3 and 3.9×10^3 $M_\odot$. The Kolmogorov-Smirnov Test rejects that the clumps with high-mass YSOs (both deeply embedded and on the edges) come from the same mass distribution to a 4% and 7% confidence level for CM and EM clumps, respectively. Note also that the two most massive clumps – N113's

clump 1 and N159's clump 7 – contain massive YSOs; N159's clump 7 contains 2.

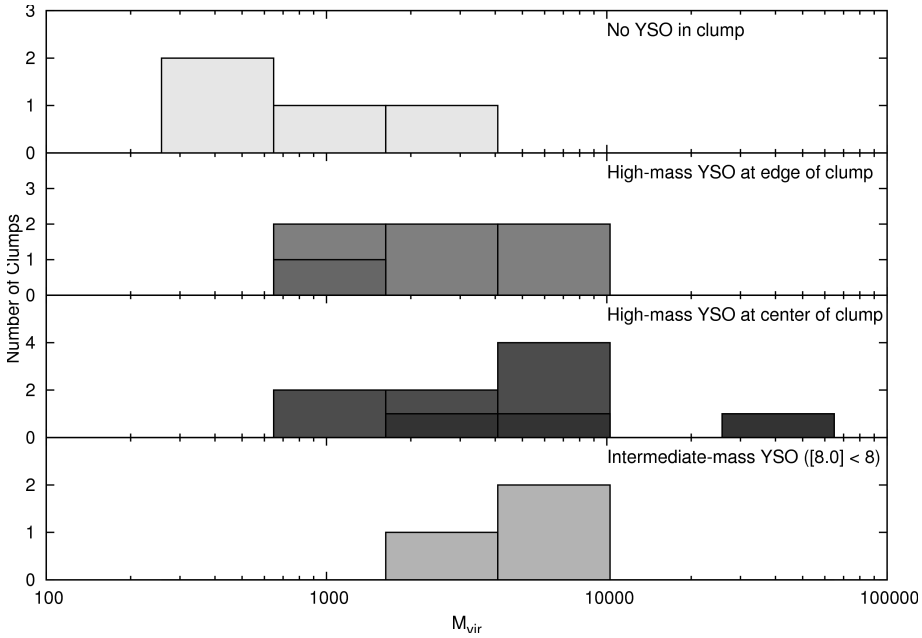

Figure 20. The distribution of masses for the HCO+ clumps found in the HII complexes. The histograms show the distribution for the four different categories of clumps: (i) those without massive or intermediate YSOs; (ii) clumps with massive YSOs at their edge, but not in their their centers; (iii) those with massive YSOs located near their centers; and (iv) those containing only intermediate mass YSOs. The clumps without YSOs are generally less massive than those with; the Kolmogorov-Smirnov test indicates that the clumps with centralized massive YSOs represent a different distribution of sources than YSO-less clumps to a 4% confidence level, while edge-YSO clumps differ from YSO-less clumps to a 7% confidence level. YSO-containing clumps also associated with masers are represented with a darker shade in the histogram than those without.

The finding of lower masses associated with these YSO-less HCO^+ cores is reminiscent of the findings of Hill et al. (2005), who studied a large sample of Galactic, 0.1-2 pc-sized 'cores' in massive star formation regions. Using 1.2-mm continuum observations to detect cold, dense gas, they found that cores without maser or UCHII emission (their primary tracer of star

formation) have median masses of 2.8×10^2 $M_\odot$, while cores with either masers or UCHII regions have a median mass of 1.0×10^3. They also find that within their sample, clumps without star formation are on average smaller in size than those with. Because we are unable to determine the size of many of our sources, the average size of the clumps in our sample is less secure; however we also find that starless clumps tend to be smaller than those with YSOs. Moreover, while ~30% of the YSO-bearing clumps cannot be deconvolved with the beam, ~70% of the YSO-less clumps cannot be, again suggesting starless clumps tend to have smaller sizes.

How exactly the YSO-less clumps fit into the picture of star formation is unclear (Burton et al. 2005). One possibility is that they are the evolutionary precursors to the clumps actively forming stars. They may represent the earliest stages of massive star formation, before the formation of a YSO massive enough to have been detected in any LMC YSO surveys. In this case, their lower masses could be attributable to their youth, and they may grow in size and mass as they accumulate more material from the molecular cloud in which they reside.

Alternatively, it may be that these cores are never destined to form stars, in which case there is something inherent about the clumps that do form stars that allows them to do so. If the latter explanation is true, then it would appear that the mass of a clump is directly related to the maximum mass of the star that it can form. This is certainly true to a certain extent as a star could never form with a mass larger than its natal clump; however the correlation may be more complex because we find that even the least massive clumps in this study have ample material to form a massive star.

Distinguishing the two scenarios (starless clumps are young future YSO-bearing clumps

or will never form massive stars) is difficult, and it may be that both hypothesis are true. For example, clump 12 of N159 is just as massive if not more so than several of the clumps currently harboring massive YSOs, suggesting it could eventually form a star. Given the dearth of low-mass clumps with YSOs, clumps with masses of only a few 10^2 $M_\odot$ may never form massive stars at all.

We suggest that there is a third possibility as to the nature of the starless clumps. It is possible that a low-mass clump will eventually form a massive star, but the clump is so quickly dispersed after the formation of the star that a low-mass clump containing a massive YSO is simply observationally rare. The number of clumps considered in this study is too small to detect a rare object with any regularity, however the (Hill et al. 2005) study of several hundred Galactic clumps does indeed find a number of clumps with maser emission at masses of only a few hundred solar masses. This hypothesis could be supported by the fact that in the same study, they found that clumps with CHII regions have a larger average mass than those with only maser emission and no CHII region. It is possible that the lower mass clumps were destroyed by the YSO through a combination of strong winds and ionizing radiation and is no longer detectable once the YSO reaches the CHII region phase, which would cause the higher average clump mass for clumps with CHII regions. Kawamura & Masson (1998), in a study of the well-known massive star formation region W3(OH), determined that its UCHII region is expanding at a rate of ~3 km/sec from either radiation pressure, stellar winds, or both. Assuming a constant expansion velocity, an HII region such as this could destroy a 0.1 pc clump in maybe several 10^4 yrs. Recent theoretical modeling of the expansion of a CHII region in a clump-fed environment

has found a larger time scale of a few 10^5 yrs for a CHII region to reach 0.1 pc sizes. A less dense or smaller clump would be destroyed even faster. We will further consider the role of a massive star in dispersing its natal clump in the following section.

4.5.2 The Time Scale of Clump Disruption

Along with a correlation between the mass of a clump and the presence or absence of a YSO, there appears to be a correlation between the location of a YSO within the clump and the clump's properties. While the sample size is small, clumps with YSOs more centrally located appear to generally have larger masses than clumps with YSOs closer to their edges. The correlation between clump characteristics and YSO positions is even more apparent in Figure 21, which shows the distribution of HCO^+ integrated flux densities for the clumps. Recall that the HCO^+ luminosity should – at least to first order – be a proxy for the mass of a clump. The correlation is also apparent in the integrated HCN flux density of the clumps (Figure 22); all clumps with centrally-located YSOs have high HCN integrated flux densities. On the other hand, little to no HCN is detected towards starless clumps, clumps with intermediate mass YSOs, or clumps with massive YSOs on the edges. Kolmogorov-Smirnov tests indicates that the the HCO^+ and HCN flux distributions for clumps with a central YSO are different than those of edge YSO clumps to a 2.5% confidence level, and different than clumps with no YSOs to a <1% confidence level.

Presumably, the massive YSOs formed at an emission peak, where the clump densities were high and a core collapsed to form the star. Indeed, recall that we find that nearly all the

maser-associated YSOs, likely the youngest in our sample, are located very close to their clumps' peaks. YSOs located at the edges of a clump therefore may represent more advanced stages of evolution; the YSOs have either moved away from the dense cores they formed in or have dissipated their immediate surroundings, leaving only the part of the clump far enough away to have not been destroyed.

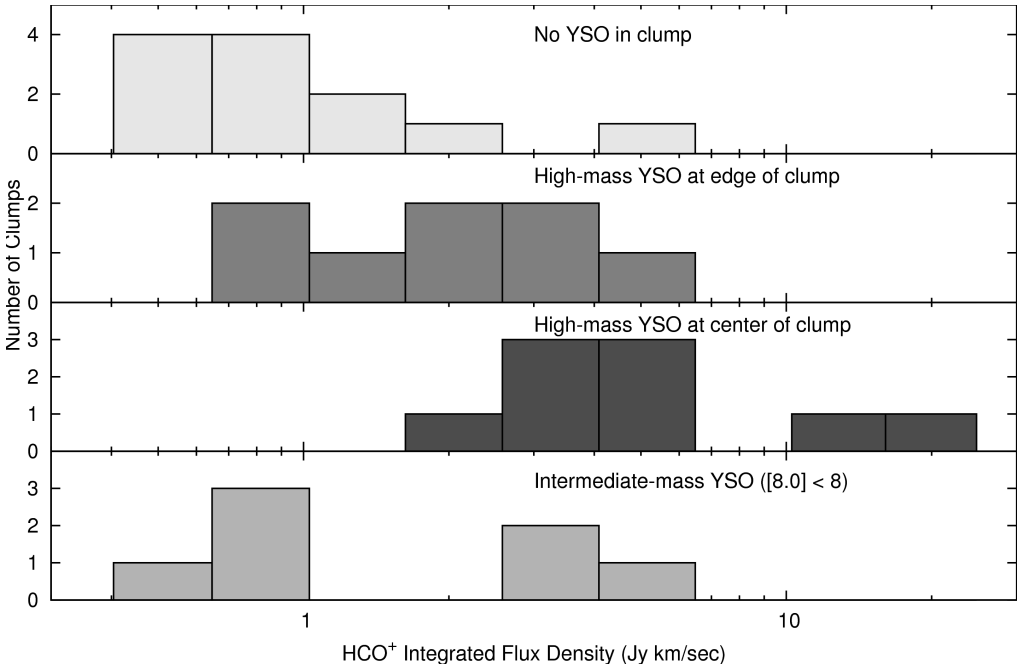

Figure 21. The distribution of HCO+ integrated flux densities for the clumps.

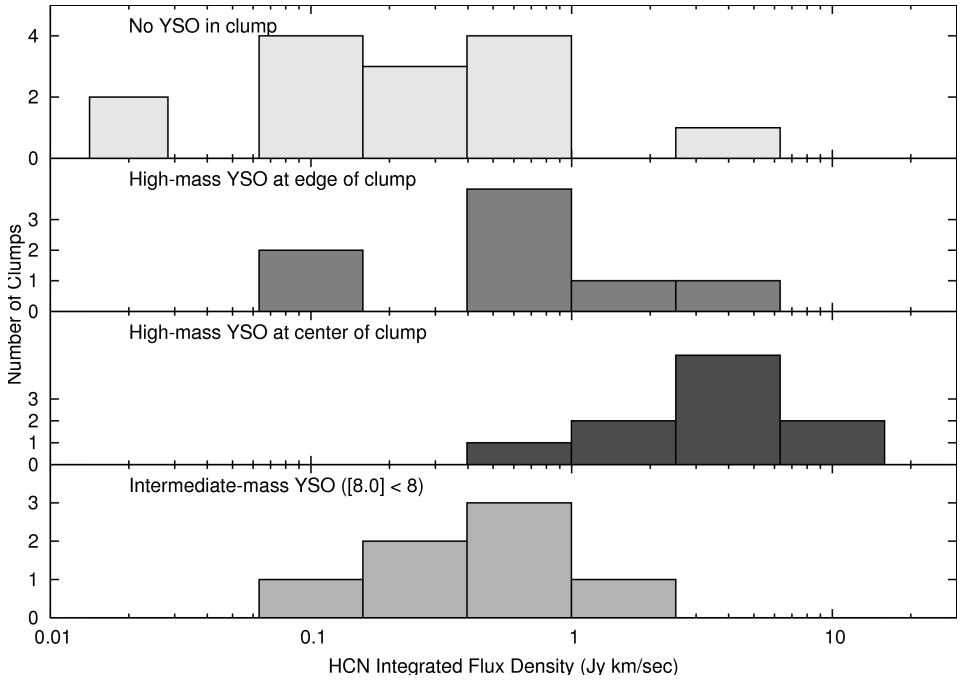

Figure 22. Same as Figure 21, but for HCN.

The different distributions of masses suggest that clump edge YSOs have destroyed a portion of their natal clumps. Clumps with YSOs at their centers have an average luminosity mass of ~6 × 10^3 $M_\odot$ while those with YSOs at their edges have an average luminosity mass of ~2 × 10^3 $M_\odot$, suggesting that by the time a YSO is at the edge of its clump, it has dissipated ~2/3 of clump. Because HCN is tracing the inner, denser region of the clump, the close association of YSO location with HCN intensity suggests that the disruption occurs from the inside, most likely from the YSO's strong stellar winds and ionizing radiation. In fact, the HCN / HCO^+ ratio for central YSO and edge YSO clumps is significantly differnet; clumps with YSOs

at their centers have an average HCN / HCO^+ ratio of over 0.4, while those with YSOs at their edge have an average of only ~0.2. This suggests the HCN / HCO^+ ratio may be a good indicator of clump density and therefore the evolutionary state of its YSO population.

Figure 23 shows the distribution of HCO^+ velocity dispersions for the four categories of YSO. Similar to the distributions of clump mass and integrated flux density, clumps with centralized YSOs appear to have higher velocity dispersions than clumps with YSOs only at their edges, however the Kolmogorov-Smirnoz test indicates the hypothesis they are from the same distribution can only be rejected to a 24% confidence level. The finding is not surprising given that the velocity dispersion should correlate with the virial mass. Massive YSOs are presumed to inject energy and turbulence into their natal clumps. Evidence for an increase of clump turbulence has been suggested as the reason for larger velocity dispersions in YSO-bearing clumps compared to infrared dark clouds, the suspected precursors to star-forming clumps and cores (e.g., Menten et al. 2005). If clumps with edge YSOs are indeed in a later stage of evolution than those with YSOs at their centers, and the YSO location-clump velocity dispersion relation difference implied by Figure 23 is true, then the edge YSO clumps previously had higher velocity dispersions when the YSOs were located at their centers. Figure 23 may suggest that once a YSO is located at the edge of a clump, it is not able to inject sufficient energy into the clump to maintain the same level of turbulence it had previously. Without a source of extra turbulent energy, the clump dissipates its internal mechanical energy. The velocity dispersion of clumps without and with YSOs at both their centers and edges have velocity dispersions consistent with what would be expected from their luminosity masses, i.e. Δv is positively correlated with

F_{HCO^+}. The velocity dispersion appears to be unrelated to the stellar content, and dependent only on a clump's mass.

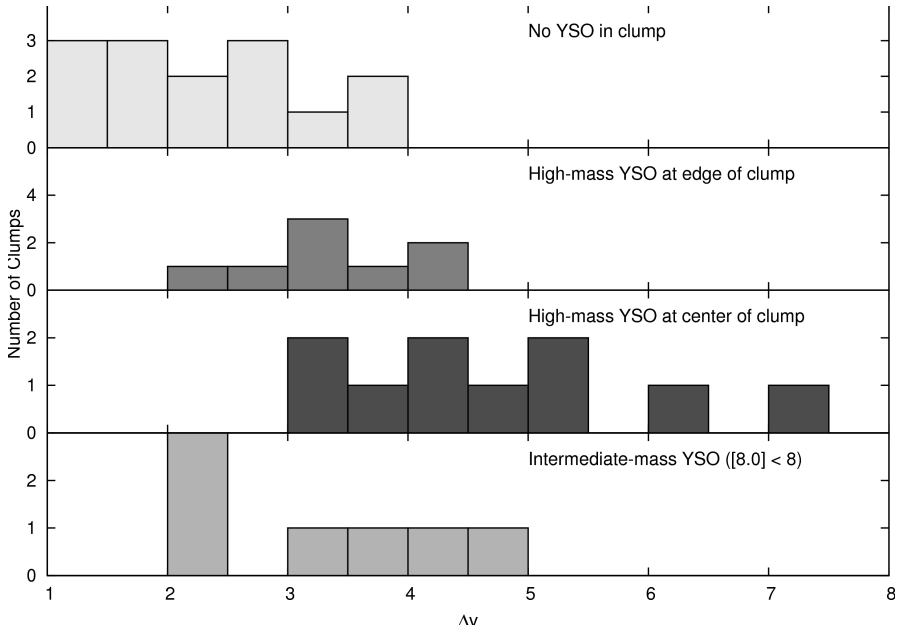

Figure 23. The distribution of HCO^+ Δv for the clumps. Panels are as in Figure 21.

As we noted in Section 4.4, there are a number of YSOs within our *ATCA* imaged area that are not located within dense clumps. Or, said more precisely, are *no longer* located within dense clumps, as they were certainly earlier formed within one. YSOs not located within clumps therefore represent the more advanced stages of YSO evolution after a YSO has dissipated its dense surroundings. Indeed, we find that the YSOs located outside clumps tend to be visible at near-IR and even optical wavelengths. YSOs visible at short wavelengths are classified as Type II and Type III YSO (defined by Chen et al. 2009). Conversely, most sources in clumps are Type I/II sources, not visible at optical wavelengths. We find that the Type classification scheme is very well correlated with the location of a YSO in a dense molecular clump and is a good indicator of

a source's 'embeddedness.'

SL09 suggests that the silicate absorption feature at 10 μm and seen in *Spitzer* IRS spectra may be a good evolutionary indicator for massive YSOs. The feature originates from silicate-bearing dust particles in a YSO's circumstellar material that absorb the thermal emission from circumstellar dust warmed by the central star. In time, the YSO dissipates its surroundings, removing circumstellar gas and dust, and thus weakening the strength of the silicate absorption feature. Many of the YSOs in this study were observed in SL09, who determined the strength of the silicate feature using the statistical method of principal component analysis (PCA). In Table 9, we list the PCA-determined strength of the silicate feature for all sources observed in SL09 and within the field of view of our *ATCA* data. The entire SL09 massive YSO spectral catalog has sources which range in silicate strength from -0.8 (very weak) to 0.7 (very strong). The range within our subsample is slightly smaller, but spans a range with both weak and strong features. SL09 notes that the silicate feature is heavily blended with numerous PAH features that saddle the 10 μm dip; this may have the effect of confusing strong PAH emission with a deep silicate feature during PCA, so the values are indicative only.

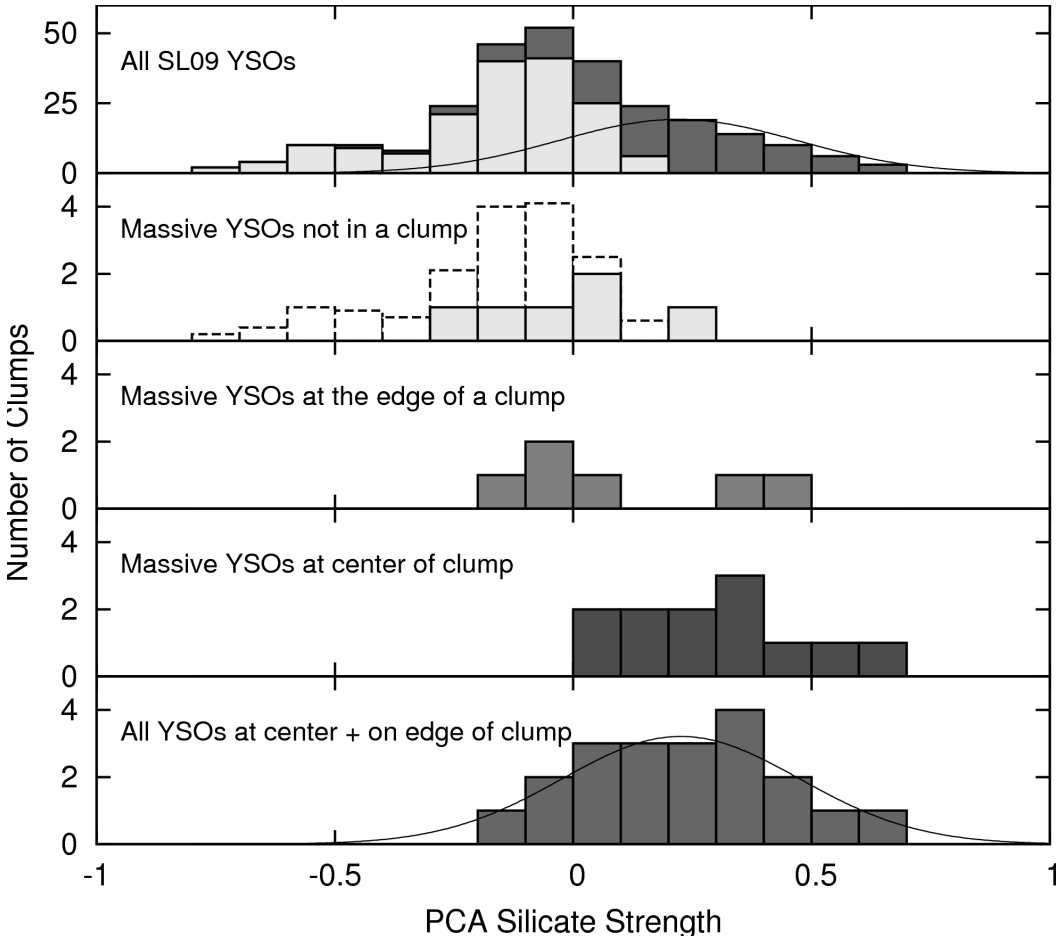

Figure 24. Distribution of the strength of the 10 μm silicate feature as determined by PCA for the YSOs contained within the observed areas of N105, N113, N159, and N44 (bottom panels) compared to the distribution for all massive YSOs for which SL09 has Spitzer IRS spectra (top panel). The bottom panel shows the distribution for YSOs in the observed regions that are located within ($d \leq 0.5$) or on the edge ($0.5 < d \leq 1.0$) of a clump along with a Gaussian fit to the distribution. The top panel shows a fit of this clump-confined Gaussian to the total distribution's high-strength wing. After subtracting the total distribution from the fit of the clump-confined distribution (represented in dark grey), the remaining distribution (60%, light grey) is attributed to the YSOs outside of clumps. The inferred distribution of silicate strengths for YSOs outside of clumps is recreated in the second from the top panel (dotted line), and shows that the observed distribution is consistent with that inferred.

Figure 24 shows the distribution of PCA silicate strengths for YSOs within ($d \leq 0.5$), on the edge of ($0.5 < d \leq 1$), and outside of ($d > 1$) a clump. The silicate feature appears strongest from sources that are located centrally within a clump; all YSOs with $d \leq 0.5$ have PCA silicate strengths > 0. This is in contrast with the YSOs located outside of clumps: half of their members have silicate strengths < 0. Figure 25 plots the silicate strength for each source as a function of the HCO^+ integrated flux density at the position of the YSO, and there is clearly a correlation. This is highly suggestive that the origin of the silicate feature is related to the dense HCO^+ clumps. In fact, the silicate absorption may be originating from dust on the same scale as the clumps. Unlike interstellar ices, silicates do not require cold, dense, radiation shielded environments; they are detected even towards diffuse interstellar clouds (e.g., Bowey et al. 1998). The silicates contributing to the 10 μm feature may not be isolated to the YSO's immediate core or envelope of accreting material, and may also reside in the parsec-scale clump. Whitney et al. (2003a,b) has recently developed a widely-used radiation transfer modeling code to fit the SEDs of both low- and high-mass YSOs. Because the silicate feature is among the more prominent and deep IR spectral features of YSOs, the (Whitney et al. 2003a,Whitney et al. 2003b) code takes into account the presence of silicate particles in order to fit observations. Robitaille et al. (2006) used the code to create an extensive catalog of YSO SEDs spanning a range of YSO properties (stellar mass, envelope mass and radius, etc.) and evolutionary stages; the catalog and corresponding SED-fitting routine is commonly used today to estimate the properties of both high and low mass stars (e.g., Seale & Looney 2008; Chen et al. 2009; Chen et al. 2010). However, the radii of the massive YSO's 'dust cocoon' has been restricted to <0.5 pc, a value that

the data presented here suggests may need to be revised to include the larger, parsec-size dense molecular material.

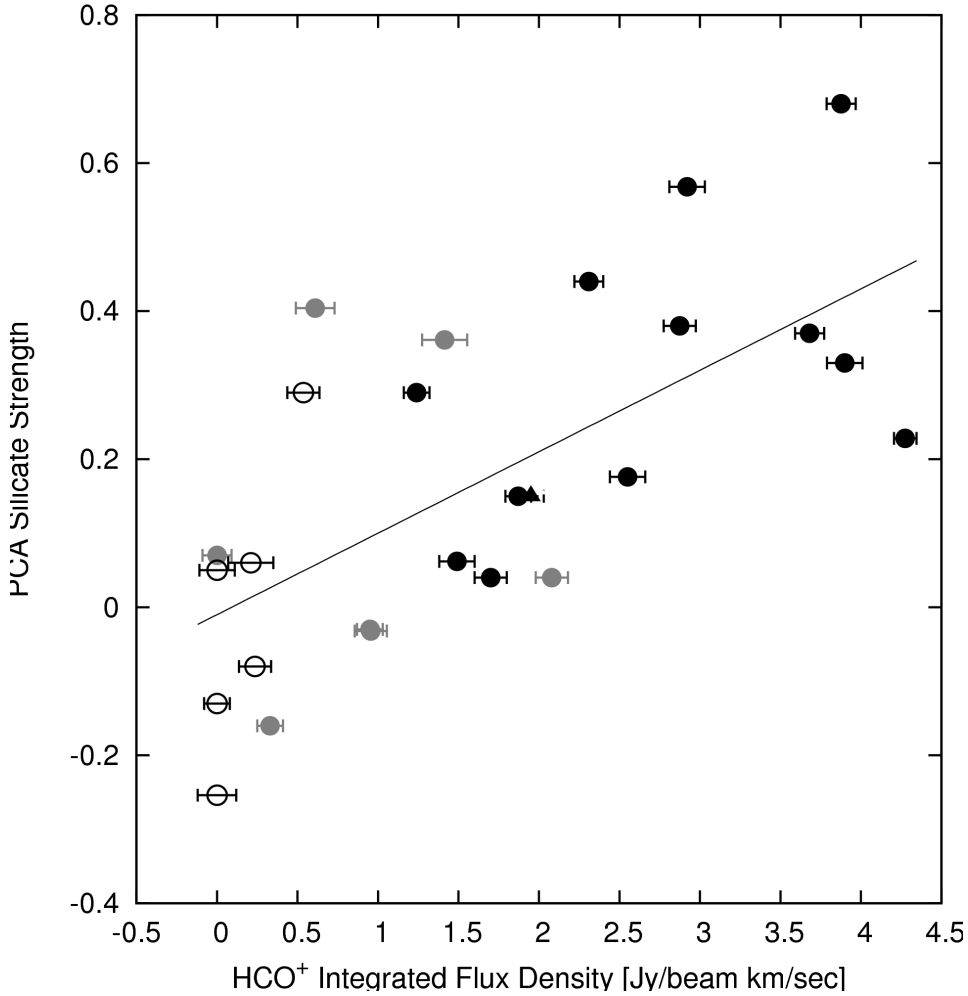

Figure 25. PCA silicate strengths for the YSOs in our ATCA imaged area as a function of on-source HCO+ integrated flux density. Symbols are as in Figure 19. The line is a linear fit to the data given by PCA Silicate Strength = 0.11 $F_{\mathrm{HCO+}}$ – 0.01, where $F_{\mathrm{HCO+}}$ is the integrated flux density on the source in Jy/beam km/sec.

The top panel of Figure 24 shows the PCA silicate strength distribution for all massive YSOs in the SL09 catalog. The SL09 IRS spectral catalog consists of nearly every YSO in the

LMC that meets the criteria for being a candidate YSO in the GC09 catalog and has [8.0] < 8.0. GC09 identified YSOs via their IRAC photometry, meaning SL09 does not have the spectra for YSOs outside of the GC09 color criterion. Because they are too dim in the IRAC bands, GC09 likely misses the most embedded, youngest YSOs. To target only the reddest objects in the LMC and to exclude such contaminants as main-sequence and AGB stars, a color criterion of [4.5]–[8.0] > 2.0 was set for candidate YSOs. This has the effect of excluding the bluest YSOs from the GC09 and SL09 catalog. Bluer YSOs are suspected to be more evolved YSOs since a YSO should become bluer as it dissipates its surroundings and reveals the central star. The net effect is that GC09 – and therefore SL09 – likely miss both the very earliest and most evolved stages of massive YSO evolution. However both surveys are nearly complete over the color-magnitude space being targeted.

The average silicate strength of the entire SL09 massive YSO catalog is ~0, lower than the average value for YSOs located within or on the edge of clumps (bottom panel; average silicate strength is 0.23). This suggests that a significant fraction of the YSOs in the SL09 catalog are located outside of clumps. Using the distribution of silicate strengths for sources we have observed in dense clumps, we attempt to estimate the number of sources in the SL09 catalog that are within clumps. The distribution for YSOs in clumps is fairly well described by a Gaussian with an average value of 0.2 and a FWHM of 0.25. We find that YSOs not in clumps generally have silicate strengths less than ~0.1. The one exception we found was source 054009.49-694453.5 in N159, which deep *Hubble Space Telescope* and *Spitzer* images show is located at the end of a dust globule reminiscent of the 'elephant trunks' seen in the Milky Way (Frieman

1954). Moreover, the HCO^+ data suggests there is a low level of HCO^+ emission coincident with the source that is too low to be identified as a clump by CPROPS. Indeed, the YSO has the highest on-source HCO^+ integrated flux density of any YSO outside of a clump. We therefore make the assumption that all YSOs with silicate strengths greater than 0.1 are within clumps.

We have fit the distribution of the entire SL09 catalog at silicate strengths greater than 0.1 to the Gaussian distribution for YSOs in clumps, and the Gaussian does a good job of fitting the right-hand wing of the SL09 distribution. Note also that the SL09 distribution appears to have a larger right-hand wing than left-hand wing. This suggests that the entire distribution is composed of two separate distributions, one with a higher average silicate strength than the other. The implied distribution of YSOs not in clumps is represented by the distribution of the entire SL09 catalog minus that of the Gaussian fit (the light grey boxes in the top panel of Figure 24). This distribution is recreated in the second panel from the top with a dotted line to show that the observed distribution of YSOs not in clumps (which is poorly represented observationally) is fairly consistent with what is observed. A Kolmogorov-Smirnov test finds no significant support for the observed and predicted distributions of clump-less YSOs being from different distributions; it rejects the hypothesis that the come from the same distribution only at a 30% confidence level. The observed distribution has a slightly larger average silicate strength than is implied by the total sample, but this may reflect both the low number of observed sources and the fact that we have specifically targeted YSOs in the densest regions of GMCs. This analysis could be greatly enhanced by specifically targeting YSOs with weak silicate absorption features for dense molecular gas observations.

It must also be considered that perhaps the strong and weak silicate strength sources do not all represent an evolutionary sequence from embedded to more evolved and less-embedded sources. It may be that some or many of the weak-silicate sources in the SL09 sample were never in the kind of bright HCO^+ and HCN clumps that could easily be observed with *ATCA*. It would then follow that we are overestimating the total number of YSOs that have evolved out of the clump-embedded stage and have dispersed their circumstellar material.

SL09 proposed an evolutionary sequence using this spectral classification procedure where the youngest sources, presumably still embedded in their natal clouds, had the strongest silicate absorption features. It is suggested in SL09 that sources with PCA silicate strengths of greater than 0.2 are deeply embedded in clumps, while those with weaker PCA strengths are not. Considering the fact that this threshold was established by conducting a by-eye comparison of the calculated PCA silicate strength to the IRS spectra, it is remarkable that the threshold is equal to the average of the Gaussian fit to clump-bound YSOs. However, these results suggest that there are a significant number of YSOs embedded in their natal clouds with silicate strengths under 0.2. Therefore the total number of YSOs still embedded in their natal clumps is likely larger than is implied in SL09 (20%). The Gaussian fit to the entire SL09 catalog presented here suggests that ~40% of all the massive YSOs in SL09 are within clumps.

It is unclear how exactly our results would change if we were to included the LMC YSOs that certainly exist but were not identified by GC09, W08, or SL09. As mentioned above, the primary means of detecting the YSOs is their characteristic mid-IR emission. Very young YSOs are too deeply embedded to emit at these wavelengths. Including these heavily obscured YSOs in

this study would increase the estimated time a YSO spends embedded in the clump. On the other hand, including the bluer, more evolved YSOs excluded from GC09 would have the opposite effect. With these factors in mind, we conclude that a massive YSO spends <40% of its lifetime embedded in its dense natal clump after the point at which it can be detected at mid-IR wavelengths. Said another way, a massive YSO disrupts its circumstellar clump in less than 40% of its lifetime spent visible in the mid-IR. Because many of the YSOs in this study are suspected multiple sources or clusters (GC09; SL09; Chen et al. 2009; Chen et al. 2010) these results have implications for the formation of the cluster. All the cluster members are born of the same clump material, and therefore have a limited time frame in which to form once a massive star has begun to form; the destruction of the clump effectively ceases further massive star formation within the cluster. Determining this timescale quantitatively is difficult because the precise ages of the sources in SL09 are unknown. The youngest observed OB associations in the LMC have ages of only a few million years, which probably can serve as a rough estimate for the age of the oldest massive YSOs in GC09 and SL09. Assuming a galaxy-wide constant LMC star formation rate and a timescale of 3×10^6 yrs to become a visible OB association would suggest that a YSO dissipates its natal molecular clump in c. Note however that this time is highly dependent on the age of the SL09 sample which is highly uncertain. Assuming an SL09 YSO age of 1 Myrs would decrease the clump dissipation time to 4×10^5 yrs. Tan & McKee (2001) simulated the destruction of a 0.1 pc, 10^3 $M_\odot$ clump by a forming cluster, and found a destruction time of 0.3-2 Myrs, depending on the internal 'clumpiness' of the clump, similar to the values we estimate here observationally.

4.6 Summary and Conclusions

We have conducted a survey of the dense molecular material in active star formation regions in the LMC using the *ATCA*. The observations were centered on the peaks of the regions' GMC, where we detect a total of 38 massive, dense molecular clumps. Much of the molecular material is associated with signposts of on-going intermediate and massive star formation including maser emission, compact HII regions, and bright IR point sources. We have categorized the clumps by the extent and nature of their star formation content, and find correlations between the categories and clump properties such as mass, size, and emission line width. Our primary conclusions are summarized below.

- The clumps' masses span several orders of magnitude from a few 10^2 $M_\odot$ to 2×10^4 $M_\odot$ as determined from either the virial theorem or their HCO+ luminosity, and they have radii that range from sub-parsec to ~2 pc.
- The clumps are found to contain varying levels of current star formation, and we classify them into four distinct groups: clumps with no on-going massive star formation, clumps containing only intermediate-mass YSOs, clumps with high-mass YSOs located near their emission peaks, and clumps with high-mass YSO located close to the clump edge.
- Analysis of the clumps without signs of recent or current star formation reveals that they are generally less massive those those containing high-mass YSOs by factors of 3-5. If these YSO-less clumps are never destined to form massive stars, then this suggests that the mass of a cluster's highest mass star(s) is determined by the mass of the clump. This

hypothesis is supported by the lower average mass of intermediate-mass YSO-bearing clumps compared to those with high-mass YSOs.

- Clumps with centrally-located massive YSOs generally have masses about twice that of clumps with massive YSOs only on their edges – virial masses for the two groups have an average value of ~6000 $M_\odot$ and ~3000 $M_\odot$, respectively. We suggest that the difference is evolutionary, with YSOs being born at the centers of clumps and becoming displaced from the clump center with time. Whether the difference is a physical relative movement of the clump and YSO or simply the destruction of the clump material nearest the YSO (or a combination of both) is unclear. This suggests that that YSOs destroy or dissipate their natal clumps, removing ~1/2 of the clump mass by the time it is located at the clump edge.
- There is a strong correlation between the intensity of HCO^+ and HCN emission and the strength of the 10 μm silicate absorption feature seen in the mid-IR spectra of YSOs. Objects located within dense clumps have the strongest silicate features while those outside of clumps show little to no silicate absorption. The suggestion is that the origin of the silicate feature is related to that of the molecular emission. Recent radiation transfer modeling of high-mass YSOs have attributed the silicate feature to dust grains located in the sub-parsec-sized envelopes, dust cocoons, and cores around massive YSOs, but our findings suggest models may need to be modified to account for larger, parsec-scale structures defined by the clumps.
- Using a large sample of massive YSO spectra from the LMC, we estimate from the

strength of the sample's silicate features that a YSO will dissipate its natal clump in less than 40% of its formation time after becoming visible in the mid-IR. Because the time scales involved are uncertain, constraining this dissipation time is difficult, but the observational results appear to be consistent with – certainly within a order of magnitude – the ~10^6 year clump destruction time estimated by theoretical modeling.

4.7 Acknowledgments

This work makes use of data collected by the *Australia Telescope Compact Array*. The Australia Telescope is funded by the Commonwealth of Australia for operation as a National Facility managed by CSIRO. This work is based in part on observations made with the *Spitzer Space Telescope*, which is operated by the Jet Propulsion Laboratory, California Institute of Technology under a contract with NASA. Support for this work was provided by NASA through an award issued by JPL/Caltech.

Chapter 5

Conclusions

5.1 Summary

By studying massive star formation on a galaxy-wide scale, it is possible to determine the stages of massive star formation and even estimate the amount of time a young stellar object (YSO) spends in each of these evolutionary stages. In this thesis, we have used the *Spitzer Space Telescope* to explore the infrared spectral evolution of massive forming stars in the Large Magellanic Cloud. We identified several distinct groups of mid-IR spectra, and have linked these variations in spectral features to stages of massive YSO evolution. The radiation detected by *SST* is the photospheric emission that has been reprocessed by the YSO's circumstellar material. The *Spitzer* spectra therefore can provide information about the nearby ISM, and we have explored how the YSOs in our study modify the surrounding dense material from which they formed.

5.1.1 Infrared Spectral Evolution of a Massive YSO

In Chapter 2, we presented and categorized *Spitzer* IRS spectra of 294 objects in the LMC to create the largest and most complete catalog of massive young stellar object (YSO) spectra in the LMC. Target sources were identified from infrared photometry and multi-

wavelength images indicative of young, massive stars enshrouded in their natal gas and dust clouds. Several objects have been spectroscopically identified as non-YSOs and have features similar to more evolved stars such as red supergiants, asymptotic giant branch (AGB), and post-AGB stars. Our sample primarily consists of 277 objects we identify as having spectral features indicative of embedded YSOs. The remaining sources are comprised of 7 C-rich evolved sources, 8 sources dominated by broad silicate emission, and 1 source with multiple broad emission features.

Those with YSO-like spectra show a range of spectral features including polycyclic aromatic hydrocarbon emission, deep silicate absorption, fine-structure lines, and ice absorption features. Based upon the relative strengths of these features, we have classified the YSO candidates into several distinct categories using the widely-used statistical procedure known as principal component analysis. We proposed that these categories represent a spectrum of evolutionary stages during massive YSO formation. Using our catalog we put statistical constraints on the relative evolutionary timescale of processes involved in massive star formation. We conclude that massive pre-main sequence stars spend a majority (possibly as high as 90%) of their massive, embedded lives emitting in the UV. Half of the sources in our study have features typical of compact HII regions, suggesting that massive YSOs can create a detectable compact HII region half-way through the formation time present in our sample. This study also provides a check on commonly used source-selection procedures including the use of photometry to identify YSOs. We determine a high success rate (> 95%) of identifying objects with YSO-like spectra can be achieved through careful use of infrared color magnitude diagrams, spectral energy

distributions, and image inspections.

5.1.2 Thermal Processing of Circumstellar Ices

We isolated our attention to the CO_2 ice absorption feature at 15.2 μm in Chapter 3 toward a subsample of 41 of the high-mass YSOs. Ices reside in the cold outer regions of a YSOs circumstellar material, and as the shape of the CO_2 absorption profile is a measure of both the composition and thermal history of the ice, we performed a decomposition of the spectral profiles to determine the nature of the CO_2 ice. We fit the absorption profiles to laboratory analogues of ice spectra with two different methods: 1) a 5-component fit with polar and apolar ices and 2) a 2-component fit with a polar and an annealed H_2O:CH_3OH:CO_2 ice mixture. Many of the LMC sources have a pronounced double peak in their CO_2 feature profiles typical of pure CO_2 or annealed CO_2 ice mixtures, and represent the first direct detections of the characteristic double peak in an extragalactic environment. We find that a majority of the CO_2 is embedded in a polar ice matrix, but that there are variations in the spectral shape that likely arise from the degree of the envelope ices' thermal processing. We find some evidence for a correlation between a massive YSO's luminosity and the fraction of circumstellar material that has been thermally processed. In addition, we find evidence for a lower methanol abundance in ices around LMC massive YSOs compared to those in the Galaxy. Finally, we corroborate mounting evidence of an enhanced CO_2 ice abundance in the LMC relative to the Milky Way, and determine a CO_2/H_2O ratio of 0.33 ± 0.01.

5.1.3 Life and Death of Dense Molecular Clumps around Massive YSOs

We acquired and presented ancillary data of the molecular gas around the forming stars using the dense gas tracers HCO^+ and HCN. In Chapter 4 we reported the results of the HCO^+ and HCN emission survey toward the giant molecular clouds of the star formation regions N105, N113, N159, and N44. The 3 mm emission was mapped using the Australia Telescope Compact Array and has an angular resolution of ~1 pc at the distance of the LMC. The emission shows that the molecular material is highly clumpy, with individual clumps of masses between 10^2 and 10^4 $M_\odot$ and sizes of <1 pc to ~2 pc. Many of the clumps are coincident with identified sites of current star formation such as maser emission, compact HII region-like emission, and bright infrared point sources, indicating that many of the clumps are associated with deeply-embedded forming stars and star clusters.

There are also several massive or intermediate-mass YSOs in the imaged regions that are devoid of HCO^+ or HCN emission that likely represent a more advanced stage of massive star formation. Of the 39 dense molecular clumps detected, 12 do not contain indicators of massive star formation. These clumps may be precursors to star/cluster-forming clumps, in which case they represent a very early stage of massive star formation. Alternatively, they could represent a separate class of clumps that will never form massive stars. We find that clumps associated with on-going massive star formation are on average more massive than those without, suggesting that the mass of the most massive member of a cluster may be determined by the mass of the cluster's

natal clump. Moreover, we find a possible correlation between the mass of a clump and the projected distance between the clump's center and the star it is forming. Evidence suggests that as a massive star forms, it becomes displaced from the clump's emission peak, and destroys or dissipates a significant fraction (> 1/2) of the surrounding clump. The massive YSOs not located within clumps presumably represent objects that have completely destroyed their clumps or have physically moved away from their birth locations. The strength of the 10μm silicate absorption feature, typically seen in the mid-infrared spectra of massive forming stars, is highly correlated with a source's association with a dense molecular clump: objects embedded in clumps have deep silicate features, while those that are free of coincident HCO^+ or HCN emission have weak to no silicate absorption. This correlation strongly suggests that the silicate feature is related to the parsec-sized clump. Using a large sample of LMC massive YSO spectra, we estimate that ~60% of the YSOs included in our spectral study are no longer located in molecular clumps; we estimate that these young stars/clusters have destroyed their natal clumps on a time scale of several 10^5 to 10^6 years.

5.2 Future Directions

The coming years hold much potential in the field of observational massive star formation research, particularly with the advent of the *Herschel Space Observatory* (Pilbratt et al. 2010) and the *Atacama Large Millimeter Array (ALMA*; Brown et al. 2004*)*. *Herschel*, operating at wavelengths between 60 and 600 μm, can identify sources surrounded by cool gas and dust, and therefore is a potentially powerful tool for identifying the youngest YSOs in the LMC. The unique capabilities of *Herschel* were recently demonstrated by Sewilo et al. (2010), who

identified 207 massive YSOs in the LMC from their colors in the mid- to far-IR obtained with the new telescope. Approximately 40% of these sources had previously never been identified. Their study focused exclusively on a single band of *Herschel* images that cover only a fraction of the entire galaxy, therefore the number of new YSOs yet to be identified could be in the hundreds. The new *Herschel* data will allow us to better cover the full SED wavelength range, which will lead to a better estimate to the total luminosity of the YSOs and a better constraint on the LMC's high-mass IMF. Moreover, the better-sampled SEDs can be compared to radiation transfer models to attempt to constrain massive YSO properties such as stellar mass, dust mass, and the spatial extent of the circumstellar material. For example, in the aforementioned study, Sewilo et al. (2010) determined from modeling that the YSO's circumstellar envelope may extend to parsec scales, a conclusion this thesis came to from separate observations (Chapter 4).

Herschel also has spectroscopic capabilities, and we have already proposed (P.I. Looney) to observe a subsample of the SL09 YSOs with its mid- and far-IR spectrometer. Questions we hope to address include: *Can we refine the evolutionary sketch of massive star formation provided by Spitzer into a more complete evolutionary picture? What are the properties and indicators of high-mass star formation and how do they change with evolution? What role do shocks play in the systems? How can we use the Herschel observations to better interpret the Spitzer IRS spectra?*

ALMA is going to provide unprecedented sensitivity and spatial resolution at millimeter wavelengths. To date, because most of modern astronomy's most powerful interferometers are located in the norther hemisphere, observations of southern sky objects at these wavelengths

have been largely limited. We plan to observe LMC YSOs with ALMA using a variety of dense gas tracers to investigate how the surrounding gas evolves with time. Using a variety of gas tracers with different critical densities, we may be able track the evolution of clump and core sizes, shapes, and density profiles.

Chapter 6

Tables

Table 1. Source Classification

Object ID	KSPW Class[a]	GC09 Class	Presence of Feature				Possible Multiple	Environment			
			Silicate Absorption (projection[b])	$PAH_{5-10\mu m}$ Emission (projection[b])	$PAH_{10-13\mu m}$ Emission (projection[b])	Fine-Structure Line Emission (projection[b])		Molecular Cloud	Compact Hα	Diffuse Hα ([SIII] concentration ratio[c])	Diffuse Dust
S Group											
045111.39—-692646.7	5.SA	C	yes (0.534)	no (0.464)	no (0.414)	no (0.251)	✓	✓	✓	✓	✓
045550.62–663434.6	5.U	C	yes (0.309)	no (0.722)	no (0.393)	no (0.311)	✓	✓	✓	✓	✓
045842.47–660835.7	5.SA	C	yes (0.285)	no (0.719)	no (0.525)	no (0.319)		✓			✓
045854.30–660718.9	5.SA	C	yes (0.340)	no (0.875)	no (0.535)	no (0.204)		✓			✓
051024.09–701406.5	5.SA	C	yes (0.344)	no (0.760)	no (0.555)	no (0.343)				✓	✓
051912.27–690907.3	5.SA	C	yes (0.554)	no (0.690)	no (0.435)	no (0.241)	✓	✓		✓	✓
052333.40–693712.2	5.SA	C	yes (0.459)	no (0.605)	no (0.468)	no (0.277)	✓				✓
052646.61–684847.2	5.SAe	C	yes (0.333)	no (0.828)	no (0.556)	no (0.255)	✓	✓	✓	✓	✓
053054.24–683428.3	5.SA	C	yes (0.508)	no (0.733)	no (0.467)	no (0.245)		✓		✓	✓
053754.82–693435.8	5.SA	C	yes (0.420)	no (0.812)	no (0.483)	no (0.228)		✓		✓	✓
053958.52–711014.6	5.UE	C	yes (0.418)	no (0.616)	no (0.508)	no (0.285)		✓		✓	✓
SE Group											
045153.29–692328.6	5.SAe	C	yes (0.342)	no (0.808)	no (0.575)	yes (0.161)	✓	✓	✓	✓(2.04)	✓
045206.97–665516.4	5.SAe	C	yes (0.401)	no (0.853)	no (0.466)	yes (–0.285)	✓	✓		✓(0.98)	✓
052212.57–675832.4	5.SAe	C	yes (0.424)	no (0.795)	no (0.438)	yes (0.088)		✓	✓	✓(1.95)	✓
052601.20–673012.1	5.SAe	C	yes (0.552)	no (0.664)	no (0.439)	yes (0.116)	✓		✓	✓(1.36)	✓
053536.88–691214.1	5.UE	C	yes (0.248)	no (0.829)	no (0.560)	yes (–0.119)		✓		✓(1.34)	✓
P Group											
044717.50–690930.3	5.U	C	no (–0.296)	yes (–0.083)	yes (0.313)	no (0.278)		✓	✓		✓
044854.41–690948.3	5.UE	C	no (–0.045)	yes (0.190)	no (0.560)	no (0.260)	✓	✓		✓	✓
045100.16–691934.4	5.U	C	no (0.009)	yes (0.010)	yes (–0.196)	no (0.300)		✓		✓	✓
045358.55–664722.8	5.U	U	no (–0.134)	yes (–0.470)	yes (–0.332)	no (0.258)	✓				✓
045358.57–691106.7	5.U	C	yes (0.505)	yes (0.078)	yes (0.287)	no (0.249)	✓	✓		✓	✓
045406.43–664601.4	5.U	C	no (–0.191)	yes (–0.032)	yes (0.067)	no (0.300)	✓	✓	✓		✓
045524.38–663117.9	5.U	C	no (–0.655)	yes (0.059)	no (0.440)	no (0.562)		✓		✓	✓
045526.71–682528.6	5.U	C	no (–0.136)	yes (–0.536)	yes (–0.276)	no (0.324)		✓	✓	✓	✓
045537.28–663423.0	5.U	C	no (–0.064)	yes (–0.204)	yes (–0.115)	no (0.452)	✓	✓			✓
045540.01–663424.2	5.U	C	no (–0.204)	yes (0.007)	yes (–0.162)	no (0.467)	✓	✓		✓	✓
045541.59–663434.1	5.U	C	no (–0.352)	yes (0.291)	yes (–0.037)	no (0.273)	✓	✓		✓	✓
045542.46–663425.8	5.U	C	no (–0.121)	yes (–0.315)	yes (–0.037)	no (0.273)		✓		✓	✓
045622.61–663656.9	5.U	C	no (–0.093)	yes (0.148)	no (0.438)	no (0.426)	✓	✓	✓		✓
045705.03–664235.8	5.U	C	no (–0.124)	yes (–0.323)	yes (–0.242)	no (0.361)			✓		✓
045709.73–684448.2	5.UE	C	no (0.068)	yes (–0.501)	yes (–0.367)	no (0.270)		✓	✓	✓	✓
045747.97–661842.4	5.U	C	no (–0.202)	yes (–0.497)	yes (–0.214)	no (0.333)	✓	✓	✓	✓	✓
045749.22–662900.3	5.U	C	no (–0.003)	yes (–0.190)	yes (–0.355)	no (0.263)		✓			✓
045851.63–660944.6	5.U	C	no (–0.522)	yes (0.106)	yes (0.249)	no (0.518)	✓	✓		✓	✓
050002.03–663011.5	5.U	C	no (–0.317)	yes (0.100)	yes (0.062)	no (0.368)	✓		✓		✓
050016.18–661531.3	5.U	C	no (–0.167)	yes (0.010)	no (0.431)	no (0.392)		✓	✓	✓	✓
050051.45–662359.9	5.U	C	no (–0.322)	yes (–0.289)	yes (–0.046)	no (0.332)		✓	✓		✓
050348.17–671828.0	5.UE	C	no (–0.084)	yes (–0.544)	yes (–0.415)	no (0.225)	✓	✓	✓	✓	✓
050355.87–672045.1	5.UE	C	no (–0.215)	yes (–0.342)	yes (–0.419)	no (0.217)	✓	✓		✓	✓

Table 1—Continued

Object ID	KSPW Class[a]	GC09 Class	Presence of Feature				Possible Multiple	Environment			
			Silicate Absorption (projection[b])	$PAH_{5-10\mu m}$ Emission (projection[b])	$PAH_{10-13\mu m}$ Emission (projection[b])	Fine-Structure Line Emission (projection[b])		Molecular Cloud	Compact Hα	Diffuse Hα ([SIII] concentration ratio[c])	Diffuse Dust
050435.85–705430.1	5.U	C	no (−0.541)	no (0.375)	yes (0.307)	no (0.455)		✓		✓	✓
050834.72–692525.1	5.U	C	no (−0.124)	yes (−0.492)	yes (−0.261)	no (0.344)	✓	✓	✓		✓
050914.52–683017.1	5.U	C	yes (0.318)	yes (−0.348)	yes (−0.316)	no (0.201)				✓	✓
050941.94–712742.1	5.U	C	no (−0.103)	yes (−0.506)	yes (−0.373)	no (0.338)	✓		✓	✓	✓
050950.53–685305.5	5.E	C	no (0.157)	yes (0.184)	no (0.666)	no (0.294)		✓		✓	✓
050953.89–685336.7	5.UE	C	yes (0.391)	yes (−0.471)	yes (−0.042)	no (0.305)	✓	✓		✓	✓
050954.63–684947.2	5.U	C	no (−0.116)	yes (−0.361)	yes (−0.210)	no (0.342)	✓				✓
051023.69–692620.2	5.U	C	no (−0.026)	no (0.454)	yes (0.284)	no (0.456)		✓		✓	✓
051030.10–670833.3	5.U	C	no (−0.405)	yes (−0.252)	yes (0.228)	no (0.294)	✓	✓		✓	✓
051217.33–702718.4	5.U	C	no (0.113)	no (0.608)	yes (0.215)	no (0.342)		✓	✓		✓
051325.09–692245.1	5.U	C	yes (0.308)	yes (−0.056)	no (0.533)	no (0.288)	✓	✓	✓	✓	✓
051341.85–693528.4	5.U	U	no (−0.031)	yes (−0.292)	yes (−0.337)	no (0.347)	✓	✓		✓	✓
051344.99–693510.6	5.U	C	no (0.002)	yes (−0.486)	yes (−0.501)	no (0.325)	✓	✓	✓		✓
051351.51–672721.9	5.U	C	yes (0.237)	yes (0.144)	no (0.544)	no (0.337)	✓		✓		✓
051408.66–672310.3	5.U	C	no (−0.149)	yes (−0.524)	yes (−0.172)	no (0.264)		✓			✓
051445.43–671204.2	5.U	C	no (−0.087)	yes (0.104)	yes (−0.144)	no (0.226)	✓		✓	✓	✓
051503.26–703351.0	5.U	C	no (−0.237)	yes (0.254)	yes (0.074)	no (0.532)		✓	✓		✓
051707.26–655933.5	5.U	C	no (−0.075)	yes (−0.415)	yes (−0.308)	no (0.365)			✓	✓	✓
051730.66–664337.4	5.U	C	no (−0.206)	yes (−0.229)	yes (0.265)	no (0.242)		✓	✓		✓
051740.87–664217.3	5.U	C	no (−0.128)	yes (−0.428)	yes (−0.236)	no (0.336)	✓	✓		✓	✓
051916.87–693757.5	5.UE	C	no (−0.020)	yes (−0.530)	yes (−0.474)	no (0.257)	✓	✓		✓	✓
051933.46–694106.7	5.UE	C	no (0.057)	yes (−0.283)	yes (−0.423)	no (0.223)	✓	✓		✓	✓
052011.96–665238.9	5.U	C	no (−0.112)	yes (−0.492)	yes (−0.337)	no (0.249)	✓	✓	✓	✓	✓
052016.71–665254.1	5.U	U	yes (0.294)	yes (0.030)	yes (−0.006)	no (0.280)	✓	✓	✓	✓	✓
052046.55–675255.0	5.U	C	no (−0.223)	yes (−0.189)	yes (−0.282)	no (0.325)	✓	✓	✓	✓	✓
052121.50–695901.9	5.U	C	no (−0.015)	yes (−0.423)	yes (−0.323)	no (0.305)	✓	✓		✓	✓
052124.90–660412.9	5.U	C	no (0.103)	yes (−0.394)	yes (−0.379)	no (0.234)	✓		✓	✓	✓
052155.18–674730.4	5.U	C	no (−0.074)	no (0.621)	yes (0.098)	no (0.490)	✓	✓		✓	✓
052208.77–675324.9	5.U	C	no (−0.296)	yes (0.296)	yes (−0.221)	no (0.223)	✓	✓	✓	✓	✓
052210.08–673459.6	5.U	C	no (−0.090)	yes (−0.390)	yes (−0.369)	no (0.344)		✓	✓		✓
052216.87–680403.9	5.U	C	yes (0.347)	no (0.667)	yes (0.270)	no (0.229)	✓	✓		✓	✓
052224.89–694232.8	5.UE	C	no (0.038)	yes (−0.506)	no (0.420)	no (0.335)	✓	✓		✓	✓
052231.72–680319.2	5.UE	C	no (−0.207)	yes (−0.310)	yes (−0.229)	no (0.260)	✓	✓		✓	✓
052232.65–680301.7	5.UE	C	no (−0.460)	yes (0.231)	yes (0.159)	no (0.359)	✓	✓		✓	✓
052241.97–675500.5	5.U	C	no (−0.039)	no (0.360)	yes (−0.233)	no (0.248)		✓		✓	✓
052245.13–713610.2	5.U	C	no (−0.599)	no (0.476)	yes (0.261)	no (0.327)			✓	✓	✓
052335.54–675235.6	5.U	A	yes (0.356)	no (0.580)	yes (0.326)	no (0.253)		✓	✓		✓
052337.88–693854.4	5.U	C	no (−0.290)	no (0.804)	yes (0.052)	no (0.242)		✓	✓	✓	✓
052343.48–680033.9	5.UE	C	yes (0.342)	yes (−0.461)	yes (0.309)	no (0.268)	✓	✓		✓	✓
052350.04–675719.6	5.U	C	yes (0.296)	yes (0.271)	yes (0.540)	no (0.269)	✓	✓			✓
052423.39–693904.7	5.U	C	no (0.038)	yes (−0.498)	yes (−0.328)	no (0.435)	✓	✓		✓	✓
052541.54–661528.6	5.UE	C	no (−0.054)	yes (−0.104)	yes (−0.330)	no (0.200)	✓	✓	✓	✓	✓
052621.74–683959.1	5.UE	C	no (−0.100)	yes (−0.410)	yes (−0.392)	no (0.346)	✓		✓		✓
052629.60–674144.7	5.UE	C	no (−0.391)	no (0.888)	yes (0.314)	no (0.228)	✓		✓	✓	✓
052630.65–674036.7	5.UE	C	no (−0.545)	no (0.427)	yes (0.186)	no (0.410)			✓	✓	✓
052638.55–673923.2	5.U	C	no (0.061)	yes (0.146)	yes (0.020)	no (0.342)				✓	✓
052743.47–672624.2	5.U	C	no (0.164)	no (0.349)	yes (0.144)	no (0.391)	✓			✓	✓
053055.56–672006.2	5.U	C	no (−0.550)	no (0.461)	yes (0.204)	no (0.472)			✓		✓

Table 1—Continued

Object ID	KSPW Class[a]	GC09 Class	Presence of Feature				Possible Multiple	Environment			
			Silicate Absorption (projection[b])	$PAH_{5-10\mu m}$ Emission (projection[b])	$PAH_{10-13\mu m}$ Emission (projection[b])	Fine-Structure Line Emission (projection[b])		Molecular Cloud	Compact Hα	Diffuse Hα ([SIII] concentration ratio[c])	Diffuse Dust
053203.82–674256.8	5.U	C	yes (0.238)	yes (0.093)	yes (0.068)	no (0.337)	✓	✓		✓	✓
053207.82–711336.4	5.U	C	no (–0.062)	yes (–0.425)	yes (–0.268)	no (0.288)	✓	✓	✓		✓
053224.97–683904.1	5.U	C	no (–0.105)	yes (–0.463)	yes (–0.315)	no (0.207)	✓	✓		✓	✓
053244.25–693005.7	5.UE	C	no (–0.090)	yes (–0.446)	yes (–0.350)	no (0.217)			✓	✓	✓
053252.29–674109.0	5.U	C	no (–0.680)	yes (0.089)	yes (0.214)	no (0.530)		✓	✓	✓	✓
053410.23–672529.4	5.U	C	no (–0.585)	no (0.450)	yes (0.293)	no (0.519)	✓		✓	✓	✓
053431.46–683513.9	5.U	C	no (–0.341)	yes (0.203)	yes (–0.032)	no (0.396)			✓	✓	✓
053615.84–693151.5	5.UE	C	no (–0.688)	yes (0.299)	yes (0.176)	no (0.208)		✓		✓	✓
053630.81–691817.2	5.M	C	no (–0.467)	yes (0.136)	no (0.513)	no (0.534)					✓
053716.29–662654.7	5.U	C	no (–0.100)	yes (–0.253)	yes (–0.342)	no (0.279)	✓		✓	✓	✓
053805.65–690909.7	5.UE	C	no (–0.674)	yes (0.096)	no (0.452)	no (0.336)		✓		✓	✓
053929.21–694719.0	5.UE	C	yes (0.340)	yes (–0.558)	yes (0.270)	no (0.328)	✓	✓		✓	✓
053931.19–701216.9	5.U	C	yes (0.297)	no (0.431)	yes (0.021)	no (0.360)	✓	✓		✓	✓
053939.15–691754.6	5.U	C	yes (0.217)	yes (–0.237)	yes (0.173)	no (0.284)	✓	✓		✓	✓
053952.11–710930.7	5.U	C	no (–0.295)	no (0.828)	yes (0.222)	no (0.292)	✓	✓		✓	✓
053953.43–710953.1	5.UE	C	yes (0.257)	yes (0.244)	no (0.368)	no (0.302)	✓	✓		✓	✓
053958.39–711005.5	5.UE	C	yes (0.364)	yes (–0.094)	no (0.561)	no (0.330)	✓	✓		✓	✓
053959.51–693730.4	5.U	C	no (–0.571)	yes (0.206)	no (0.428)	no (0.567)		✓		✓	✓
054012.00–700916.0	5.U	C	no (–0.134)	yes (–0.338)	yes (–0.329)	no (0.228)	✓	✓			✓
054125.95–711753.9	5.U	C	no (–0.191)	yes (–0.555)	yes (–0.076)	no (0.413)	✓	✓	✓		✓
054233.71–711727.8	5.U	C	yes (0.442)	yes (0.115)	yes (0.195)	no (0.336)	✓	✓	✓	✓	✓
054248.90–694446.3	5.U	C	no (–0.086)	yes (–0.478)	yes (–0.392)	no (0.244)	✓	✓		✓	✓
054449.63–671934.7	5.U	C	no (–0.165)	yes (–0.517)	yes (–0.330)	no (0.312)	✓	✓	✓	✓	✓
054520.03–694644.8	5.U	C	yes (0.204)	yes (–0.231)	yes (0.024)	no (0.218)	✓	✓	✓	✓	✓
054629.32–693514.2	5.U	C	no (–0.734)	no (0.700)	yes (0.272)	no (0.252)	✓	✓		✓	✓
054712.97–704416.9	5.U	C	no (–0.202)	yes (0.273)	no (0.349)	no (0.287)	✓	✓			
054826.21–700850.2	5.UE	C	no (–0.505)	yes (0.301)	yes (0.280)	no (0.353)	✓	✓		✓	✓
PE Group											
044849.85–690930.6	5.UE	C	no (–0.068)	yes (–0.231)	yes (–0.395)	yes (0.111)	✓	✓		✓(1.05)	✓
044927.29–691206.3	5.UE	C	no (0.013)	yes (–0.198)	yes (0.064)	yes (–0.378)	✓	✓		✓(1.99)	✓
045009.52–692906.4	5.UE	C	no (–0.056)	yes (–0.535)	yes (–0.464)	yes (0.106)				✓(1.13)	✓
045200.43–692342.6	5.UE	C	no (0.047)	yes (–0.253)	yes (0.013)	yes (–0.215)	✓	✓	✓	✓(3.34)	✓
045204.56–692046.4	5.UE	C	no (0.035)	yes (–0.169)	yes (–0.354)	yes (–0.143)	✓	✓		✓(1.35)	✓
045205.39–665513.8	5.UE	D	no (0.120)	yes (–0.495)	yes (–0.041)	yes (–0.414)	✓	✓		✓(1.64)	✓
045208.94–665537.4	5.UE	C	no (–0.045)	yes (0.314)	yes (0.052)	yes (–0.388)		✓		✓(1.4)	✓
045209.22–665521.9	5.UE	C	no (0.173)	no (0.540)	yes (0.098)	yes (–0.368)		✓		✓(1.37)	✓
045258.09–680336.1	5.UE	C	no (–0.589)	no (0.689)	yes (0.184)	yes (0.198)		✓	✓	✓(5.57)	✓
045258.67–680256.0	5.UE	C	no (–0.060)	yes (–0.548)	yes (–0.401)	yes (–0.046)	✓	✓	✓	✓(2.03)	✓
045400.10–691155.5	5.UE	C	yes (0.598)	yes (0.179)	yes (0.035)	yes (–0.333)		✓		✓(1.43)	✓
045401.14–691152.9	5.UE	C	yes (0.586)	yes (0.214)	yes (0.035)	yes (–0.333)		✓		✓(1.43)	✓
045403.04–691139.7	5.UE	C	yes (0.243)	yes (–0.580)	yes (–0.353)	yes (–0.442)	✓	✓		✓(0.97)	✓
045408.28–664631.4	5.UE	C	no (–0.058)	yes (–0.406)	yes (–0.522)	yes (0.055)	✓	✓	✓	(7.87)	✓
045426.06–691102.3	5.UE	C	no (–0.059)	yes (–0.170)	yes (0.050)	yes (–0.243)		✓	✓	(5.01)	✓
045546.40–662509.1	5.UE	C	no (–0.196)	yes (0.141)	yes (–0.570)	yes (–0.004)	✓	✓		✓(1.11)	✓
045625.99–663155.5	5.UE	C	no (–0.105)	yes (–0.409)	yes (–0.568)	yes (–0.102)	✓	✓	✓	✓(1.25)	✓
045629.02–663159.3	5.UE	C	no (0.043)	yes (0.014)	yes (–0.295)	yes (0.075)		✓	✓	✓(1.14)	✓

Table 1—Continued

Object ID	KSPW Class[a]	GC09 Class	Presence of Feature				Possible Multiple	Environment			
			Silicate Absorption (projection[b])	$PAH_{5-10\mu m}$ Emission (projection[b])	$PAH_{10-13\mu m}$ Emission (projection[b])	Fine-Structure Line Emission (projection[b])		Molecular Cloud	Compact Hα	Diffuse Hα ([SIII] concentration ratio[c])	Diffuse Dust
045638.76–662446.2	5.UE	C	no (0.062)	yes (−0.340)	yes (−0.078)	yes (−0.420)		✓	✓	✓(1.19)	✓
045647.23–662431.8	5.UE	U	no (0.140)	yes (−0.616)	yes (−0.175)	yes (−0.432)	✓	✓		✓(1.71)	✓
045651.82–663133.0	5.UE	C	no (−0.230)	yes (−0.508)	yes (−0.134)	yes (−0.157)				✓(1.14)	✓
045657.25–662513.0	5.UE	C	no (0.110)	yes (−0.349)	yes (−0.181)	yes (−0.327)	✓	✓		✓(1.47)	✓
045659.85–662425.9	5.UE	C	no (−0.476)	yes (−0.010)	yes (0.036)	yes (−0.364)		✓	✓	✓(1.43)	✓
045713.47–661900.1	5.U	CG	no (−0.222)	yes (−0.274)	yes (−0.363)	yes (0.187)	✓	✓	✓	(0.96)	✓
045714.98–682629.5	5.UE	C	no (−0.064)	yes (−0.121)	yes (−0.121)	yes (−0.426)	✓	✓	✓	✓(1.57)	✓
045716.25–662319.9	5.UE	C	no (−0.017)	yes (−0.059)	yes (0.045)	yes (−0.390)		✓	✓	(2.81)	✓
045716.82–682648.0	5.UE	C	no (−0.090)	yes (−0.533)	yes (−0.299)	yes (−0.290)		✓	✓	✓(1.42)	✓
045719.77–682526.4	5.UE	C	no (0.051)	yes (−0.238)	yes (−0.200)	yes (−0.419)	✓	✓		✓(1.29)	✓
045720.72–662814.4	5.UE	C	no (−0.174)	yes (−0.402)	yes (−0.585)	yes (−0.221)				✓(1.25)	✓
045742.00–662634.4	5.UE	C	no (−0.024)	yes (−0.343)	yes (−0.602)	yes (−0.225)	✓	✓		✓(1.13)	✓
045747.68–662816.9	5.UE	C	yes (0.243)	no (0.686)	yes (0.133)	yes (−0.358)	✓	✓		✓(1.18)	✓
045811.70–662211.3	5.UE	C	no (−0.334)	yes (−0.197)	yes (−0.055)	yes (−0.355)	✓	✓	✓	✓(1.45)	✓
050006.21–661556.8	5.UE	C	no (−0.237)	yes (0.035)	yes (−0.489)	yes (−0.001)		✓		✓(1.22)	✓
050356.03–671845.2	5.UE	CS	no (−0.157)	yes (−0.809)	yes (−0.221)	yes (−0.188)		✓	✓	(3.61)	✓
050356.13–672038.8	5.UE	C	no (−0.078)	yes (−0.443)	yes (−0.549)	yes (0.075)		✓	✓	✓(1.25)	✓
050424.82–704343.7	5.UE	C	no (0.002)	yes (−0.366)	yes (−0.413)	yes (0.122)	✓	✓	✓	✓(1.33)	✓
050438.09–705443.1	5.UE	U	no (−0.034)	yes (−0.410)	yes (0.047)	yes (−0.148)	✓	✓	✓	(2.89)	✓
050439.86–705419.0	5.UE	C	no (−0.173)	yes (−0.235)	yes (0.243)	yes (0.192)		✓	✓	✓(10.28)	✓
050520.27–665506.5	5.UE	C	yes (0.202)	yes (−0.565)	yes (−0.100)	yes (−0.008)		✓	✓	✓(6.19)	✓
050952.26–685327.3	5.UE	C	yes (0.552)	yes (−0.577)	yes (−0.117)	yes (−0.377)	✓	✓		✓(1.33)	
050952.73–685300.7	5.UE	C	no (0.054)	yes (−0.402)	yes (0.084)	yes (−0.105)	✓	✓	✓	✓(1.77)	✓
051229.69–670918.6	5.UE	C	no (−0.234)	no (0.818)	yes (0.140)	yes (0.180)		✓	✓	✓(–)	✓
051259.82–693436.9	5.U	C	no (−0.052)	yes (−0.271)	yes (−0.333)	yes (0.197)	✓	✓	✓	(–)	✓
051315.73–692135.9	5.UE	C	no (0.088)	yes (−0.415)	yes (−0.223)	yes (−0.399)		✓		✓(1.32)	✓
051317.69–692225.0	5.UE	C	yes (0.225)	yes (−0.368)	yes (0.170)	yes (−0.208)	✓	✓		✓(5.49)	✓
051318.26–692135.5	5.UE	C	no (−0.200)	yes (0.245)	yes (−0.070)	yes (−0.355)		✓		✓(1.21)	✓
051319.14–692151.0	5.UE	C	no (0.023)	yes (−0.443)	yes (−0.450)	yes (−0.277)	✓	✓		✓(1.51)	✓
051321.43–692241.5	5.UE	C	no (0.146)	yes (−0.127)	yes (0.161)	yes (−0.320)	✓	✓	✓	✓(3.34)	✓
051324.50–691048.3	5.UE	C	no (−0.093)	yes (−0.683)	yes (−0.073)	yes (−0.375)		✓	✓	(3.79)	✓
051338.34–692300.7	5.UE	C	no (0.100)	yes (−0.503)	yes (−0.527)	yes (−0.372)	✓	✓		✓(1.23)	✓
051340.92–692301.6	5.UE	C	no (−0.198)	no (0.769)	yes (0.216)	yes (−0.050)		✓		✓(1.19)	✓
051354.06–672018.9	5.U	C	no (−0.256)	no (0.656)	yes (0.023)	yes (0.175)			✓	✓(1.0)	✓
051728.44–664307.0	5.UE	C	no (−0.214)	yes (−0.507)	yes (0.007)	yes (0.124)		✓	✓	(11.56)	✓
051734.73–711456.5	5.UE	C	no (0.008)	yes (−0.396)	yes (−0.038)	yes (−0.430)	✓	✓	✓	✓(2.71)	✓
051903.42–693812.9	5.UE	U	no (0.113)	yes (−0.715)	yes (−0.130)	yes (−0.154)	✓	✓	✓	✓(1.49)	✓
051905.93–693841.2	5.UE	C	no (−0.043)	yes (−0.711)	yes (−0.328)	yes (−0.308)	✓	✓		✓(1.36)	✓
051906.69–682137.4	5.UE	C	no (−0.078)	yes (−0.649)	yes (−0.070)	yes (−0.351)			✓	(3.38)	✓
051907.31–693842.0	5.UE	C	no (0.010)	yes (−0.661)	yes (−0.076)	yes (−0.341)	✓	✓	✓	✓(1.82)	✓
051916.98–693816.4	5.UE	C	no (−0.081)	yes (−0.610)	yes (−0.394)	yes (−0.319)	✓	✓		✓(1.36)	✓
052011.56–683753.7	5.U	C	no (0.071)	no (0.356)	yes (−0.320)	yes (0.195)		✓	✓	✓(4.27)	✓
052117.24–695950.2	5.U	C	no (−0.019)	yes (−0.517)	yes (−0.311)	yes (0.196)	✓	✓		(19.9)	✓
052117.49–680204.4	5.U	C	no (−0.113)	yes (−0.268)	yes (−0.240)	yes (0.188)	✓	✓		✓(–)	✓
052121.99–674728.9	5.U	C	no (0.139)	yes (−0.553)	yes (−0.176)	yes (0.186)		✓	✓	✓(7.31)	✓
052133.20–652920.8	5.U	C	no (0.112)	yes (−0.453)	yes (−0.428)	yes (0.180)	✓		✓	✓(3.24)	✓
052133.23–694019.9	5.UE	C	no (0.021)	yes (−0.782)	yes (−0.203)	yes (−0.423)	✓	✓		✓(1.5)	✓
052141.84–675324.0	5.UE	C	no (−0.195)	yes (−0.207)	yes (−0.511)	yes (0.193)		✓		✓(1.03)	✓

Table 1—Continued

Object ID	KSPW Class[a]	GC09 Class	Presence of Feature				Possible Multiple	Environment			
			Silicate Absorption (projection[b])	$PAH_{5-10\mu m}$ Emission (projection[b])	$PAH_{10-13\mu m}$ Emission (projection[b])	Fine-Structure Line Emission (projection[b])		Molecular Cloud	Compact Hα	Diffuse Hα ([SIII] concentration ratio[c])	Diffuse Dust
052147.09–675656.8	5.UE	C	no (−0.080)	yes (−0.419)	yes (−0.460)	yes (−0.007)	✓	✓	✓	✓(1.47)	✓
052156.97–675700.1	5.UE	C	no (0.079)	yes (−0.019)	yes (0.032)	yes (−0.321)		✓		✓(1.31)	✓
052202.11–675753.6	5.UE	C	yes (0.295)	yes (−0.657)	yes (−0.359)	yes (−0.009)		✓		✓(1.19)	✓
052202.72–674702.1	5.UE	C	no (−0.045)	yes (−0.712)	yes (−0.250)	yes (0.190)	✓	✓		✓(3.65)	✓
052203.30–675747.0	5.UE	C	no (0.132)	yes (−0.648)	yes (−0.119)	yes (−0.223)	✓	✓		✓(1.15)	✓
052204.85–675800.3	5.UE	D	no (0.044)	yes (−0.773)	yes (−0.417)	yes (−0.284)	✓	✓		✓(1.35)	✓
052207.27–675819.7	5.UE	C	no (−0.096)	yes (−0.555)	yes (−0.513)	yes (−0.034)		✓		✓(1.5)	✓
052219.69–680437.4	5.UE	C	no (0.087)	yes (−0.475)	yes (0.033)	yes (−0.417)	✓	✓	✓	(3.12)	✓
052227.70–675412.8	5.UE	C	no (−0.187)	yes (−0.462)	yes (−0.540)	yes (−0.046)				✓(1.13)	✓
052228.98–675339.3	5.UE	C	no (−0.188)	yes (−0.186)	yes (−0.547)	yes (−0.316)	✓	✓	✓	✓(1.18)	✓
052249.13–680129.1	5.UE	C	no (−0.097)	yes (−0.522)	yes (−0.479)	yes (−0.242)	✓	✓		✓(1.11)	✓
052249.88–664056.1	5.UE	C	no (−0.059)	yes (−0.446)	yes (−0.374)	yes (0.048)	✓	✓	✓	✓(7.43)	✓
052253.27–695111.1	5.UE	C	no (−0.098)	yes (−0.489)	yes (−0.584)	yes (−0.004)		✓	✓	✓(1.83)	✓
052255.12–680409.4	5.UE	C	no (−0.012)	yes (−0.526)	yes (−0.189)	yes (−0.275)		✓		✓(1.63)	✓
052256.79–680406.8	5.UE	C	no (−0.131)	yes (−0.582)	yes (−0.381)	yes (0.110)	✓	✓		✓(1.17)	✓
052308.60–680006.5	5.UE	C	no (0.130)	yes (−0.053)	yes (−0.418)	yes (0.176)	✓	✓		✓(1.12)	✓
052315.18–680017.1	5.UE	CS	no (0.126)	yes (−0.145)	yes (0.035)	yes (−0.194)		✓	✓	(1.61)	✓
052331.37–680108.0	5.UE	C	no (−0.087)	yes (−0.473)	yes (−0.408)	yes (0.152)	✓	✓		✓(3.07)	✓
052521.16–672937.6	5.UE	C	no (−0.020)	yes (−0.471)	yes (−0.550)	yes (0.118)				✓(1.29)	✓
052549.27–661508.7	5.UE	C	no (0.185)	yes (0.042)	no (0.677)	yes (0.196)		✓	✓	(9.19)	✓
052629.01–691756.1	5.UE	C	no (−0.157)	yes (−0.265)	yes (−0.314)	yes (0.168)			✓	✓(1.37)	✓
052757.09–672522.3	5.UE	C	no (−0.123)	yes (−0.205)	yes (−0.382)	yes (−0.226)	✓	✓	✓	✓(2.52)	✓
052803.20–672525.6	5.UE	C	no (−0.104)	yes (−0.522)	yes (−0.555)	yes (0.040)	✓	✓		✓(1.25)	✓
052804.78–685947.2	5.U	C	no (−0.429)	no (0.763)	yes (0.015)	yes (0.160)	✓		✓	(1.57)	✓
053020.32–710748.9	5.UE	C	no (0.082)	yes (−0.772)	yes (−0.136)	yes (−0.262)	✓	✓	✓	✓(2.57)	✓
053020.79–710738.6	5.UE	C	no (0.113)	yes (−0.559)	yes (−0.136)	yes (−0.262)	✓	✓		✓(2.57)	✓
053023.18–710556.3	5.U	C	no (−0.089)	yes (−0.353)	yes (−0.519)	yes (−0.007)	✓	✓		✓(1.23)	✓
053122.85–710409.9	5.UE	C	no (−0.029)	yes (−0.657)	yes (−0.171)	yes (−0.439)	✓	✓		✓(1.31)	✓
053154.43–682640.6	5.UE	C	no (−0.042)	yes (−0.549)	yes (−0.012)	yes (−0.144)	✓	✓	✓	✓(4.03)	✓
053214.97–711323.9	5.UE	C	no (0.071)	yes (−0.348)	yes (−0.462)	yes (0.166)	✓	✓		✓(1.74)	✓
053217.49–674155.6	5.UE	C	no (0.031)	yes (−0.123)	yes (−0.148)	yes (−0.343)	✓	✓		✓(1.38)	✓
053227.42–674132.9	5.UE	C	no (0.066)	yes (−0.496)	yes (0.020)	yes (−0.260)	✓	✓		✓(1.47)	✓
053232.06–662715.2	5.UE	C	no (−0.173)	yes (−0.408)	yes (−0.403)	yes (0.172)	✓	✓		✓(1.57)	✓
053251.50–674059.4	5.UE	C	no (0.031)	yes (−0.575)	yes (−0.172)	yes (−0.399)	✓	✓	✓	(4.25)	✓
053252.41–694620.1	5.UE	C	yes (0.427)	yes (−0.674)	yes (−0.085)	yes (−0.271)	✓	✓	✓	(1.46)	✓
053342.15–684602.8	5.UE	C	yes (0.208)	yes (−0.414)	yes (0.023)	yes (−0.435)	✓			✓(1.47)	✓
053524.05–673455.6	5.UE	C	no (0.143)	yes (−0.599)	yes (−0.008)	yes (−0.384)		✓		✓(1.09)	✓
053554.36–693848.1	5.UE	C	no (0.058)	yes (−0.653)	yes (−0.145)	yes (−0.414)				✓(1.24)	✓
053554.94–693903.0	5.UE	CD	no (0.011)	yes (−0.720)	yes (−0.211)	yes (−0.397)				✓(0.99)	✓
053704.78–662207.2	5.U	C	no (−0.092)	yes (−0.104)	yes (−0.043)	yes (−0.078)	✓			✓(408.6)	✓
053746.08–691050.3	5.UE	C	no (0.081)	no (0.499)	yes (−0.125)	yes (−0.430)		✓		✓(1.19)	✓
053839.23–690552.2	5.UE	C	no (0.084)	yes (0.045)	yes (0.141)	yes (−0.272)	✓	✓		✓(1.39)	✓
053839.69–690538.2	5.SAe	C	yes (0.259)	no (0.775)	yes (0.195)	yes (−0.284)	✓	✓		✓(1.17)	✓
053845.15–690507.9	5.UE	C	no (0.086)	yes (0.007)	yes (0.172)	yes (−0.307)	✓	✓		✓(1.31)	✓
053849.27–690444.4	5.UE	C	yes (0.249)	yes (−0.233)	yes (0.136)	yes (−0.329)	✓	✓		✓(1.29)	✓
053852.67–690437.5	5.UE	C	no (0.151)	yes (−0.636)	yes (−0.009)	yes (−0.356)		✓		✓(1.17)	✓
053853.88–690931.3	5.UE	C	no (0.045)	yes (−0.335)	yes (−0.294)	yes (−0.318)				✓(1.2)	✓
053858.42–690434.7	5.UE	C	no (0.156)	yes (−0.385)	yes (0.016)	yes (−0.381)				✓(1.19)	✓

Table 1—Continued

Object ID	KSPW Class[a]	GC09 Class	Presence of Feature				Possible Multiple	Environment			
			Silicate Absorption (projection[b])	$PAH_{5-10\mu m}$ Emission (projection[b])	$PAH_{10-13\mu m}$ Emission (projection[b])	Fine-Structure Line Emission (projection[b])		Molecular Cloud	Compact Hα	Diffuse Hα ([SIII] concentration ratio[c])	Diffuse Dust
053904.42–690413.9	5.UE	C	no (0.124)	yes (−0.652)	yes (−0.109)	yes (−0.400)		✓		✓(1.23)	✓
053904.88–692949.9	5.UE	C	no (−0.033)	no (0.649)	yes (−0.047)	yes (−0.396)	✓	✓		✓(1.16)	✓
053906.31–693043.8	5.UE	C	no (−0.112)	yes (−0.655)	yes (−0.548)	yes (−0.356)	✓	✓		✓(1.15)	✓
053915.77–693039.9	5.UE	U	no (0.093)	yes (−0.643)	yes (−0.112)	yes (−0.408)	✓	✓		✓(1.35)	✓
053935.99–694604.1	5.UE	C	no (−0.045)	yes (−0.587)	yes (−0.494)	yes (−0.150)	✓	✓		✓(1.35)	✓
053937.04–694536.7	5.UE	C	yes (0.661)	no (0.337)	yes (0.102)	yes (0.043)	✓	✓		✓(1.03)	✓
053937.53–694609.8	5.UE	C	no (0.029)	yes (−0.062)	yes (0.185)	yes (−0.358)	✓	✓		✓(2.32)	✓
053937.60–694525.0	5.UE	U	yes (0.358)	yes (−0.293)	yes (0.092)	yes (−0.327)	✓	✓		✓(2.59)	✓
053938.73–693904.3	5.UE	C	yes (0.454)	yes (−0.676)	yes (0.061)	yes (0.052)	✓	✓		✓(1.32)	✓
053939.02–693911.4	5.UE	C	yes (0.450)	yes (−0.701)	yes (0.061)	yes (0.052)	✓	✓		✓(1.32)	✓
053941.89–694612.0	5.UE	C	yes (0.400)	yes (0.327)	yes (0.171)	yes (−0.218)	✓	✓		✓(1.17)	✓
053945.18–694450.4	5.UE	C	no (0.052)	yes (−0.168)	yes (−0.017)	yes (0.001)		✓	✓	✓(2.64)	✓
053951.60–694510.5	5.UE	U	no (0.155)	yes (−0.179)	yes (0.156)	yes (−0.356)	✓	✓		✓(1.33)	✓
053952.29–694516.5	5.UE	U	no (0.156)	yes (−0.191)	yes (0.156)	yes (−0.356)	✓	✓		✓(1.33)	✓
053955.66–711000.9	5.UE	C	yes (0.231)	no (0.814)	yes (−0.298)	yes (0.150)	✓	✓		✓(1.94)	✓
053959.34–694526.3	5.UE	C	no (−0.562)	no (0.892)	yes (0.302)	yes (0.116)		✓		✓(1.1)	✓
054000.69–694713.4	5.UE	C	no (−0.370)	yes (0.217)	yes (0.266)	yes (−0.283)	✓	✓	✓	(1.78)	✓
054004.19–693812.4	5.UE	C	no (−0.143)	yes (−0.373)	yes (−0.507)	yes (−0.033)	✓	✓		✓(1.06)	✓
054004.40–694437.6	5.UE	C	no (0.028)	yes (−0.075)	yes (0.132)	yes (−0.311)	✓	✓	✓	✓(3.52)	✓
054009.50–694023.0	5.UE	U	no (0.085)	yes (−0.099)	yes (0.108)	yes (−0.392)	✓			✓(1.52)	✓
054009.49–694453.5	5.UE	C	yes (0.296)	yes (−0.708)	yes (−0.148)	yes (−0.380)	✓	✓		✓(1.29)	✓
054025.15–694012.1	5.UE	U	no (−0.004)	yes (0.037)	yes (0.067)	yes (−0.374)				✓(1.59)	✓
054044.03–692554.6	5.UE	C	no (−0.529)	yes (−0.182)	yes (−0.088)	yes (0.165)	✓		✓	✓(2.55)	✓
054044.98–702807.0	5.UE	CS	no (−0.008)	no (0.753)	yes (0.016)	yes (−0.303)		✓	✓	(6.86)	✓
054055.77–694047.3	5.UE	C	no (−0.097)	yes (−0.016)	yes (−0.147)	yes (0.130)	✓			✓(0.93)	✓
054137.57–711902.0	5.UE	CD	no (0.002)	yes (−0.568)	yes (−0.069)	yes (−0.412)	✓	✓	✓	✓(2.66)	✓
054138.76–711913.9	5.UE	C	no (−0.063)	yes (−0.461)	yes (−0.264)	yes (−0.351)	✓	✓		✓(1.0)	✓
054221.16–690621.0	5.UE	C	no (−0.089)	yes (−0.311)	yes (−0.600)	yes (−0.117)				✓(1.25)	✓
054527.92–694622.6	5.UE	C	no (−0.235)	yes (−0.048)	yes (0.025)	yes (−0.235)	✓	✓	✓	✓(2.74)	✓
054818.15–700109.0	5.U	C	yes (0.383)	yes (−0.458)	yes (−0.108)	yes (0.197)	✓			✓(8.68)	✓
054838.23–700208.1	5.UE	C	yes (0.209)	yes (−0.485)	yes (0.031)	yes (0.088)		✓	✓	✓(8.38)	✓
E Group											
050949.11–685230.6	5.UE	C	no (−0.538)	no (0.803)	no (0.353)	yes (0.131)	✓	✓		✓(1.4)	✓
052504.10–682824.5	5.UE	C	no (−0.174)	no (0.549)	no (0.636)	yes (−0.001)		✓		✓(1.26)	✓
F Group											
045201.15–692007.7	5.UE	C	no (−0.499)	no (0.371)	no (0.610)	no (0.430)		✓		✓	✓
045245.62–691149.5	5.SA	CA	no (−0.230)	no (0.787)	no (0.564)	no (0.293)		✓	✓		✓
045403.62–671618.5	5.U	CS	no (−0.116)	no (0.516)	no (0.410)	no (0.333)			✓	✓	✓
045506.50–691708.8	5.UE	C	no (−0.531)	no (0.699)	no (0.556)	no (0.248)				✓	✓
045640.79–663230.5	5.SA	C	no (−0.163)	no (0.763)	no (0.420)	no (0.440)		✓		✓	✓
051359.84–672251.4	5.UE	C	no (−0.729)	no (0.775)	no (0.412)	no (0.391)		✓	✓		✓
051909.02–691156.1	5.UE	C	no (−0.051)	no (0.578)	no (0.598)	no (0.279)		✓		✓	✓
052222.46–713532.2	5.U	C	no (0.149)	no (0.682)	no (0.511)	no (0.447)		✓		✓	✓
052736.93–672728.6	5.E	C	no (−0.474)	no (0.487)	no (0.652)	no (0.227)	✓		✓	✓	✓

Table 1—Continued

Object ID	KSPW Class[a]	GC09 Class	Presence of Feature				Possible Multiple	Environment			
			Silicate Absorption (projection[b])	$PAH_{5-10\mu m}$ Emission (projection[b])	$PAH_{10-13\mu m}$ Emission (projection[b])	Fine-Structure Line Emission (projection[b])		Molecular Cloud	Compact Hα	Diffuse Hα ([SIII] concentration ratio[c])	Diffuse Dust
053203.43–674225.7	5.U	C	no (–0.459)	no (0.343)	no (0.517)	no (0.506)		✓	✓	✓	✓
054544.78–670928.2	5.U	C	no (–0.265)	no (0.819)	no (0.479)	no (0.310)	✓	✓		✓	✓
Embedded objects with unknown classification											
053142.44–683454.3	5.UE	C	···	···	···	···	✓		✓	✓	✓
053943.26–693854.6	5.E	C	···	···	···	···	✓	✓		✓	✓
053943.82–693834.0	5.E	C	···	···	···	···	✓	✓		✓	✓
053944.33–693847.5	5.E	C	···	···	···	···	✓	✓		✓	✓
053945.94–693839.2	5.E	C	···	···	···	···	✓	✓		✓	✓
O Group											
045405.74–664507.2	4.SE	C	···	···	···	···	✓	✓	✓		✓
045747.96–662844.7	4.SE	U	···	···	···	···		✓		✓	✓
051654.05–672005.1	4.SE	C	···	···	···	···			✓	✓	✓
052605.26–683609.3	4.SE	C	···	···	···	···		✓	✓	✓	✓
053010.33–690933.9	4.SE	C	···	···	···	···				✓	✓
053642.42–700746.7	4.SE	CS	···	···	···	···		✓	✓		✓
054033.97–692509.9	4.SE	A	···	···	···	···			✓	✓	
054330.33–692446.6	4.SE	C	···	···	···	···		✓	✓	✓	✓
ERO Group											
050231.49–680535.8	4.CR	E	···	···	···	···					
050405.60–682340.3	4.CR	E	···	···	···	···					
051811.70–703027.0	4.CR	E	···	···	···	···					
051848.36–693334.7	4.CR	E	···	···	···	···					
052540.63–700827.2	4.CR	E	···	···	···	···					
052937.89–724952.9	4.CR	E	···	···	···	···	✓			✓	
055026.08–695603.1	4.CR	E	···	···	···	···					
B Grouo											
054054.25–693318.7	4.CT	C	···	···	···	···	✓			✓	✓
Instrument miss											
052219.71–654319.0	4.M	A	···	···	···	···		✓		✓	✓

[a]Primary GC09 classifications for the entire source sample. When applicable, the primary classification is followed by the secondary classification. GC09 classifications are as follows: C – candidate YSO; A – AGB or post-AGB star (non-ERO); D – diffuse source; G – background galaxy; S – normal star; E – extremely red object. Sources without a GC09 classification are assigned a U – unknown – classification.

[b]Dot-product of the source's spectrum with the eigenvector containing the pertaining spectral feature.

[c]Ratio of the equivalent width per pixel of the [SIII] 18.7 μm fine-structure line of the full slit extraction to the equivalent width per pixel of the same line taken at the 1-pixel wide 'off-source' slit position. Sources without values do not have a measureable [SIII] line.

Table 2. Comparison between GC09 and Our Classification

Our Classification		GC09 Primary & Secondary Classification[a]						
Group	Total	YSO	AGB (non-ERO)	Galaxy	Diffuse	Stellar	ERO	Unknown
Total	···	**269**	**3 (1)**	**0 (1)**	**2 (2)**	0 **(5)**	**7**	**13**
YSO	**277**	262	1 (1)	0 (1)	2 (2)	0 (4)	0	12
S	**11**	11	0	0	0	0	0	0
SE	**5**	5	0	0	0	0	0	0
P	**98**	94	1	0	0	0	0	3
PE	**145**	133	0	0 (1)	2 (2)	0 (3)	0	9
E	**2**	2	0	0	0	0	0	0
F	**11**	11	0 (1)	0	0	0 (1)	0	0
U[b]	**5**	5	0	0	0	0	0	0
O	**8**	6	1	0	0	0 (1)	0	1
ERO	**7**	0	0	0	0	0	7	0
B	**1**	1	0	0	0	0	0	0
miss	**1**	0	1	0	0	0	0	0

Note. — The total number of sources in the spectral groups assigned in this paper are provided in the *column* labeled 'Total,' and the total number of sources in each GC09 class are provided in the *row* labeled 'Total.' Unbolded numbers show the overlap betweeb the two classification schemes.

[a]GC09 primary classification counts are given for every GC09 class. When applicable, secondary classification counts are provided in parentheses.

[b]Objects in the U group are not able to be classified due to incomplete spectral coverage.

Table 3. Sources with CO_2 Ice Features

Object ID	Alternate Names	RA (h:m:s)	Dec (d:m:s)	Mean Model Luminosity ($10^4 L_\odot$)	SL09 Spectral Group	Silicate[1] Feature	Mean Model Stage	Literature notes
045111.39-692646.7	IRAS 04514-6931 MSX LMC 1200	04:51:11.39	-69:26:46.7	9.5 ± 2.6	S	✓	1 ± 0	HII region[a]
045400.10-691155.5		04:54:00.10	-69:11:55.5	4.5 ± 2.1	PE	✓	1 ± 0	
045403.04-691139.7		04:54:03.04	-69:11:39.7	3.2 ± 1.3	PE	✓	1.3 ± 0.4	
045403.62-671618.5	IRAS 04540-6721 SSTISAGE045403.62-671618.2	04:54:03.62	-67:16:18.5	4.5 ± 2.3	F		1 ± 0	Stage I YSO[h]
045524.38-663117.9	SSTISAGE045524.39-663117.7	04:55:24.38	-66:31:17.9	0.64 ± 0.24	P		1 ± 0.2	Stage I YSO[h]
045550.62-663434.6	IRAS 04557-6639 SSTISAGE045550.58-663434.6	04:55:50.62	-66:34:34.6	2.4 ± 0.9	S	✓	1 ± 0.2	UCHII region[b] ; Stage I YSO[h]
045640.79-663230.5*	J04564078-6632307 MSX LMC 1229 SSTISAGE045640.75-663230.4	04:56:40.79	-66:32:30.5	2.3 ± 0.6	F		1 ± 0	HII region[c] ; Stage I YSO[h]
045742.00-662634.4		04:57:42.00	-66:26:34.4	1.0 ± 0.4	PE		1 ± 0	
045747.68-662816.9		04:57:47.68	-66:28:16.9	1.9 ± 0.6	PE	✓	1 ± 0	
045842.47-660835.7	SSTISAGE045403.62-671618.2	04:58:42.47	-66:08:35.7	2.0 ± 0.7	S	✓	1 ± 0	Stage I YSO[h]
045854.30-660718.9	J04585433-6607187 SSTISAGE045854.30-660718.7	04:58:54.30	-66:07:18.9	2.0 ± 1.1	S	✓	1 ± 0	Stage I YSO[h]
050435.85-705430.1		05:04:35.85	-70:54:30.1	2.6 ± 0.7	P		1 ± 0	
051023.69-692620.2	SSTISAGE051023.72-692620.3	05:10:23.69	-69:26:20.2	1.3 ± 0.3	P		1 ± 0	Stage I YSO[h]
051024.09-701406.5	IRAS 05108-7017 SSTISAGE051024.09-701406.4	05:10:24.09	-70:14:06.5	3.9 ± 0.9	S	✓	1 ± 0	Stage I YSO[h]
051351.51-672721.9		05:13:51.51	-67:27:21.9	15 ± 4.2	P	✓	1 ± 0	within a cluster of B-type stars[d]
051445.43-671204.2		05:14:45.43	-67:12:04.2	0.76 ± 0.01	P		1 ± 0	
051909.02-691156.1		05:19:09.02	-69:11:56.1	1.1 ± 0.4	F		1 ± 0	
051933.46-694106.7		05:19:33.46	-69:41:06.7	0.97 ± 0.28	P		1 ± 0	
052016.71-665254.1	J0501653-6652544	05:20:16.71	-66:52:54.1	···	P	✓	···	
052133.20-652920.8	IRAS 05214-6532	05:21:33.20	-65:29:20.8	5.2 ± 1.9	P		1 ± 0	UCHII region[b]
052155.18-674730.4	[WSI2008] 563 SSTISAGE0052155.17-674730.3	05:21:55.18	-67:47:30.4	0.24 ± .08	P		1 ± 0	Type II YSO candidate[e] ; Stage I YSO[h]
052202.72-674702.1		05:22:02.72	-67:47:02.1	3.7 ± 1.1	P		1 ± 0	
052212.57-675832.4*	J052212-675832 NGC 1936 [WSI2008] 579	05:22:12.57	-67:58:32.4	30 ± 5.6	SE	✓	1 ± 0	Type I YSO[e]
052222.46-713532.2	J05222250-7135323 SSTISAGE052222.45-713531.9	05:22:22.46	-71:35:32.2	1.3 ± 0.5	F		1 ± 0	Stage I YSO[h]
052308.60-680006.5	[WSI2008] 609	05:23:08.60	-68:00:06.5	1.1 ± 0.4	PE		1.5 ± 0.5	young star cluster in dark cloud[e]
052333.40-693712.2	SSTISAGE052333.41-693712.0	05:23:33.40	-69:37:12.2	3.8 ± 1.1	S	✓	1 ± 0	Stage I YSO[h]
052350.04-675719.6		05:23:50.04	-67:57:19.6	7.1 ± 2.2	P	✓	1 ± 0	
052601.20-673012.1	SSTISAGE052601.22-673011.8	05:26:01.20	-67:30:12.1	0.92 ± 0.15	SE	✓	1 ± 0	Stage I YSO[h]
052638.55-673923.2		05:26:38.55	-67:39:23.2	0.75 ± 0.23	P		1 ± 0	
053054.24-683428.3*	J053054-683428 IRAS 05311-6836 MSX LMC 596	05:30:54.24	-68:34:28.3	8.1 ± 2.4	S	✓	1 ± 0	HII region[c]
053214.97-711323.9		05:32:14.97	-71:13:23.9	2.4 ± 1.1	PE		1 ± 0	
053217.49-674155.6		05:32:17.49	-67:41:55.6	0.73 ± 0.21	PE		1 ± 0	
053754.82-693435.8	SSTISAGE053754.78-693435.6	05:37:54.82	-69:34:35.8	···	S	✓	···	Stage I YSO[h]
053929.21-694719.0		05:39:29.21	-69:47:19.0	4.6	P	✓	1	Type I YSO[f] ; associated H_2O maser[g]
053931.19-701216.9*	SSTISAGE053931.15-701216.8	05:39:31.19	-70:12:16.9	···	P	✓	···	Stage I YSO[h]
053937.04-694536.7	J05393712-6945370	05:39:37.04	-69:45:36.7	10 ± 3.4	PE	✓	1 ± 0	Type I, Stage 1 YSO[e]
053939.15-691754.6		05:39:39.15	-69:17:54.6	5.2 ± 1.5	P	✓	1 ± 0	

Table 3—Continued

Object ID	Alternate Names	RA (h:m:s)	Dec (d:m:s)	Mean Model Luminosity ($10^4 L_\odot$)	SL09 Spectral Group	Silicate[1] Feature	Mean Model Stage	Literature notes
053953.43-710953.1		05:39:53.43	-71:09:53.1	6.0 ± 2.2	P	✓	1 ± 0	
053955.66-711000.9		05:39:55.66	-71:10:00.9	4.0 ± 1.2	PE		1 ± 0	
053958.39-711005.5		05:39:58.39	-71:10:05.5	3.1 ± 1.1	S	✓	1 ± 0	
053958.52-711014.6		05:39:58.52	-71:10:14.6	3.0 ± 0.9	S	✓	1 ± 0	

[1]Check marks indicate that a principal component analysis by SL09 reveals the presence of strong 9.8 μm silicate absorption feature. Weak features or those heavily blended with nearby PAH emission may not be indentified in the SL09 procedure.

*Sources with CO_2 column densities also determined in other papers. See Table 4 for references.

Note. — The SEDs of YSOs 052016.71-665254.1 and 053754.82-693435.8 could not be fit to radiation transfer models within goodness of fit limits (**?**), and therefore do not have associated modeled luminosities or modeled evolutionary stages. The spectrum of YSO 053931.19-701216.9 has an extremely poor signal-to-noise ratio, and is not included in our CO_2 ice feature decomposition analysis.

Note. — References: (a) **?**, (b) **?**, (c) **?**, (d) **?**, (e) **?**, (f) **?**, (g) **?**, (h) **?**

Table 4. Polar–Apolar Ice Fits

Object ID	$N(CO_2)$ (10^{17} cm^{-2})	5-Component fit						2-Component fit		
		H_2O:CO_2 fraction	CO:CO_2 fraction	Pure CO_2 fraction	Shoulder fraction	Dilute CO_2 fraction	CO:CO_2 mix	H_2O:CO_2 fraction	CO:CO_2 fraction	CO:CO_2 mix
045111.39-692646.7	7.29 ± 0.31	0.67 ± 0.03	0.1 ± 0.02	0.21 ± 0.02	0.02 ± 0.01	0 ± 0	100:70	···	···	···
045400.10-691155.5	16.79 ± 0.47	0.54 ± 0.02	0.16 ± 0.02	0.27 ± 0.01	0.03 ± 0.01	0 ± 0	100:70	···	···	···
045403.04-691139.7	1.87 ± 0.37	0.92 ± 0.07	0.08 ± 0.04	0 ± 0	0 ± 0	0 ± 0	100:26	0.92 ± 0.07	0.08 ± 0.04	100:26
045403.62-671618.5	4.07 ± 0.08	0.54 ± 0.04	0.02 ± 0.02	0.36 ± 0.02	0.08 ± 0.02	0 ± 0	100:8	···	···	···
045524.38-663117.9	8.57 ± 0.24	0.72 ± 0.02	0.11 ± 0.02	0.14 ± 0.01	0.03 ± 0.01	0 ± 0	100:26	···	···	···
045550.62-663434.6	6.93 ± 0.49	0.76 ± 0.02	0 ± 0	0.24 ± 0.01	0 ± 0	0 ± 0	···	···	···	···
045640.79-663230.5	11.88 ± 0.43	0.67 ± 0.02	0.17 ± 0.02	0.13 ± 0.02	0.03 ± 0.01	0.01 ± 0.01	100:70	···	···	···
045742.00-662634.4	4.69 ± 0.46	0.84 ± 0.02	0 ± 0	0.16 ± 0.02	0 ± 0	0 ± 0.02	···	···	···	···
045747.68-662816.9	3.03 ± 0.45	0.45 ± 0.13	0.25 ± 0.11	0.2 ± 0.06	0.07 ± 0.05	0.03 ± 0.06	100:26	0.62 ± 0.06	0.38 ± 0.05	100:70
045842.47-660835.7	12.65 ± 0.54	0.61 ± 0.02	0.1 ± 0.02	0.24 ± 0.01	0.02 ± 0.01	0.02 ± 0.01	100:23	···	···	···
045854.30-660718.9	2.8 ± 0.44	0.6 ± 0.1	0.07 ± 0.08	0.18 ± 0.06	0.07 ± 0.04	0.09 ± 0.04	100:70	0.77 ± 0.05	0.23 ± 0.03	100:70
050435.85-705430.1	2.69 ± 0.25	0.41 ± 0.08	0.26 ± 0.08	0.2 ± 0.07	0.13 ± 0.03	0 ± 0	100:70	···	···	···
051023.69-692620.2	13.98 ± 0.28	0.64 ± 0.04	0.06 ± 0.03	0.29 ± 0.03	0.02 ± 0.02	0 ± 0	100:70	···	···	···
051024.09-701406.5	12.08 ± 0.17	0.65 ± 0.02	0.15 ± 0.02	0.16 ± 0.01	0.04 ± 0.01	0 ± 0	100:70	···	···	···
051351.51-672721.9	1.36 ± 0.05	0 ± 0	0.3 ± 0.07	0.51 ± 0.06	0.15 ± 0.02	0.04 ± 0.03	100:70	···	···	···
051445.43-671204.2	10.25 ± 0.87	0.67 ± 0.04	0.19 ± 0.04	0.09 ± 0.03	0.05 ± 0.02	0.01 ± 0.01	100:70	0.77 ± 0.02	0.23 ± 0.01	100:70
051909.02-691156.1	2.6 ± 0.39	0.56 ± 0.13	0.17 ± 0.11	0.21 ± 0.1	0.06 ± 0.05	0 ± 0	100:70	0.68 ± 0.06	0.32 ± 0.05	100:70
051933.46-694106.7	4.37 ± 0.25	0.85 ± 0.06	0 ± 0.04	0.09 ± 0.04	0.02 ± 0.02	0.02 ± 0.03	···	0.92 ± 0.03	0.08 ± 0.02	100:70
052016.71-665254.1	8.59 ± 0.17	0.57 ± 0.03	0 ± 0	0.33 ± 0.01	0.05 ± 0.01	0.06 ± 0.02	···	···	···	···
052133.20-652920.8	1.51 ± 0.05	0.58 ± 0.07	0 ± 0	0.3 ± 0.03	0.06 ± 0.03	0.06 ± 0.02	···	···	···	···
052155.18-674730.4	7.2 ± 0.92	0.66 ± 0.05	0.31 ± 0.11	0.03 ± 0.08	0 ± 0	0 ± 0	100:70	0.66 ± 0.05	0.34 ± 0.06	100:70
052202.72-674702.1	2.61 ± 0.24	0.6 ± 0.06	0.04 ± 0.03	0.24 ± 0.03	0.12 ± 0.02	0 ± 0	100:26	···	···	···
052212.57-675832.4	3.59 ± 0.2	0.56 ± 0.06	0.17 ± 0.04	0.26 ± 0.03	0.01 ± 0.02	0 ± 0	100:70	···	···	···
052222.46-713532.2	9.23 ± 0.26	0.52 ± 0.04	0.11 ± 0.03	0.28 ± 0.02	0.05 ± 0.01	0.05 ± 0.02	100:70	···	···	···
052308.60-680006.5	7.45 ± 0.21	0.92 ± 0.05	0 ± 0.03	0.06 ± 0.02	0.01 ± 0.02	0 ± 0	···	0.96 ± 0.02	0.04 ± 0.02	100:70
052333.40-693712.2	8.37 ± 0.42	0.71 ± 0.01	0.12 ± 0.02	0.16 ± 0.02	0 ± 0	0 ± 0.01	100:70	···	···	···
052350.04-675719.6	15.43 ± 0.44	0.54 ± 0.02	0.13 ± 0.02	0.27 ± 0.01	0.05 ± 0.01	0 ± 0	100:70	···	···	···
052601.20-673012.1	4.02 ± 0.23	0.52 ± 0.05	0.12 ± 0.03	0.3 ± 0.02	0.06 ± 0.02	0 ± 0	100:26	···	···	···
052638.55-673923.2	1.12 ± 0.16	0.45 ± 0.11	0.16 ± 0.08	0.24 ± 0.06	0.15 ± 0.04	0 ± 0.06	100:26	0.76 ± 0.05	0.24 ± 0.04	100:70
053054.24-683428.3	10.32 ± 0.29	0.58 ± 0.04	0.08 ± 0.02	0.33 ± 0.02	0.01 ± 0.02	0 ± 0	100:26	···	···	···
053214.97-711323.9	6.92 ± 0.98	0.74 ± 0.05	0.08 ± 0.09	0.13 ± 0.1	0 ± 0	0.05 ± 0.05	100:70	0.78 ± 0.05	0.22 ± 0.03	100:70
053217.49-674155.6	3.81 ± 0.51	0.77 ± 0.06	0 ± 0	0.21 ± 0.03	0.02 ± 0.02	0 ± 0	100:70	···	···	···
053754.82-693435.8	7.98 ± 0.85	0.87 ± 0.02	0 ± 0.04	0.11 ± 0.02	0 ± 0	0.02 ± 0.04	···	0.87 ± 0.02	0.13 ± 0.02	100:70
053929.21-694719.0	1.24 ± 0.21	0.59 ± 0.1	0.09 ± 0.07	0.2 ± 0.04	0.12 ± 0.04	0 ± 0.03	100:26	0.81 ± 0.05	0.19 ± 0.03	100:70
053937.04-694536.7	3.74 ± 0.32	0.83 ± 0.05	0 ± 0	0.15 ± 0.02	0.01 ± 0.02	0.01 ± 0.01	100:8	···	···	···
053939.15-691754.6	3.62 ± 0.33	0.8 ± 0.05	0 ± 0	0.19 ± 0.03	0.01 ± 0.02	0.01 ± 0.03	100:8	···	···	···
053953.43-710953.1	2.8 ± 0.03	0.65 ± 0.04	0.14 ± 0.03	0.17 ± 0.02	0.04 ± 0.02	0 ± 0	100:70	···	···	···
053955.66-711000.9	0.8 ± 0.03	0.79 ± 0.12	0.11 ± 0.07	0 ± 0	0.08 ± 0.05	0.01 ± 0.03	100:26	0.95 ± 0.05	0.05 ± 0.02	100:8
053958.39-711005.5	9.55 ± 0.41	0.71 ± 0.03	0.14 ± 0.02	0.12 ± 0.01	0.02 ± 0.01	0 ± 0.01	100:70	···	···	···
053958.52-711014.6	11.06 ± 0.4	0.53 ± 0.03	0.15 ± 0.02	0.28 ± 0.02	0.03 ± 0.01	0 ± 0	100:70	···	···	···

Table 5. Polar–Anealed Ice Fits

Object ID	Annealed H_2O:CH_3OH:CO_2 fit				Annealed H_2O:CO_2 fit			Annealed CH_3OH:CO_2 fit		
	$\chi^2_{anneal}/\chi^2_{5-comp}$	Annealed fraction	H_2O:CH_3OH:CO_2 mixing ratio	Temperature (K)	Annealed fraction	H_2O:CO_2 mixing ratio	Temperature (K)	Annealed fraction	CH_3OH:CO_2 mixing ratio	Temperature (K)
045111.39-692646.7	0.91	0.96 ± 0.03	1.8:0.5:1	125	···	···	···	···	···	···
045400.10-691155.5	1.58	0.92 ± 0.02	1.8:0.5:1	130	0.92 ± 0.02	1:1	100	···	···	···
045403.04-691139.7	0.88	0.7 ± 0.13	4.5:2.4:1	145	0.73 ± 0.15	5.7:1	170	···	···	···
045403.62-671618.5	1.09	1 ± 0.02	2.1:0.1:1	120	0.93 ± 0.06	1:1	105	0.46 ± 0.03	1:1	120
045524.38-663117.9	1.01	0.33 ± 0.02	1:0.9:1	115	···	···	···	0.31 ± 0.01	1:1	115
045550.62-663434.6	1	0.87 ± 0.05	1:1.4:1	105	0.59 ± 0.03	1:1	100	···	···	···
045640.79-663230.5	0.86	0.73 ± 0.03	2.1:0.1:1	130	···	···	···	···	···	···
045742.00-662634.4	0.91	0.79 ± 0.07	2.1:0.1:1	105	0.55 ± 0.05	1:1	90	0.25 ± 0.03	0.1:1	110
045747.68-662816.9	0.93	0.92 ± 0.11	5.3:0.6:1	145	1 ± 0.05	1.9:1	145	0.73 ± 0.08	0.1:1	5
045842.47-660835.7	1.91	0.84 ± 0.03	2.1:0.1:1	130	0.79 ± 0.02	1:1	95	0.6 ± 0.02	0.1:1	25
045854.30-660718.9	1	0.81 ± 0.11	1:1.7:1	105	0.61 ± 0.09	1:1	105	0.75 ± 0.11	1:1	100
050435.85-705430.1	0.94	0.86 ± 0.07	2.1:0.1:1	140	1 ± 0.04	1.9:1	145	···	···	···
051023.69-692620.2	1.03	1 ± 0.02	1.8:0.5:1	125	0.96 ± 0.04	1:1	105	···	···	···
051024.09-701406.5	1.06	0.45 ± 0.01	1:0.9:1	115	···	···	···	···	···	···
051351.51-672721.9	1.16	1 ± 0.04	1:0.9:1	115	···	···	···	0.98 ± 0.07	1:1	120
051445.43-671204.2	1.03	0.95 ± 0.06	2:0.9:1	120	···	···	···	···	···	···
051909.02-691156.1	0.97	0.76 ± 0.11	2.1:0.1:1	135	0.94 ± 0.14	1:1	105	0.6 ± 0.09	1:1	105
051933.46-694106.7	0.95	0.19 ± 0.04	5.3:0.6:1	170	0.71 ± 0.14	1.9:1	95	0.48 ± 0.09	0.5:1	75
052016.71-665254.1	1.18	1 ± 0.02	1:0.9:1	110	0.95 ± 0.04	1:1	105	0.49 ± 0.02	0.1:1	110
052133.20-652920.8	0.98	1 ± 0.03	2.1:0.1:1	100	0.75 ± 0.07	1:1	100	0.44 ± 0.04	0.1:1	110
052155.18-674730.4	0.95	0.6 ± 0.09	4.5:2.4:1	140	1 ± 0.05	1:1	75	0.25 ± 0.04	0.1:1	115
052202.72-674702.1	1.09	0.59 ± 0.07	1:0.9:1	110	0.51 ± 0.06	1:1	105	0.17 ± 0.02	13:1	135
052212.57-675832.4	1.1	0.95 ± 0.04	1.8:0.5:1	130	0.94 ± 0.04	1:1	100	···	···	···
052222.46-713532.2	1.07	0.64 ± 0.02	1:0.9:1	115	0.85 ± 0.03	1:1	100	···	···	···
052308.60-680006.5	0.93	0.08 ± 0.02	1:1.4:1	140	0.73 ± 0.14	1.9:1	100	0.08 ± 0.02	2.9:1	125
052333.40-693712.2	0.98	0.98 ± 0.04	2.1:0.1:1	125	···	···	···	···	···	···
052350.04-675719.6	1.36	0.84 ± 0.02	1.8:0.5:1	130	···	···	···	···	···	···
052601.20-673012.1	0.98	0.84 ± 0.04	1.8:0.5:1	130	0.8 ± 0.04	1:1	100	0.52 ± 0.02	1:1	120
052638.55-673923.2	0.99	0.73 ± 0.11	2.1:0.1:1	130	1 ± 0.04	1.9:1	135	0.36 ± 0.05	1:1	115
053054.24-683428.3	0.98	0.69 ± 0.02	1:0.9:1	115	0.95 ± 0.03	1:1	100	···	···	···
053214.97-711323.9	0.89	0.92 ± 0.1	1:1.4:1	105	1 ± 0.04	1.9:1	130	1 ± 0.04	0.5:1	50
053217.49-674155.6	0.95	0.95 ± 0.1	2.1:0.1:1	100	0.69 ± 0.07	1:1	105	···	···	···
053754.82-693435.8	0.97	0.63 ± 0.08	2.1:0.1:1	90	1 ± 0.02	1:1	15	0.73 ± 0.09	0.5:1	25
053929.21-694719.0	0.97	0.9 ± 0.13	2.1:0.1:1	100	0.94 ± 0.15	1.9:1	135	0.21 ± 0.03	0.1:1	115
053937.04-694536.7	0.89	0.74 ± 0.06	2.1:0.1:1	100	0.74 ± 0.05	1:1	80	0.24 ± 0.02	0.1:1	110
053939.15-691754.6	0.95	0.64 ± 0.07	1:0.9:1	110	0.44 ± 0.05	1:1	100	0.59 ± 0.07	0.5:1	90
053953.43-710953.1	1.01	1 ± 0.01	2.1:0.1:1	120	···	···	···	···	···	···
053955.66-711000.9	0.87	1 ± 0.04	5:1.1:1	140	0.81 ± 0.14	1:1	120	···	···	···
053958.39-711005.5	1.14	0.88 ± 0.03	2.1:0.1:1	115	···	···	···	···	···	···
053958.52-711014.6	1.25	0.94 ± 0.02	1.8:0.5:1	130	0.95 ± 0.03	1:1	100	···	···	···

Table 6. CO_2 Abundance

Object Name	RA	Dec	N(CO_2)	N(H_2O)	N(CO_2)/N(H_2O)	CO_2 Reference	H_2O Reference
045640.79-663230.5	04:56:40.80	–66:32:30.40	11.99 ± 0.42	39.8 ± 5	0.3 ± 0.04	1,2	1
SAGE 051449.41 671221.5	05:14:49.41	–67:12:21.5	7 ± 0.4	19.5 ± 0.78	0.36 ± 0.03	1,3,4	1,4
052212.57-675832.4	05:22:12.56	–67:58:32.2	3.6 ± 0.18	11.68 ± 0.85	0.31 ± 0.03	1,2,4	1,4
IRAS 05240 6809	05:23:51.15	–68:07:12.2	12.85 ± 0.28	27.91 ± 0.95	0.46 ± 0.02	1,3,4	1,5
SAGE 052546.49 661411.3	05:25:46.69	–66:14:11.3	8.85 ± 0.18	34.59 ± 2.97	0.26 ± 0.02	1,3,4	1,4
ST11	05:26:46.63	–68:48:47.10	0.9 ± 0.23	8.9 ± 0.3	0.1 ± 0.03	1	1
053054.24-683428.3	05:30:54.27	–68:34:28.2	10.3 ± 0.27	26.45 ± 1.19	0.39 ± 0.02	1,2,4	1,4
IRAS 05328 6827	05:32:38.59	–68:25:22.20	0.9 ± 0.11	2.49 ± 0.11	0.36 ± 0.05	1,3	1,6
ST8	05:37:28.17	–69:08:47.00	9.34 ± 1.1	20.1 ± 1.2	0.46 ± 0.06	1	1
053931.19-701216.9	05:39:31.15	–70:12:16.80	5.68 ± 0.62	19.88 ± 0.86	0.29 ± 0.03	1,2,4	1,4
ST6	05:39:41.08	–69:29:16.8	17.1 ± 3	47.6 ± 14.77	0.36 ± 0.13	1	1,4

Note. — Reference: 1) **?**, 2) This paper, 3) **?**, 4) **?**, 5) Recalculated by **?** from spectra in **?**, 6) Estimated from Figure 1 of **?** by **?**.

Table 7. Observations

Region	Observation Dates	Number of Mosaic Pointings	HCO^+ Beam Size [arcsec × arcsec]	HCO^+ Peak Sensitivity [Jy/beam]	HCN Peak Sensitivity [Jy/beam]	Spectral Channel Width km s^{-1}
N105	October 2007	10	6.4×5.8	0.039	0.041	0.2
N113	September 2007	9	6.3×5.8	0.035	0.025	0.2
N159	September 2006	40	6.3×5.7	0.035	0.034	0.4
N44 North (Region 1)	August 2008	36	5.5×6.5	0.034	0.036	0.4
N44 South (Region 2)	August 2008	9	6.0×7.2	0.032	0.034	0.4

Table 8. Clump Properties

Clump ID Number	RA (J2000)	Dec (J2000)	Δv [km/sec]	CPROPS Radius [pc]	Virial Mass [$M_\odot$]	Luminosity Mass [$M_\odot$]	HCO^+ flux [Jy km/sec]	HCN flux [Jy km/sec]	Class[a]
				N105					
1	05:09:52.2	–68:53:28	4.06 ± 0.29	1.7 ± 0.2	5.2 ± 0.9 $\times 10^3$	8.0 ± 0.7 $\times 10^3$	7.55 ± 0.70	3.43 ± 0.72	CM, maser
2	05:09:49.6	–68:54:03	2.49 ± 0.48	···	···	9.2 ± 1.0 $\times 10^2$	0.87 ± 0.09	0.29 ± 0.09	I
3	05:09:52.2	–68:53:01	3.02 ± 0.40	0.6 ± 0.3	1.0 ± 0.4 $\times 10^3$	2.0 ± 0.2 $\times 10^3$	1.86 ± 0.17	0.43 ± 0.18	CM
4	05:09:50.4	–68:53:04	4.20 ± 0.31	1.5 ± 0.2	5.0 ± 0.9 $\times 10^3$	6.5 ± 0.6 $\times 10^3$	6.10 ± 0.53	2.15 ± 0.54	CM
5	05:09:51.7	–68:52:45	1.70 ± 0.53	···	···	5.6 ± 0.8 $\times 10^2$	0.53 ± 0.08	0.12 ± 0.08	N
				N113					
1	05:13:17.4	–69:22:23	6.24 ± 0.44	···	···	1.1 ± 0.2 $\times 10^4$	10.02 ± 1.67	5.78 ± 1.39	CM, maser
2	05:13:16.8	–69:22:40	3.56 ± 0.75	1.1 ± 0.7	2.6 ± 2.0 $\times 10^3$	4.7 ± 0.8 $\times 10^3$	4.41 ± 0.79	2.52 ± 0.66	I
3	05:13:18.1	–69:22:05	2.74 ± 0.25	···	···	7.0 ± 1.7 $\times 10^2$	0.66 ± 0.16	0.41 ± 0.13	N
4	05:13:18.7	–69:21:50	4.48 ± 0.61	0.5 ± 0.1	1.9 ± 0.7 $\times 10^3$	9.2 ± 2.3 $\times 10^2$	0.87 ± 0.22	0.41 ± 0.19	EM
5	05:13:21.0	–69:22:42	5.05 ± 0.46	1.5 ± 0.2	7.2 ± 1.5 $\times 10^3$	3.3 ± 0.8 $\times 10^3$	3.11 ± 0.80	1.65 ± 0.66	CM
6	05:13:25.2	–69:22:46	4.88 ± 0.52	0.7 ± 0.1	3.1 ± 0.9 $\times 10^3$	4.3 ± 0.7 $\times 10^3$	4.05 ± 0.68	1.67 ± 0.56	CM, maser
				N159					
1	05:39:37.4	–69:46:09	3.89 ± 0.61	1.5 ± 0.4	4.2 ± 1.7 $\times 10^3$	2.4 ± 0.5 $\times 10^3$	2.26 ± 0.49	0.48 ± 0.47	EM
2	05:39:37.3	–69:46:16	1.47 ± 0.69	···	···	2.5 ± 1.5 $\times 10^2$	0.24 ± 0.14	0.10 ± 0.13	N
3	05:39:29.9	–69:47:21	3.43 ± 0.57	0.7 ± 0.2	1.5 ± 0.7 $\times 10^3$	3.2 ± 0.4 $\times 10^3$	2.99 ± 0.40	0.96 ± 0.37	EM, maser
4	05:40:08.1	–69:44:41	2.56 ± 0.61	1.2 ± 0.3	1.4 ± 0.8 $\times 10^3$	1.7 ± 0.4 $\times 10^3$	1.62 ± 0.40	0.42 ± 0.39	EM
5	05:40:04.4	–69:44:34	3.17 ± 0.38	1.4 ± 0.4	2.6 ± 0.9 $\times 10^3$	4.5 ± 0.6 $\times 10^3$	4.23 ± 0.53	1.74 ± 0.50	EM
6	05:40:05.0	–69:44:23	2.52 ± 0.61	0.8 ± 0.3	9.5 ± 5.6 $\times 10^2$	1.7 ± 0.3 $\times 10^3$	1.62 ± 0.26	0.62 ± 0.25	N
7	05:39:36.6	–69:45:36	7.41 ± 0.60	2.5 ± 0.2	2.6 ± 0.4 $\times 10^4$	1.8 ± 0.3 $\times 10^4$	16.54 ± 2.67	5.83 ± 2.52	CM, maser
8	05:40:02.9	–69:44:59	3.44 ± 0.89	···	···	1.1 ± 0.2 $\times 10^3$	1.02 ± 0.20	0.34 ± 0.19	N
9	05:39:40.9	–69:46:35	3.16 ± 0.94	···	···	7.5 ± 2.1 $\times 10^2$	0.71 ± 0.19	0.14 ± 0.20	I
10	05:39:58.6	–69:45:05	3.87 ± 0.45	0.5 ± 0.1	1.4 ± 0.5 $\times 10^3$	3.9 ± 1.6 $\times 10^3$	3.65 ± 0.40	1.84 ± 0.51	N
11	05:39:41.8	–69:46:10	2.70 ± 1.26	0.4 ± 0.5	5.5 ± 8.6 $\times 10^2$	6.1 ± 0.6 $\times 10^2$	0.58 ± 0.12	0.17 ± 0.15	CM
12	05:39:44.9	–69:45:10	1.55 ± 0.59	···	···	8.8 ± 0.3 $\times 10^2$	0.83 ± 0.19	0.16 ± 0.19	N
13	05:39:42.4	–69:45:08	2.13 ± 0.38	···	···	1.6 ± 1.9 $\times 10^3$	1.56 ± 0.25	0.44 ± 0.38	N
14	05:39:43.5	–69:45:08	2.03 ± 0.70	···	···	9.3 ± 1.9 $\times 10^2$	0.88 ± 0.20	0.10 ± 0.13	N
				N44 Region 1					
1	05:22:05.7	–67:57:51	4.89 ± 0.14	1.5 ± 0.4	6.7 ± 0.4 $\times 10^3$	3.3 ± 0.7 $\times 10^3$	3.15 ± 0.70	0.36 ± 0.13	I
2.1	05:22:03.4	–67:57:44	3.54 ± 0.18	1.4 ± 0.5	3.3 ± 0.3 $\times 10^3$	3.4 ± 0.8 $\times 10^3$	3.23 ± 0.80	0.76 ± 0.18	I
2.2	05:22:02.1	–67:57:51	3.13 ± 0.15	1.6 ± 0.8	3.0 ± 0.3 $\times 10^3$	4.5 ± 1.0 $\times 10^3$	4.21 ± 0.91	0.85 ± 0.18	CM
3	05:22:12.6	–67:58:32	5.15 ± 0.25	1.0 ± 0.1	5.2 ± 0.5 $\times 10^3$	3.6 ± 0.6 $\times 10^3$	3.37 ± 0.57	0.94 ± 0.13	CM
4	05:22:08.5	–67:58:06	2.29 ± 0.21	···	···	9.7 ± 3.8 $\times 10^2$	0.91 ± 0.36	0.05 ± 0.05	I
5	05:22:12.3	–67:58:14	4.30 ± 0.16	1.6 ± 0.3	5.6 ± 0.4 $\times 10^3$	4.6 ± 0.9 $\times 10^3$	4.31 ± 0.84	0.57 ± 0.16	I
6	05:22:07.8	–67:58:27	4.21 ± 0.39	1.4 ± 0.4	4.8 ± 0.9 $\times 10^3$	3.8 ± 0.9 $\times 10^3$	3.61 ± 0.89	0.48 ± 0.14	EM
7	05:22:00.4	–67:57:38	1.09 ± 0.22	···	···	6.2 ± 2.7 $\times 10^2$	0.58 ± 0.26	0.01 ± 0.05	N
				N44 Region 2					
1	05:22:54.3	-68:04:29	3.92 ± 0.50	···	···	8.0 ± 2.3 $\times 10^2$	0.76 ± 0.22	0.06 ± 0.07	N
2	05:22:51.8	-68:04:16	1.72 ± 0.22	···	···	4.7 ± 1.3 $\times 10^2$	0.45 ± 0.12	0.07 ± 0.05	N

Table 8—Continued

Clump ID Number	RA (J2000)	Dec (J2000)	Δv [km/sec]	CPROPS Radius [pc]	Virial Mass [$M_\odot$]	Luminosity Mass [$M_\odot$]	HCO^+ flux [Jy km/sec]	HCN flux [Jy km/sec]	Class[a]
3	05:22:56.8	-68:04:10	2.30 ± 0.19	···	···	9.0 ± 2.2 $\times 10^2$	0.85 ± 0.21	0.09 ± 0.27	EM
4	05:22:55.2	-68:04:07	3.19 ± 0.18	···	···	1.5 ± 0.4 $\times 10^3$	1.39 ± 0.34	0.07 ± 0.07	EM
5	05:22:58.2	-68:03:47	2.07 ± 0.38	···	···	5.8 ± 1.4 $\times 10^2$	0.55 ± 0.13	0.14 ± 0.07	I
6	05:22:53.9	-68:04:32	1.15 ± 0.13	···	···	2.6 ± 0.6 $\times 10^2$	0.24 ± 0.06	0.01 ± 0.02	N

[a]Clump classes: N – No YSO in clump; CM – Centralized massive YSO in clump; EM – Massive YSO only on the edge of the clump; I – Intermediate mass YSO in clump, no massive YSO in clump. Clumps with previously-identified maser activity are also indicated.

Table 9. YSO Properties

YSO ID	RA (J2000)	Dec (J2000)	Clump[a] located in	[8.0][b]	IRS Group[c]	PCA silicate strength	Closeness factor	HCO^+ Flux Density [Jy/beam km s^{-1})]	Notes
				N105					
050949.80–685402.1	05:09:49.80	–68:54:02.1	2	7.80 ± 0.08	···	···	0.15	0.82 ± 0.12	
050950.11–685349.4	05:09:50.11	–68:53:49.4	···	9.35 ± 0.11	···	···	2.18	0.13 ± 0.11	
050950.12–685426.9	05:09:50.12	–68:54:26.9	···	8.16 ± 0.09	···	···	3.15	0.14 ± 0.15	
050950.53–685305.5	05:09:50.53	–68:53:05.5	4	5.24 ± 0.05	P	0.18	0.25	2.55 ± 0.11	
050952.26–685327.3	05:09:52.26	–68:53:27.3	1	6.82 ± 0.07	PE	0.57	0.23	2.92 ± 0.11	maser
050952.73–685300.7	05:09:52.73	–68:53:00.7	3	5.86 ± 0.08	PE	0.06	0.41	1.49 ± 0.11	
050953.89–685336.7	05:09:53.89	–68:53:36.7	1	7.85 ± 0.07	P	0.40	0.83	0.61 ± 0.12	
				N113					
051315.73–692135.9	05:13:15.73	–69:21:35.9	···	6.97 ± 0.06	PE	0.06	5.13	0.21 ± 0.14	
051317.30–692236.7	05:13:17.30	–69:22:36.7	2	···	···	···	0.54	2.23 ± 0.08	
051317.54–692208.5	05:13:17.54	–69:22:08.5	(3)	9.45 ± 0.13	···	···	1.13	0.40 ± 0.09	
051317.69–692225.0	05:13:17.69	–69:22:25.0	1	5.62 ± 0.06	PE	0.23	0.45	4.28 ± 0.07	maser
051318.26–692135.5	05:13:18.26	–69:21:35.5	···	7.98 ± 0.07	PE	–0.25	3.18	0.00 ± 0.12	
051319.14–692151.0	05:13:19.14	–69:21:51.0	4	6.78 ± 0.07	PE	–0.03	0.93	0.96 ± 0.10	
051320.75–692151.4	05:13:20.75	–69:21:51.4	···	8.75 ± 0.10	···	···	3.08	0.00 ± 0.13	
051321.43–692241.5	05:13:21.43	–69:22:41.5	5	5.67 ± 0.07	PE	0.15	0.50	1.87 ± 0.08	
051325.09–692245.1	05:13:25.09	–69:22:45.1	6	5.53 ± 0.06	P	0.32	0.09	3.90 ± 0.11	maser
				N159					
053929.21–694719.0	05:39:29.21	–69:47:19.0	3	7.20 ± 0.07	P	0.36	0.69	1.41 ± 0.14	Type I; maser
053935.99–694604.1	05:39:35.99	–69:46:04.1	(1)	6.84 ± 0.06	PE	–0.08	1.10	0.24 ± 0.10	Type I
053937.04–694536.7	05:39:37.04	–69:45:36.7	7	6.60 ± 0.07	PE	0.68	0.41	3.88 ± 0.09	Type I
053937.53–694609.8	05:39:37.53	–69:46:09.8	1	5.82 ± 0.06	PE	0.04	0.29	1.70 ± 0.10	Type I/II
053937.56–694525.3	05:39:37.56	–69:45:25.3	7	6.13 ± 0.08	PE	0.37	0.33	3.68 ± 0.09	Type I
053940.78–694632.1	05:39:40.78	–69:46:32.1	9	8.02 ± 0.07	···	···	0.65	0.65 ± 0.09	Type II
053941.89–694612.0	05:39:41.89	–69:46:12.0	11	5.93 ± 0.06	PE	0.38	0.25	2.87 ± 0.10	Type I/II
053943.74–694540.3	05:39:43.74	–69:45:40.3	···	9.91 ± 0.05	···	···	3.28	0.15 ± 0.20	Type III
053945.18–694450.4	05:39:45.18	–69:44:50.4	···	7.44 ± 0.06	PE	0.05	3.03	0.00 ± 0.11	Type III
053947.68–694526.1	05:39:47.68	–69:45:26.1	···	8.14 ± 0.03	···	···	3.10	0.19 ± 0.11	Type II
053951.60–694510.5	05:39:51.60	–69:45:10.5	···	···	PE	···	4.92	0.18 ± 0.10	
053952.60–694517.0	05:39:52.60	–69:45:17.0	···	8.14 ± 0.03	···	···	4.97	0.00 ± 0.10	Type III
053959.34–694526.3	05:39:59.34	–69:45:26.3	···	6.54 ± 0.06	PE	–0.37	4.07	0.00 ± 0.20	Type II
054004.39–694437.6	05:40:04.39	–69:44:37.6	5	5.40 ± 0.06	PE	0.04	0.57	2.08 ± 0.10	Type III; The Papillon
054009.49–694453.5	05:40:09.49	–69:44:53.5	(4)	7.31 ± 0.07	PE	0.29	1.60	0.53 ± 0.10	Type I/II
				N44 Region 1					
052156.97–675700.1	05:21:56.97	–67:57:00.1	···	10.03 ± 0.10	PE	0.06	7.28	0.00 ± 0.09	Type III (O8.5V+N)
052159.6–675721.7	05:21:59.6	–67:57:21.7	···	10.09 ± 0.24	···	···	3.64	0.27 ± 0.09	Type III (O7.5V+N)
052202.0–675758.2	05:22:02.0	–67:57:58.2	(2.2)	7.77 ± 0.03	···	···	1.31	0.15 ± 0.09	Type II
052202.11–675753.6	05:22:02.11	–67:57:53.6	2.2	7.68 ± 0.70	PE	0.29	0.49	1.24 ± 0.08	Type II
052203.30–675747.0	05:22:03.30	–67:57:47.0	2.1	8.36 ± 0.11	PE	0.15	0.43	1.95 ± 0.08	Type I/II
052203.9–675743.7	05:22:03.9	–67:57:43.7	2.1	8.98 ± 0.10	···	···	0.49	1.64 ± 0.09	Type II
052204.8–675744.6	05:22:04.8	–67:57:44.6	(2.1)	8.76 ± 0.20	···	···	1.07	0.00 ± 0.09	Type II/III

Table 9—Continued

YSO ID	RA (J2000)	Dec (J2000)	Clump[a] located in	[8.0][b]	IRS Group[c]	PCA silicate strength	Closeness factor	HCO^+ Flux Density [Jy/beam km s^{-1})]	Notes
052205.2–675741.6	05:22:05.2	–67:57:41.6	(1)	8.61 ± 0.23	···	···	1.64	0.06 ± 0.09	
052205.3–675748.5	05:22:05.3	–67:57:48.5	1	8.13 ± 0.04	···	···	0.59	0.94 ± 0.09	Type II
052206.28–675659.1	05:22:06.28	–67:56:59.1	···	8.40 ± 0.06	···	···	6.64	0.00 ± 0.09	Type II
052207.27–675819.7	05:22:07.27	–67:58:19.7	(6)	8.00 ± 0.06	PE	–0.13	1.32	0.00 ± 0.08	Type III
052207.32–675826.8	05:22:07.32	–67:58:26.8	6	8.30 ± 0.08	···	···	0.49	1.12 ± 0.08	Type II
052208.6–675805.5	05:22:08.6	–67:58:05.5	4	9.01 ± 0.09	···	···	0.17	0.84 ± 0.09	
052211.86–675818.1	05:22:11.86	–67:58:18.1	5	8.95 ± 0.08	···	···	0.75	0.95 ± 0.09	Type I
052212.24–675813.2	05:22:12.24	–67:58:13.2	5	8.97 ± 0.10	···	···	0.13	1.92 ± 0.09	Type II/III
052212.57–675832.3	05:22:12.57	–67:58:32.4	3	5.08 ± 0.05	SE	0.44	0.24	2.31 ± 0.09	Type I
N44 Region 2									
052251.62–680436.6	05:22:51.62	–68:04:36.6	···	8.60 ± 0.09	···	···	2.18	0.13 ± 0.10	Star near dark cloud?
052255.12–680409.4	05:22:55.12	–68:04:09.4	4	7.64 ± 0.07	PE	–0.03	0.55	0.95 ± 0.08	Type II
052256.79–680406.8	05:22:56.79	–68:04:06.8	3	7.77 ± 0.07	PE	–0.16	0.70	0.33 ± 0.08	Type II
052257.55–680414.1	05:22:57.55	–68:04:14.1	3	8.60 ± 0.07	···	···	0.92	0.28 ± 0.08	Type I/II
052259.0–680346.3	05:22:59.0	–68:03:46.3	5	10.46 ± 0.14	···	···	0.94	0.41 ± 0.14	Type II

[a]Column indicates which clump the YSO candidate is located in. Clump numbers in parenthesis indicate that while the YSO in not located within the clump, the YSO's proximity to the clump suggests that it may have once been associated with it.

[b]Sources without a listed [8.0] value do not have associated 8 μm point sources.

[c]IRS Spectral Classes: S – Silicate absorption only; SE – Silicate absorption and fine-structure lines; P – PAH emission; PE – PAH emission and fine-structure lines

Appendix A

Presented are the spectra for every embedded source presented in Chapter 2, a sample of which was presented in Figure 1. Spectra are ordered by spectral Group and then by increasing RA.

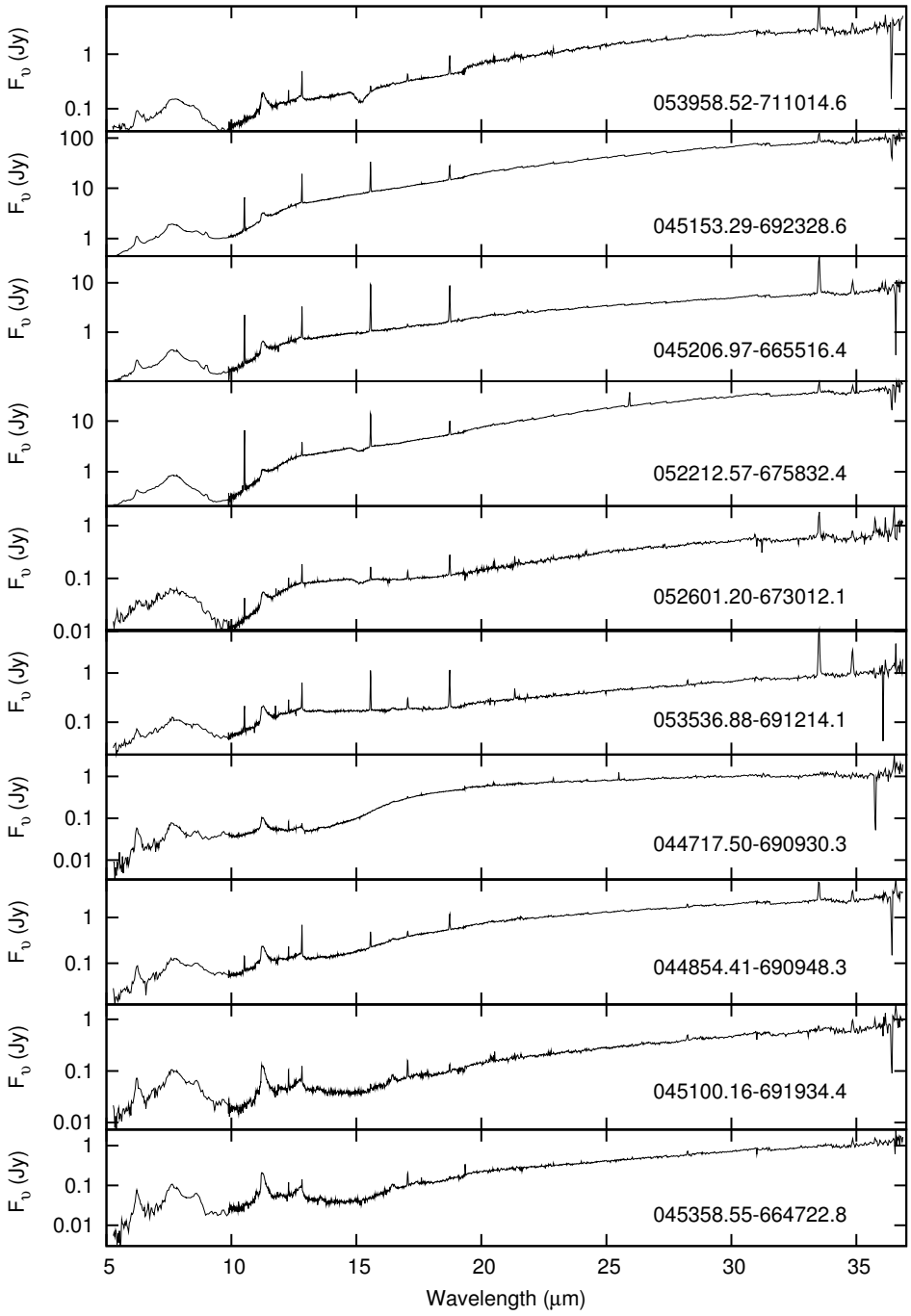
F$_\upsilon$ (Jy)
053958.52-711014.6
045153.29-692328.6
045206.97-665516.4
052212.57-675832.4
052601.20-673012.1
053536.88-691214.1
044717.50-690930.3
044854.41-690948.3
045100.16-691934.4
045358.55-664722.8
Wavelength (μm)

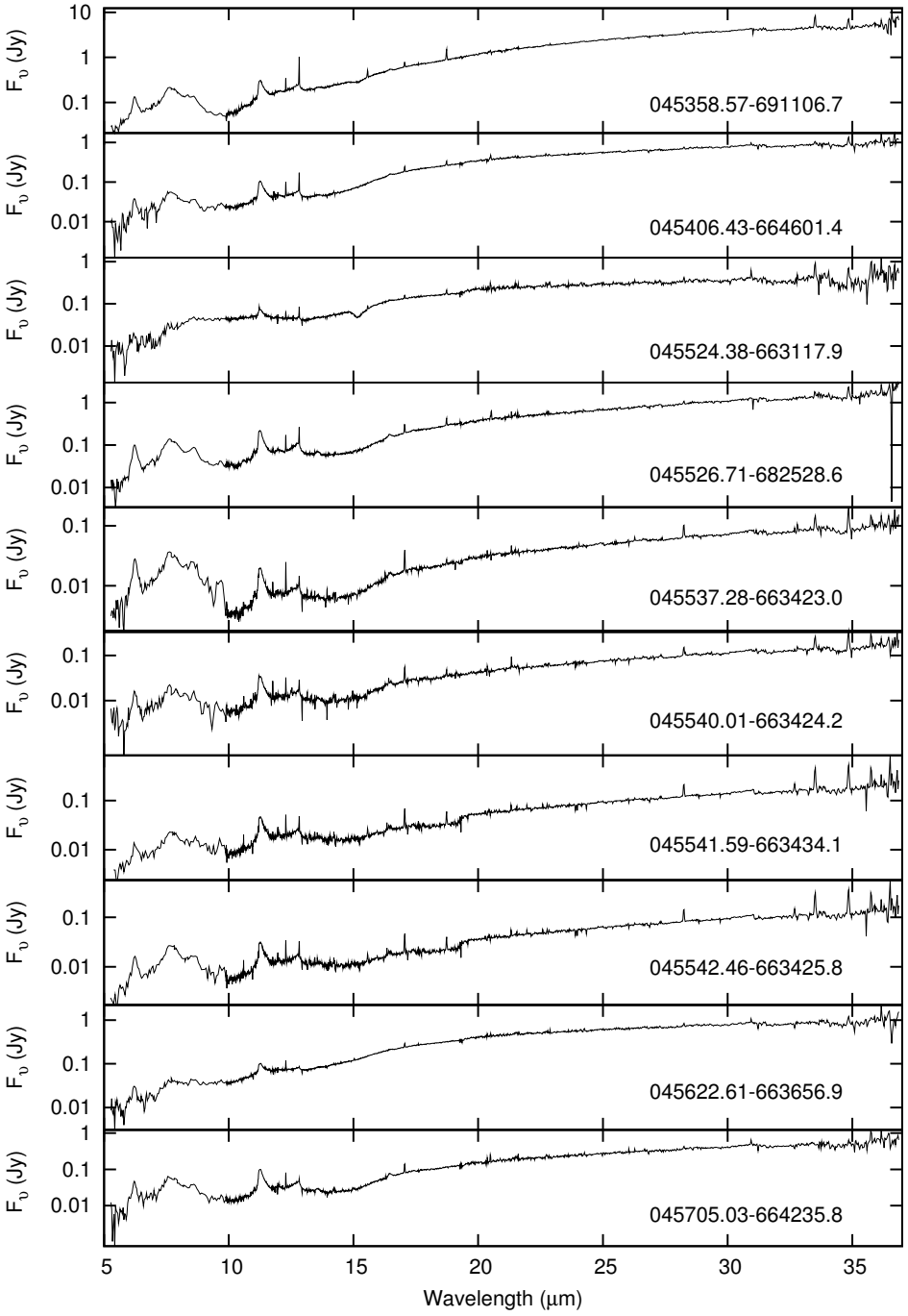
F$_\upsilon$ (Jy)
045358.57-691106.7
045406.43-664601.4
045524.38-663117.9
045526.71-682528.6
045537.28-663423.0
045540.01-663424.2
045541.59-663434.1
045542.46-663425.8
045622.61-663656.9
045705.03-664235.8
Wavelength (μm)

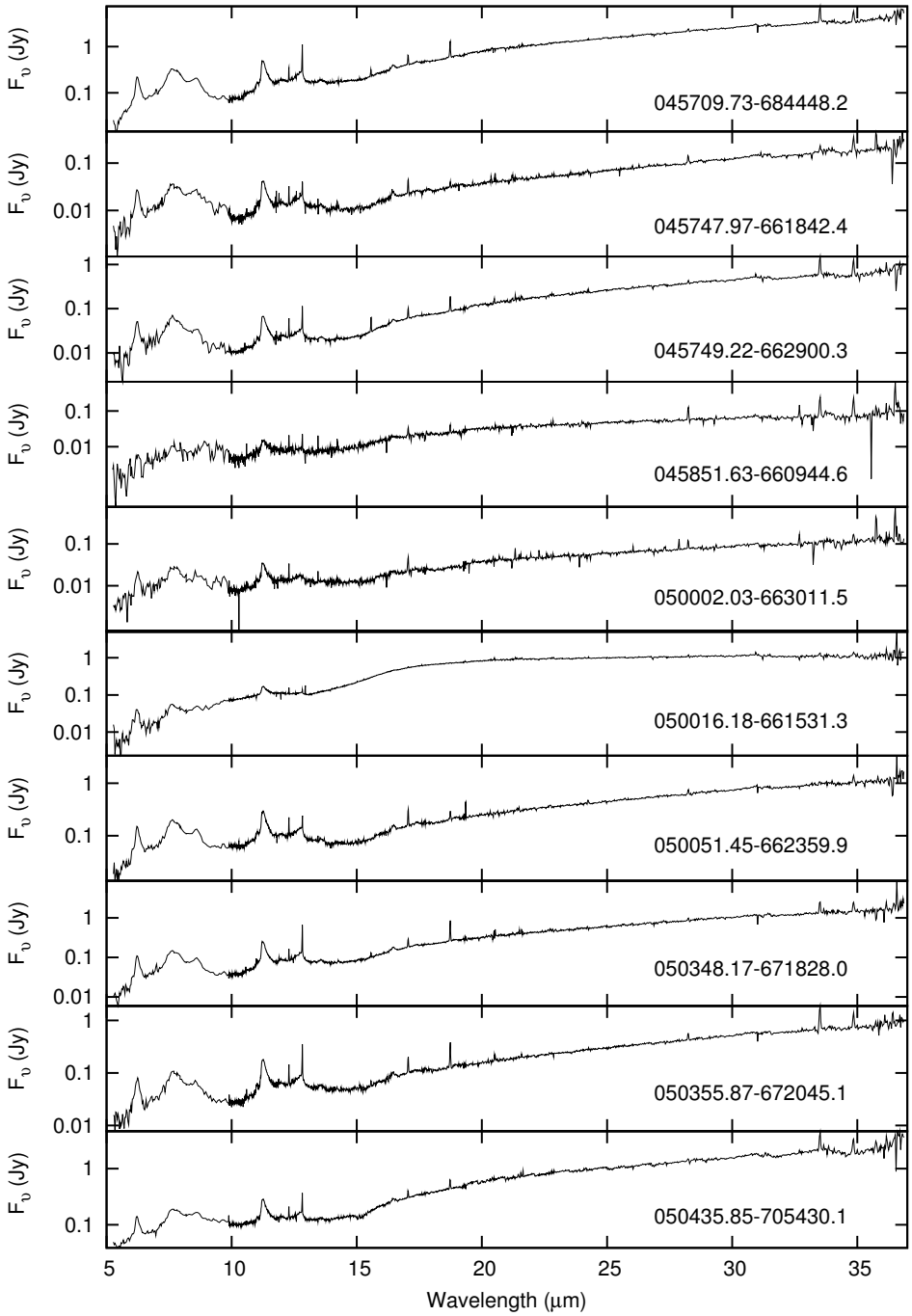
F$_\upsilon$ (Jy)
045709.73-684448.2
045747.97-661842.4
045749.22-662900.3
045851.63-660944.6
050002.03-663011.5
050016.18-661531.3
050051.45-662359.9
050348.17-671828.0
050355.87-672045.1
050435.85-705430.1
Wavelength (μm)

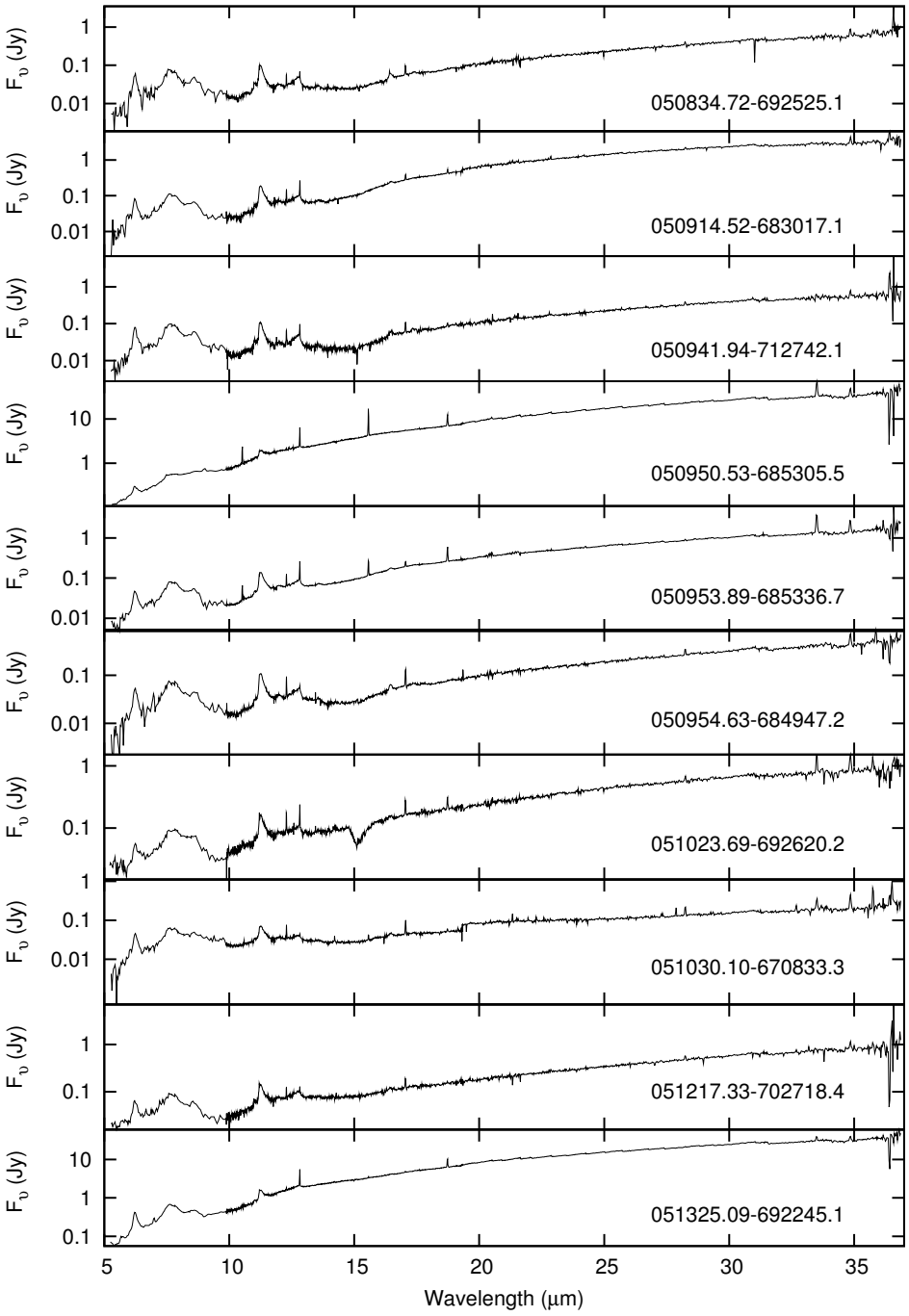
F$_\upsilon$ (Jy)
050834.72-692525.1
050914.52-683017.1
050941.94-712742.1
050950.53-685305.5
050953.89-685336.7
050954.63-684947.2
051023.69-692620.2
051030.10-670833.3
051217.33-702718.4
051325.09-692245.1
Wavelength (μm)

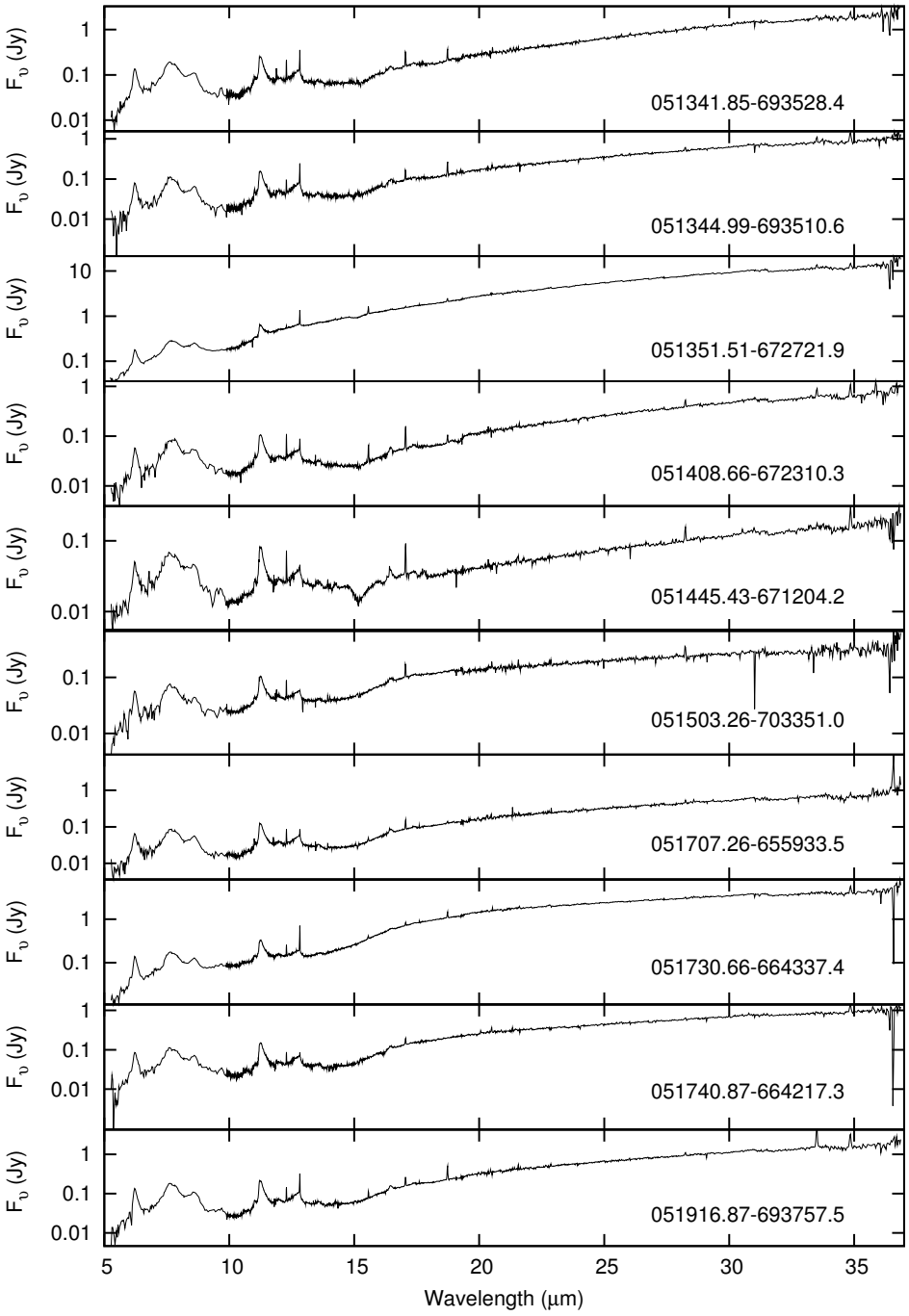
F$_\upsilon$ (Jy)
051341.85-693528.4
051344.99-693510.6
051351.51-672721.9
051408.66-672310.3
051445.43-671204.2
051503.26-703351.0
051707.26-655933.5
051730.66-664337.4
051740.87-664217.3
051916.87-693757.5
Wavelength (μm)

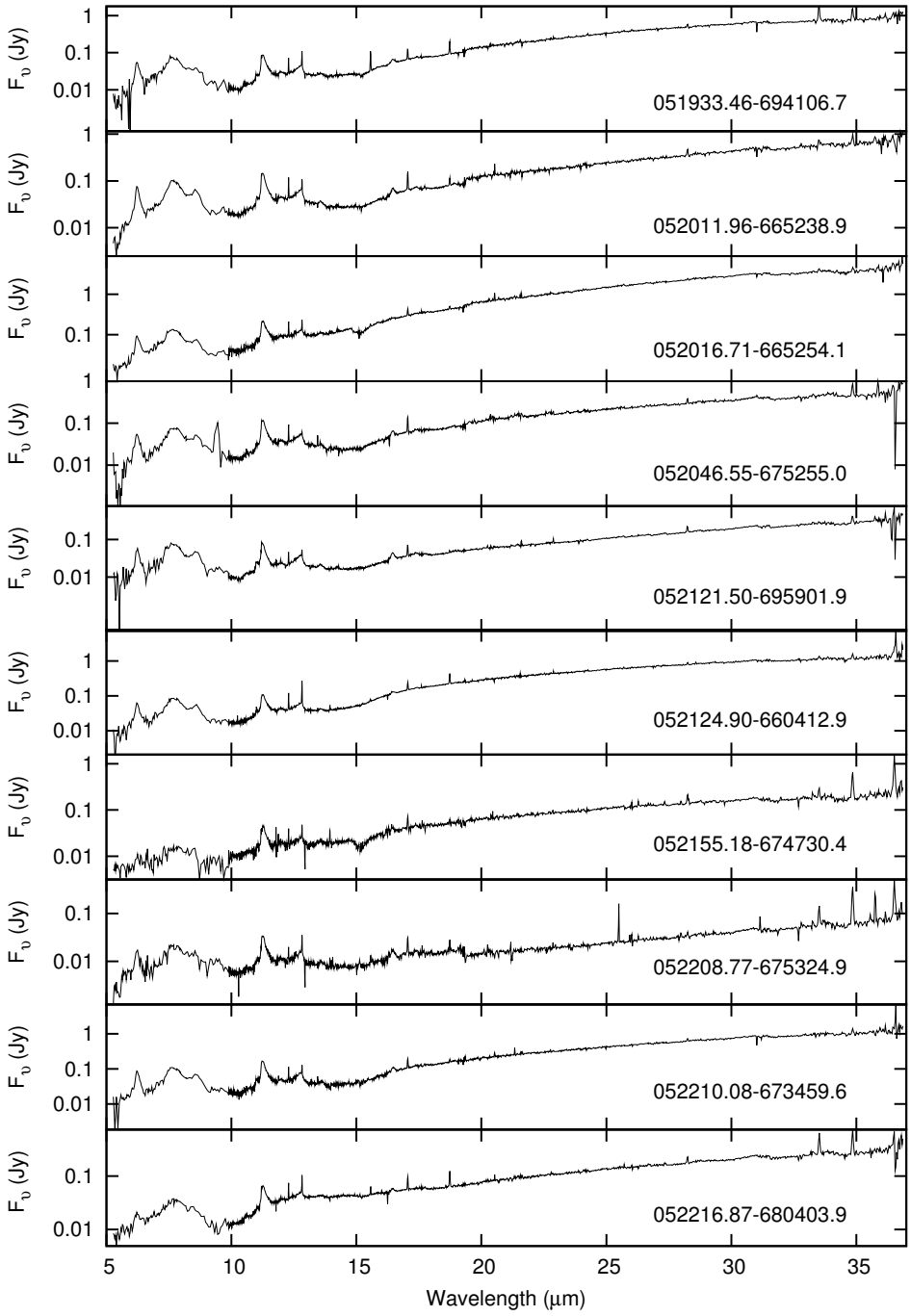
F$_\upsilon$ (Jy)
1
0.1
0.01
051933.46-694106.7
052011.96-665238.9
052016.71-665254.1
052046.55-675255.0
052121.50-695901.9
052124.90-660412.9
052155.18-674730.4
052208.77-675324.9
052210.08-673459.6
052216.87-680403.9
5
10
15
20
25
30
35
Wavelength (μm)

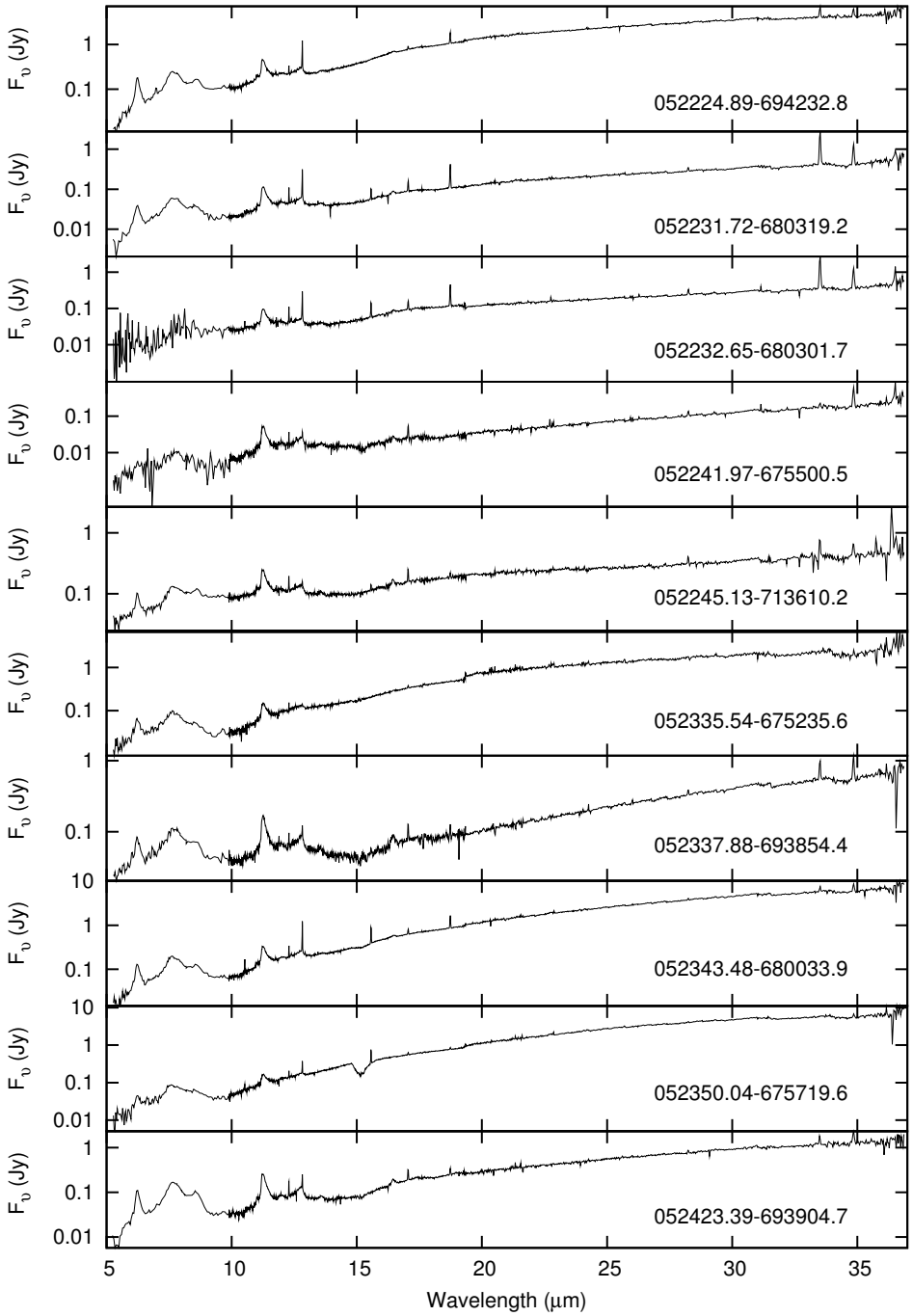
F$_\upsilon$ (Jy)
052224.89-694232.8
052231.72-680319.2
052232.65-680301.7
052241.97-675500.5
052245.13-713610.2
052335.54-675235.6
052337.88-693854.4
052343.48-680033.9
052350.04-675719.6
052423.39-693904.7
Wavelength (μm)

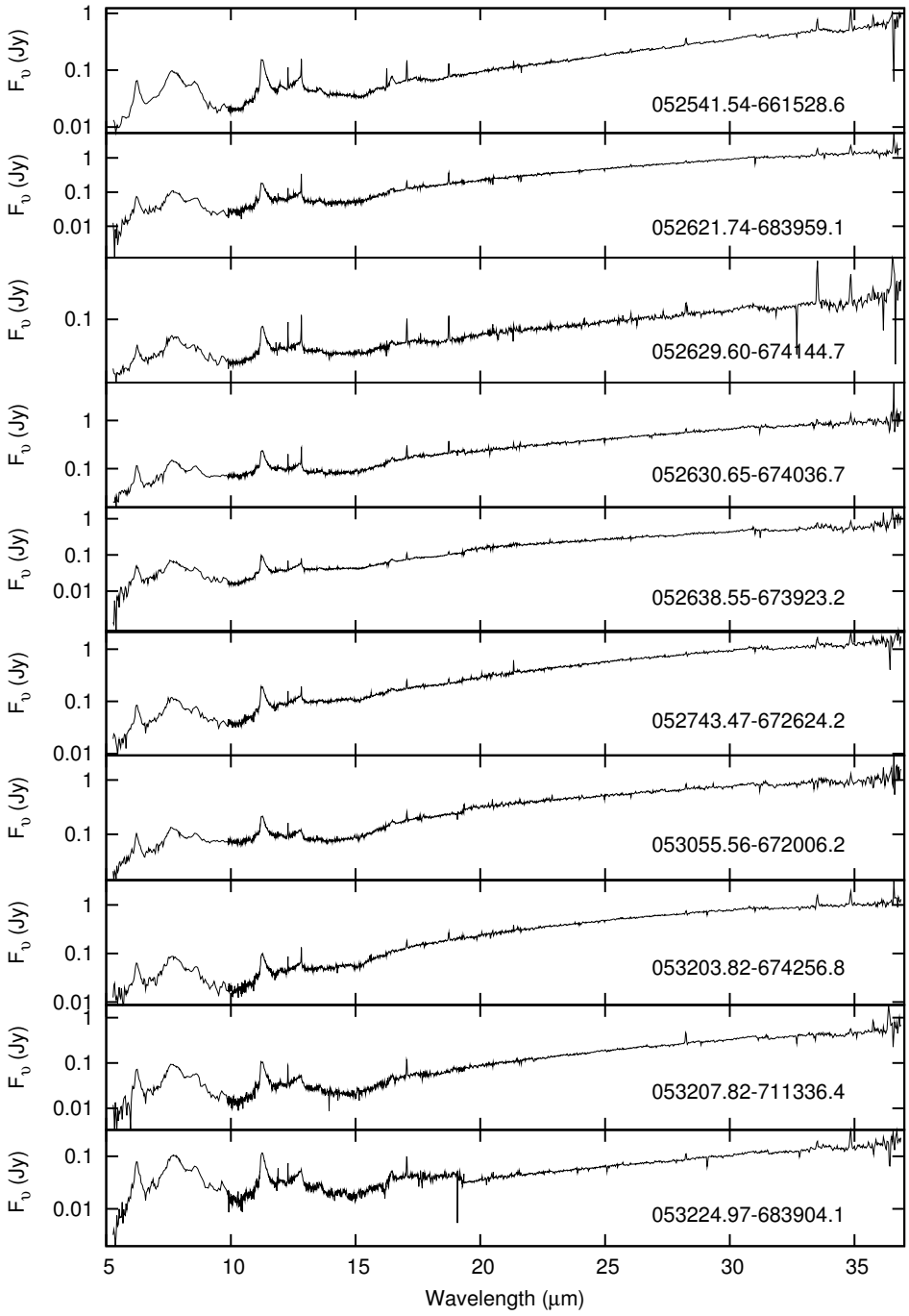
F$_\upsilon$ (Jy)
1
0.1
0.01
052541.54-661528.6
052621.74-683959.1
052629.60-674144.7
052630.65-674036.7
052638.55-673923.2
052743.47-672624.2
053055.56-672006.2
053203.82-674256.8
053207.82-711336.4
053224.97-683904.1
5
10
15
20
25
30
35
Wavelength (μm)

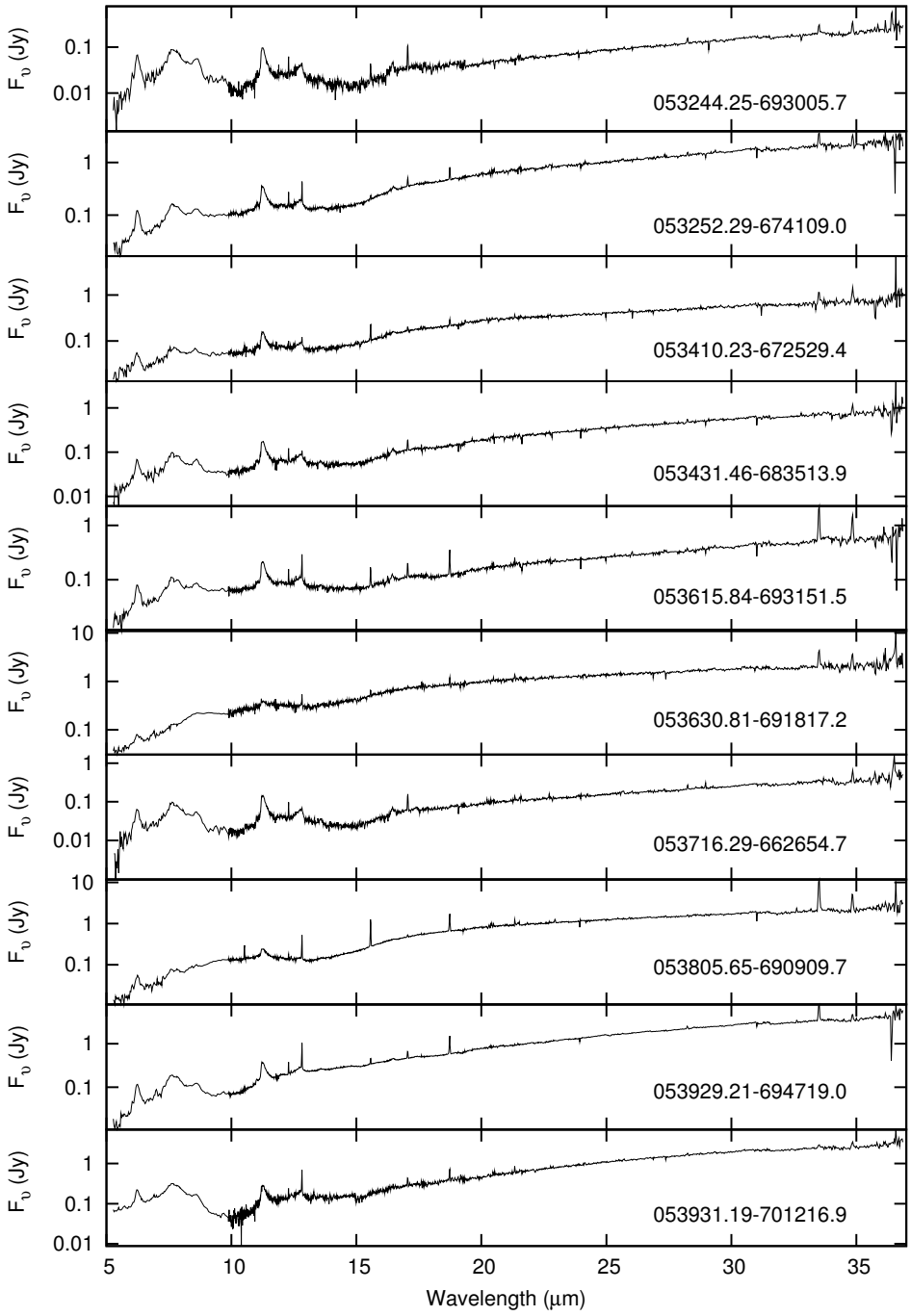
F$_\upsilon$ (Jy)
053244.25-693005.7
053252.29-674109.0
053410.23-672529.4
053431.46-683513.9
053615.84-693151.5
053630.81-691817.2
053716.29-662654.7
053805.65-690909.7
053929.21-694719.0
053931.19-701216.9
Wavelength (μm)

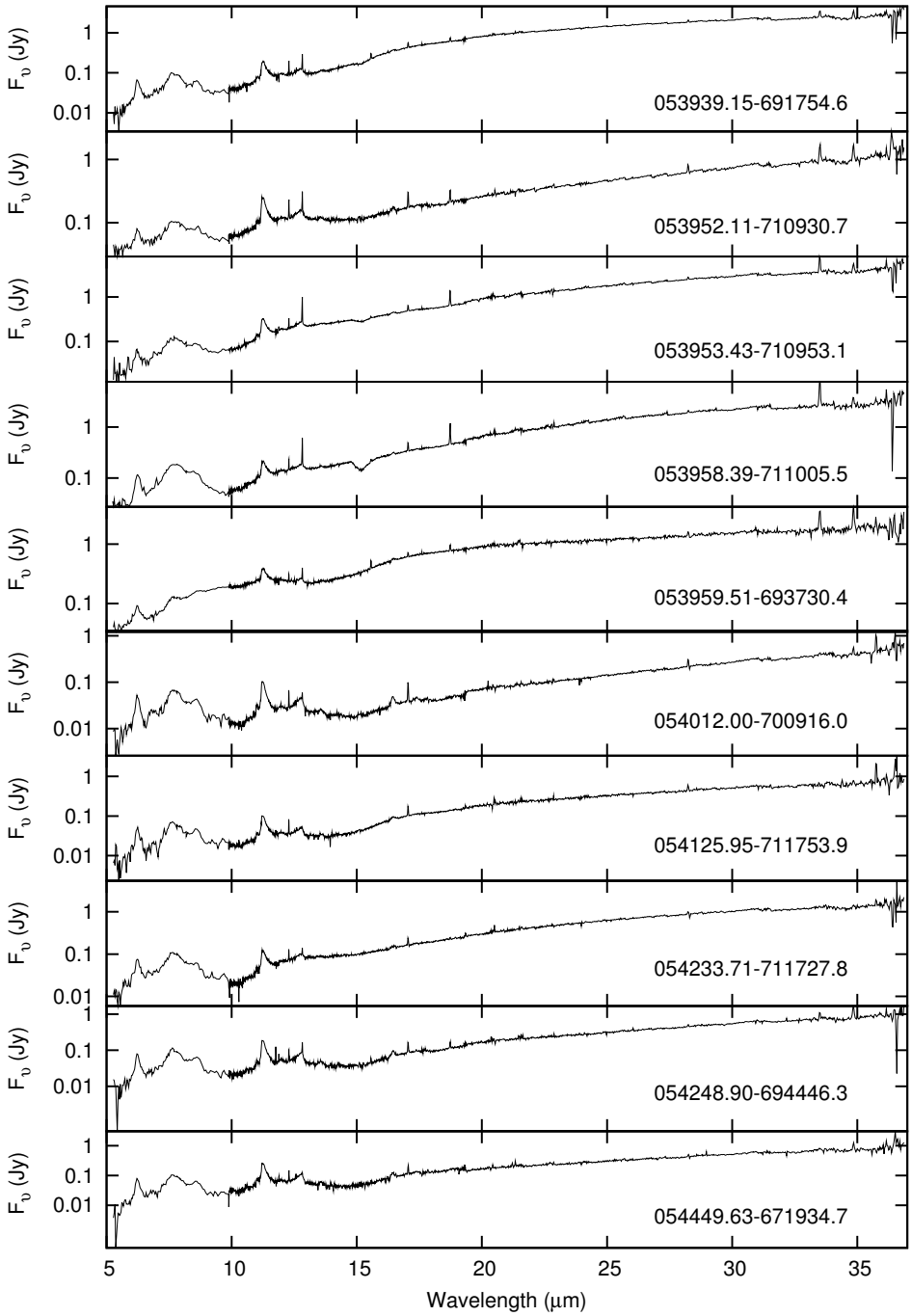
F$_\upsilon$ (Jy)
1
0.1
0.01
053939.15-691754.6
053952.11-710930.7
053953.43-710953.1
053958.39-711005.5
053959.51-693730.4
054012.00-700916.0
054125.95-711753.9
054233.71-711727.8
054248.90-694446.3
054449.63-671934.7
5
10
15
20
25
30
35
Wavelength (μm)

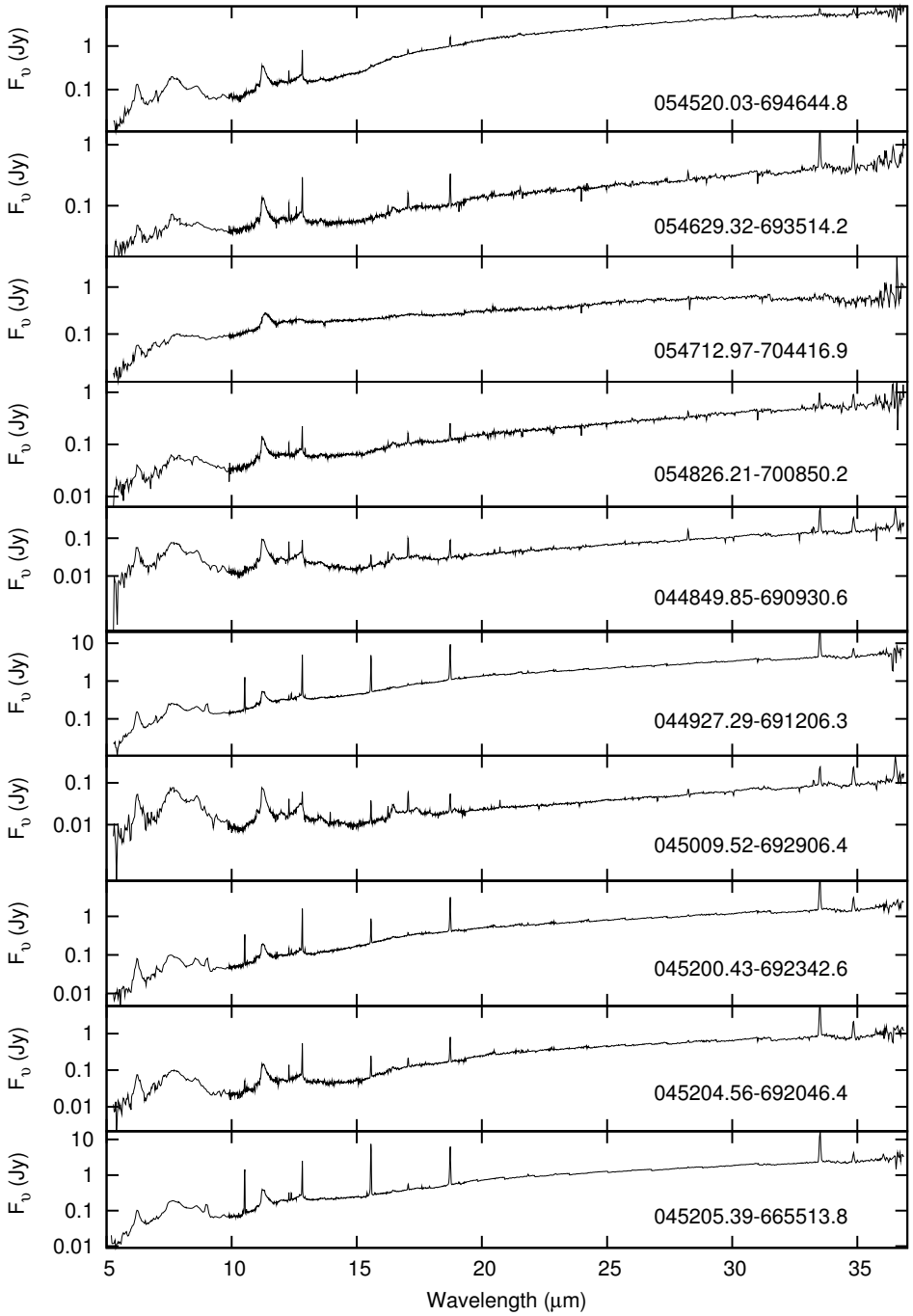
F$_\upsilon$ (Jy)
1
0.1
054520.03-694644.8
F$_\upsilon$ (Jy)
1
0.1
054629.32-693514.2
F$_\upsilon$ (Jy)
1
0.1
054712.97-704416.9
F$_\upsilon$ (Jy)
1
0.1
0.01
054826.21-700850.2
F$_\upsilon$ (Jy)
0.1
0.01
044849.85-690930.6
F$_\upsilon$ (Jy)
10
1
0.1
044927.29-691206.3
F$_\upsilon$ (Jy)
0.1
0.01
045009.52-692906.4
F$_\upsilon$ (Jy)
1
0.1
0.01
045200.43-692342.6
F$_\upsilon$ (Jy)
1
0.1
0.01
045204.56-692046.4
F$_\upsilon$ (Jy)
10
1
0.1
0.01
045205.39-665513.8
5
10
15
20
25
30
35
Wavelength (μm)

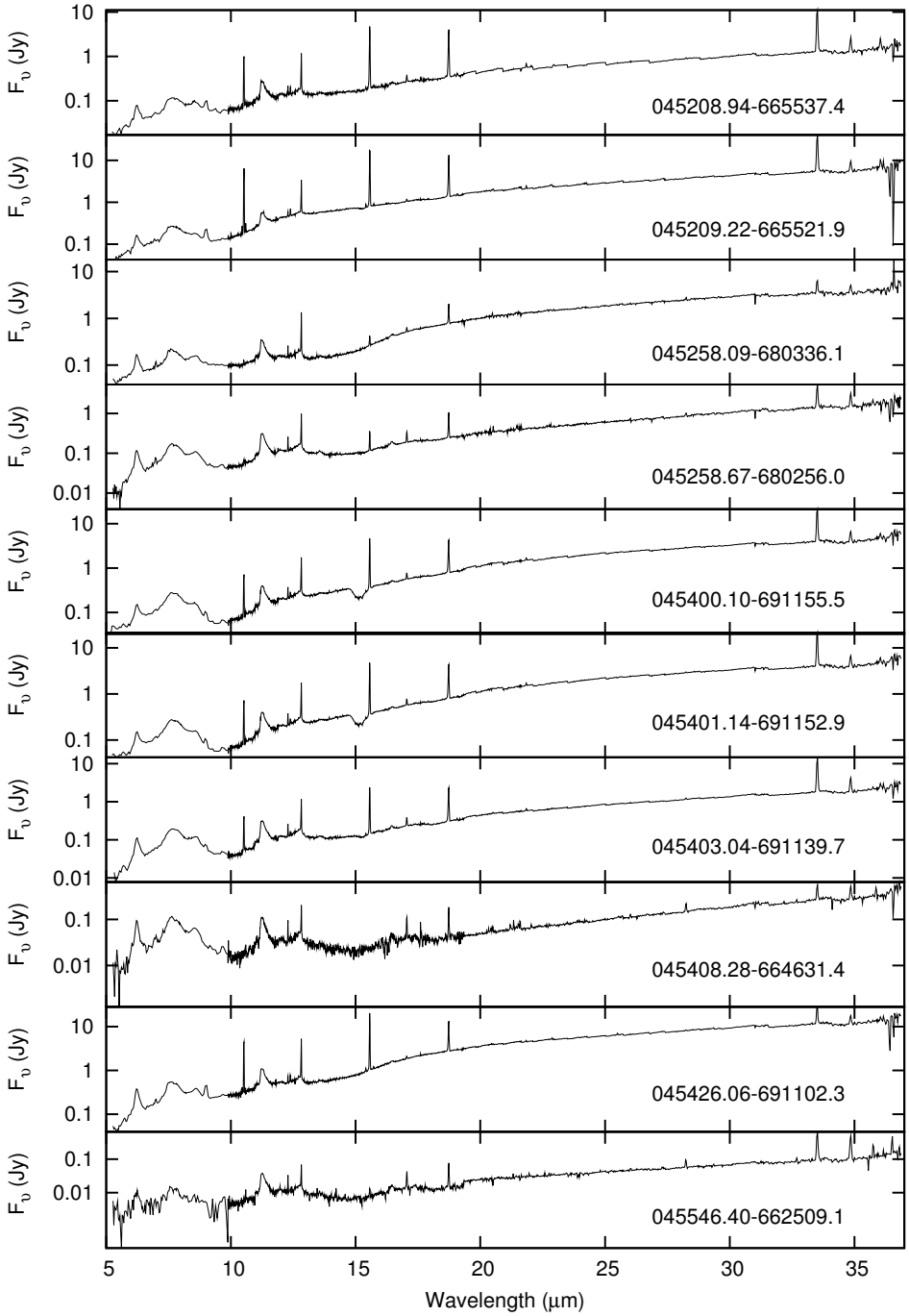
045208.94-665537.4
045209.22-665521.9
045258.09-680336.1
045258.67-680256.0
045400.10-691155.5
045401.14-691152.9
045403.04-691139.7
045408.28-664631.4
045426.06-691102.3
045546.40-662509.1
F$_\upsilon$ (Jy)
Wavelength (μm)

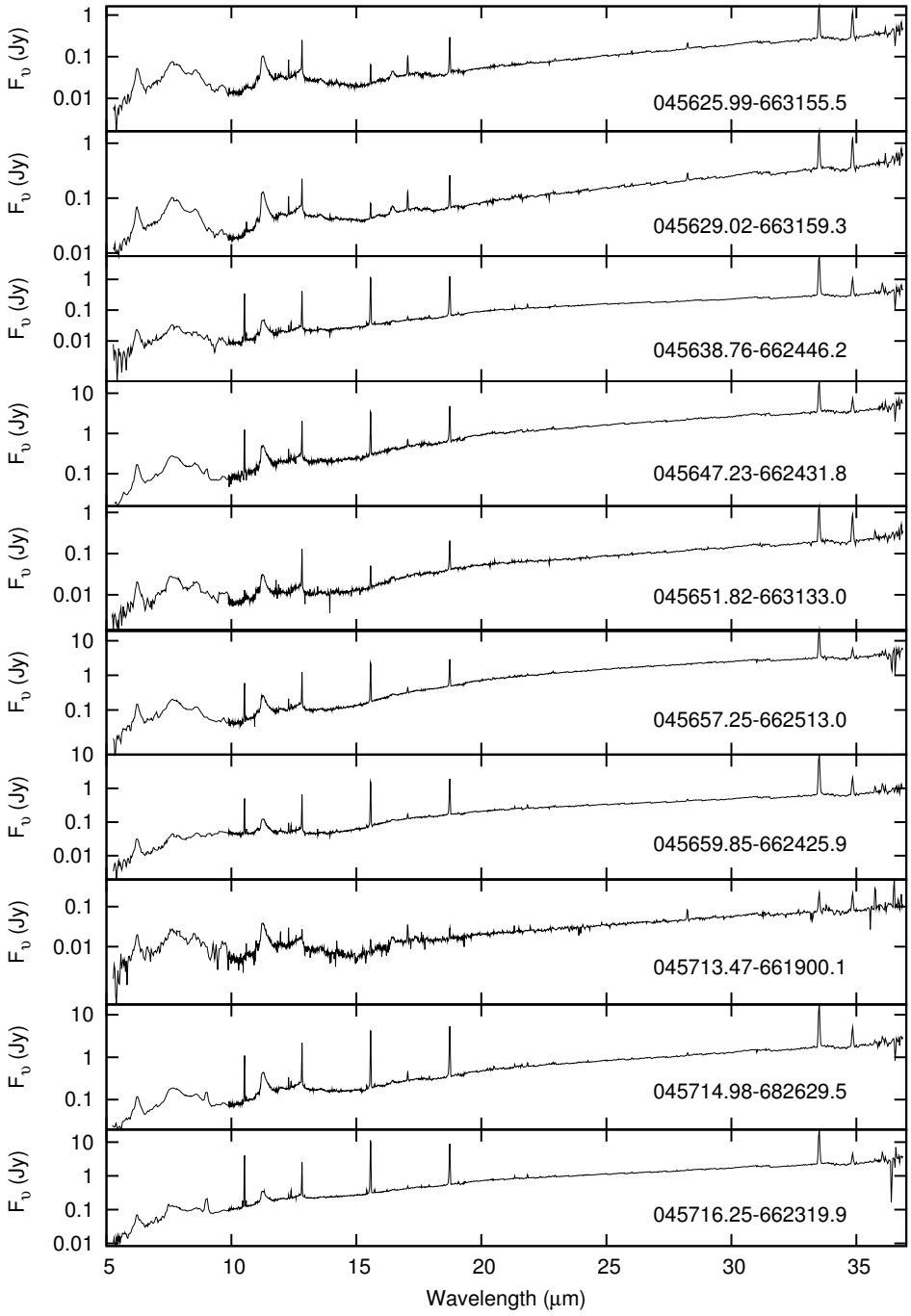
F$_\upsilon$ (Jy)
045625.99-663155.5
045629.02-663159.3
045638.76-662446.2
045647.23-662431.8
045651.82-663133.0
045657.25-662513.0
045659.85-662425.9
045713.47-661900.1
045714.98-682629.5
045716.25-662319.9
Wavelength (μm)

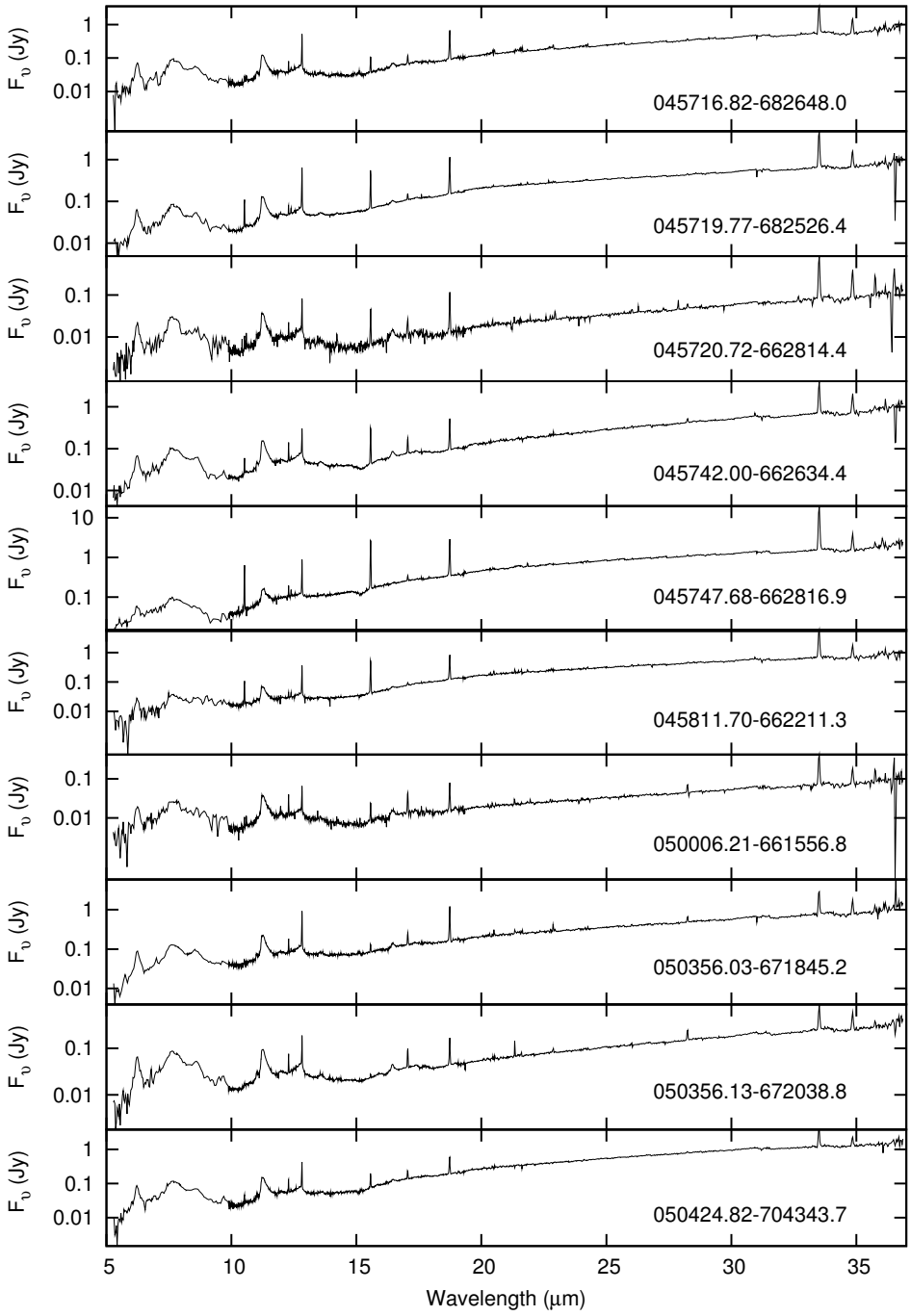
F$_\upsilon$ (Jy)
045716.82-682648.0
045719.77-682526.4
045720.72-662814.4
045742.00-662634.4
045747.68-662816.9
045811.70-662211.3
050006.21-661556.8
050356.03-671845.2
050356.13-672038.8
050424.82-704343.7
Wavelength (μm)

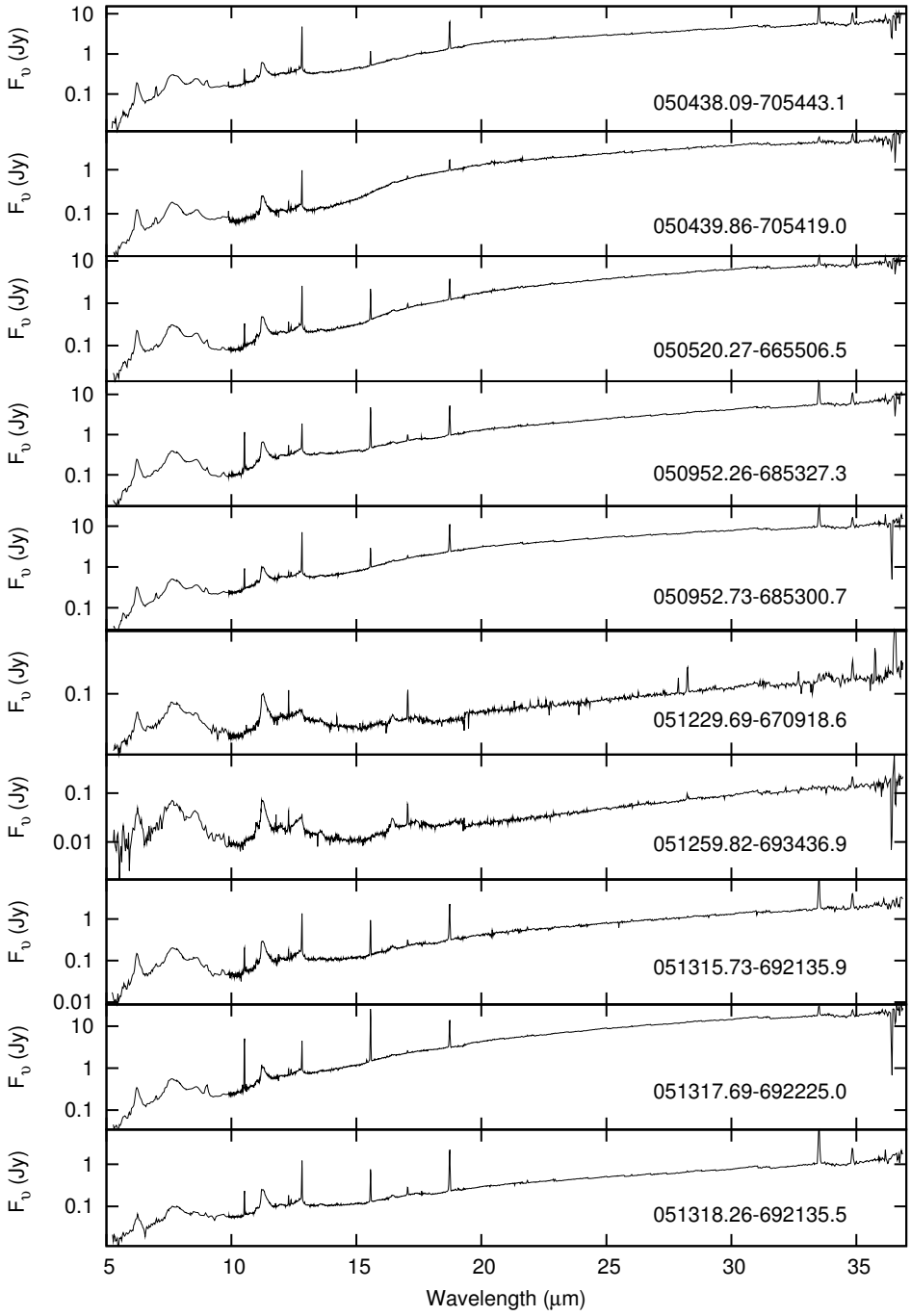
F$_\upsilon$ (Jy)
050438.09-705443.1
050439.86-705419.0
050520.27-665506.5
050952.26-685327.3
050952.73-685300.7
051229.69-670918.6
051259.82-693436.9
051315.73-692135.9
051317.69-692225.0
051318.26-692135.5
Wavelength (μm)

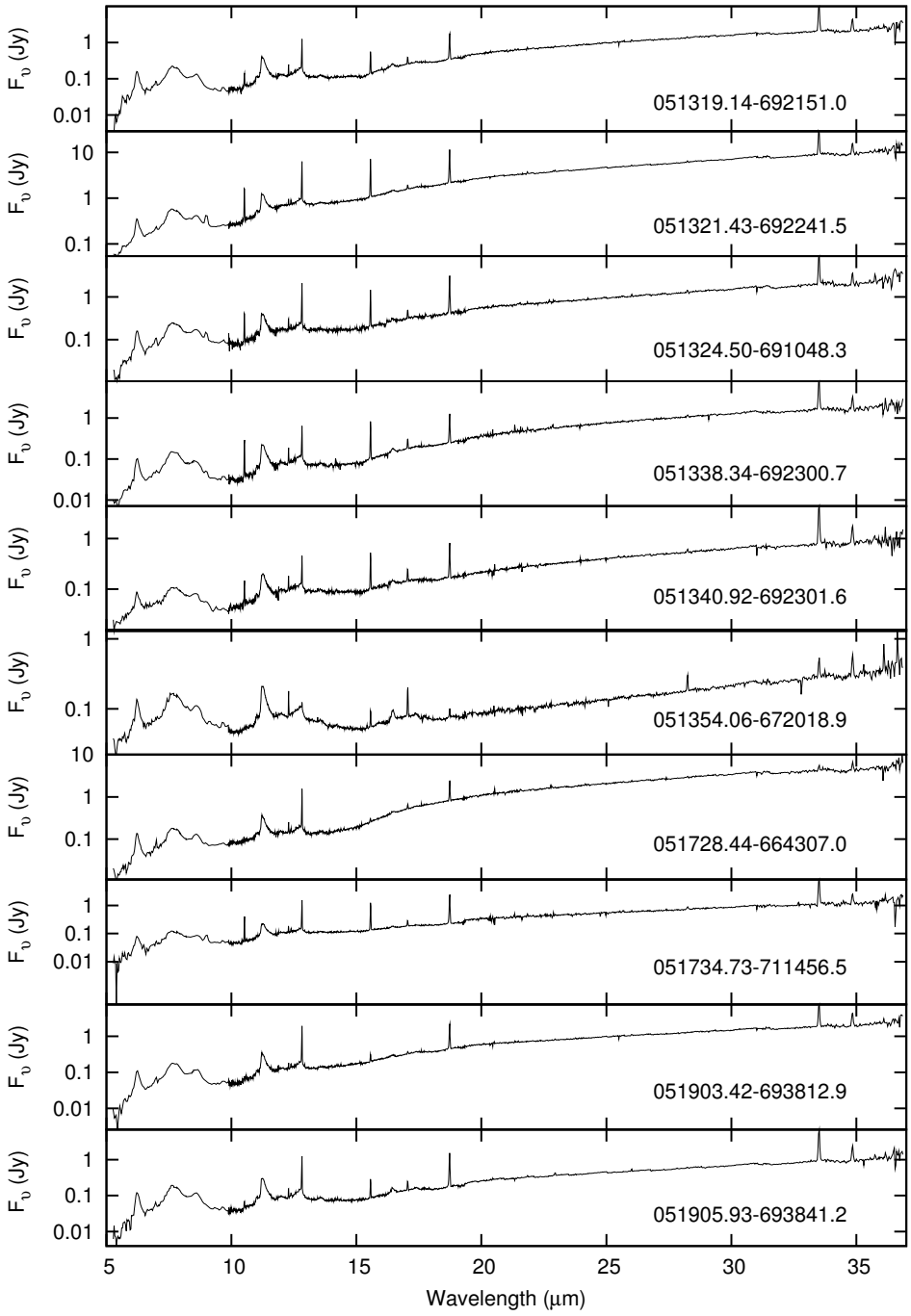
F$_\upsilon$ (Jy)
051319.14-692151.0
051321.43-692241.5
051324.50-691048.3
051338.34-692300.7
051340.92-692301.6
051354.06-672018.9
051728.44-664307.0
051734.73-711456.5
051903.42-693812.9
051905.93-693841.2
Wavelength (μm)

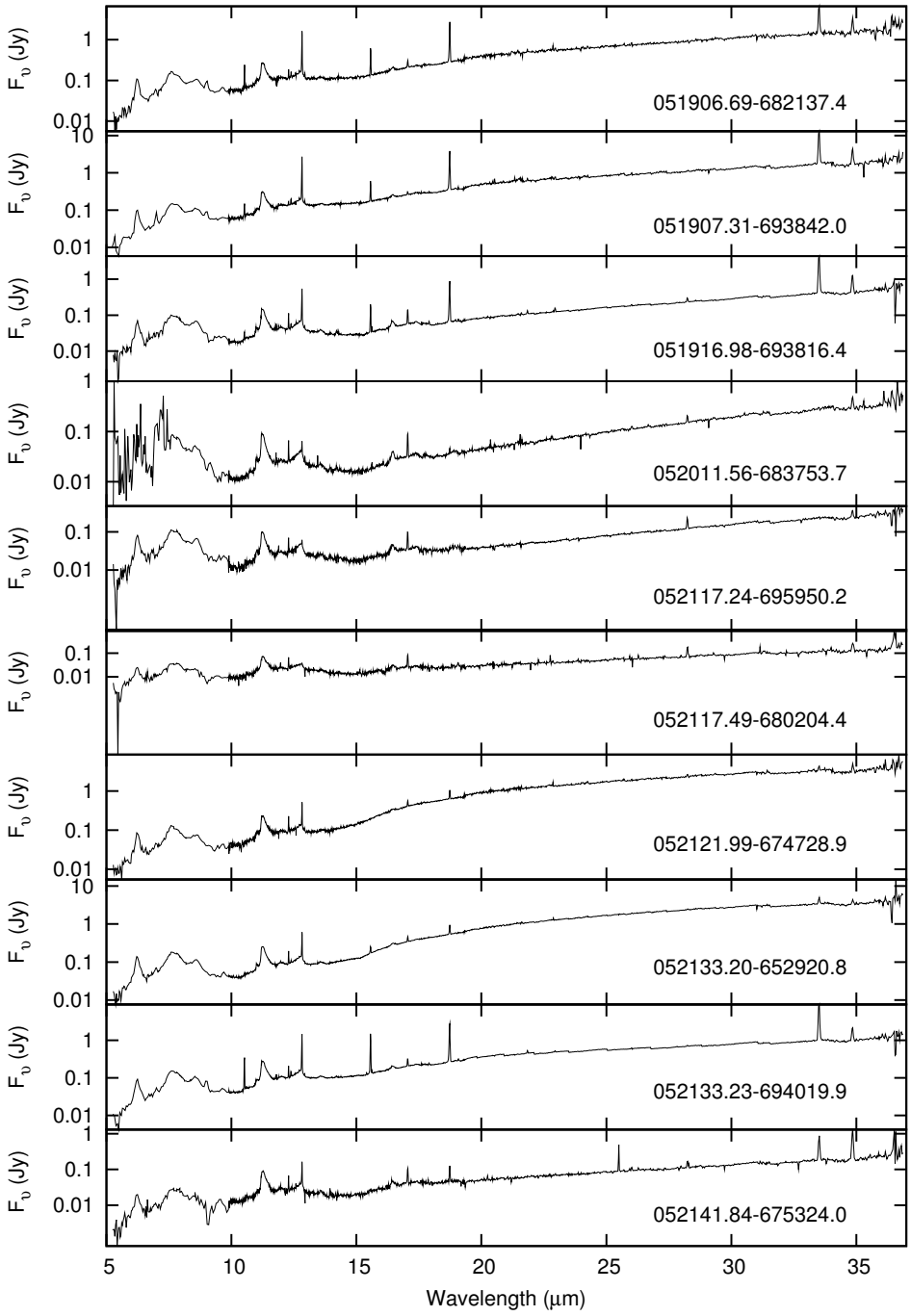
F$_\upsilon$ (Jy)
051906.69-682137.4
051907.31-693842.0
051916.98-693816.4
052011.56-683753.7
052117.24-695950.2
052117.49-680204.4
052121.99-674728.9
052133.20-652920.8
052133.23-694019.9
052141.84-675324.0
Wavelength (μm)

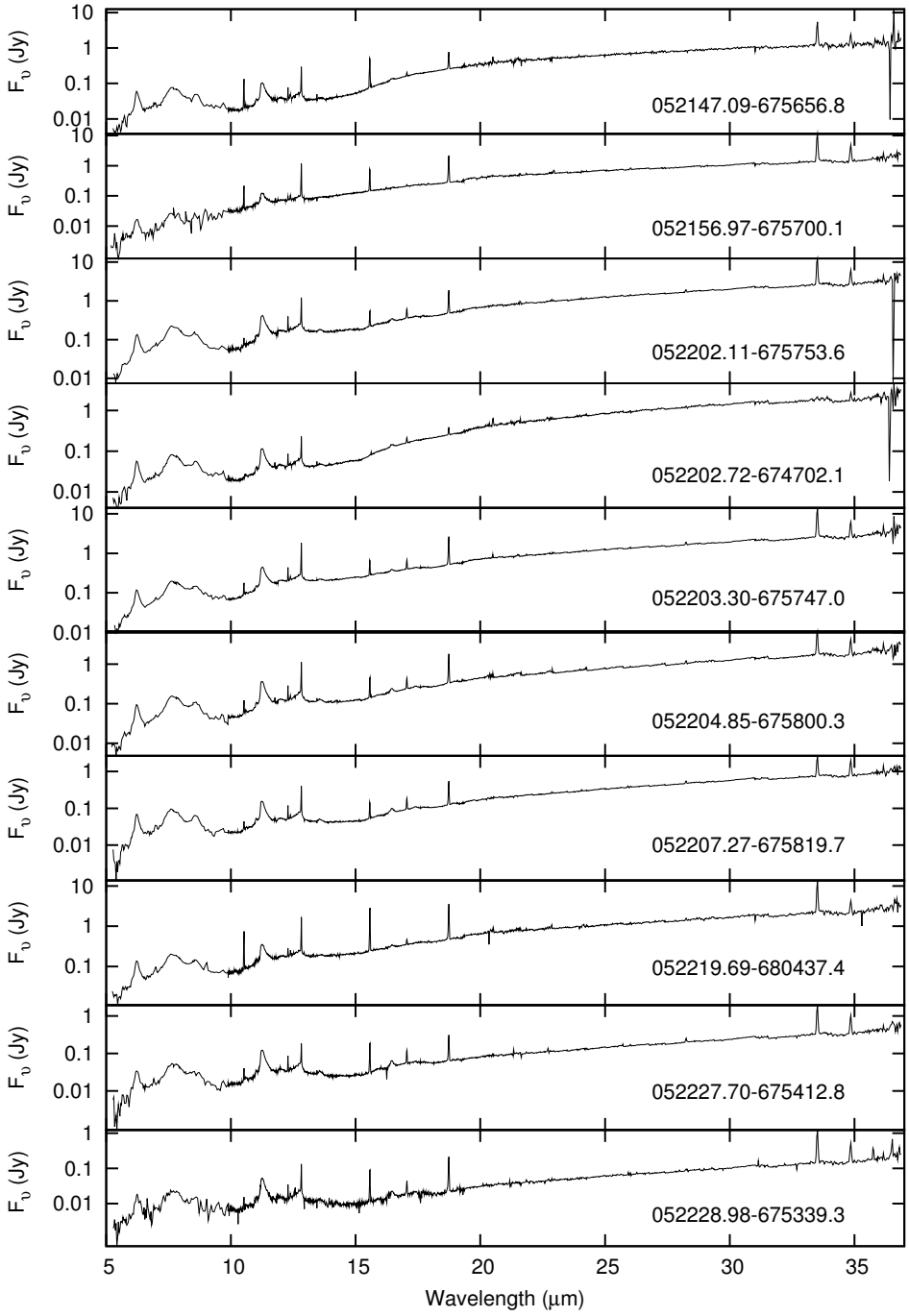
052147.09-675656.8
052156.97-675700.1
052202.11-675753.6
052202.72-674702.1
052203.30-675747.0
052204.85-675800.3
052207.27-675819.7
052219.69-680437.4
052227.70-675412.8
052228.98-675339.3
F$_\upsilon$ (Jy)
Wavelength (μm)
10
1
0.1
0.01
5
10
15
20
25
30
35

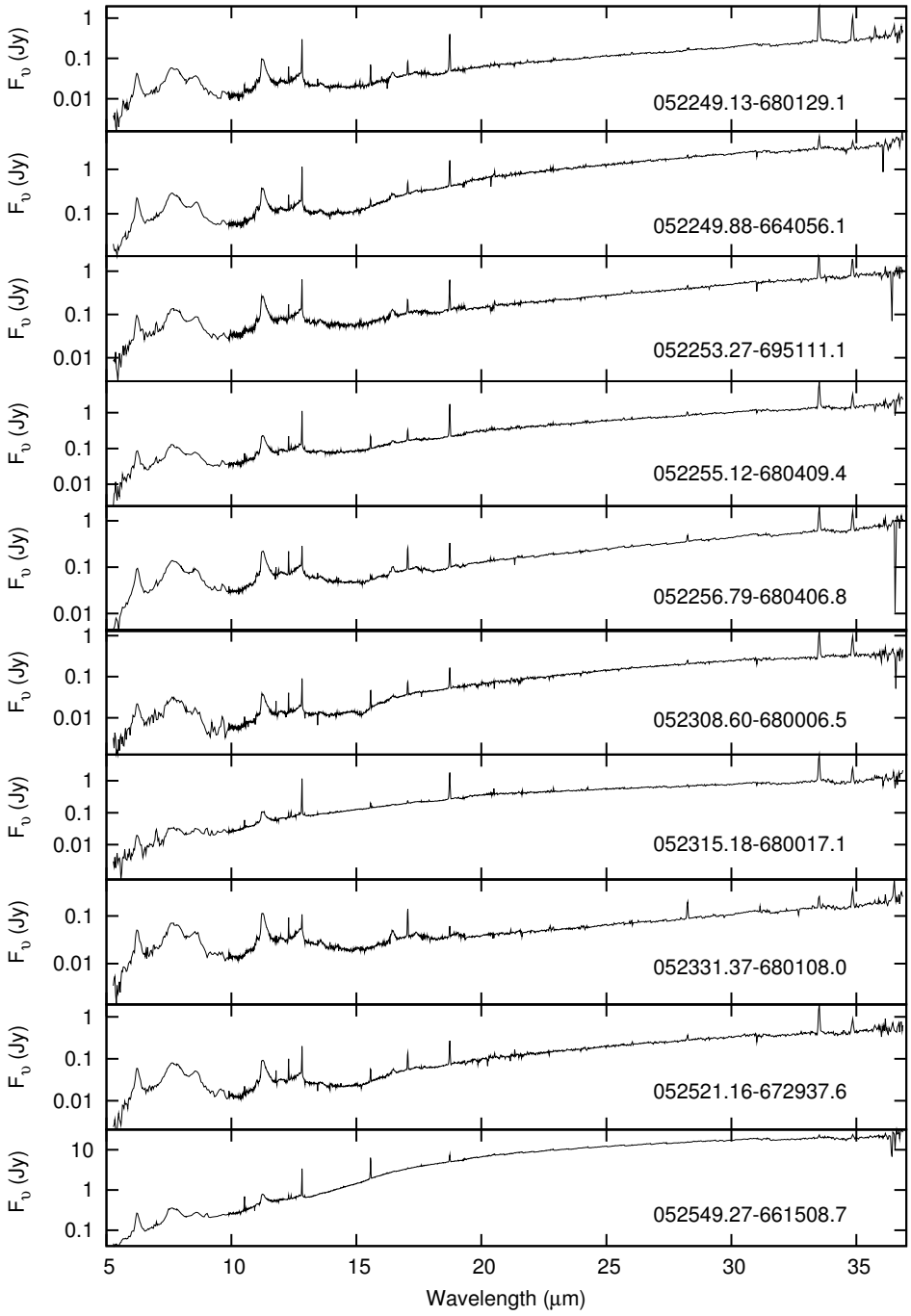
F$_\upsilon$ (Jy)
052249.13-680129.1
052249.88-664056.1
052253.27-695111.1
052255.12-680409.4
052256.79-680406.8
052308.60-680006.5
052315.18-680017.1
052331.37-680108.0
052521.16-672937.6
052549.27-661508.7
Wavelength (μm)

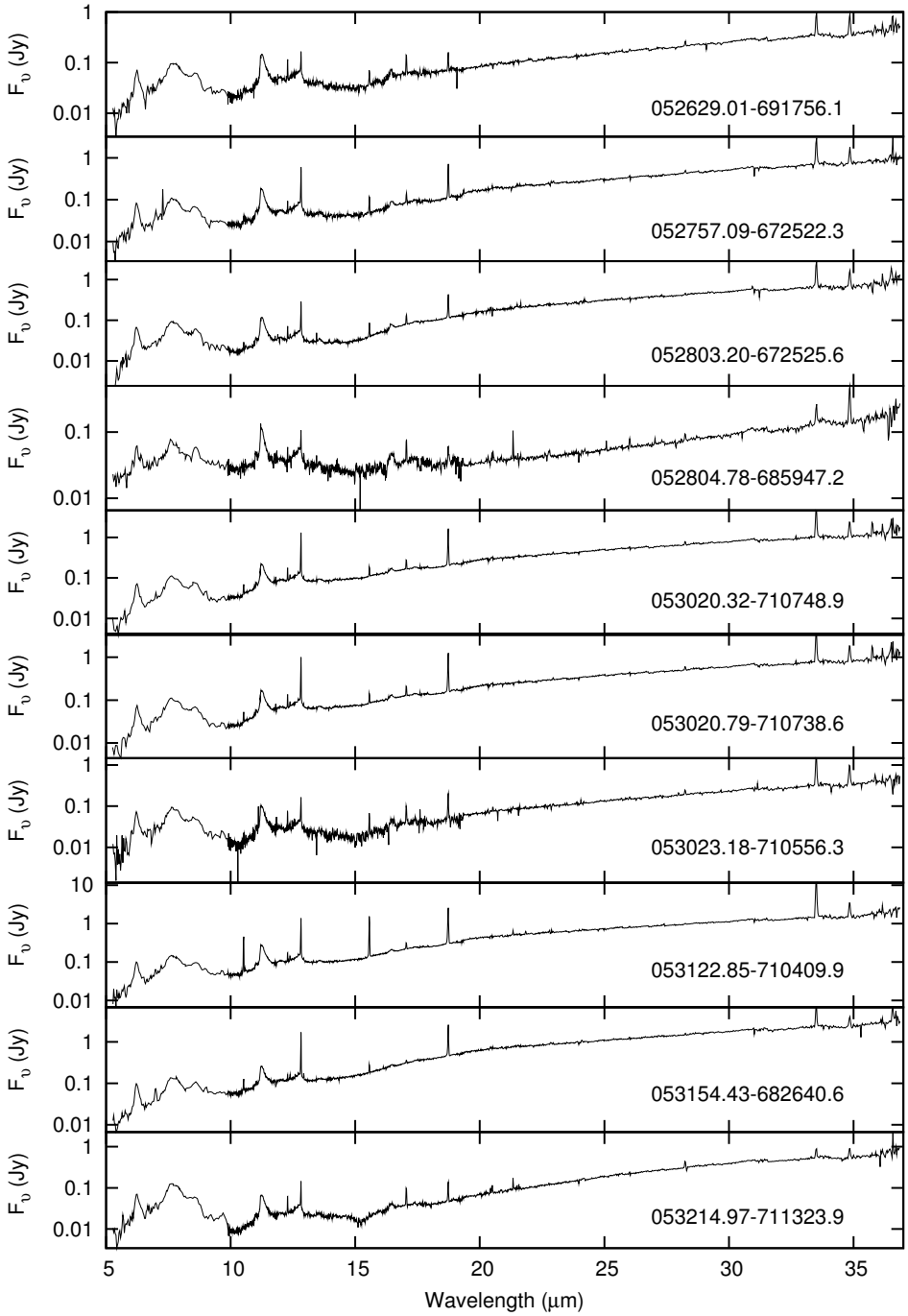
052629.01-691756.1
052757.09-672522.3
052803.20-672525.6
052804.78-685947.2
053020.32-710748.9
053020.79-710738.6
053023.18-710556.3
053122.85-710409.9
053154.43-682640.6
053214.97-711323.9
F$_\upsilon$ (Jy)
Wavelength (μm)

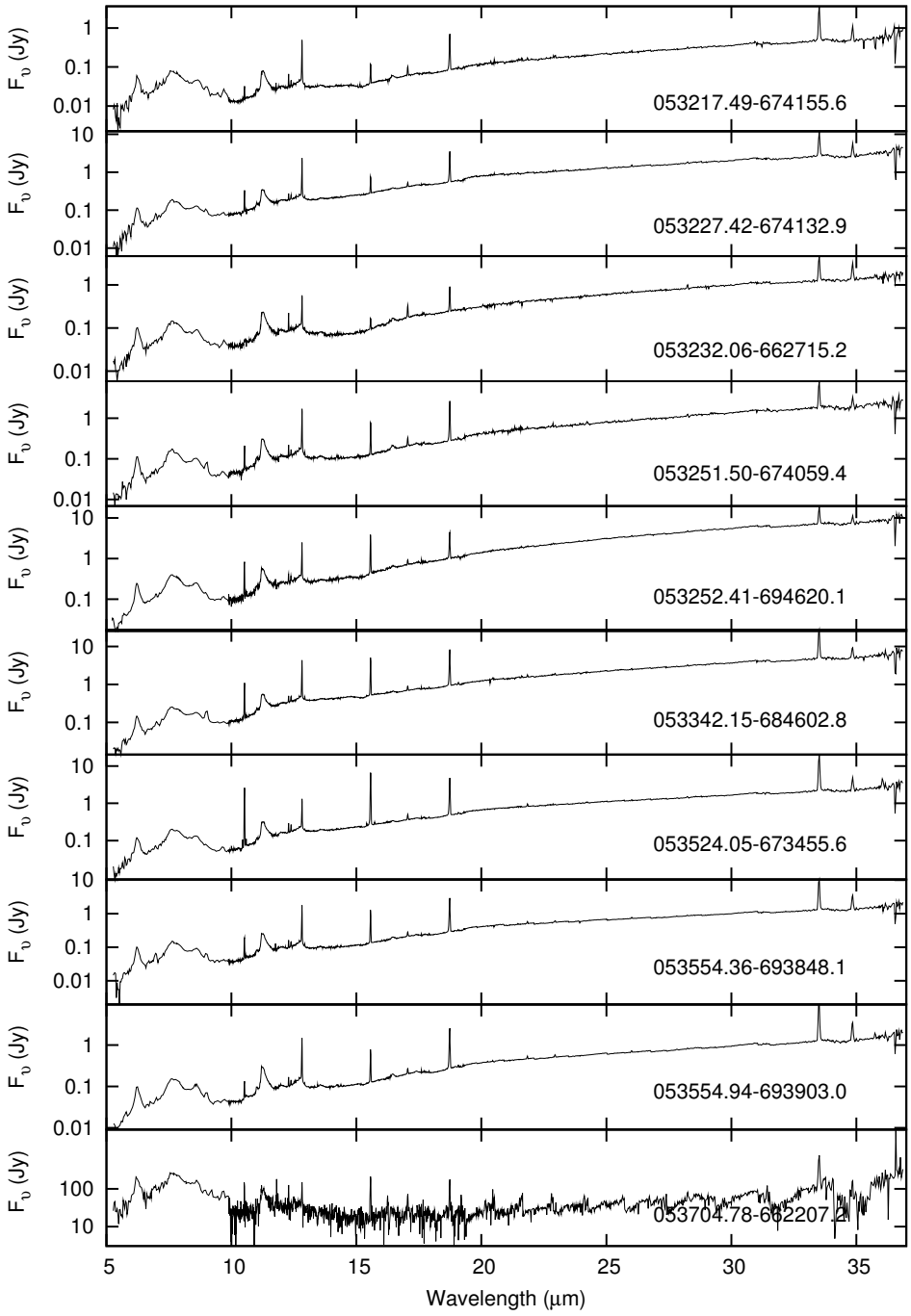
F$_\upsilon$ (Jy)
053217.49-674155.6
053227.42-674132.9
053232.06-662715.2
053251.50-674059.4
053252.41-694620.1
053342.15-684602.8
053524.05-673455.6
053554.36-693848.1
053554.94-693903.0
053704.78-662207.2
Wavelength (μm)

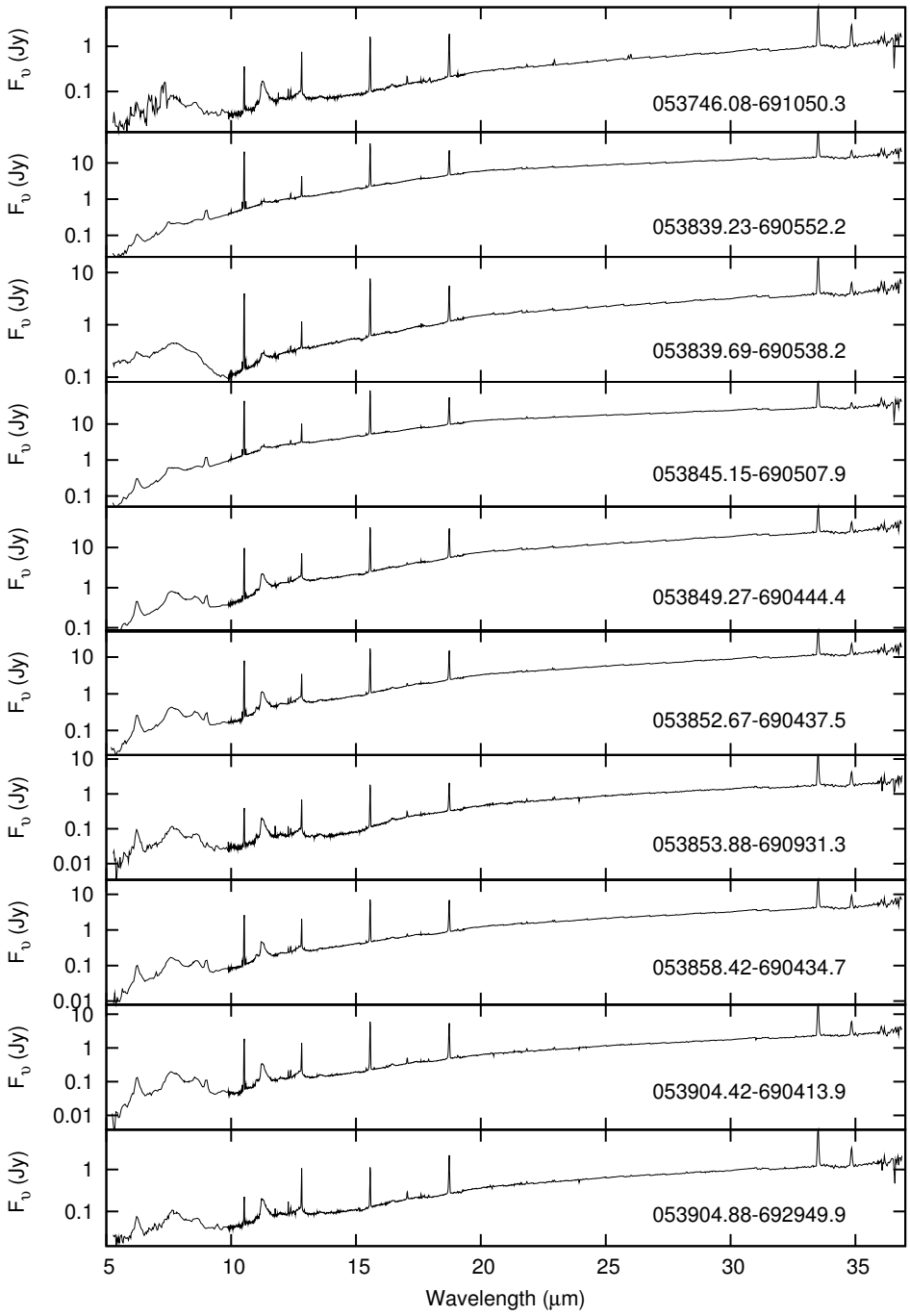
F$_\upsilon$ (Jy)
053746.08-691050.3
053839.23-690552.2
053839.69-690538.2
053845.15-690507.9
053849.27-690444.4
053852.67-690437.5
053853.88-690931.3
053858.42-690434.7
053904.42-690413.9
053904.88-692949.9
5
10
15
20
25
30
35
Wavelength (μm)

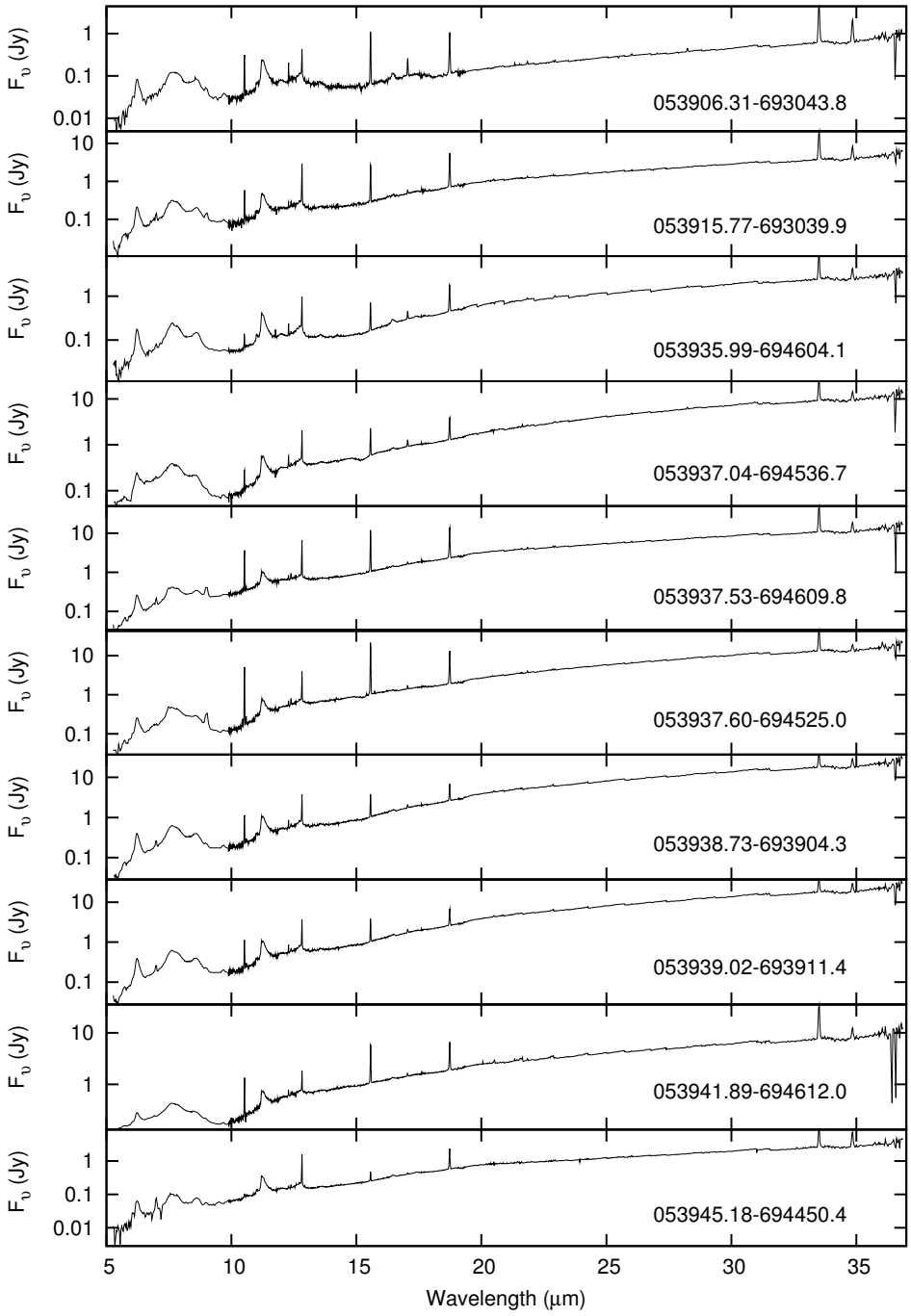
F$_\upsilon$ (Jy)
053906.31-693043.8
053915.77-693039.9
053935.99-694604.1
053937.04-694536.7
053937.53-694609.8
053937.60-694525.0
053938.73-693904.3
053939.02-693911.4
053941.89-694612.0
053945.18-694450.4
Wavelength (μm)

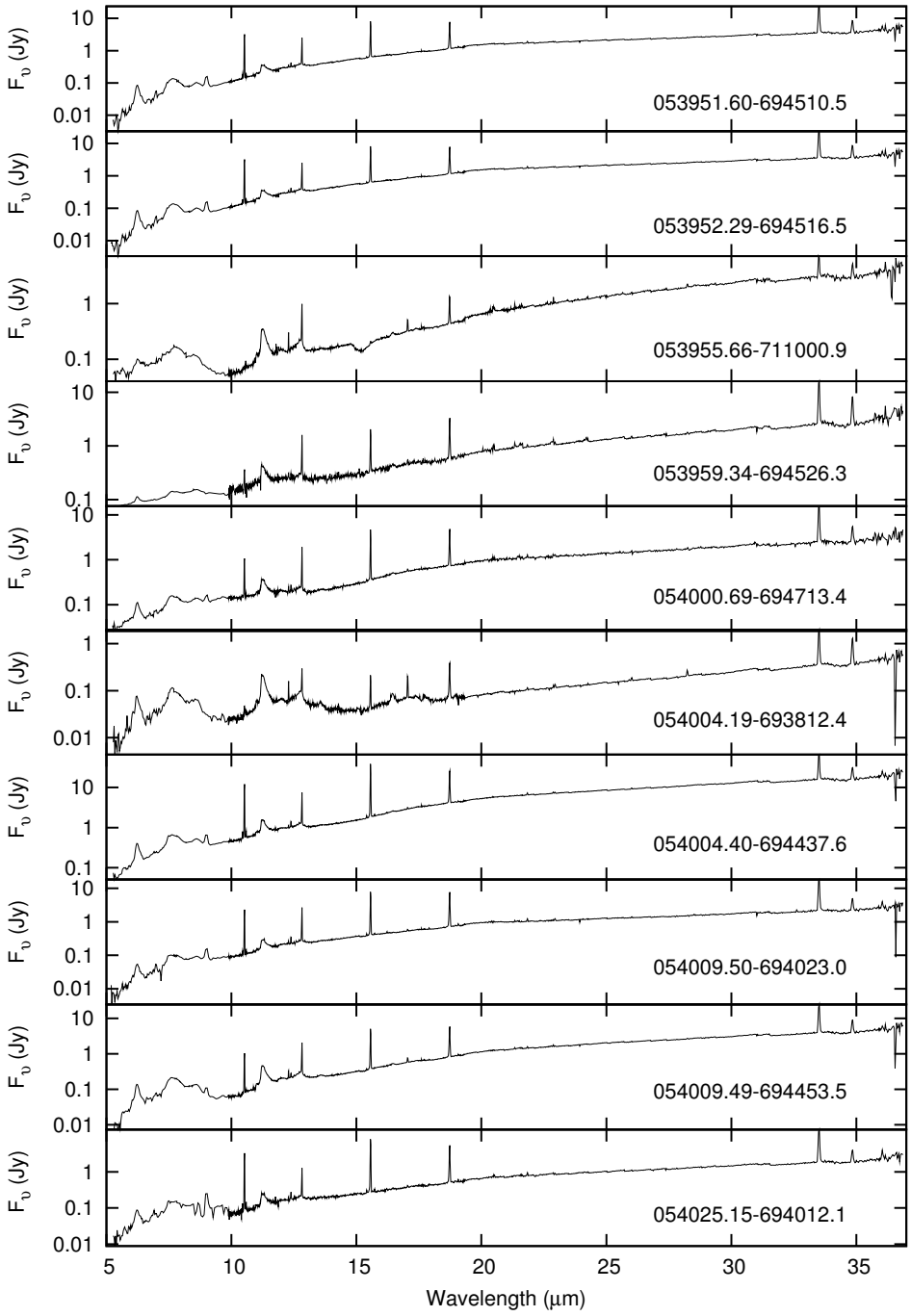
053951.60-694510.5
053952.29-694516.5
053955.66-711000.9
053959.34-694526.3
054000.69-694713.4
054004.19-693812.4
054004.40-694437.6
054009.50-694023.0
054009.49-694453.5
054025.15-694012.1
F$_\upsilon$ (Jy)
Wavelength (μm)

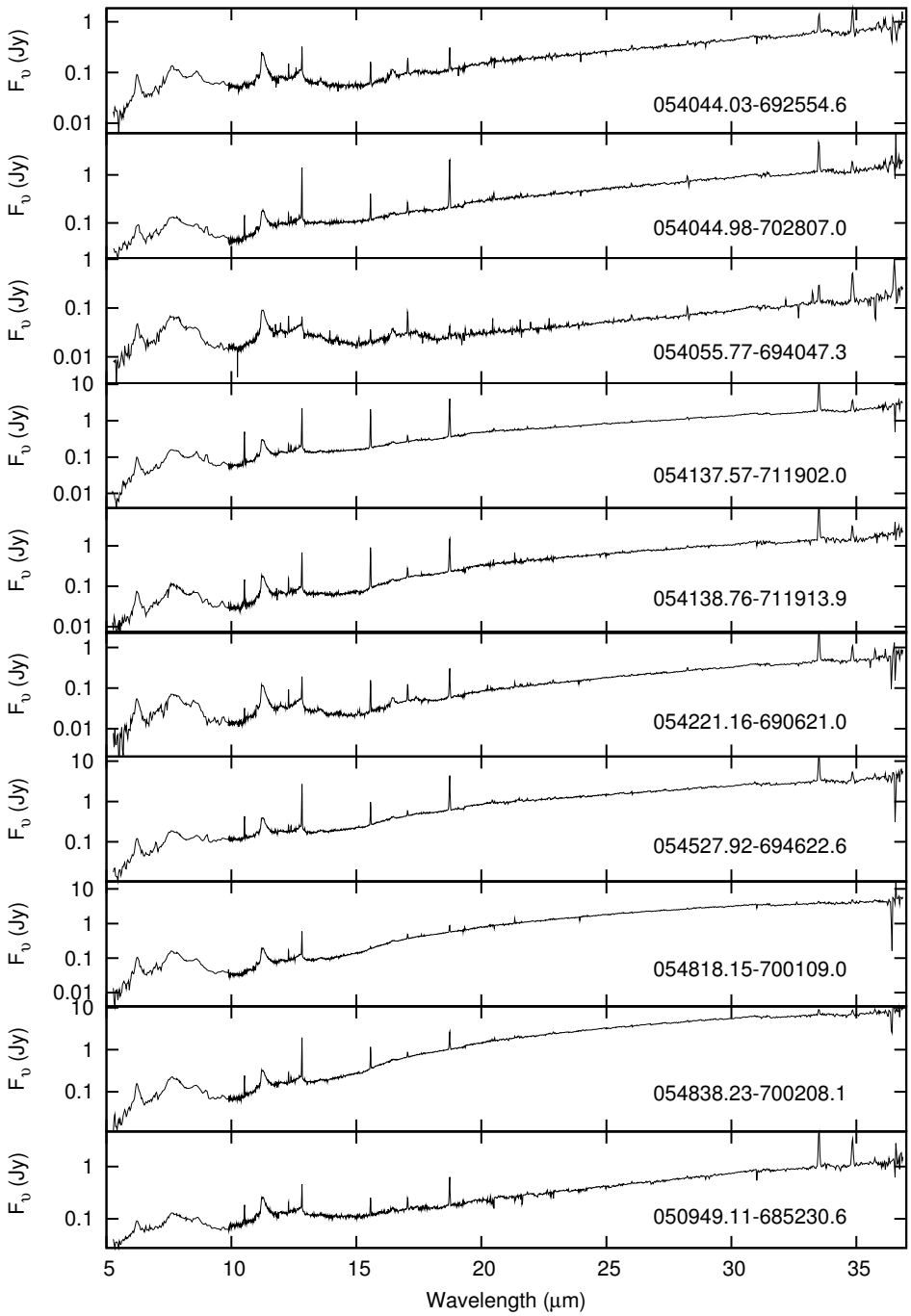
F$_\upsilon$ (Jy)
1
0.1
0.01
054044.03-692554.6
F$_\upsilon$ (Jy)
1
0.1
054044.98-702807.0
F$_\upsilon$ (Jy)
1
0.1
0.01
054055.77-694047.3
F$_\upsilon$ (Jy)
10
1
0.1
0.01
054137.57-711902.0
F$_\upsilon$ (Jy)
1
0.1
0.01
054138.76-711913.9
F$_\upsilon$ (Jy)
1
0.1
0.01
054221.16-690621.0
F$_\upsilon$ (Jy)
10
1
0.1
054527.92-694622.6
F$_\upsilon$ (Jy)
10
1
0.1
0.01
054818.15-700109.0
F$_\upsilon$ (Jy)
10
1
0.1
054838.23-700208.1
F$_\upsilon$ (Jy)
1
0.1
050949.11-685230.6
5
10
15
20
25
30
35
Wavelength (μm)

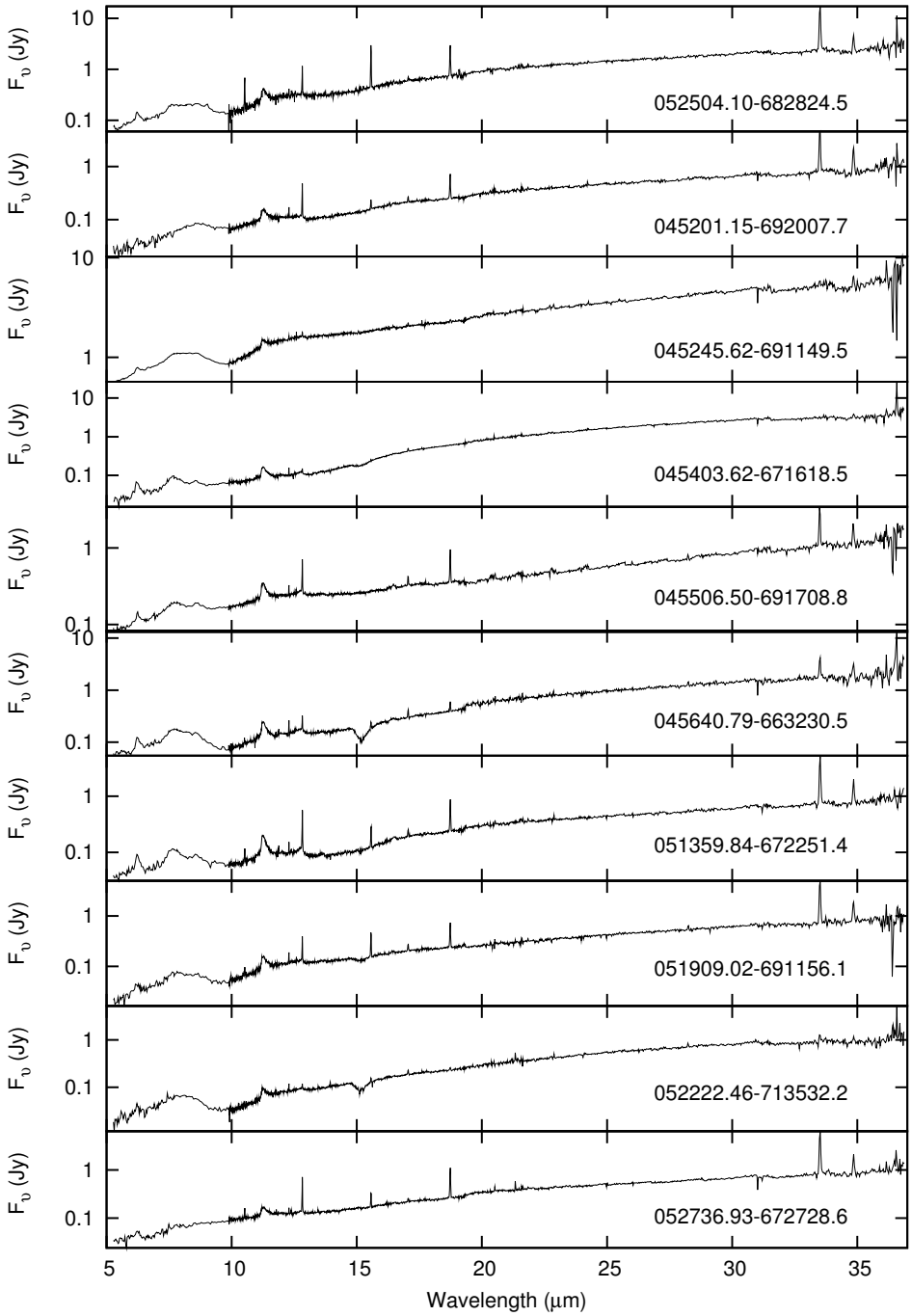
F$_\upsilon$ (Jy)
10
1
0.1
052504.10-682824.5
045201.15-692007.7
045245.62-691149.5
045403.62-671618.5
045506.50-691708.8
045640.79-663230.5
051359.84-672251.4
051909.02-691156.1
052222.46-713532.2
052736.93-672728.6
5
10
15
20
25
30
35
Wavelength (μm)

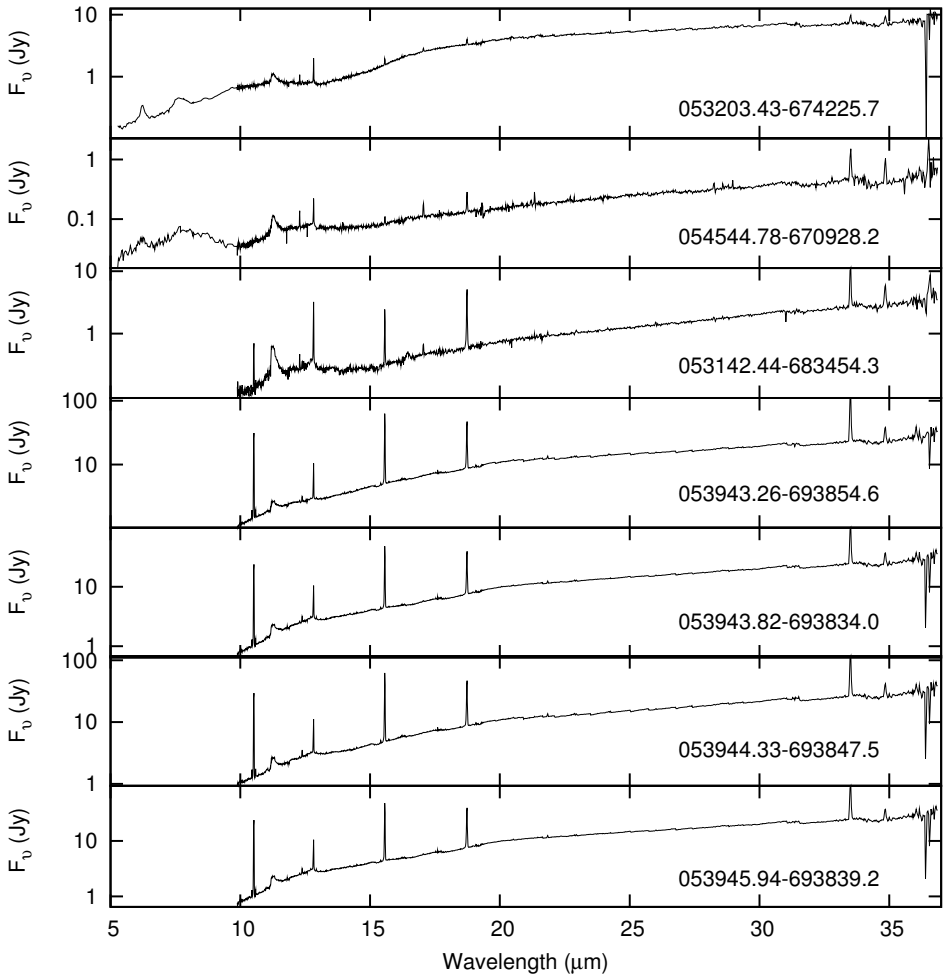
F$_\upsilon$ (Jy)
10
1
053203.43-674225.7
F$_\upsilon$ (Jy)
1
0.1
054544.78-670928.2
F$_\upsilon$ (Jy)
10
1
053142.44-683454.3
F$_\upsilon$ (Jy)
100
10
053943.26-693854.6
F$_\upsilon$ (Jy)
10
1
053943.82-693834.0
F$_\upsilon$ (Jy)
100
10
1
053944.33-693847.5
F$_\upsilon$ (Jy)
10
1
053945.94-693839.2
5
10
15
20
25
30
35
Wavelength (μm)

Appendix B

Presented are the spectra for every less-embedded source presented in Chapter 2, a sample of which was presented in Figure 2. Spectra are ordered by spectral Group and then by increasing RA.

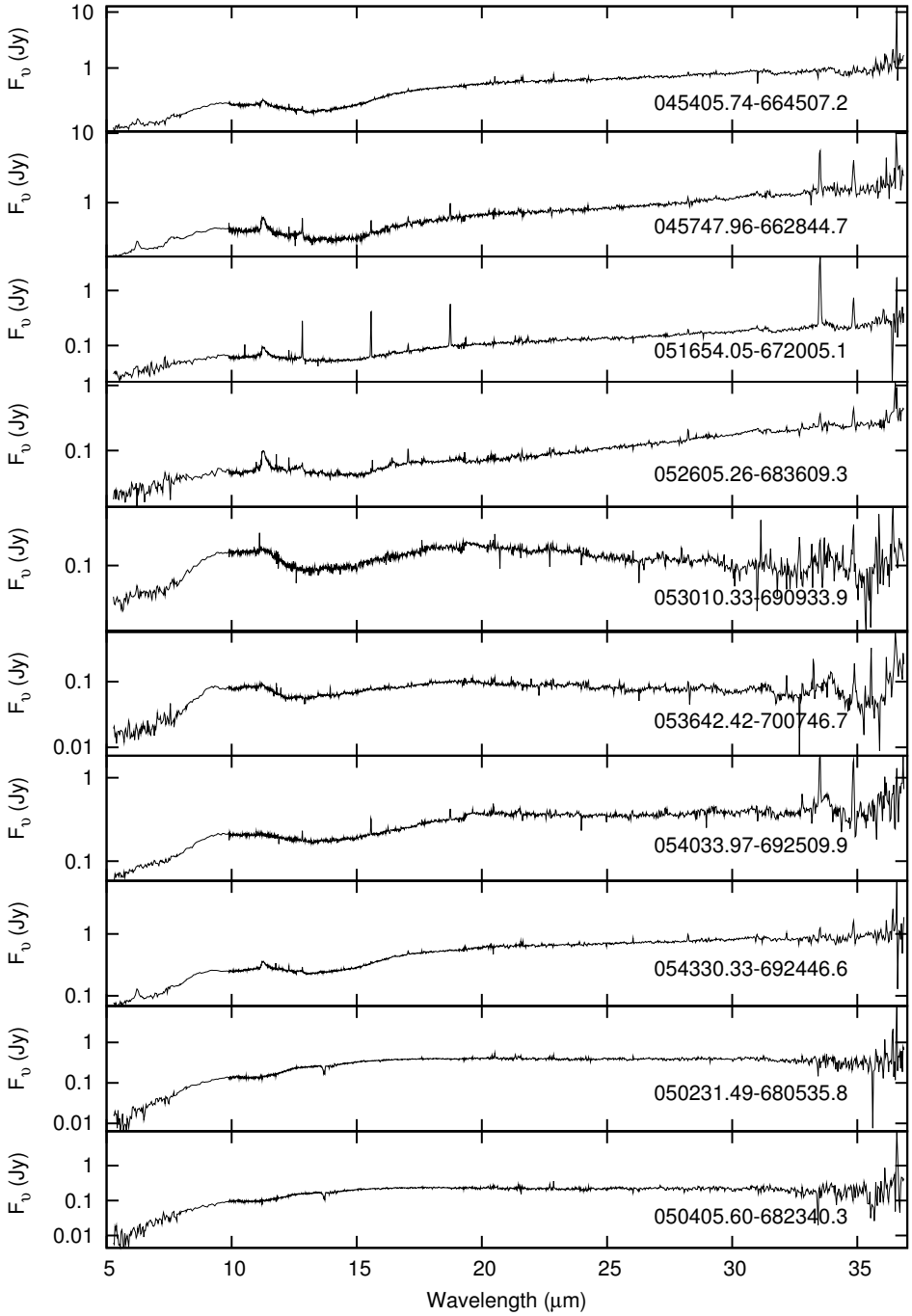

Fig. 0.— Spectra of the complete source catalog from which selected sources are shown in Figure 2. Sources are ordered as in Table 1, and source identifications are given below each curve.

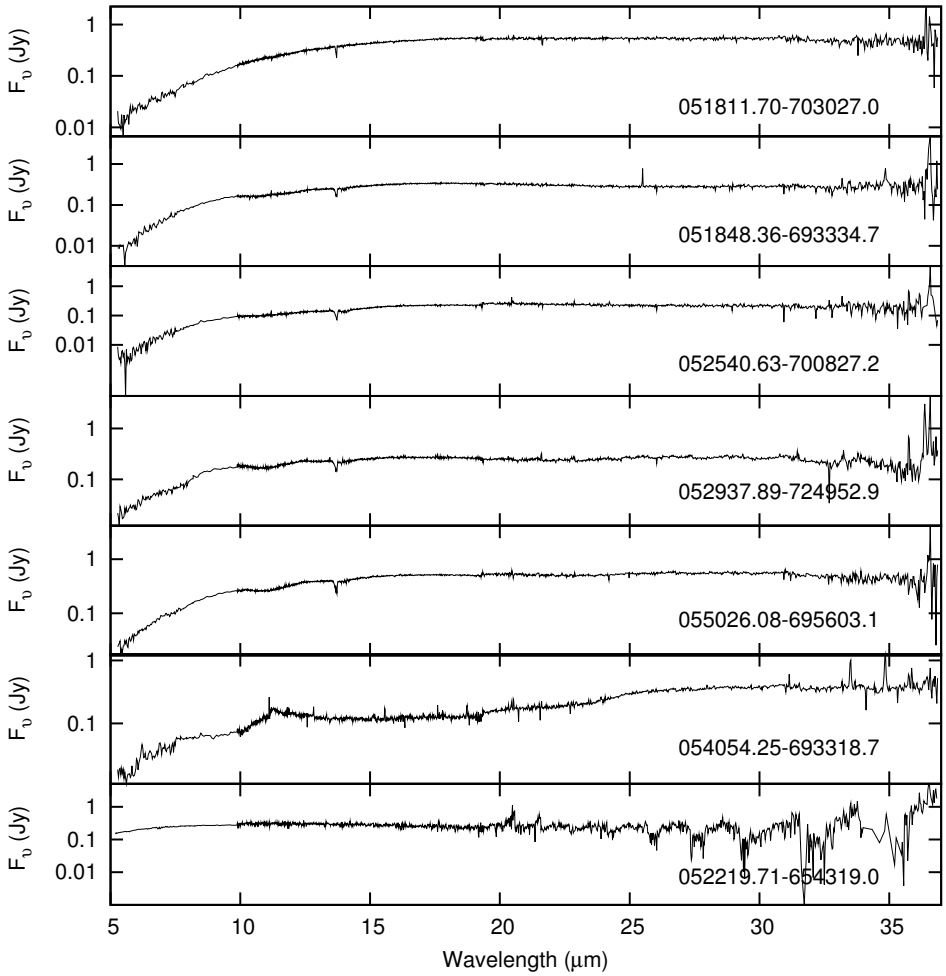

Fig. 1.— Continuation of Figure 2b.

Appendix C

Presented are the spectra for every source analyzed in Chapter 3, a sample of which was presented in Figure 7. Spectra are ordered by increasing RA.

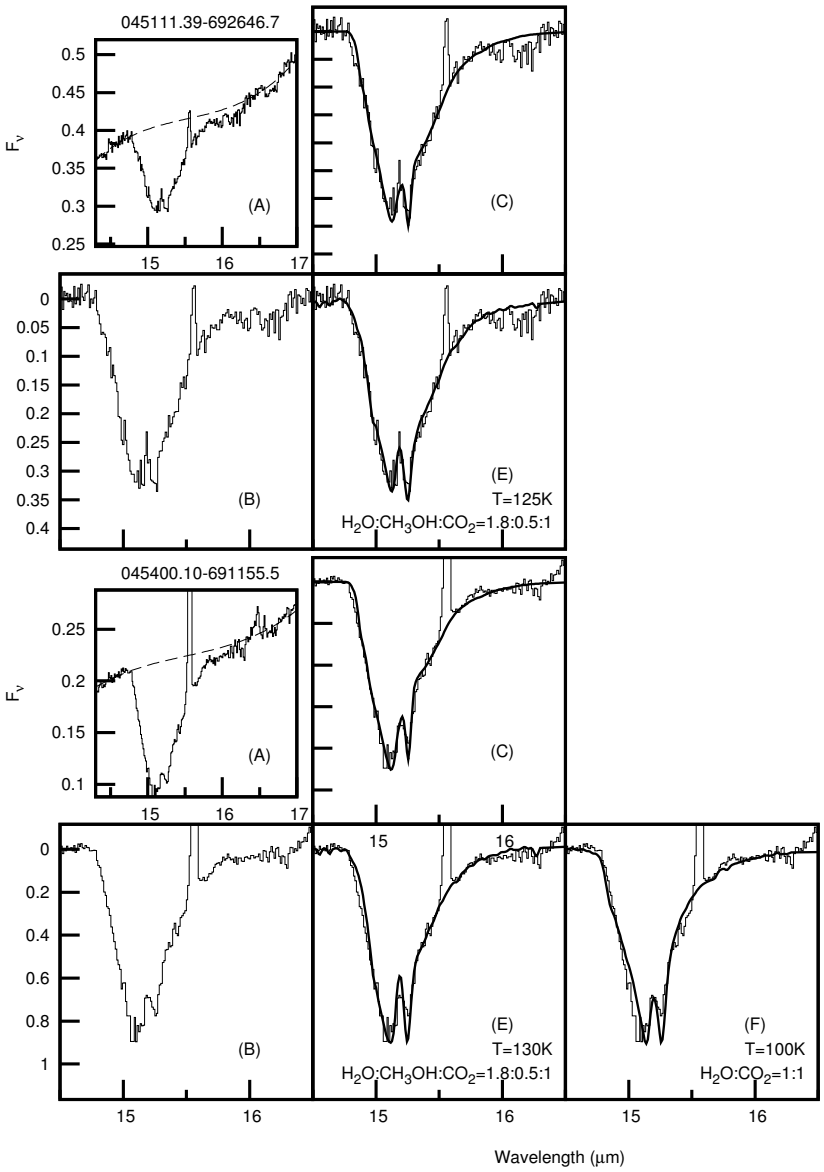

Fig. 2.— continued.

$$\frac{\chi^2_{H2O:CO2}}{\chi^2_{H2O:CH3OH:CO2}} = 1.05$$

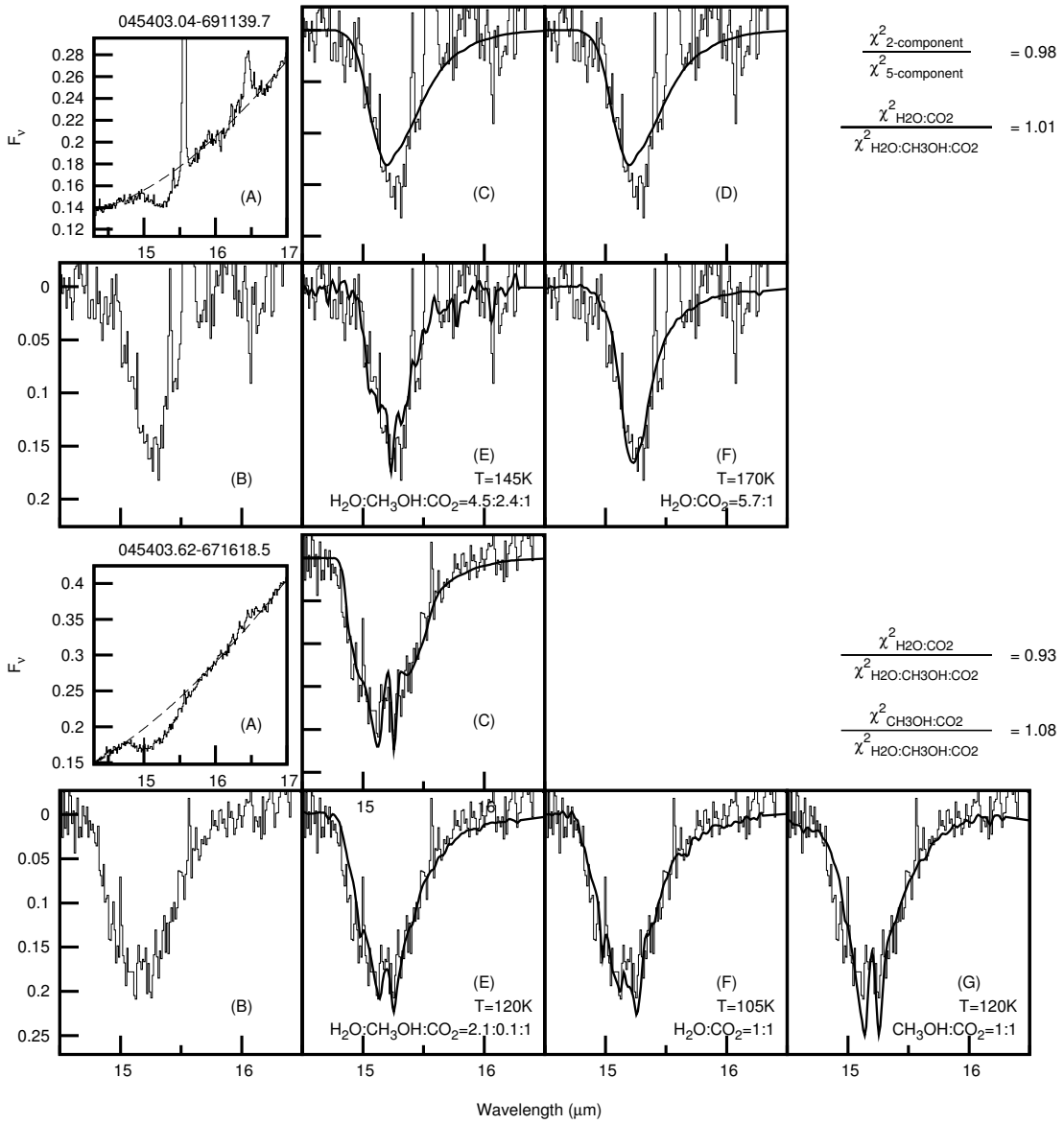

Fig. 3.— continued.

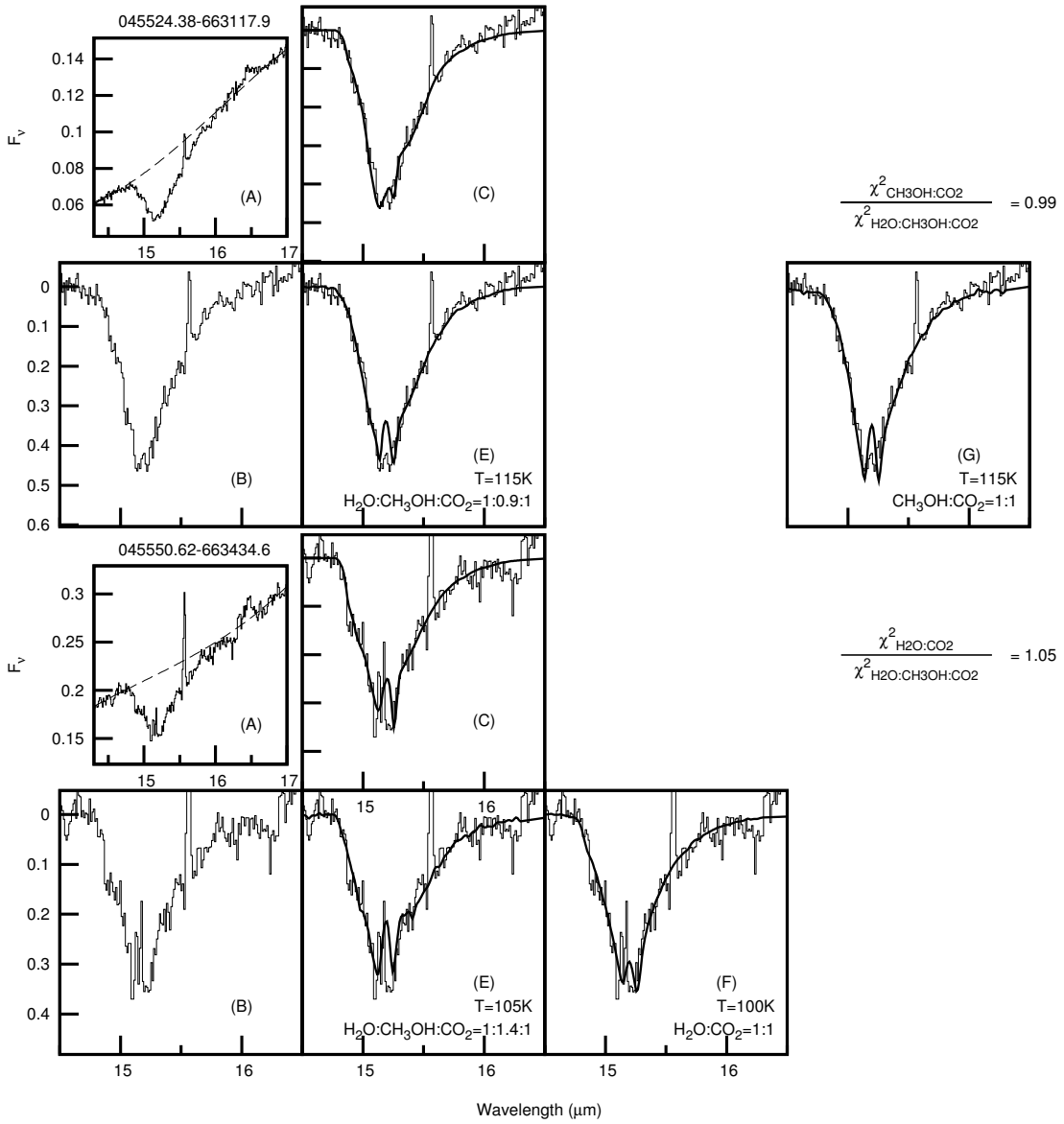

Fig. 4.— continued.

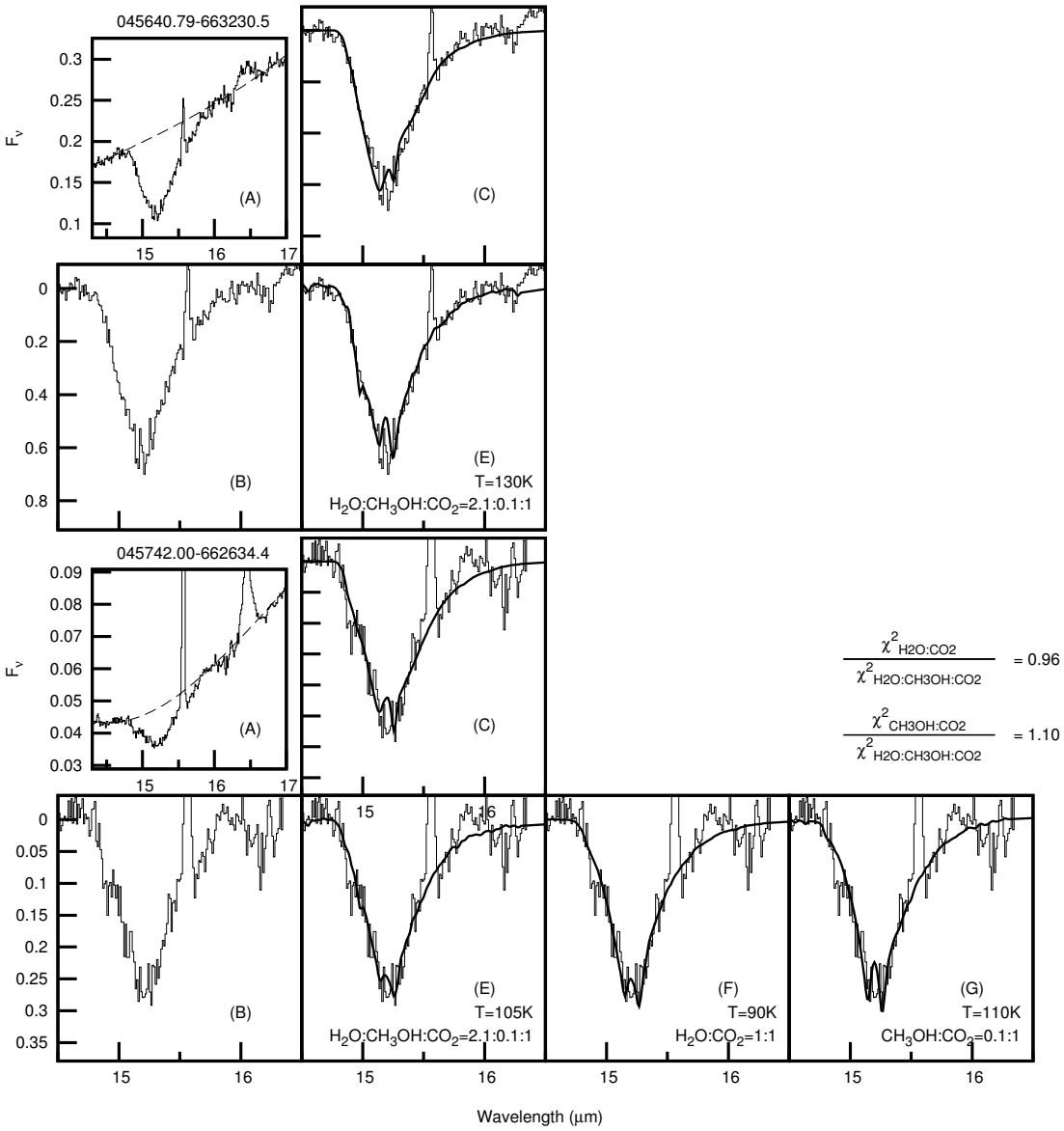

Fig. 5.— continued.

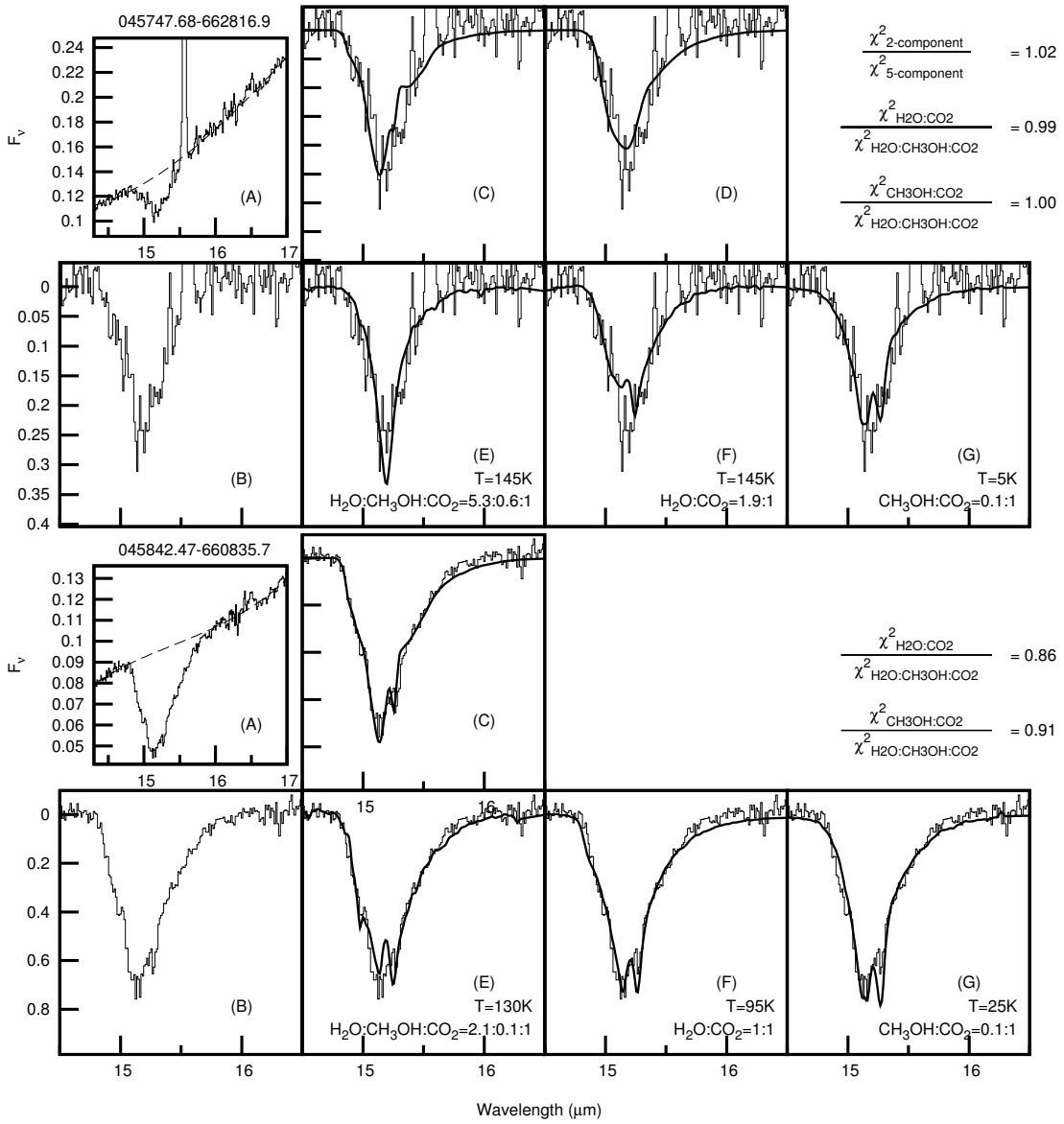

Fig. 6.— continued.

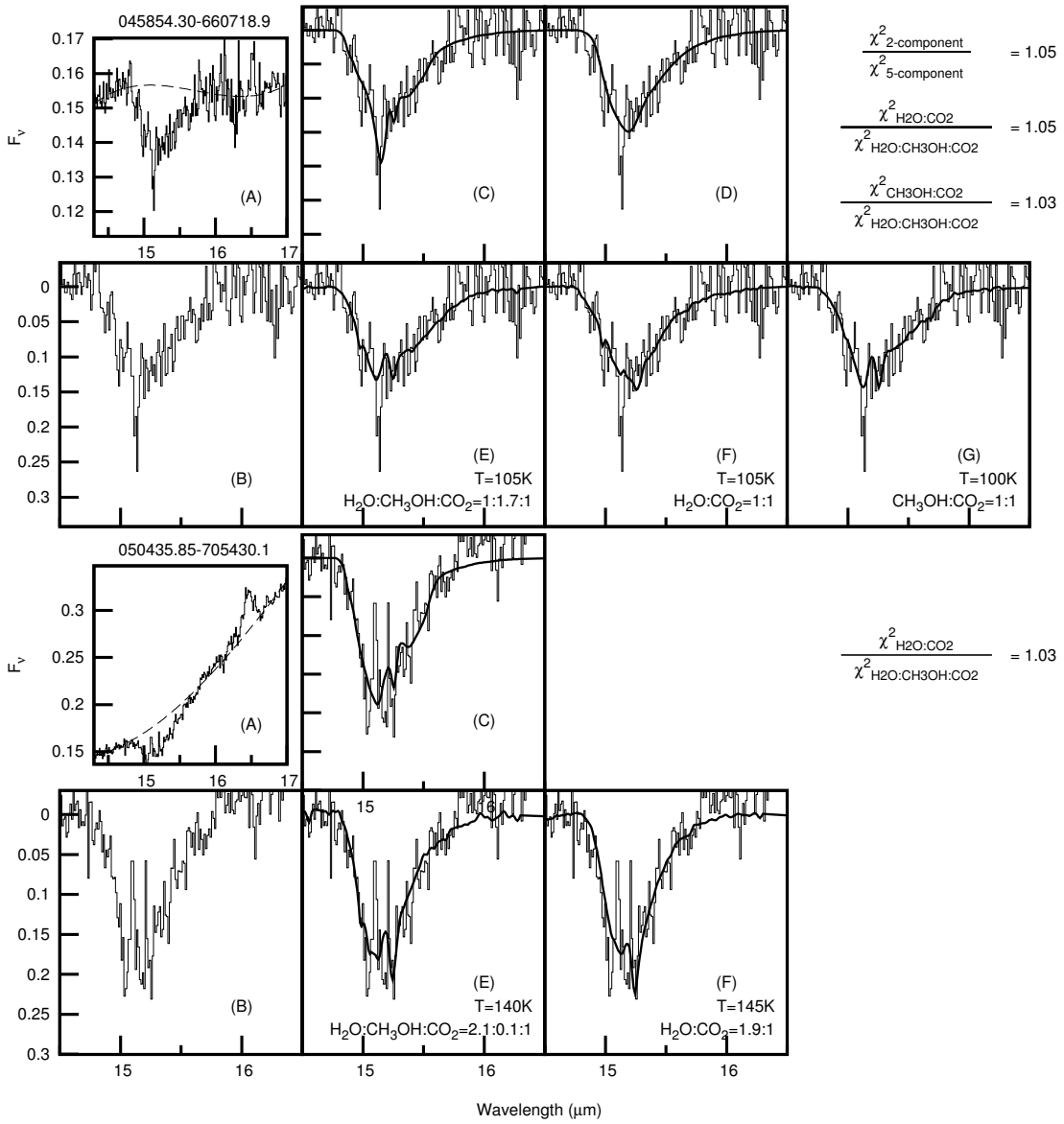

Fig. 7.— continued.

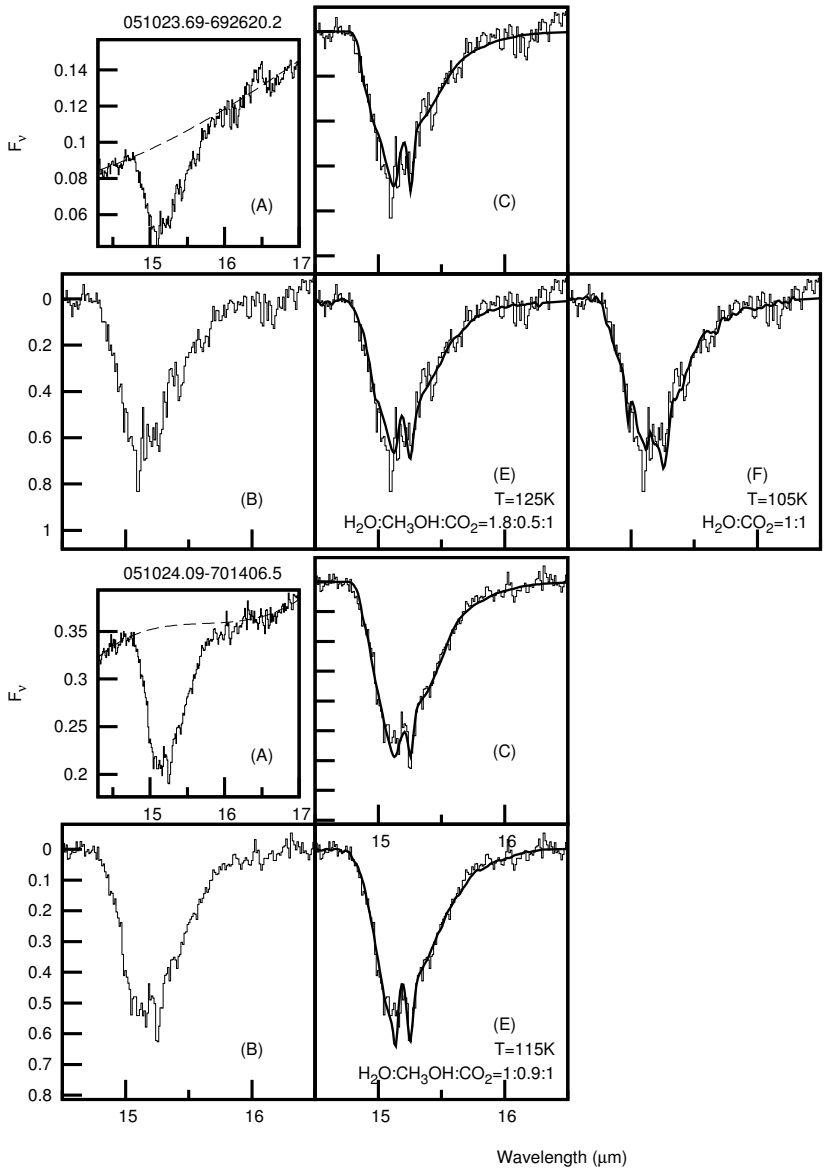

Fig. 8.— continued.

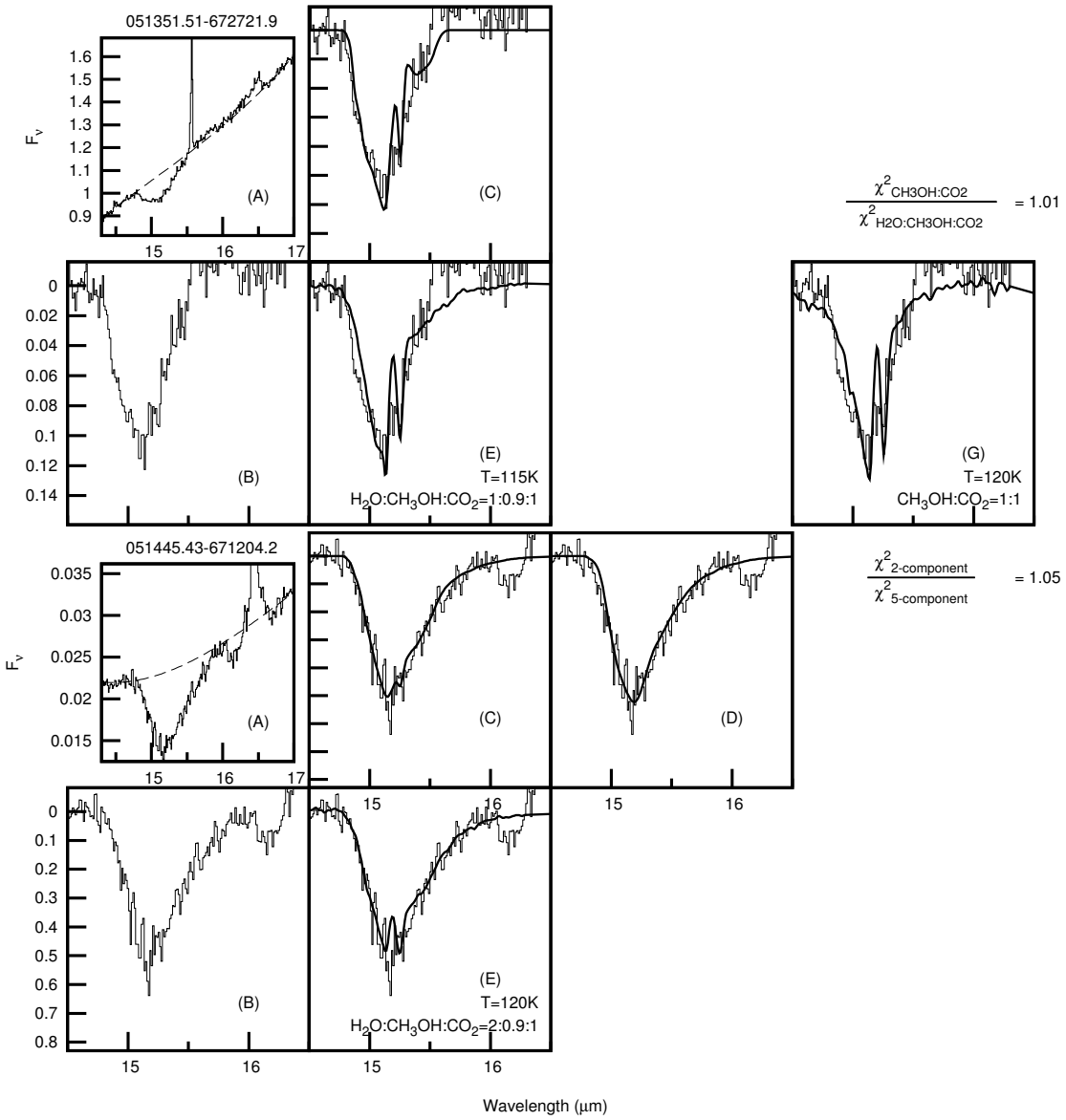

Fig. 9.— continued.

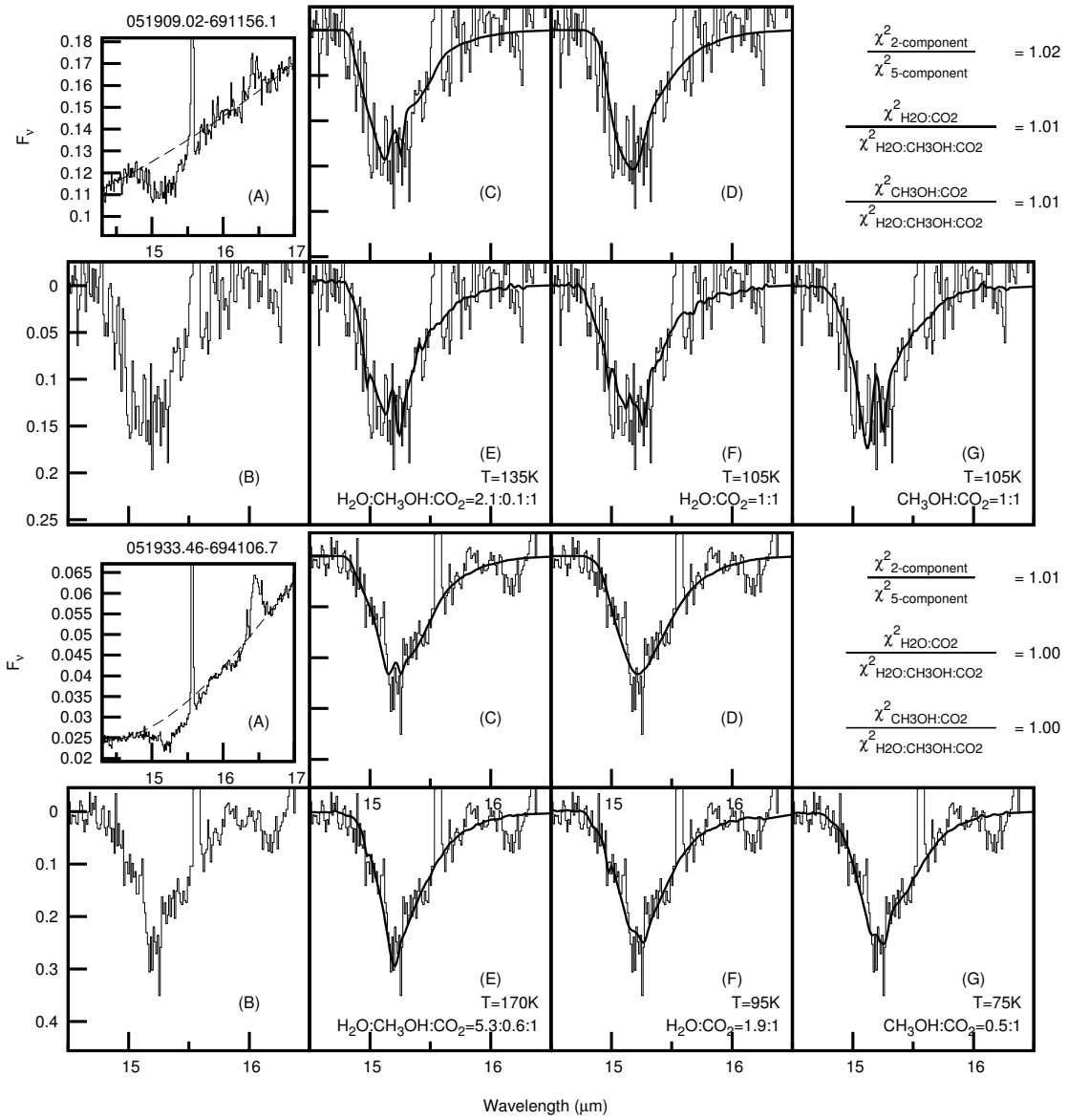

Fig. 10.— continued.

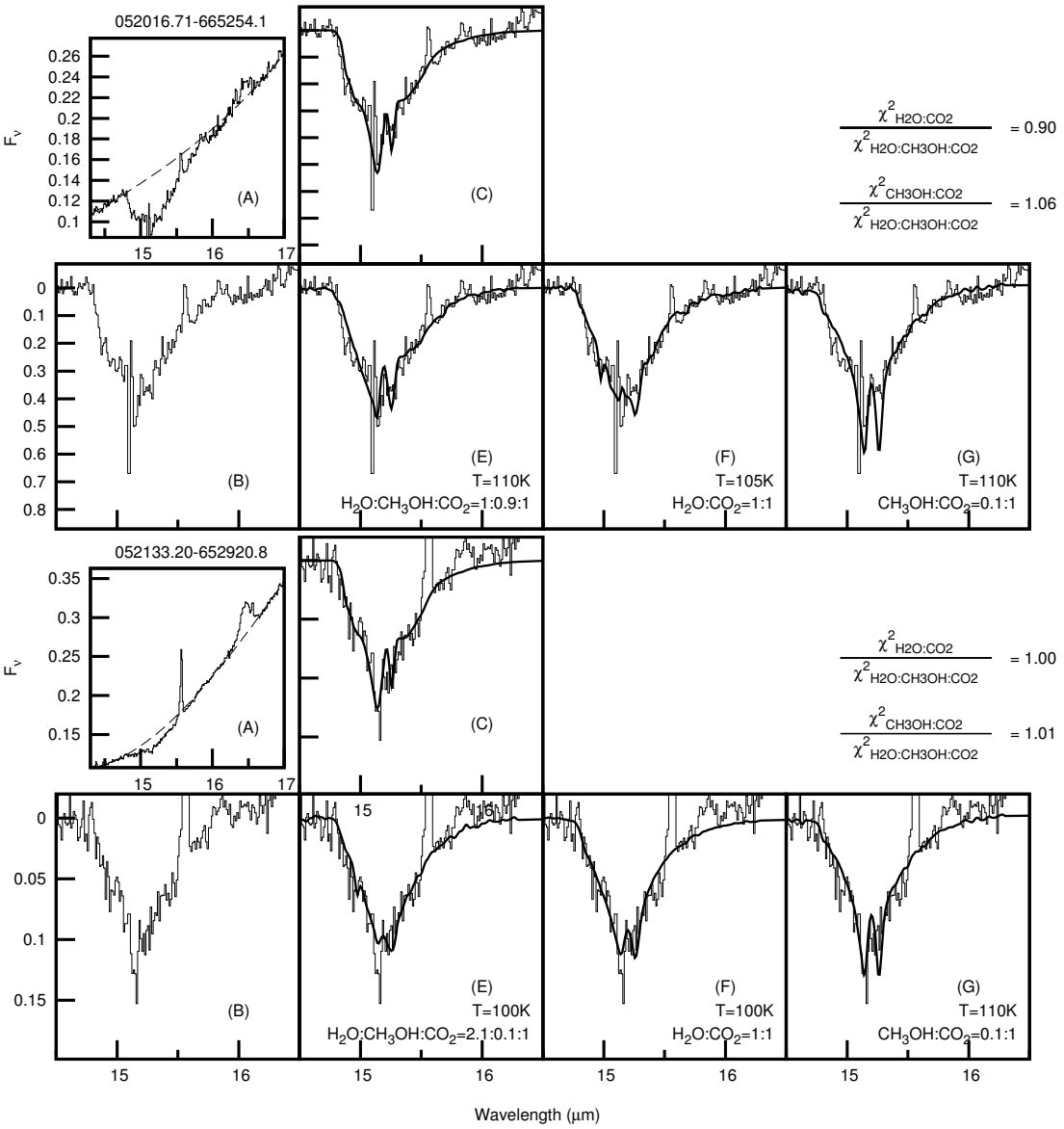

Fig. 11.— continued.

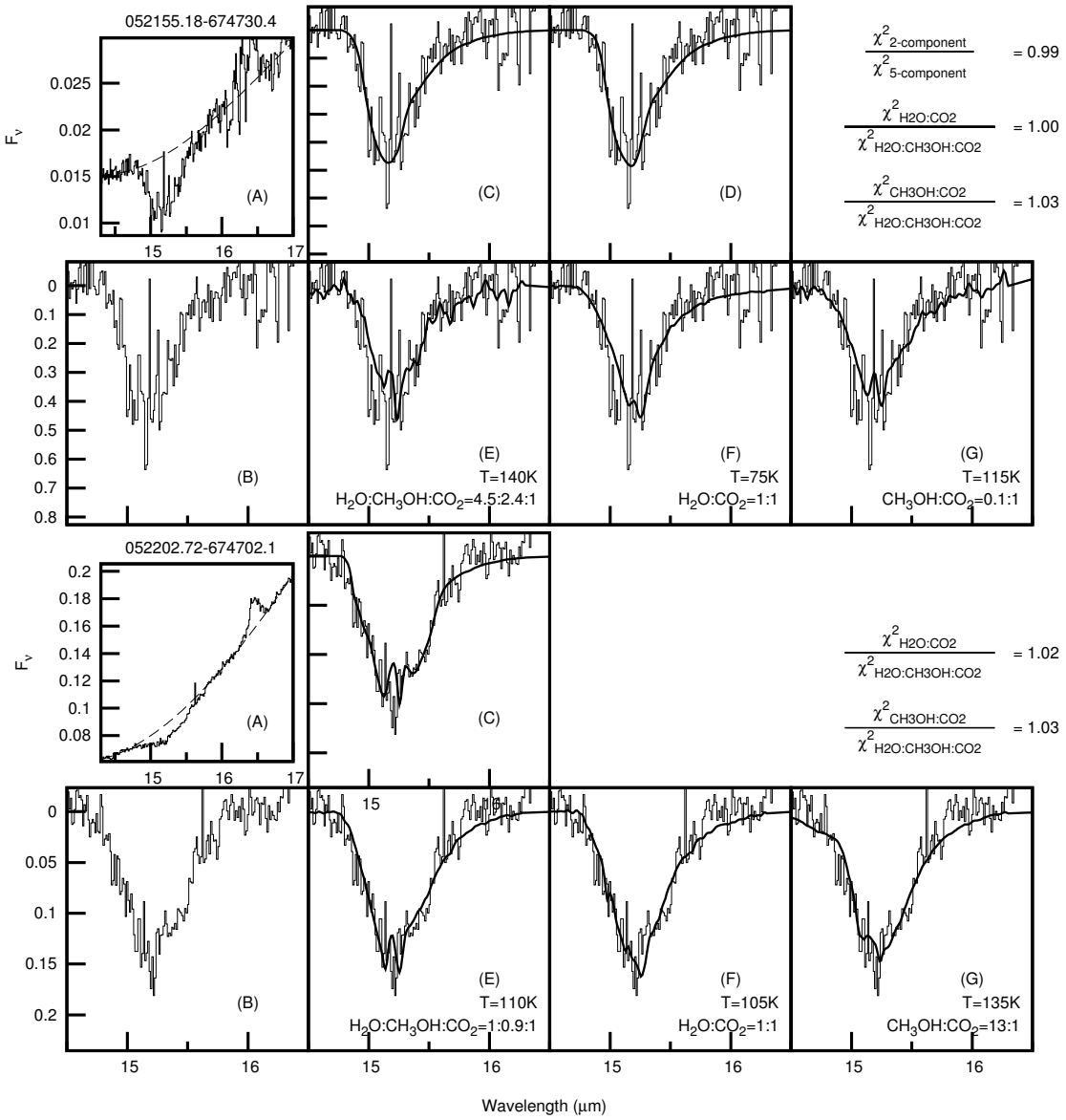

Fig. 12.— continued.

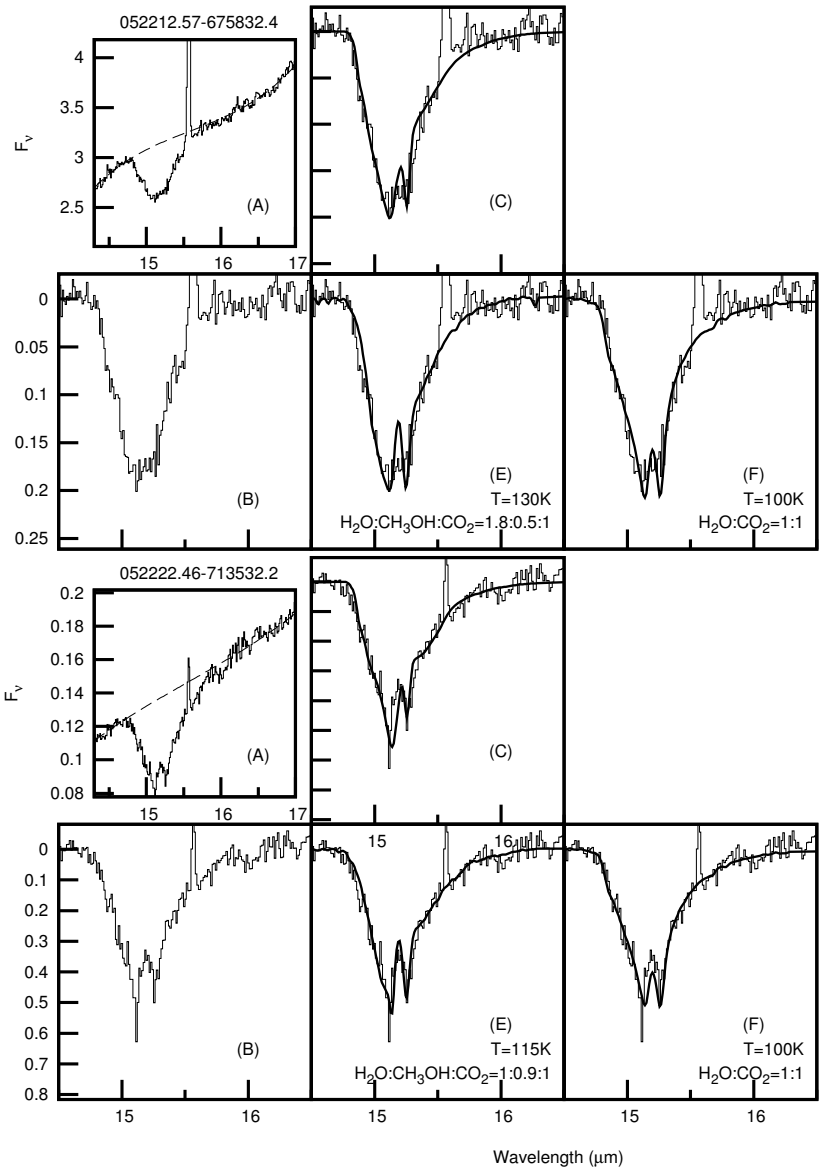

$\frac{\chi^2_{H2O:CO2}}{\chi^2_{H2O:CH3OH:CO2}} = 0.88$

$\frac{\chi^2_{H2O:CO2}}{\chi^2_{H2O:CH3OH:CO2}} = 1.03$

Fig. 13.— continued.

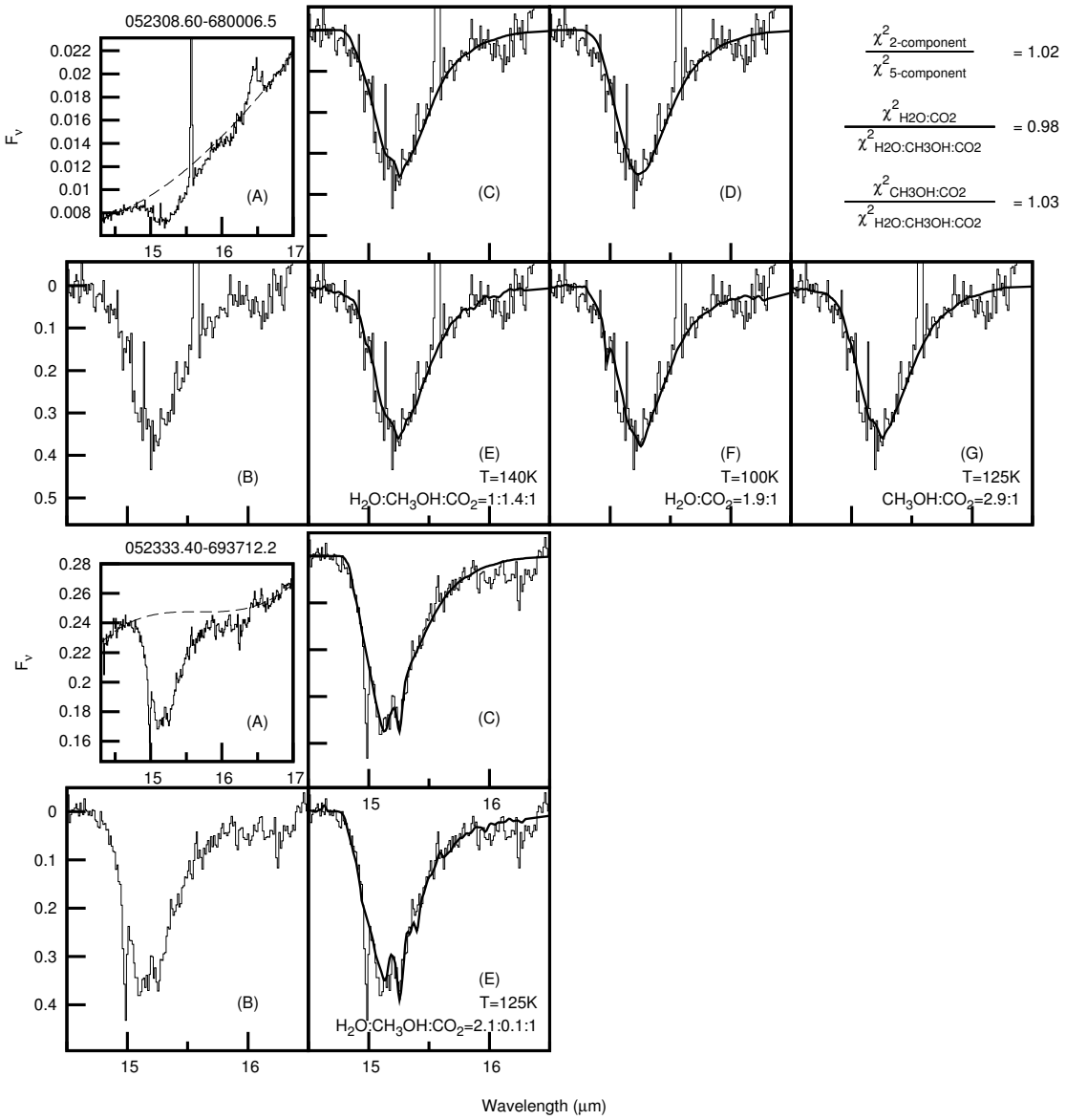

Fig. 14.— continued.

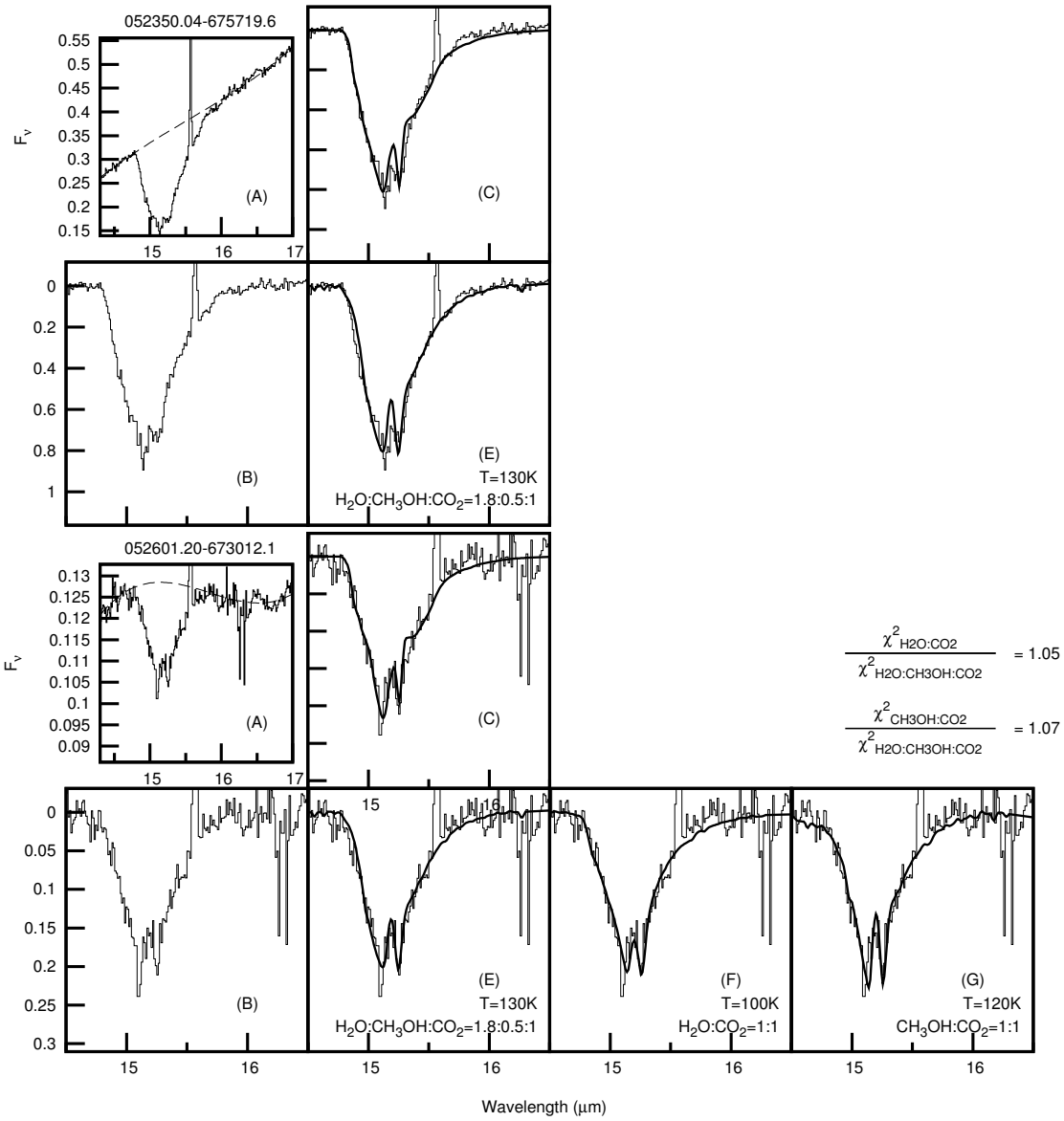

Fig. 15.— continued.

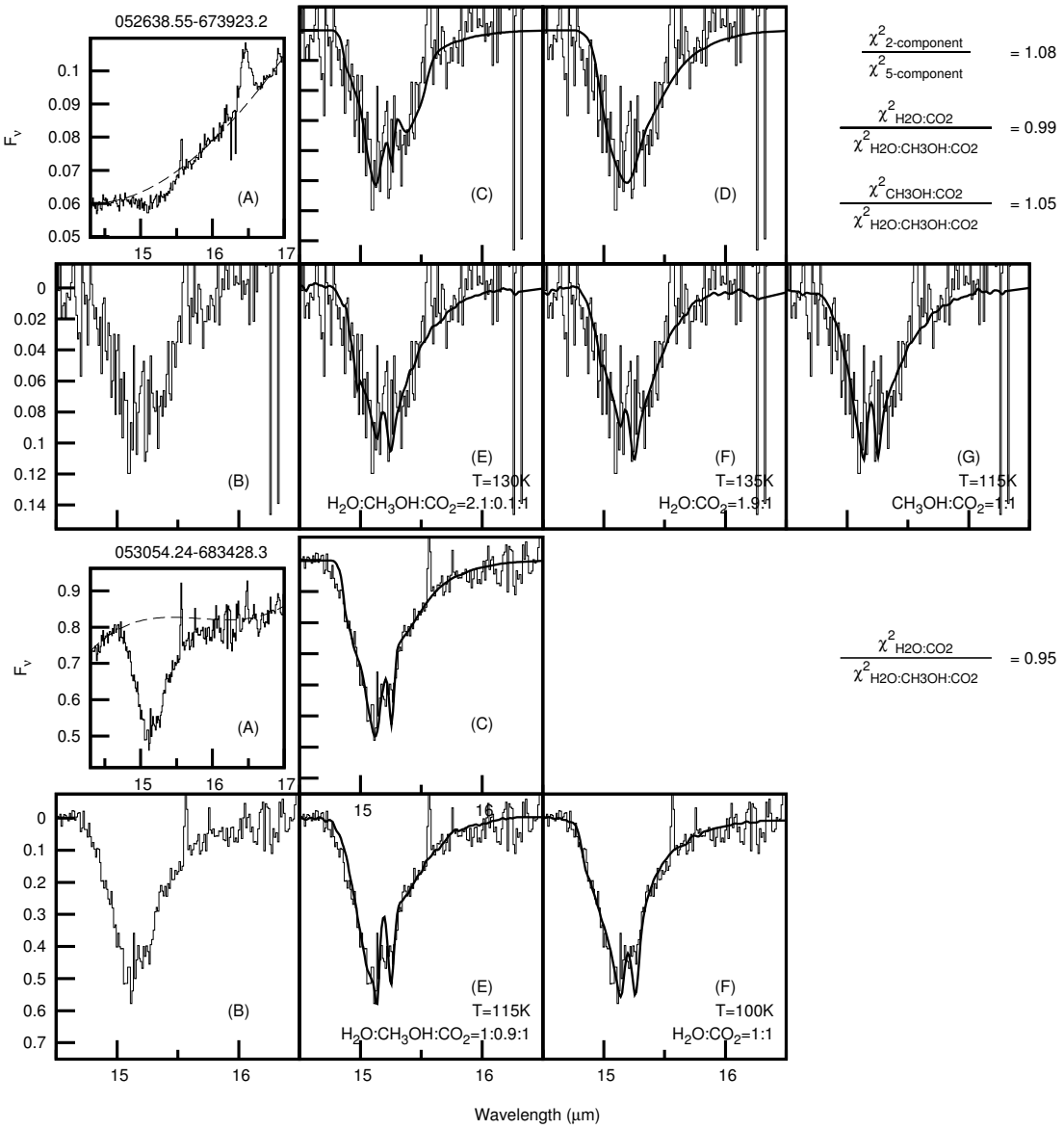

Fig. 16.— continued.

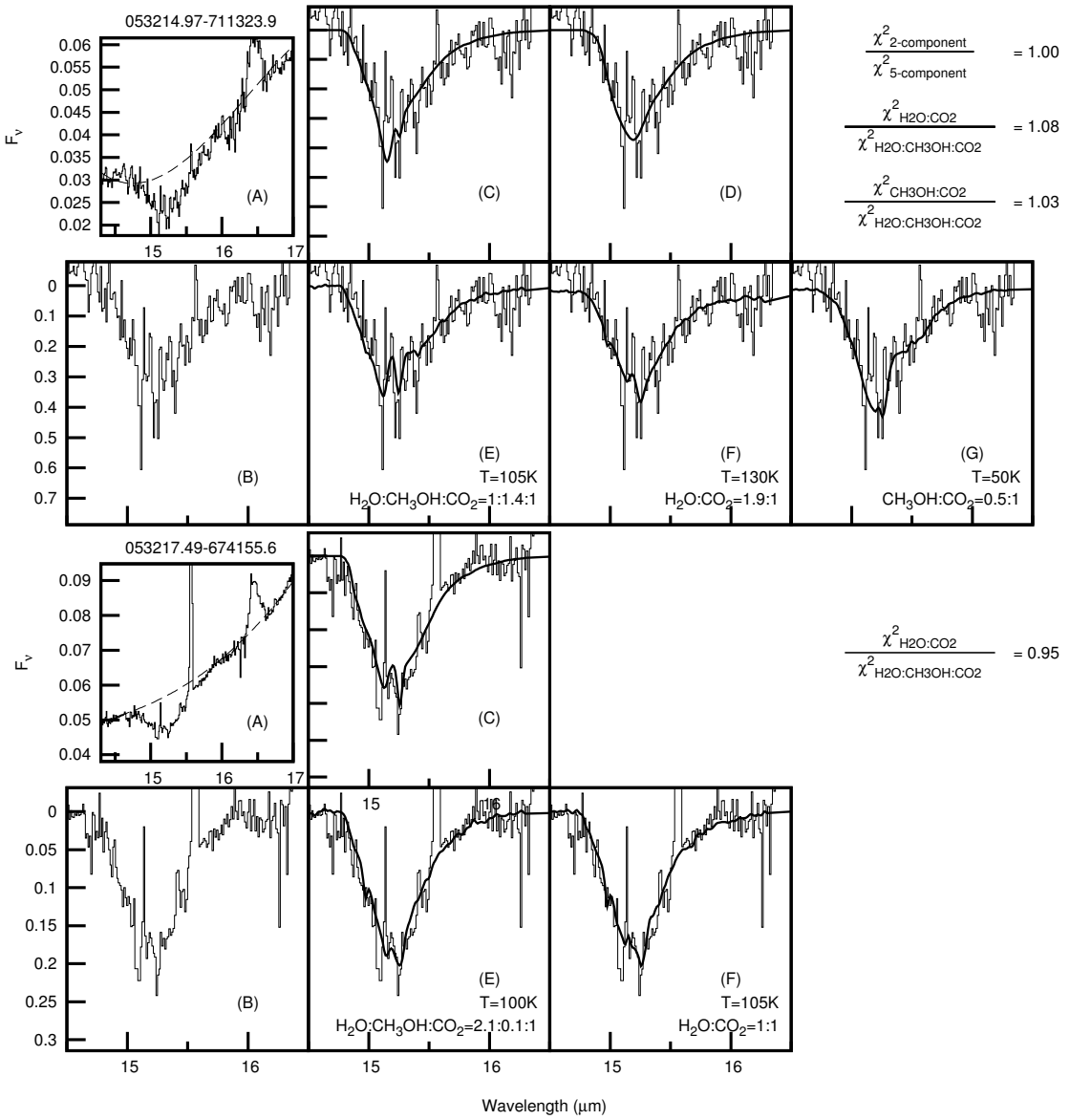

Fig. 17.— continued.

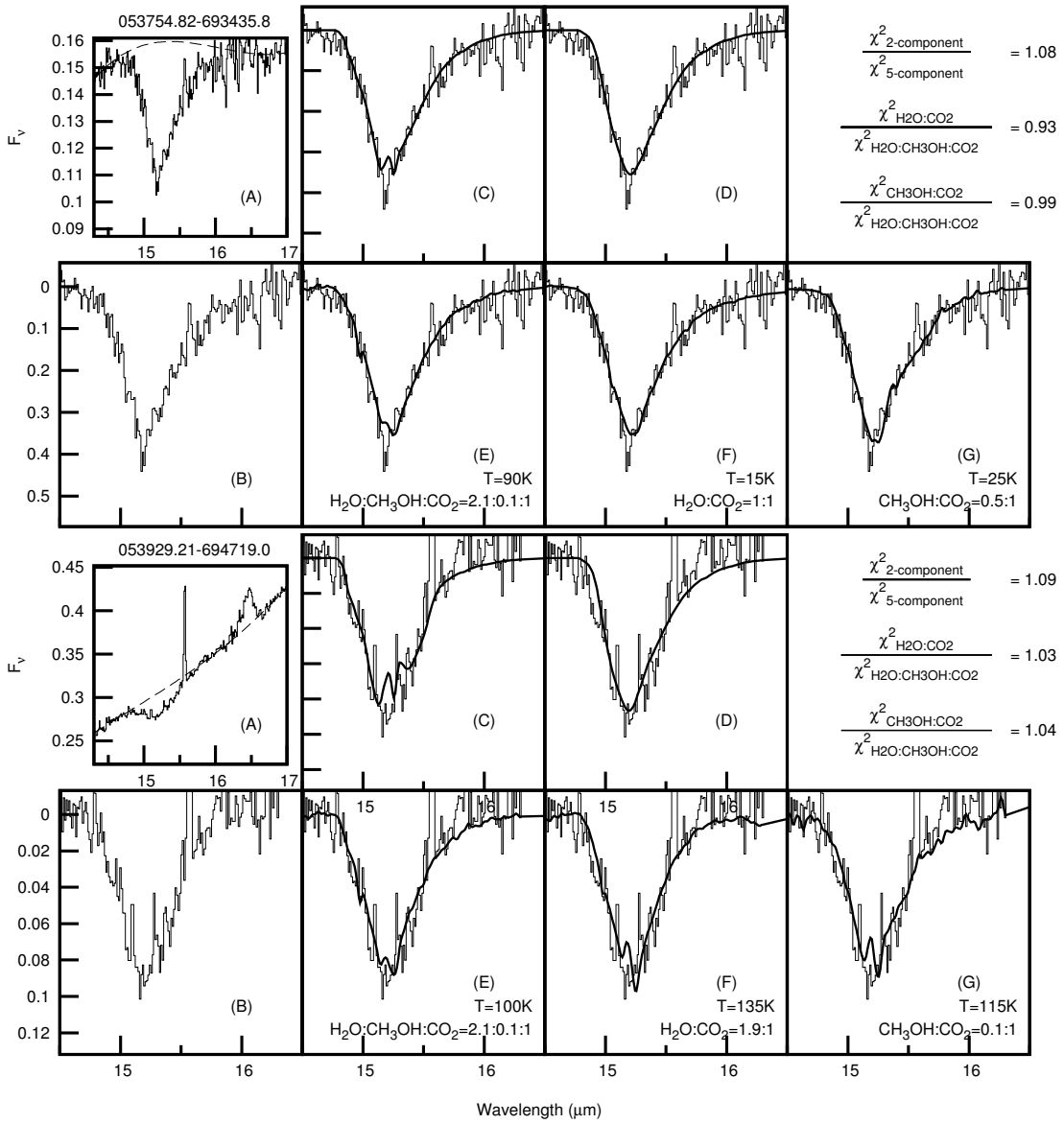

Fig. 18.— continued.

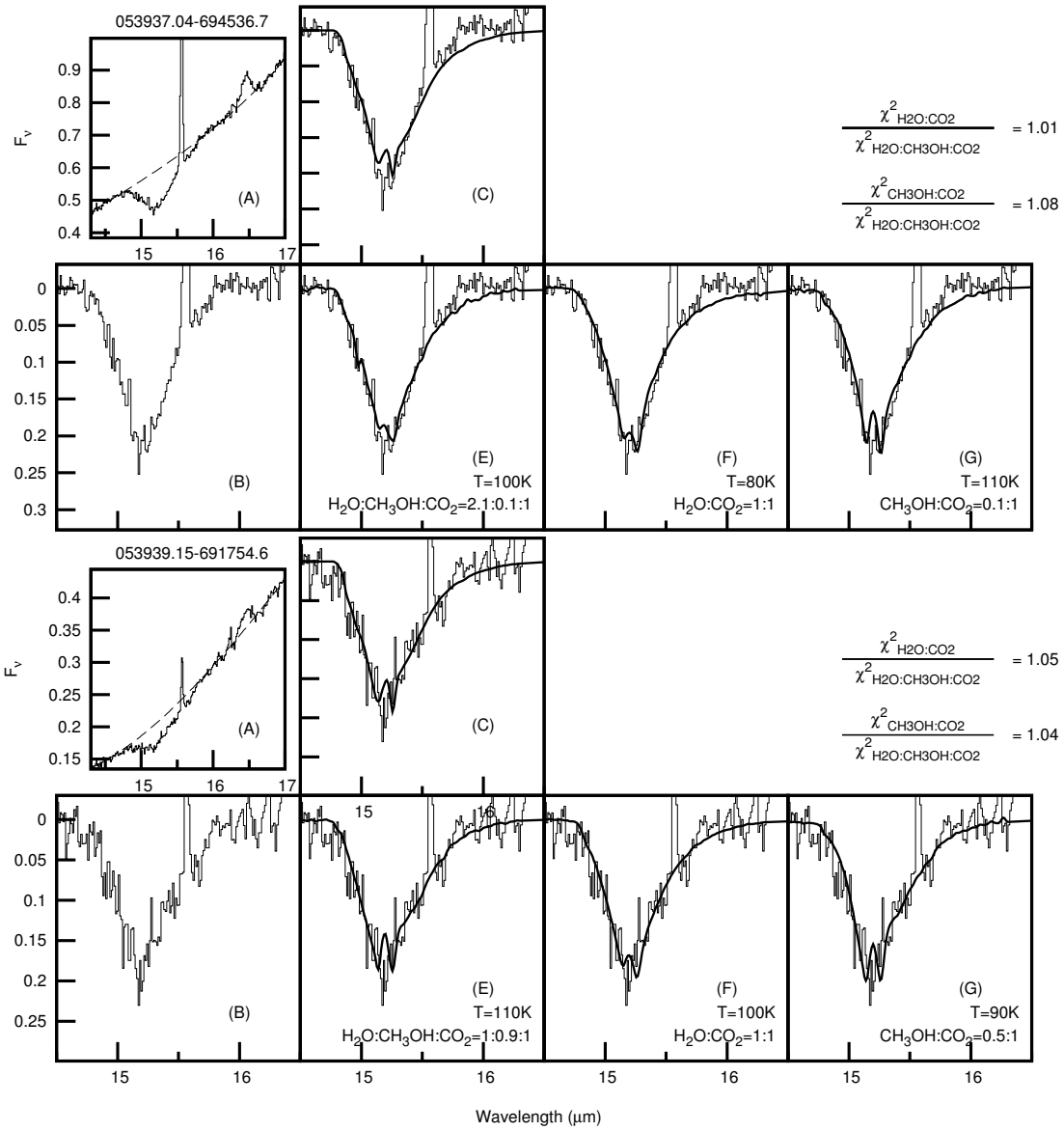

Fig. 19.— continued.

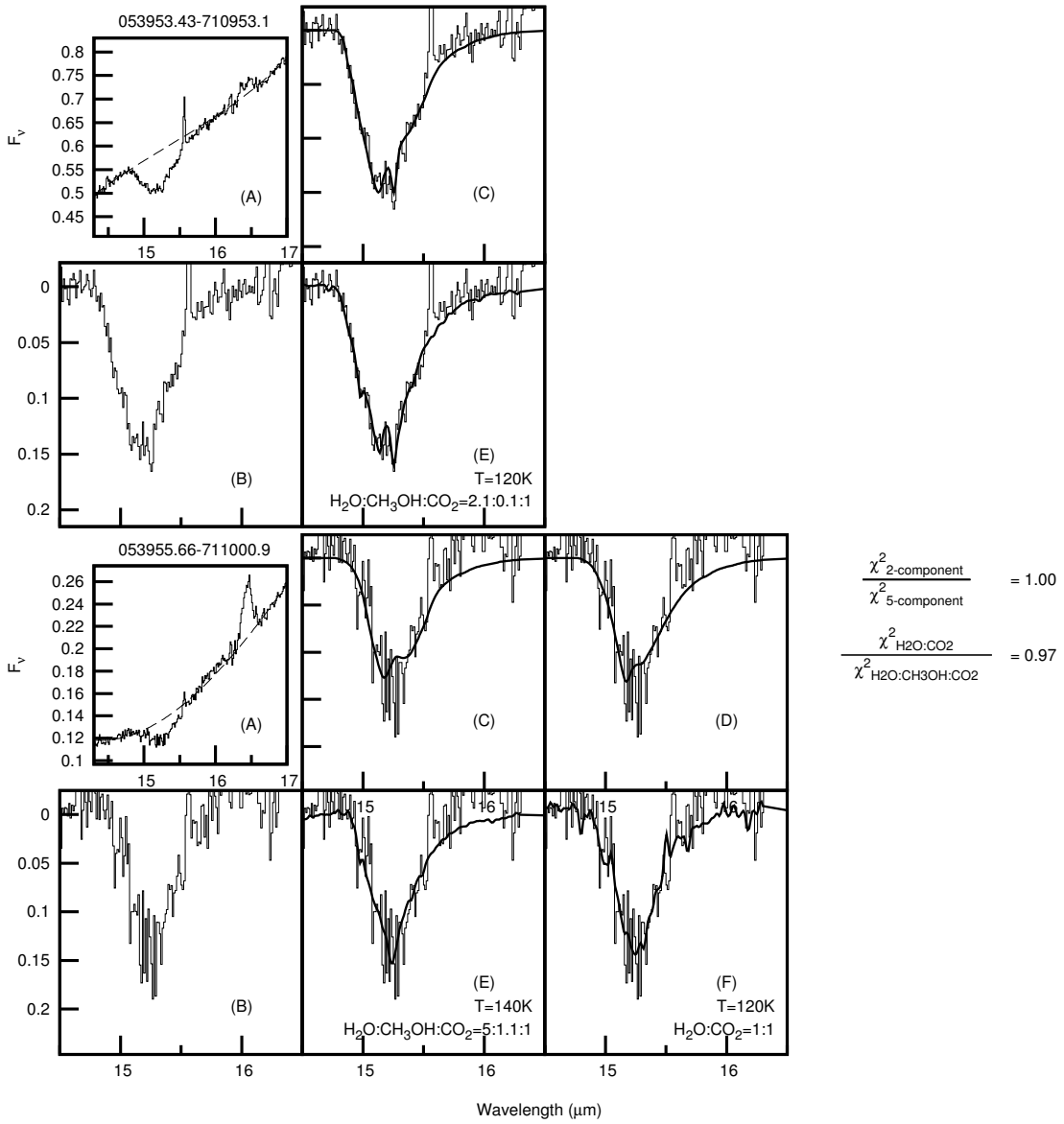

$$\frac{\chi^2_{\text{2-component}}}{\chi^2_{\text{5-component}}} = 1.00$$

$$\frac{\chi^2_{\text{H2O:CO2}}}{\chi^2_{\text{H2O:CH3OH:CO2}}} = 0.97$$

Fig. 20.— continued.

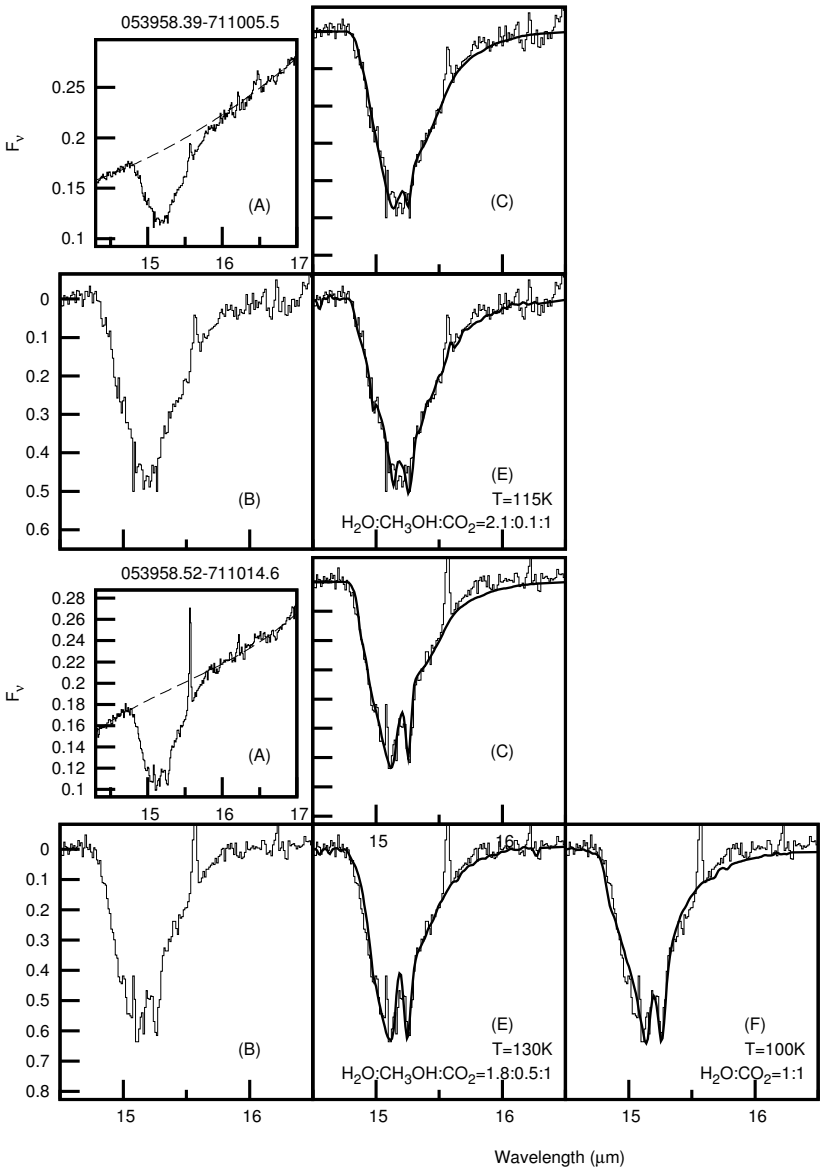

Fig. 21.— continued.

$$\frac{\chi^2_{H2O:CO2}}{\chi^2_{H2O:CH3OH:CO2}} = 1.09$$

References

Aguirre, J.E., et al. 2003, ApJ, 596, 273

Allamandola, L.J., Sandford, S.A., Tielens, A.G.G.M., & Herbst, T.M. 1992, ApJ, 399, 134

Andre, P., Ward-Thompson, D., & Barsony, M. 2000, Protostars and Planets IV, 59

Barkana, R., & Loeb, A. 2001, Physics Reports, 349, 125

Bate, M.R. 2009, MNRAS, 392, 1363

Beasley, A.J., Ellingsen, S.P., Claussen, M.J., & Wilcots, E. 1996, ApJ, 459, 600

Bel, N., Viala, Y.P., & Guidi, I. 1986, AAP, 160, 301

Bergin, E.A., Melnick, G.J., Gerakines, P.A., Neufeld, D.A., & Whittet, D.C.B. 2005, ApJL, 627, L33

Bergin, E.A., Langer, W.D., & Goldsmith, P.F. 1995, ApJ, 441, 222

Bergin, E.A., & Tafalla, M. 2007, ARAA, 45, 339

Beuther, H., Churchwell, E.B., McKee, C.F., & Tan, J.C. 2007, Protostars and Planets V, 165

Bonnell, I.A., Bate, M.R., Clarke, C.J., & Pringle, J.E. 1997, MNRAS, 285, 201

Boogert, A.C.A., et al. 2000, AAP, 353, 349

Boogert, A.C.A., Tielens, A.G.G.M., Ceccarelli, C., Boonman, A.M.S., van Dishoeck, E.F., Keane, J.V., Whittet, D.C.B., & de Graauw, T. 2000, AAP, 360, 683

Boogert, A.C.A., et al. 2004, ApJS, 154, 359

Boogert, A.C.A., et al. 2008, ApJ, 678, 985

Brooke, T.Y., Sellgren, K., & Geballe, T.R. 1999, ApJ, 517, 883

Book, L.G., Chu, Y.-H., Gruendl, R.A., & Fukui, Y. 2009, arXiv:0901.0400

Boulanger F, Abergel A, Cesarsky D, Bernard JP, Miville-Deschˆenes MA, et al. 2000. In ISO Beyond Point Sources: Studies of Extended Infrared Emission, ed. RJ Laureijs, K Leech, MF Kessler, ESA SP-455, p. 91

Brown, R.L., Wild, W., & Cunningham, C. 2004, Advances in Space Research, 34, 555

Cameron, A.G.W., & Truran, J.W. 1977, Icarus, 30, 447

Carey, S.J., Clark, F.O., Egan, M.P., Price, S.D., Shipman, R.F., & Kuchar, T.A. 1998, ApJ, 508, 721

Carpenter, J.M. 2000, AJ, 120, 3139

Cesaroni, R. 2005, Massive Star Birth: A Crossroads of Astrophysics, 227, 59

Cesaroni, R., Galli, D., Lodato, G., Walmsley, M., & Zhang, Q. 2006, NAT, 444, 703

Cesaroni, R., Galli, D., Lodato, G., Walmsley, C.M., & Zhang, Q. 2007, Protostars and Planets V, 197

Ceverino, D., & Klypin, A. 2009, ApJ, 695, 292

Chabrier, G. 2003, PASP, 115, 763

Chen, C.-H.R., Chu, Y.-H., Gruendl, R.A., Gordon, K.D., & Heitsch, F. 2009, ApJ, 695, 511

Chen, C.-H.R., Indebetouw1, R., Chu, Y.-H. Gruendl, R.A., Testor, G, Heitsch, F., Seale, J.P., Meixner, M., & Sewilo, M., 2010a, accepted to ApJ

Chen, C.-H.R., et al., 2010b, in preparation

Chiar, J.E., Adamson, A.J., & Whittet, D.C.B. 1996, ApJ, 472, 665

Chiar, J.E., Gerakines, P.A., Whittet, D.C.B., Pendleton, Y.J., Tielens, A.G.G.M., Adamson, A.J., & Boogert, A.C.A. 1998, ApJ, 498, 716

Chu, Y.-H., Chen, C.-H.R., Danforth, C., Dunne, B.C., Gruendl, R.A., Naz'e , Y., Oey, M.S., & Points, S.D. 2003, AJ, 125, 2098

Chu, Y.-H., et al. 2005, ApJL, 634, L189

Churchwell, E. 1990, AApR, 2, 79

Churchwell, E. 2002, ARAA, 40, 27

Churchwell, E.B., Indebetouw, R., Benjamin, R.A., & GLIMPSE Team 2002, Bulletin of the American Astronomical Society, 34, 1188

Connolly, A.J., Szalay, A.S., Bershady, M.A., Kinney, A.L., & Calzetti, D. 1995, AJ, 110, 1071

Crowther, P.A. 2005, Massive Star Birth: A Crossroads of Astrophysics, 227, 389

Cuppen, H.M., & Herbst, E. 2007, ApJ, 668, 294

Dartois, E., Schutte, W., Geballe, T.R., Demyk, K., Ehrenfreund, P., & D'Hendecourt, L. 1999, aap, 342, L32

De Buizer, J.M., Radomski, J.T., Telesco, C.M., & Pina, R.K. 2004, Bulletin of the American Astronomical Society, 36, 1619

de Graauw, T., et al. 1996, AAP, 315, L345

D'Hendecourt, L.B., Allamandola, L.J., Grim, R.J.A., & Greenberg, J.M. 1986, AAP, 158, 119

Egan, M.P., Shipman, R.F., Price, S.D., Carey, S.J., Clark, F.O., & Cohen, M. 1998, ApJL, 494, L199

Ehrenfreund, P., Boogert, A.C.A., Gerakines, P.A., Jansen, D.J., Schutte, W.A., Tielens, A.G.G.M., & van Dishoeck, E.F. 1996, AAP, 315, L341

Ehrenfreund, P., Boogert, A.C.A., Gerakines, P.A., Tielens, A.G.G.M., & van Dishoeck, E.F. 1997, AAP, 328, 649

Ehrenfreund, P., Dartois, E., Demyk, K., & D'Hendecourt, L. 1998, AAP, 339, L17

Ehrenfreund, P., et al. 1999, AAP, 350, 240

Ehrenfreund, P., d'Hendecourt, L., Charnley, S., & Ruiterkamp, R. 2001, JGR, 106, 33291

Ellis, J., Fields, B.D., & Schramm, D.N. 1996, ApJ, 470, 1227

Fazio, G.G., et al. 2004, ApJ, 154, 10

Feast, M. 1999, New Views of the Magellanic Clouds, 190, 542

Fontani, F., Cesaroni, R., Caselli, P., & Olmi, L. 2002, AAP, 389, 603

Francis, P.J., Hewett, P.C., Foltz, C.B., & Chaffee, F.H. 1992, ApJ, 398, 476

Fukui, Y., Mizuno, N., Yamaguchi, R., Mizuno, A., & Onishi, T. 2001, PASJ, 53, L41

Fukui, Y. 2002, Extragalactic Star Clusters, 207, 505

Garay, G. 2004, Star Formation at High Angular Resolution, 221, 169

Garcia-Segura, G., & Franco, J. 1996, ApJ, 469, 171

Garay, G., & Lizano, S. 1999, PASP, 111, 1049

Gardner, J.P., et al. 2006, Space Science Reviews, 123, 485

Gaume, R.A., Goss, W.M., Dickel, H.R., Wilson, T.L., & Johnston, K.J. 1995, ApJ, 438, 776

Gerakines, P.A., et al. 1999, ApJ, 522, 357

Gerakines, P.A., Schutte, W.A., Greenberg, J.M., & van Dishoeck, E.F. 1995, AAP, 296, 810

Gibb, E.L., Gerakines, P.A., & Whittet, D.C.B. 1998, Bulletin of the American Astronomical Society, 30, 1355

Gibb, E.L., et al. 2000, ApJ, 536, 347

Gibb, E.L., Whittet, D.C.B., Boogert, A.C.A., & Tielens, A.G.G.M. 2004, ApJS, 151, 35

Grim, R.J.A., Greenberg, J.M., Schutte, W.A., & Schmitt, B. 1989, ApJL, 341, L87

Gruendl, R.A., & Chu, Y.-H. 2009, ApJS, 184, 172

Gruendl, R.A., Chu, Y.-H., Seale, J.P., Matsuura, M., Speck, A.K., Sloan, G.C., & Looney, L.W. 2008, ApJl, 688, L9

Hagen, W., Allamandola, L.J., & Greenberg, J.M. 1979, APSS, 65, 215

Hartmann, L., Megeath, S.T., Allen, L., Luhman, K., Calvet, N., D'Alessio, P., Franco-Hernandez, R., & Fazio, G. 2005, ApJ, 629, 881

Henry, T.J. 2004, Spectroscopically and Spatially Resolving the Components of the Close Binary

Stars, 318, 159

Higdon, S.J.U., et al. 2004, PASP, 116, 975

Hoare, M.G., Kurtz, S.E., Lizano, S., Keto, E., & Hofner, P. 2007, Protostars and Planets V, 181

Houck, J.R., et al. 2004, ApJS, 154, 18

Hudson, R.L., & Moore, M.H. 1999, Icarus, 140, 451

Indebetouw, R., Whitney, B.A., Johnson, K.E., & Wood, K. 2006, ApJ, 636, 362

Ivezic, Z., & Elitzur, M. 1997, MNRAS, 287, 799

Janka, H.-T., Langanke, K., Marek, A., MartÍnez-Pinedo, G., Mueller, B. 2007, Physics Reports, 442, 38

Kastner, J.H., Thorndike, S.L., Romanczyk, P.A., Buchanan, C.L., Hrivnak, B.J., Sahai, R., & Egan, M. 2008, AJ, 136, 1221

Keane, J.V., Tielens, A.G.G.M., Boogert, A.C.A., Schutte, W.A., & Whittet, D.C.B. 2001, AAP, 376, 254

Kennicutt, R.C., Jr. 1998, ARAA, 36, 189

Kemper, F., et al. 2010, arXiv:1004.1142

Kennicutt, R.C. 2005, Massive Star Birth: A Crossroads of Astrophysics, 227, 3

Knez, C., et al. 2005, ApJL, 635, L145

Kessler, M.F., et al. 1996, AAP, 315, L27

Keto, E. 2007, ApJ, 666, 976

Kowalski, M., et al. 2008, ApJ, 686, 749

Kraemer, K.E., Sloan, G.C., Price, S.D., & Walker, H.J. 2002, ApJS, 140, 389

Krumholz, M.R., & Bonnell, I.A. 2007, arXiv:0712.0828

Krumholz, M.R., Klein, R.I., McKee, C.F., Offner, S.S.R., & Cunningham, A.J. 2009, Science,

323, 754

Kurtz, S., Cesaroni, R., Churchwell, E., Hofner, P., & Walmsley, C.M. 2000, Protostars and Planets IV, 299

Kwon, W., Looney, L.W., Crutcher, R.M., & Kirk, J.M. 2006, ApJ, 653, 1358

Lada, C.J., & Lada, E.A. 2003, ARAA, 41, 57

Larson, R.B. 1969, MNRAS, 145, 271

Lazendic, J.S., Whiteoak, J.B., Klamer, I., Harbison, P.D., & Kuiper, T.B.H. 2002, MNRAS, 331, 969

Lis, D.C., Menten, K.M., Serabyn, E., & Zylka, R. 1994, ApJL, 423, L39

Lis, D.C., & Menten, K.M. 1998, ApJ, 507, 794

Lizano, S., Canto, J., Garay, G., & Hollenbach, D. 1996, ApJ, 468, 739

Looney, L.W., Mundy, L.G., & Welch, W.J. 2003, ApJ, 592, 255

Looney, L.W., Tobin, J.J., & Fields, B.D. 2006, ApJ, 652, 1755

Loup, C., Zijlstra, A.A., Waters, L.B.F.M., & Groenewegen, M.A.T. 1997, AAPs, 125, 419

Luhman, K.L., & Rieke, G.H. 1999, ApJ, 525, 440

Martin-Hernandez, N.L., et al. 2002, AAP, 381, 606

Mathis, J.S., Rumpl, W., & Nordsieck, K.H. 1977, ApJ, 217, 425

McCray, R., & Kafatos, M. 1987, ApJ, 317, 190

McKee, C.F., & Ostriker, E.C. 2007, ARAA, 45, 565

Meixner, M., et al. 2006, AJ, 132, 2268

Meyer, B.S., & Clayton, D.D. 2000, Space Science Reviews, 92, 133

Mill, J.D., et al. 1994, Journal of Spacecraft and Rockets, 31, 900

Murakami, H., et al. 2007, PASJ, 59, 369

Murtagh, F., & Heck, A. 1987, Astrophysics and Space Science Library, 131

Oberg, K.I., Fayolle, E.C., Cuppen, H.M., van Dishoeck, E.F., & Linnartz, H. 2009, arXiv:0907.3948

Oliveira, J.M., van Loon, J.T., Stanimirovi'c , S., & Zijlstra, A.A. 2006, MNRAS, 372, 1509

Oliveira, J.M., et al. 2009, arXiv:0911.0532

Onaka, T., et al. 2007, PASJ, 59, 401

Perlmutter, S., et al. 1999, ApJ, 517, 565

Peeters, E., Hony, S., Van Kerckhoven, C., Tielens, A.G.G.M., Allamandola, L.J., Hudgins, D.M., & Bauschlicher, C.W. 2002, AAP, 390, 1089

Peeters, E., Mattioda, A.L., Hudgins, D.M., & Allamandola, L.J. 2004, ApJL, 617, L65

Perault, M., et al. 1996, AAP, 315, L165

Pilbratt, G.L., et al. 2010, AAP, 518, L1

Pontoppidan, K.M., et al. 2008, ApJ, 678, 1005

Reid, N., Tinney, C., & Mould, J. 1990, ApJ, 348, 98

Rieke, G.H., et al. 2004, ApJS, 154, 25

Robitaille, T.P., Whitney, B.A., Indebetouw, R., Wood, K., & Denzmore, P. 2006, ApJS, 167, 256

Robitaille, T.P., Whitney, B.A., Indebetouw, R., & Wood, K. 2007, ApJS, 169, 328

Sakon, I., et al. 2006, ApJ, 651, 174

Sandford, S.A., & Allamandola, L.J. 1993, ApJ, 417, 815

Schutte, W.A., et al. 1999, AAP, 343, 966

Shapiro, S.L., & Teukolsky, S.A. 1983, Research supported by the National Science Foundation. New York, Wiley-Interscience, 1983, 663

Shimonishi, T., Onaka, T., Kato, D., Sakon, I., Ita, Y., Kawamura, A., & Kaneda, H. 2008, ApJL, 686, L99

Shimonishi, T., Onaka, T., Kato, D., Sakon, I., Ita, Y., Kawamura, A., & Kaneda, H. 2010, arXiv:1004.0049

Shu, F.H., Adams, F.C., & Lizano, S. 1987, ARAA, 25, 23

Shu, F.H., Adams, F.C., & Lizano, S. 1987, ARAA, 25, 23

Seale, J.P., & Looney, L.W. 2008, ApJ, 675, 427

Seale, J.P., Looney, L.W., Chu, Y.-H., Gruendl, R.A., Brandl, B., Rosie Chen, C.-H., Brandner, W., & Blake, G.A. 2009, ApJ, 699, 150

Shepherd, D.S., & Churchwell, E. 1996, ApJ, 472, 225

Smith, R.C., & The MCELS Team 1999, New Views of the Magellanic Clouds, 190, 28

Smith, R.G., Sellgren, K., & Tokunaga, A.T. 1989, ApJ, 344, 413

Smith, J.D.T., et al. 2007, ApJ, 656, 770

Soifer, B.T., Russell, R.W., & Merrill, K.M. 1976, ApJ, 210, 334

Sridharan, T.K., Beuther, H., Saito, M., Wyrowski, F., & Schilke, P. 2005, ApJL, 634, L57

Srinivasan, G., Sahijpal, S., Ulyanov, A.A., & Goswami, J.N. 1996, GCA, 60, 1823

Tachibana, S., & Huss, G.R. 2003, ApJL, 588, L41

Tan, J.C. 2005, Massive Star Birth: A Crossroads of Astrophysics, 227, 318

Tan, J.C., & McKee, C.F. 2003, arXiv:astro-ph/0309139

Tenorio-Tagle, G., & Bodenheimer, P. 1988, ARAA, 26, 145

Tielens, A.G.G.M., & Hagen, W. 1982, AAP, 114, 245

Tielens, A.G.G.M., Allamandola, L.J., Bregman, J., Goebel, J., Witteborn, F.C., & D'Hendecourt, L.B. 1984, ApJ, 287, 697

Tielens, A.G.G.M., & Allamandola, L.J. 1987, Interstellar Processes, 134, 397

Tielens, A.G.G.M., Tokunaga, A.T., Geballe, T.R., & Baas, F. 1991, ApJ, 381, 181

Tobin, J.J., Looney, L.W., Mundy, L.G., Kwon, W., & Hamidouche, M. 2007, ApJ, 659, 1404

Vaidya, K., Chu, Y.-H., Gruendl, R.A., Chen, C.-.R., & Looney, L.W. 2009, arXiv:0910.5901

van Broekhuizen, F.A., Groot, I.M.N., Fraser, H.J., van Dishoeck, E.F., & Schlemmer, S. 2006, AAP, 451, 723

van der Tak, F.F.S., van Dishoeck, E.F., Evans, N.J., II, & Blake, G.A. 2000, ApJ, 537, 283

van Dishoeck, E.F. 2004, ARAA, 42, 119

van Dishoeck, E.F., & Blake, G.A. 1998, ARAA, 36, 317

van Dishoeck, E.F., et al. 1996, AAP, 315, L349

van Dishoeck, E.F., Wright, C.M., Cernicharo, J., Gonzalez-Alfonso, E., de Graauw, T., Helmich, F.P., & Vandenbussche, B. 1998, ApJL, 502, L173

van Loon, J.T., Zijlstra, A.A., Bujarrabal, V., & Nyman, L.-AA . 2001, AAP, 368, 950

van Loon, J.T., et al. 2005, MNRAS, 364, L71

van Loon, J.T., et al. 2010, AJ, 139, 68

Vanhala, H.A.T., & Boss, A.P. 2000, ApJ, 538, 911

Wang, P., Li, Z.-Y., Abel, T., & Nakamura, F. 2010, ApJ, 709, 27

Watanabe, N., & Kouchi, A. 2002, ApJL, 571, L173

Welty, D.E., Federman, S.R., Gredel, R., Thorburn, J.A., & Lambert, D.L. 2006, ApJS, 165, 138

Werner, M.W., et al. 2004, ApJS, 154, 1

White, D.W., Gerakines, P.A., Cook, A.M., & Whittet, D.C.B. 2009, ApJS, 180, 182

Whitney, B.A., Wood, K., Bjorkman, J.E., & Wolff, M.J. 2003, ApJ, 591, 1049

Whitney, B.A., Wood, K., Bjorkman, J.E., & Cohen, M. 2003, ApJ, 598, 1079

Whitney, B.A., et al. 2008, AJ, 136, 18

Whittet, D.C.B., Bode, M.F., Longmore, A.J., Adamson, A.J., McFadzean, A.D., Aitken, D.K., & Roche, P.F. 1988, MNRAS, 233, 321

Whittet, D.C.B., et al. 1997, ApJ, 490, 729

Whittet, D.C.B., et al. 1998, ApJL, 498, L159

Whittet, D.C.B., Shenoy, S.S., Bergin, E.A., Chiar, J.E., Gerakines, P.A., Gibb, E.L., Melnick, G.J., & Neufeld, D.A. 2007, ApJ, 655, 332

Whittet, D.C.B., Cook, A.M., Chiar, J.E., Pendleton, Y.J., Shenoy, S.S., & Gerakines, P.A. 2009, ApJ, 695, 94

Wood, P.R., Whiteoak, J.B., Hughes, S.M.G., Bessell, M.S., Gardner, F.F., & Hyland, A.R. 1992, ApJ, 397, 552

Woosley, S.E., Heger, A., & Weaver, T.A. 2002, Reviews of Modern Physics, 74, 1015

Yorke, H.W., & Sonnhalter, C. 2002, ApJ, 569, 846

Zasowski, G., Kemper, F., Watson, D.M., Furlan, E., Bohac, C.J., Hull, C., & Green, J.D. 2009, ApJ, 694, 459

Zinnecker, H., & Yorke, H.W. 2007, ARAA, 45, 481

Zubko, V.G., Mennella, V., Colangeli, L., & Bussoletti, E. 1996, MNRAS, 282, 1321